SEISMIC WAVE MODELLING USING FINITE DIFFERENCE METHODS

ISMAIL DEMIR B.Sc.

A submission presented in partial fulfilment of the
requirements of the University of Glamorgan / Prifysgol Morgannwg
for the degree of Doctor of Philosophy.

School of Accounting and Mathematics
Division of Maths and Computing

November 1998

CERTIFICATE OF RESEARCH

This is to certify that, except where specific reference is made, the work presented within this thesis is the result of the investigation undertaken by the candidate.

Candidate: .....

Director of Studies: .....

Supervisor: .....

Date: .....

DECLARATION

This is to certify that neither this thesis or any part of it has been presented or is currently being submitted in candidature for any other degree other than the degree of Doctor Philosophy of the University of Glamorgan / Prifysgol Morgannwg.

Candidate: 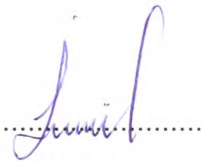

I wish to thank my director of studies, Dr. R. W. Williams, and to my supervisor Prof. R. J. Wiltshire for their help, encouragement, guidance and constructive criticism provided during this research project.

I am grateful to the Canakkale Onsekiz Mart University for their financal support during my research period, and also to the Turkish Government and peoples for their support.

Finally, I would like to express my deepest gratitude to my wife Fatma, my mother, father and all my family for their support and constant encourgement during the period of accomplishing this thesis. Also my thanks to all colleagues, and the technicians of the Maths and Computing Division.

The main aim of the thesis is to determine the most satisfactory numerical approach to model numerically seismic wave propagation, and also to ascertain if rock interfaces could be inferred from signals received at a geophone.

We mainly employ two different models together, namely the "Parsimonious staggered grid" and the "Box" model. So far as we are aware nobody else has studied these two models in conjunction and this is a particularly novel aspect of this work. Also this approach enhances flexibility and accuracy of the numerical solution.

We consider the propagation of seismic waves in both 2-D and 3-D coordinate systems and include the use of boreholes for the source of signals, and also for geophones. One goal of this work was to begin to fill in this gap by including simple borehole configurations within elastic media our new approach modelling, which we have completed successfully.

We investigate the appropriateness of the different boundary conditions used to manufacture a finite computational domain. The Reynolds ABCs are found to be marginally better than Clayton-Engquist ABCs and are stable in all cases for our approach. We also adopt a scaling technique with variable grid geometry so as to extend the scope of the domain under consideration. The approach can prove most useful in single borehole modelling if used with care.

We also consider particularly the interface boundary conditions for 2-D coordinate systems and some of the models used by other researchers. Where possible we compare our work with that of others. These conditions proved stable for both 2-D acoustic and elastic wave propagation and enhanced interface reflections.

Strong interface reflections were visible in all Cartesian seismograms though somewhat weaker in the case of cylindrical coordinates.

ABCs	Absorbing boundary conditions
$\boldsymbol{a}$	Acceleration
θ	Angle
ω	Angular frequency
ξ,θ,z	Bipolar coordinates
κ	Bulk modulus
x,y,z.	Cartesian coordinates
P	Compresional wave
v_p	Compressional wave velocity
r,θ,z	Cylindrical coordinates
ρ	Density
∂	Differential operator
γ	Dispersion parameter
$\mathbf{u}$	Displacements
FDM	Finite Difference Method
FEM	Finite Element Method
f(t)	Gaussian source function
Δx_i	Grid increments
q_s	Group velocity (non-dimensional)
H(t)	Heaviside function
u, v	Horizontal Displacements
δ_{ij}	Kronecker delta
λ.	Lame elastic constant
h_i	Line elements
q_i	Mesh ratio
PDE	Partial Differential Equation
q_p	Phase velocity (non-dimensional)
σ	Poisson's ratio
α	Pulse width parameter
R	Radius

UR	Reflection displacement components
Δ	Sharpness of pulse
μ	Shear modulus
S	Shear wave
SH	Shear wave perpendicular to the vertical plane
SV	Shear wave in the vertical plane
v_s	Shear wave velocity
US	Source displacement componenets
q	Stability parameter
E_i	Strain components
P_{ij}	Stress components
t	Time
Δt	Time increment
t_s	Time shift parameter
O(h)	Truncation error
i, j, k	Unit vector
f_{max}	Upper half-power frequency
$A(\xi)$	Variable scale coefficient
α	Variable scale constants
β	Variable scale constants
VSM	Variable scale method
v	Velocity components
w	Vertical Displacement
VSP	Vertical seismic profile
V	Volume
ϕ	Volume dilatation
λ	Wavelength
k	Wave number
Y	Young modulus

CHAPTER 1

INTRODUCTION

1.1 Seismology

Seismology is, the science of earthquakes, involving observations of natural ground vibrations and artificially generated seismic signals, with many theoretical and practical ramifications. This thesis concerns the method of explosion seismology in unravelling crustal structure. The method brings a degree of control to seismic investigations, since origin times and locations of explosions, unlike natural earthquakes, are known with negligible errors. Explosion experiments can be planned in advance, so that a suitable disposition of recording stations can be contrived and seismograms with much finer detail obtained. The source energy comes usually from chemical explosions. Nuclear explosions have produced the possibility of extending the seismic explosion method and all the experimental controls that go with it, to problems of the earth's deeper interior. The earth is made up of a series of plates, (huge segments) which slide over, past and into each other (See Figure 1.1). More details in Birkeland et al. [**11**], and Bullen [**13**].

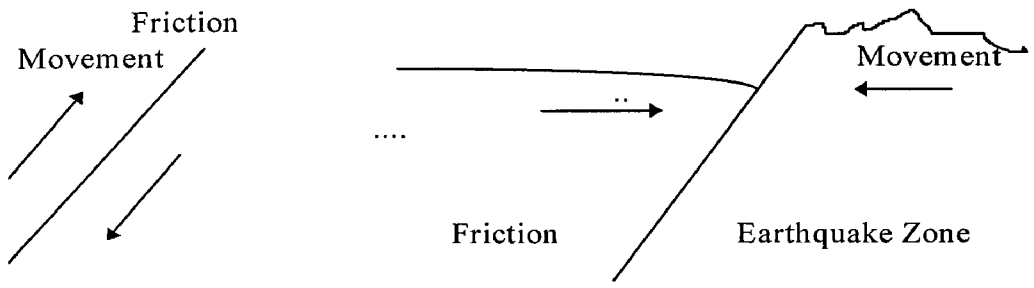

Figure 1.1

1.1.1 Seismographs

The purpose of the seismograph is to record as much data as possible concerning the nature of the earth's movement. The movement recorded is in the vicinity of a particular point of the earth's surface, following an earthquake. The movement usually receives most attention. Seismographs are usually constructed to record details from which translations components of the local earth movement may be inferred. As a rule the components taken are the two horizontal components, north-south, east-west, and the vertical z component. The constructional details of seismographs for measuring horizontal and vertical components are rather different. However, the same type of differential equation, representing the motion in the seismograph relative to the ground, is inherent in both. More details in Birkeland et al. [**11**], and Bullen [**13**].

1.1.2 Earthquakes

An Earthquake causes vibrations in the earth's crust when rocks in which elastic strain has been building up suddenly rupture, and then rebound. The vibrations can range from barely noticeable to catastrophically destructive. Seismic waves have energy that is given off in waves of two types; P-waves and S-waves. P-waves are sometimes called " push and pull " or longitudinal waves because the particles in the medium that the wave is travelling through are compressed and decompressed (See Figure 1.2). S-waves are sometimes called " shake or transverse " waves and behave very like water-waves. The wave travels forward, but the particles are shaken from side to side (See Figure 1.3). In the same medium, P-waves are faster than S-waves. More details in Birkeland et al. [**11**], and Bullen [**13**].

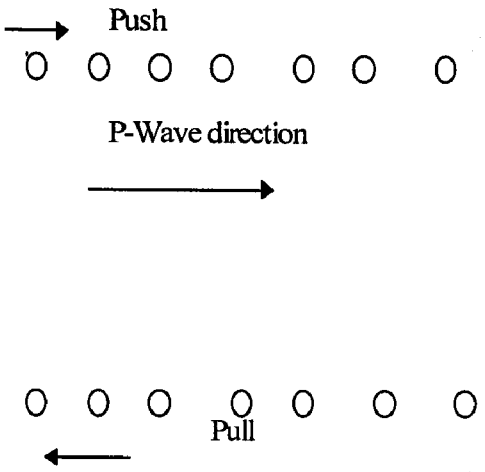

Figure 1.2

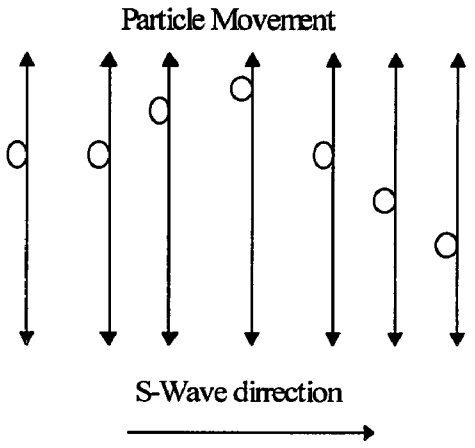

Figure 1.3

1.1.3 Sedimentary Rocks

Of the three generic rock families sedimentary rocks are perhaps the most readily comprehended because many of them bear a resemblance to the materials from which they are made. Also many of them, due to the processes responsible for their formation, occur in accessible environments. About 75% of the earth's surface is covered by sediments. Even so, they form only a thin discontinuous veneer that is spread over the much more abundant igneous and metamorphic rocks, which are the true foundations of continents and ocean basins. Many sedimentary rocks can be thought of as secondary or derived, in that they are composed of bits and pieces of pre-existing rocks held together by a suitable cement. Such a texture is called clastic and the fragments can be called clasts. Sedimentary rocks are built up through the slow deposition of material and so are typically formed layer on layer. Individual layers may range from paper thin sheets up to massive beds 30m or more thick.

Sandstone

The sedimentary rock called sandstone consist of cemented particles whose diameter ranges between 2mm and 1/16 of a mm. Commonly they include shale layers, or beds of sandstone that may alternate regularly with beds of shale.

Pure well-sorted sandstone was often used as a building material before the advent of pre-stressed concrete or of lightweight aggregate.

Shale

The original constituents of this fine-grained rock were clay-size grains and silt particles which matured into a typically laminated rock that splits readily into thin layers. Since shale is composed of clay grains and of individual mineral grains or rock particles less than 1/16 of a mm in diameter, a few of the constituents can be distinguished by eye. Shales constitute very nearly half of all sedimentary rocks.

Limestone

The most abundant of the organic sedimentary rocks is limestone, and probably most examples of it are truly organic (deposits are either fossils of organisms in growth position or calcareous shell materials that have been reworked and moved about by currents). In a strict sense limestone made up of shell debris that has been reworked by currents should be classed as clastic sedimentary rocks. Of the limestones made up of large fossils and fossil fragments, perhaps the most impressive are the reefs - and certainly the most impressive modern one is Australia's Great Barrier Reef. More details are given in Birkeland et al. [**11**], and Bullen [**13**].

1.2 Outline of Thesis

Chapter 2 contains the 2-D and 3-D equations of wave motion for particle displacement in the cases of acoustic and elastic propagation. Firstly, we consider the equations of generalized motion in orthogonal coordinates and later we focus on Cartesian coordinates, cylindrical coordinates and bipolar coordinates that naturally fit the problems (including boreholes) to be considered.

Chapter 3 contains a Finite Difference (FDM) modelling outline for the partial differential equations considered. Firstly, we consider the FDM formulation and its accuracy for solving the equations of motion. Secondly, we focus on the dispersion and dissipation analysis of the numerical solutions. Finally, we consider the use of the main far field absorbing boundary conditions (ABCs) techniques. The two approaches used are those of Reynolds's and of Clayton-Engquist.

Chapter 4 contains a specific numerical model of the computational seismic wave propagation problem. We describe all the models we shall use which are namely the (UR+US), Box, Staggered grid and Variable Scale Methods. Finally, we describe the sources and recievers used.

Chapter 5 contains a 2-D purely acoustic wave equation numerical simulation as an introduction to the more general problems to be considered later. Firstly, we investigate the numerical convergence criterion of the finite-difference explicit method and VSM (variable scale method) as used in one rock medium, two media, and multimedia. The boundary conditions used are Dirichlet boundary conditions and ABCs (absorbing boundary conditions). A Gaussian pulse source term is used while investigating some problems.

Chapter 6 contains a 2-D elastic wave equation problem which we investigate using Cartesian and cylindrical coordinates, and we accommodate discontinuities in the media such as varying rock structures. Dirichlet and absorbing boundary conditions (ABCs) in one medium, two media and multimedia are used with a compressional point source term. In this chapter we use three different models namely the "(ur+us)" model, "standard FDM & Box" model and "Staggered grid & Box" model. We analyse the convergence criteria for all models used, and then the results obtained by three different boundary conditions namely Dirichlet boundary conditions, Reynolds's and Clayton-Engquist ABCs.

Chapter 7 contains a 3-D acoustic and elastic wave equation problem in Cartesian coordinates. We investigate both the standard FDM & box and staggered grid & box models and analyse the convergence criteria for each. The numerical solutions are obtained for one rock medium, two media, and multimedia.

Chapter 8 contains a 2-D and 3-D borehole modelling exercise with Cartesian and cylindrical coordinates. The numerical solutions are obtained by using the staggered grid & box and variable scale methods. Results are presented for one borehole and two boreholes modelling.

Chapter 9 contains a 3-D acoustic and elastic wave equation numerical solutions with Cartesian coordinates which employs the staggered grid method with a compressional line source term. Here we focus more closely on internal rock structures and investigate the special interface conditions for the two media and multimedia models.

Chapter 10 has a summary of the thesis work, and its main conclusions in relation to the research aims as far as seismic modelling is concerned. Also included are suggestions for further work based on that carried out here.

CHAPTER 2

BASIC EQUATIONS OF MOTIONS OF A CONTINUUM

2.1 Introduction

We will consider the equations of motion for particle displacement in various coordinate systems modelling naturally the physical geometry. To this end we shall develop the equations of motion in general orthogonal coordinates. The equations of motion are derived in part from texts such as Aki et al. [**1**], Batchelor [**8**], Lai et al. [**40**], Lavergne [**42**], and White [**85**].

2.2 The Stress Equations of Motion

The stress tensor defines the stress components P_{ij} acting upon each of the six faces of the elementary cube dx_1, dx_2, dx_3 in Cartesian coordinates $x_1=x$, $x_2=y$, $x_3=z$ (Figure 2.1).

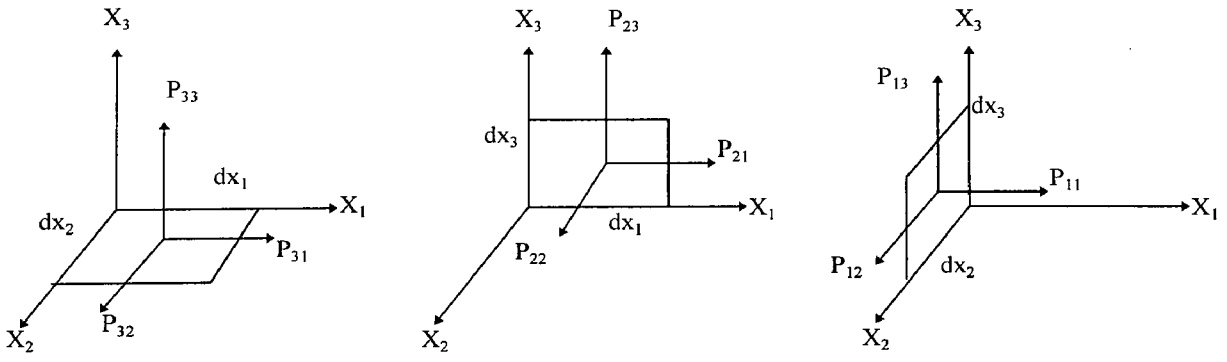

Figure (2.1) Stress tensor. Stresses on the sides of an elementary Cartesian cube dx_1, dx_2, dx_3.

A systematic approach to the wave equation in general orthogonal coordinates is presented which has the advantage of introducing tensors in a simplified form. The equations needed in classical problems are then determined in an elementary way and the equations of motion in orthogonal coordinates derived as below.

In general orthogonal coordinates with the usual Cartesian vector notation we write for displacement $\mathbf{r} = x_1\mathbf{i} + x_2\mathbf{j} + x_3\mathbf{k}$ where **i**, **j** and **k** are the usual unit vectors, or $\mathbf{r} = \mathbf{r}(x_1, x_2, x_3)$.

Let $\mathbf{e}_1$, $\mathbf{e}_2$, $\mathbf{e}_3$ denote an orthogonal triplet of unit vectors in the orthogonal system. The line element is then

$$(ds)^2 = \sum_n h_n^2 (dx_n)^2, \tag{2.1}$$

and the scale factors h_n are given by

$$h_n^2 = \left(\frac{\partial x}{\partial x_n}\right)^2 + \left(\frac{\partial y}{\partial x_n}\right)^2 + \left(\frac{\partial z}{\partial x_n}\right)^2, \tag{2.2}$$

where x, y, z are in Cartesian coordinates.

The Cauchy equations of motion result from the applications of Newton's laws of motion.

In Figure (2.2), P, Q, R, S, T, U, V, and W are the vertices of a cuboid and are given by

$P(x_1, x_2, x_3)$, $Q(x_1+dx_1, x_2, x_3)$, $R(x_1+dx_1, x_2, x_3+dx_3)$,

$S(x_1, x_2, x_3+dx_3)$, $T(x_1, x_2+dx_2, x_3)$, $U(x_1+dx_1, x_2+dx_2, x_3)$,

$V(x_1+dx_1, x_2+dx_2, x_3+dx_3)$, $W(x_1, x_2+dx_2, x_3+dx_3)$.

The forces acting on WVUT due to stresses $P_{i,j}$ are given by

$$\{\text{Area PQRS}\}\{P_{21}\mathbf{e}_1 + P_{22}\mathbf{e}_2 + P_{23}\mathbf{e}_3\}'$$
$$\{\text{Area PQRS}\}\{P_{11}\mathbf{e}_1 + P_{12}\mathbf{e}_2 + P_{13}\mathbf{e}_3\}'$$
$$\{\text{Area PQRS}\}\{P_{31}\mathbf{e}_1 + P_{32}\mathbf{e}_2 + P_{33}\mathbf{e}_3\}'$$

where the dashes indicate that the expression is evaluated on TUVW. Similarly, the forces acting on PQRS are given by

$$\{\text{Area TUVW}\}\{P_{21}\mathbf{e}_1 + P_{22}\mathbf{e}_2 + P_{23}\mathbf{e}_3\}''$$
$$\{\text{Area TUVW}\}\{P_{11}\mathbf{e}_1 + P_{12}\mathbf{e}_2 + P_{13}\mathbf{e}_3\}''$$
$$\{\text{Area TUVW}\}\{P_{31}\mathbf{e}_1 + P_{32}\mathbf{e}_2 + P_{33}\mathbf{e}_3\}''$$

where the two dashes indicate that the expression is evaluated on PQRS.

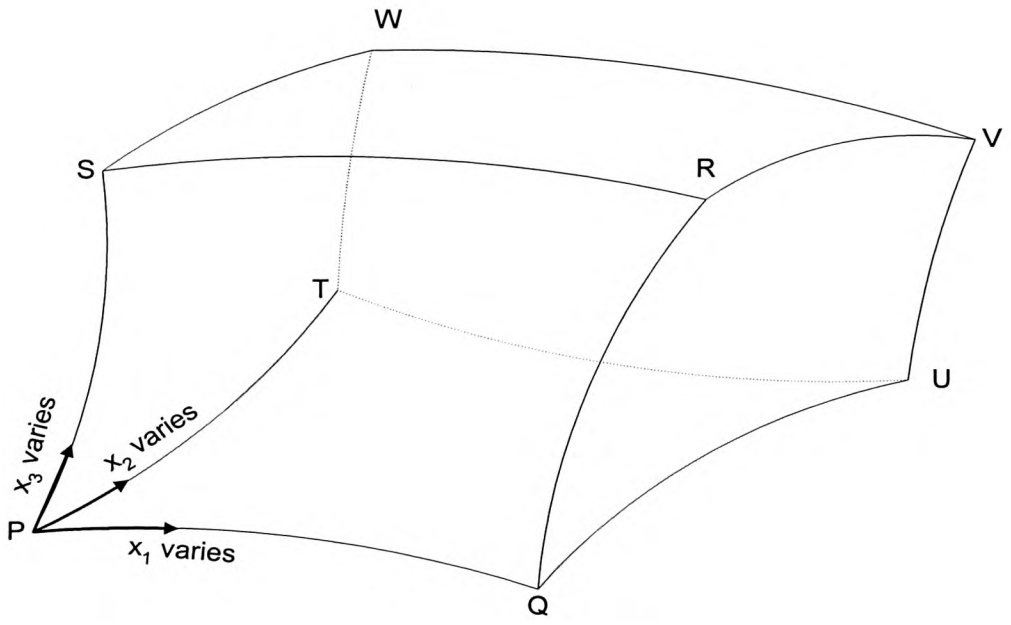

Figure (2.2) An elementary orthogonal cuboid.

The only coordinate that has changed is x_2 and so by the first term in a Taylor expansion change in force is given approximately by

$$\left\{\frac{\partial}{\partial x_2}\left[\text{area}_1\left(P_{21}\mathbf{e}_1 + P_{22}\mathbf{e}_2 + P_{23}\mathbf{e}_3\right)\right]\right\}dx_2$$

and similarly

$$\left\{\frac{\partial}{\partial x_1}\left[\text{area}_2\left(P_{11}\mathbf{e}_1 + P_{12}\mathbf{e}_2 + P_{13}\mathbf{e}_3\right)\right]\right\}dx_1$$

$$\left\{\frac{\partial}{\partial x_3}\left[\text{area}_3\left(P_{31}\mathbf{e}_1 + P_{32}\mathbf{e}_2 + P_{33}\mathbf{e}_3\right)\right]\right\}dx_3$$

The areas involved are $\text{area}_1=h_1h_3dx_1dx_3$ for PQRS, $\text{area}_2=h_1h_2dx_1dx_2$ for PQTU and $\text{area}_3=h_3h_2dx_3dx_2$ for PSTW respectively, where h_1, h_2 and h_3 are again evaluated at some point in the box and $h_1h_2h_3dx_1dx_2dx_3$ is equal to the box volume dV. Hence the changes are given to a first order approximation by

$$\frac{\partial}{\partial x_2}\left(h_1h_3P_{21}\mathbf{e}_1 + h_1h_3P_{22}\mathbf{e}_2 + h_1h_3P_{23}\mathbf{e}_3\right)dV \tag{2.3}$$

$$\frac{\partial}{\partial x_1}\left(h_2h_3P_{11}\mathbf{e}_1 + h_2h_3P_{12}\mathbf{e}_2 + h_2h_3P_{13}\mathbf{e}_3\right)dV \tag{2.4}$$

$$\frac{\partial}{\partial x_3}\left(h_1h_2P_{31}\mathbf{e}_1 + h_1h_2P_{32}\mathbf{e}_2 + h_1h_2P_{33}\mathbf{e}_3\right)dV \tag{2.5}$$

Thus the net force acting on the box is given by summation of (2.3), (2.4) and (2.5). By Newton's law, this net force is equal to:

$$\rho dV\cdot\mathbf{a} = \text{Net Force} \tag{2.6}$$

where ρ is density, $\mathbf{a}$ is an acceleration and where $(h_1h_2h_3)$ is evaluated at point P for small dV. On division by dV and with $dV\rightarrow 0$ we obtain

$$\begin{aligned}\rho\cdot\mathbf{a} = \frac{1}{h_1h_2h_3}\Bigg\{&\frac{\partial}{\partial x_1}\left(h_2h_3P_{11}\mathbf{e}_1 + h_2h_3P_{12}\mathbf{e}_2 + h_2h_3P_{13}\mathbf{e}_3\right)\\ &+\frac{\partial}{\partial x_2}\left(h_1h_3P_{21}\mathbf{e}_1 + h_1h_3P_{22}\mathbf{e}_2 + h_1h_3P_{23}\mathbf{e}_3\right)\\ &+\frac{\partial}{\partial x_3}\left(h_1h_2P_{31}\mathbf{e}_1 + h_1h_2P_{32}\mathbf{e}_2 + h_1h_2P_{33}\mathbf{e}_3\right)\Bigg\}\end{aligned} \tag{2.7}$$

Using Astin [7] equations I, II and III, we can select the first component of the above to obtain

$$\rho \cdot a_1 = \frac{1}{h_1 h_2 h_3}\left\{\frac{\partial}{\partial x_1}\left(h_2 h_3 P_{11}\right) + \frac{\partial}{\partial x_2}\left(h_1 h_3 P_{12}\right) + \frac{\partial}{\partial x_3}\left(h_2 h_1 P_{13}\right)\right\} + \frac{P_{12}}{h_1 h_2}\frac{\partial h_1}{\partial x_2} + \frac{P_{13}}{h_1 h_3}\frac{\partial h_1}{\partial x_3} - \frac{P_{22}}{h_1 h_2}\frac{\partial h_2}{\partial x_1} - \frac{P_{33}}{h_1 h_3}\frac{\partial h_3}{\partial x_1} \tag{2.8}$$

Similarly the x_2, x_3 components are:

$$\rho \cdot a_2 = \frac{1}{h_1 h_2 h_3}\left\{\frac{\partial}{\partial x_1}\left(h_2 h_3 P_{12}\right) + \frac{\partial}{\partial x_2}\left(h_1 h_3 P_{22}\right) + \frac{\partial}{\partial x_3}\left(h_2 h_1 P_{23}\right)\right\} + \frac{P_{12}}{h_1 h_2}\frac{\partial h_2}{\partial x_1} + \frac{P_{23}}{h_2 h_3}\frac{\partial h_2}{\partial x_3} - \frac{P_{11}}{h_1 h_2}\frac{\partial h_1}{\partial x_2} - \frac{P_{33}}{h_2 h_3}\frac{\partial h_3}{\partial x_2}\,, \tag{2.9}$$

and,

$$\rho \cdot a_3 = \frac{1}{h_1 h_2 h_3}\left\{\frac{\partial}{\partial x_1}\left(h_2 h_3 P_{13}\right) + \frac{\partial}{\partial x_2}\left(h_1 h_3 P_{23}\right) + \frac{\partial}{\partial x_3}\left(h_2 h_1 P_{33}\right)\right\} + \frac{P_{13}}{h_1 h_3}\frac{\partial h_3}{\partial x_1} + \frac{P_{23}}{h_2 h_3}\frac{\partial h_3}{\partial x_2} - \frac{P_{11}}{h_1 h_3}\frac{\partial h_1}{\partial x_3} - \frac{P_{22}}{h_2 h_3}\frac{\partial h_2}{\partial x_3}\,. \tag{2.10}$$

We have written the Cauchy's equations of motion, to be satisfied by any continuum, in the following form

$$\rho \cdot \mathbf{a} = \mathrm{div}(\mathbf{P}) \tag{2.11}$$

where ρ is the density, **a** the acceleration and **P** the stress tensor. All terms in the equation are quantities associated with a particle of the medium that is currently at that position. The **a** for small displacements **u** is replaced by $\frac{\partial^2 \mathbf{u}}{\partial t^2}$ to give:

$$\rho \frac{\partial^2 \mathbf{u}}{\partial t^2} = \mathrm{div}(\mathbf{P}) = \underline{\nabla} \cdot \mathbf{P}\,. \tag{2.12}$$

2.2.1 Stress and Strain Relation

Using a simple elastic medium model we have, from symmetry, six components of stress P_{ij} and of strain E_{ij}. For homogeneous materials we assume a linear relation for the resulting strain from the applied stress. We write

$$E_{ij} = \frac{1}{2}\left[(\underline{\nabla}\cdot\mathbf{u})_{ij} + (\underline{\nabla}\cdot\mathbf{u})_{ji}\right] \tag{2.13}$$

$$\phi = E_{11}+E_{22}+E_{33} = \mathrm{div}(\mathbf{u})$$

where **u** is the material displacement.

We have in general orthogonal coordinates from Astin [7]

$$\begin{aligned}
E_{11} &= \frac{1}{h_1}\frac{\partial u_1}{\partial x_1} + \frac{u_2}{h_1h_2}\frac{\partial h_1}{\partial x_2} + \frac{u_3}{h_1h_3}\frac{\partial h_1}{\partial x_3} \\
E_{22} &= \frac{1}{h_2}\frac{\partial u_2}{\partial x_2} + \frac{u_1}{h_1h_2}\frac{\partial h_2}{\partial x_1} + \frac{u_3}{h_2h_3}\frac{\partial h_2}{\partial x_3} \\
E_{33} &= \frac{1}{h_3}\frac{\partial u_3}{\partial x_3} + \frac{u_1}{h_1h_3}\frac{\partial h_3}{\partial x_1} + \frac{u_2}{h_2h_3}\frac{\partial h_3}{\partial x_2} \\
E_{12} &= \frac{1}{2}\left[\frac{1}{h_1}\frac{\partial u_2}{\partial x_1} + \frac{1}{h_2}\frac{\partial u_1}{\partial x_2} - \frac{u_1}{h_1h_2}\frac{\partial h_1}{\partial x_2} - \frac{u_2}{h_1h_2}\frac{\partial h_2}{\partial x_1}\right] \\
E_{13} &= \frac{1}{2}\left[\frac{1}{h_1}\frac{\partial u_3}{\partial x_1} + \frac{1}{h_3}\frac{\partial u_1}{\partial x_3} - \frac{u_1}{h_1h_3}\frac{\partial h_1}{\partial x_3} - \frac{u_3}{h_1h_3}\frac{\partial h_3}{\partial x_1}\right] \\
E_{23} &= \frac{1}{2}\left[\frac{1}{h_2}\frac{\partial u_3}{\partial x_2} + \frac{1}{h_3}\frac{\partial u_2}{\partial x_3} - \frac{u_2}{h_3h_2}\frac{\partial h_2}{\partial x_3} - \frac{u_3}{h_3h_2}\frac{\partial h_3}{\partial x_2}\right]
\end{aligned} \tag{2.14}$$

The fact that the stresses acting on an elementary volume of this solid can be expressed as a linear combination of the strains was established experimentally for many substances in the seventeenth century, and the relation is now known as Hooke's law.

2.2.2 Hooke's Law

Hooke's law expresses the linear relationship existing between strain and stress, when the value of strain is small. In anisotropic media, the relationships between stress and strain depends on 21 elastic parameters, and in transversely isotropic media (identical elastic properties in two perpendicular directions to an axis of symmetry), depends on only five parameters. However, in homogeneous and isotropic media, the relationships between stress and strain depends on only two parameters.

Hooke's law is written as:

$$P_{ij} = \lambda\phi\delta_{ij} + 2\mu E_{ij}. \tag{2.15}$$

where δ_{ij} is the Kronecker symbol (δ_{ij}= 1 if i=j, and δ_{ij}= 0 if i≠j) and λ and μ are the Lame constants. Also

$$\phi = \frac{\partial u_1}{\partial x} + \frac{\partial u_2}{\partial y} + \frac{\partial u_3}{\partial z} = \mathrm{div}(\mathbf{u}) \tag{2.16}$$

is the volume dilatation.

By developing (2.15), six linear equations are obtained between stresses and displacements in Cartesian coordinates:

$$\begin{aligned}
P_{11} &= \lambda\phi + 2\mu\frac{\partial u_1}{\partial x} \\
P_{22} &= \lambda\phi + 2\mu\frac{\partial u_2}{\partial y} \\
P_{33} &= \lambda\phi + 2\mu\frac{\partial u_3}{\partial z} \\
P_{12} &= \mu\left(\frac{\partial u_1}{\partial y} + \frac{\partial u_2}{\partial x}\right) \\
P_{13} &= \mu\left(\frac{\partial u_1}{\partial z} + \frac{\partial u_3}{\partial y}\right) \\
P_{23} &= \mu\left(\frac{\partial u_3}{\partial y} + \frac{\partial u_2}{\partial z}\right)
\end{aligned} \tag{2.17}$$

The **Lame parameter** μ, is also called the **shear** or **rigidity modulus**, which defines the ratio of the tangential stress to the corresponding shear in a simple shearing system according to

$$\mu = \frac{1}{2}\frac{P_{12}}{E_{12}}$$

Consider a block sheared as shown Figure (2.3). The deformations are $u_1=AB=E_{12}$, $u_1=u_3=0$.

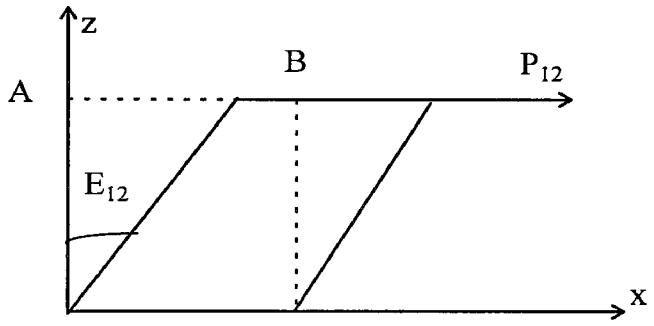

Figure (2.3)

The shear modulus describes how difficult it is to deform a cube (Figure 2.2) of the material under an unidirectional applied shearing force. For example, imagine we have a cube of material firmly cemented to a table top. Now, push one of the top edges of the material parallel to the table top. If the material has a small shear modulus, we will be able to deform the cube in the direction we are pushing it so that the cube will take on the shape of a parallelogram. If the material has a large shear modulus, it will take a large force applied in this direction to deform the cube. Gases and other fluids cannot support shear forces; that is they have shear modulii of zero. From the equations given above, notice that this implies that fluids and gases do not allow the propagation of S waves.

The **Young's modulus** Y or **Modulus of Elasticity:** Consider the elongation of a bar as in Figure (2.4). The cross-sectional area of the bar will contact as the overall volume of the bar remains the same as it expends lengthwise. There is no shear in this situation and the only stress is P_{11}. So

$$E=\frac{1}{Y}\begin{bmatrix} P_{11} & 0 & 0 \\ 0 & -\sigma P_{11} & 0 \\ 0 & 0 & -\sigma P_{11} \end{bmatrix}$$

and

$$Y=\frac{P_{11}}{E_{11}}$$

is ratio of the normal stress to the corresponding compression. It can be shown, Lai et al. [**40**] that:

$$Y=\frac{\mu(3\lambda+2\mu)}{\lambda+\mu} \tag{2.18}$$

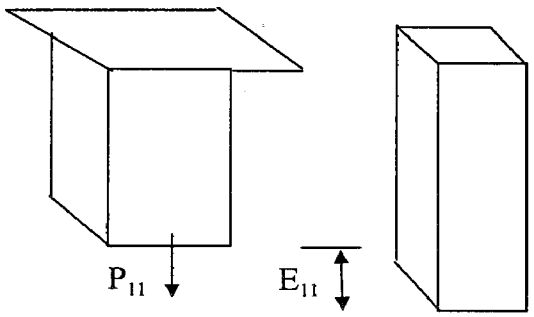

Figure (2.4)

Poisson's ratio σ, which is equal to the negative ratio of the transverse strain (E_{22}, E_{33}) to the axial strain is found to be

$$\sigma=-\frac{E_{22}}{E_{11}}=-\frac{E_{33}}{E_{11}} \tag{2.19}$$

and accommodating the cross-sectional contraction through Poisson's ratio σ (see Figure (2.5)).

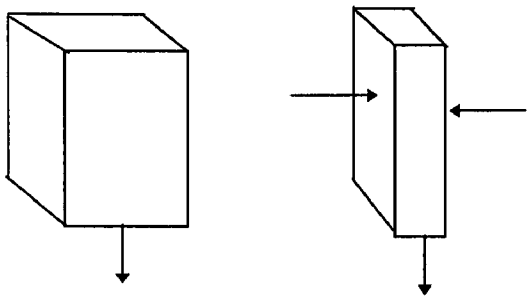

Figure (2.5)

the ratio of compression in one direction to extension in the perpendicular direction. It can be shown Lai et al. **[40]** that:

$$\sigma = \frac{\lambda}{2(\lambda + \mu)} \tag{2.20}$$

Bulk modulus *K*: Is also known as the *incompressibility* of the medium. Imagine we have a small cube (Figure 2.2) of the material making of the medium and that we subject this cube to pressure by squeezing it equally on all sides. If the material is not very stiff, we can imagine that it would be possible to squeeze the material in this cube into a smaller cube. The bulk modulus describes the ratio of the pressure applied to the amount of volume change that the cube undergoes. If *K* is very large, then the material is very stiff, meaning that it does not compress very much even under large pressures. If *K* is small, then small pressure can compress the material by large amounts. For example, gases have very small incompressibilities and are easily compressed. By contrast solids and liquids have large incompressibilities. The applied pressure, Δp, and ϕ, the change in volume per initial volume. We have

$$\kappa = -\frac{\Delta p}{\phi}$$

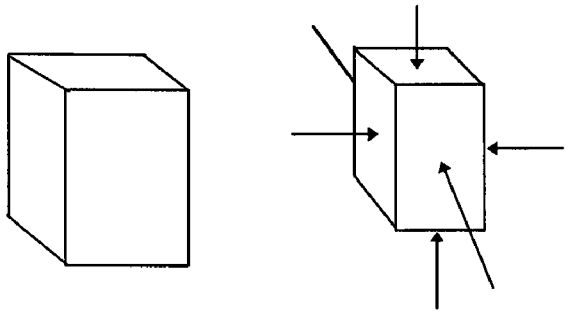

Figure (2.6)

the ratio of pressure variation to the volume dilatation. It can be shown Lai et al. [**40**] that:

$$\kappa = \lambda + \frac{2}{3}\mu \tag{2.21}$$

The values of the parameters λ, μ, Y and K generally range between 10^9 and 10^{11} N/m^2 for commonly encountered formations and σ varies from 0 to 0.5 in isotropic media.

2.3 Equation of Motion in Cartesian Coordinates

We have here for line elements, $h_1 = h_2 = h_3 = 1$ and rectangular coordinates (x_1, x_2, x_3) rewritten as (x, y, z). Now we substitute from equations (2.8), (2.9) and (2.10) to obtain

$$\rho\left(\frac{\partial^2 u_1}{\partial t^2}\right) = \frac{\partial P_{11}}{\partial x} + \frac{\partial P_{12}}{\partial y} + \frac{\partial P_{13}}{\partial z} \quad ,$$

$$\rho\left(\frac{\partial^2 u_2}{\partial t^2}\right) = \frac{\partial P_{12}}{\partial x} + \frac{\partial P_{22}}{\partial y} + \frac{\partial P_{23}}{\partial z} \quad ,$$

and (2.22)

$$\rho\left(\frac{\partial^2 u_3}{\partial t^2}\right) = \frac{\partial P_{13}}{\partial x} + \frac{\partial P_{23}}{\partial y} + \frac{\partial P_{33}}{\partial z}$$

The relations between stress and strain and strain tensor are for small displacements a_i is as:

$$
\begin{aligned}
P_{11} &= \lambda\phi + 2\mu E_{11} \\
P_{22} &= \lambda\phi + 2\mu E_{22} \\
P_{33} &= \lambda\phi + 2\mu E_{33} \\
P_{13} &= 2\mu E_{13} \\
P_{12} &= 2\mu E_{12} \\
P_{23} &= 2\mu E_{23} \\
\phi &= E_{11} + E_{22} + E_{33}
\end{aligned}
\tag{2.23}
$$

where,

$$
\begin{aligned}
E_{11} &= \frac{\partial u_1}{\partial x} \quad E_{22} = \frac{\partial u_2}{\partial y} \quad E_{33} = \frac{\partial u_3}{\partial z} \\
E_{12} &= \frac{1}{2}\left[\frac{\partial u_2}{\partial x} + \frac{\partial u_1}{\partial y}\right] \\
E_{23} &= \frac{1}{2}\left[\frac{\partial u_2}{\partial z} + \frac{\partial u_3}{\partial y}\right] \\
E_{13} &= \frac{1}{2}\left[\frac{\partial u_3}{\partial x} + \frac{\partial u_1}{\partial z}\right]
\end{aligned}
\tag{2.24}
$$

The strains are expressed in terms of displacements by means of equation (2.14). Then the equations of motion in terms of particle displacement are

$$
\begin{aligned}
\rho\frac{\partial^2 u_1}{\partial t^2} &= (\lambda + 2\mu)\frac{\partial^2 u_1}{\partial x^2} + \mu\left(\frac{\partial^2 u_1}{\partial y^2} + \frac{\partial^2 u_1}{\partial z^2}\right) + (\lambda + \mu)\left(\frac{\partial^2 u_2}{\partial x \partial y} + \frac{\partial^2 u_3}{\partial x \partial z}\right) \\
\rho\frac{\partial^2 u_2}{\partial t^2} &= (\lambda + 2\mu)\frac{\partial^2 u_2}{\partial y^2} + \mu\left(\frac{\partial^2 u_2}{\partial x^2} + \frac{\partial^2 u_2}{\partial z^2}\right) + (\lambda + \mu)\left(\frac{\partial^2 u_1}{\partial x \partial y} + \frac{\partial^2 u_3}{\partial y \partial z}\right) \\
\rho\frac{\partial^2 u_3}{\partial t^2} &= (\lambda + 2\mu)\frac{\partial^2 u_3}{\partial z^2} + \mu\left(\frac{\partial^2 u_3}{\partial x^2} + \frac{\partial^2 u_3}{\partial y^2}\right) + (\lambda + \mu)\left(\frac{\partial^2 u_1}{\partial x \partial z} + \frac{\partial^2 u_2}{\partial y \partial z}\right)
\end{aligned}
\tag{2.25}
$$

2.4 Equation of Motion in Cylindrical Coordinates

Cylindrical coordinates naturally represent the geometry of one borehole which are defined by the relations between Cartesian coordinates

$$x = r\cos\theta \qquad y = r\sin\theta \qquad z = z$$

These may be solved explicitly for the curvilinear coordinates,

$$r = (x^2+y^2)^{1/2}, \qquad \theta = \text{'}\tan^{-1}(y/x)\text{'}, \qquad z = z \tag{2.26}$$

This system of coordinates is depicted from various points of view in Figures (2.7, 2.8).

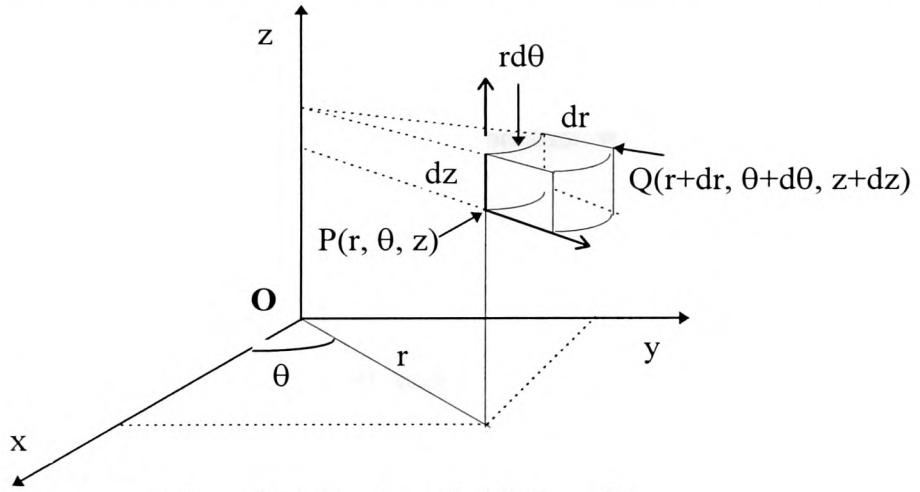

Figure (2.7) Circular cylindrical coordinates.

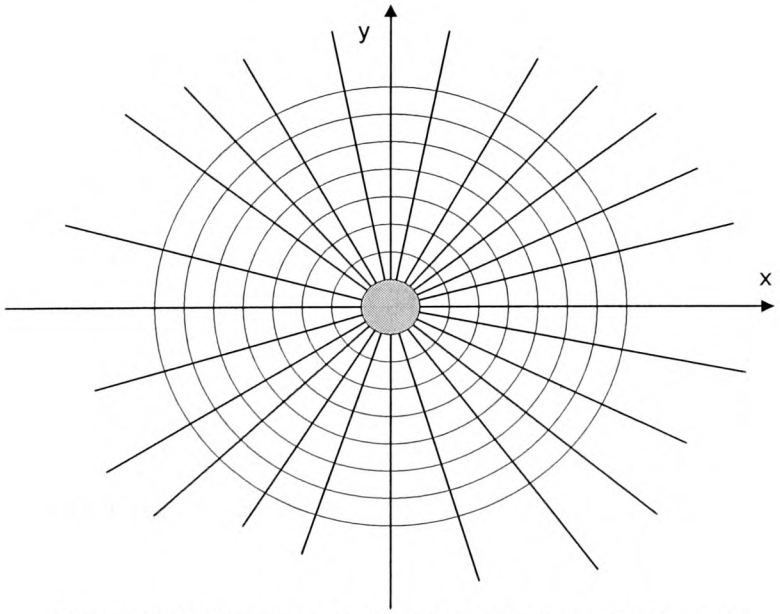

Figure (2.8) Circular cylindrical coordinate system curves.

By restricting the ranges of these coordinates as follows:

$$0 \leq r < \infty, \qquad 0 \leq \theta < 2\pi, \qquad -\infty < z < \infty \tag{2.27}$$

each point in space is given once and only once with the exception of those points along the z axis, for which θ is undetermined. It is understood that when applying equation (2.26), θ (radians) is to be measured in the quadrant in which the point lies. The r co-ordinate curves, formed by the intersection of the planes θ = constant and z = constant, are horizontal rays issuing from the z axis. The θ coordinate curves, produced by the intersection of the cylinders r = constant with the planes z = constant, are concentric, horizontal circles having the z axis at their centre. The z coordinate curves, resulting from the intersection of the cylinders r = constant with the planes θ = constant, are vertical lines.

Firstly we use the line elements $h_1 = 1$, $h_2 = r$, and $h_3 = 1$ corresponding to the usual expressions in the cylindrical coordinates where (x_1, x_2, x_3) are replaced by (r, θ, z). To simplify the discussion, let us now limit our attention to the case of axial symmetry, i.e. take u_2 to be zero and u_1 and u_3 to be independent of θ. A circular borehole is represented by r= constant. We substitute again from equations (2.8), (2.9) and (2.10) and find

$$\begin{aligned} \rho\left(\frac{\partial^2 u_1}{\partial t^2}\right) &= \frac{1}{r}\frac{\partial}{\partial r}(rP_{11}) + \frac{\partial}{\partial z}(P_{13}) - \frac{P_{22}}{r} \\ \rho\left(\frac{\partial^2 u_3}{\partial t^2}\right) &= \frac{1}{r}\frac{\partial}{\partial r}(rP_{13}) + \frac{\partial}{\partial z}(P_{33}) \end{aligned} \tag{2.28}$$

The stress-strain relation has a similar form as for Cartesian coordinates. That is

$$
\begin{aligned}
P_{11} &= \lambda\phi + 2\mu E_{11} \\
P_{22} &= \lambda\phi + 2\mu E_{22} \\
P_{33} &= \lambda\phi + 2\mu E_{33} \\
P_{13} &= 2\mu E_{13} \\
\phi &= E_{11} + E_{22} + E_{33}
\end{aligned}
\tag{2.29}
$$

where,

$$
\begin{aligned}
E_{11} &= \frac{\partial u_r}{\partial r}, \\
E_{22} &= \frac{u_r}{r}, \\
E_{33} &= \frac{\partial u_z}{\partial z}, \\
E_{13} &= \frac{1}{2}\left[\frac{\partial u_z}{\partial r} + \frac{\partial u_r}{\partial z}\right]
\end{aligned}
\tag{2.30}
$$

In terms of displacements, these equations of motion are:

$$
\begin{aligned}
\rho\left(\frac{\partial^2 u_1}{\partial t^2}\right) &= (\lambda + 2\mu)\left(\frac{\partial^2 u_1}{\partial r^2} + \frac{1}{r}\frac{\partial u_1}{\partial r} - \frac{u_1}{r^2}\right) + \mu\frac{\partial^2 u_1}{\partial z^2} + (\lambda + \mu)\frac{\partial^2 u_3}{\partial z \partial r} \\
\rho\left(\frac{\partial^2 u_3}{\partial t^2}\right) &= (\lambda + \mu)\left(\frac{\partial^2 u_1}{\partial z \partial r} + \frac{1}{r}\frac{\partial u_1}{\partial z}\right) + \mu\left(\frac{\partial^2 u_3}{\partial r^2} + \frac{1}{r}\frac{\partial u_3}{\partial r}\right) + (\lambda + 2\mu)\frac{\partial^2 u_3}{\partial z^2}.
\end{aligned}
\tag{2.31}
$$

2.5 Equation of Motion in Bipolar Coordinates

This coordinate system can in principle represent a two borehole model. Bipolar coordinates (ξ,θ) in a plane z = constant are defined by the transformation (Feshbach et al. [24], Spiegel [69])

$$x + iy = ia\cot(\theta + i\xi)/2$$

where $a>0$ and $i = \sqrt{-1}$, from which we obtain

$$x = \frac{a\sinh\xi}{\cosh\xi - \cos\theta} \quad , y = \frac{a\sin\theta}{\cosh\xi - \cos\theta} \quad , z = z \tag{2.32}$$

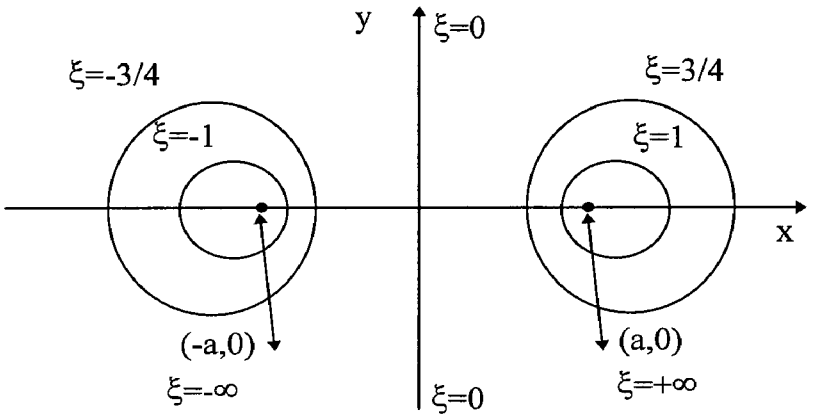

Figure (2.9) Bipolar coordinates; ξ=constant.

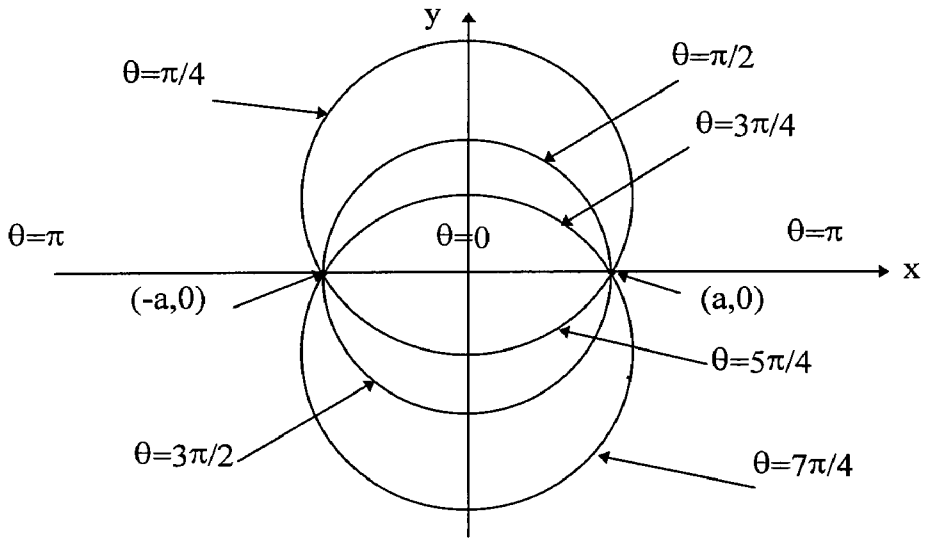

Figure (2.10) Bipolar coordinates; θ = constant.

The foregoing denominators are essentially positive. Since this coordinate system is not in general widespread use, we describe some of the main features of the system. As is evident from Figures (2.9), (2,10), each point (x, y) in the xy plane is represented at least once by limiting θ and ξ to the ranges

$$0 \leq \theta < 2\pi, \qquad -\infty < \xi < \infty \tag{2.33}$$

With the exception of the two points ($x = \pm a$, $y = 0$), at which ξ is infinitely many-valued, there is now a one-to-one correspondence between the Cartesian sub-coordinates (x, y) and bipolar sub-coordinates (ξ,θ).

When ξ is constant we eliminate θ from equation (2.32) to obtain

$$(x - a\coth\xi)^2 + y^2 = a^2 \operatorname{cosech}^2 \xi \tag{2.34}$$

In the xy plane, the curves ξ = constant are, therefore, a family of nonintersecting circles whose centres lie along the x axis (coaxial circles). The centre of a typical circle $\xi = \xi_0$ = constant is located at the point ($x = a\coth\xi_0$, $y = 0$) and its radius is $a|\operatorname{cosech}\xi_0|$. For $\xi_0 > 0$, the circles lie entirely about the origin; for values of $\xi_0 < 0$ the circles are to left of the origin. The value $\xi_0 = 0$ generates a circle of infinite radius whose centre is at either ($x = \pm \infty$, $y = 0$) so that $\xi_0 = 0$ corresponds to the entire y axis. When $\xi_0 = \pm \infty$ the radius is zero and the centres are located at the points ($x = \pm a$, $y = 0$), respectively. As ξ_0 varies from $+\infty$ to 0 the radius of the circle corresponding to this value of ξ_0 increases from 0 to ∞ and the centre moves from ($x = a$, $y = 0$) along the x axis. On the other hand, as ξ_0 varies from $-\infty$ to 0 the centre moves from ($x = -a$, $y = 0$) to ($x = -\infty$, $y = 0$) along the x axis.

When θ is constant elimination of ξ from equation (2.32) results in

$$x^2 + (y - a\cot\theta)^2 = a^2 \operatorname{cosec}^2 \theta \tag{2.35}$$

Thus, the family of curves in the xy plane which arise by assigning different constant values to the parameter θ appear to be intersecting circles whose centres all lie along the y axis. Every circle of the family passes through the *limiting points* of the system, (x =±a, y = 0). The centre of a typical circle $\theta = \theta_0$ = constant is at (x = 0, y = acot θ_0) and its radius is acosec θ_0. More careful examination of equation (2.32) shows, however, that the curves characterised by θ = constant are not complete circles but, rather, are circular arcs terminating on the x axis at the limiting points of the system. If the circular arc $\theta = \theta_0$ = constant < π is the part of the circle lying above the x axis, its extension below the x axis is given by the value $\theta = \theta_0 + \pi$. When $\theta_0 = \pi$, the arc is degenerate and corresponds to that portion of the x axis lying between the limiting points of the system. The value $\theta_0 = 0$ is a circular arc of infinite radius with centre at +∞ on the y axis, and gives the entire x axis with the exception of those points between (x =±a, y = 0), for which $\theta_0 = \pi$. The values $\theta_0 = \pi/2$ and $3\pi/2$ are semicircles of radii a, having their centres at the origin.

Bipolar coordinates are important when modelling a pair of circular boreholes eg ξ = 1, ξ = -1. as in Figure (2.9).

In this co-ordinate system we have line elements

$$h_\xi = \frac{a}{X}, \quad h_\theta = \frac{a}{X}, \quad h_z = 1$$

where X = coshξ - cosθ and in the expression of the bipolar coordinates (x_1, x_2, x_3) is replaced by (ξ, θ, z) see Figures (2.9), (2.10). We substitute again from equations (2.8), (2.9) and (2.10) to find:

$$\rho\left(\frac{\partial^2 u_\xi}{\partial t^2}\right) = \frac{X}{a}\frac{\partial P_{\xi\xi}}{\partial \xi} + \frac{X}{a}\frac{\partial P_{\theta\xi}}{\partial \theta} + \frac{\partial P_{\xi z}}{\partial z} + \frac{P_{\theta\theta} - P_{\xi\xi}}{a}\sinh\xi + \frac{P_{\theta\xi} + P_{\xi\theta}}{a}\sin\theta$$

$$\rho\left(\frac{\partial^2 u_\theta}{\partial t^2}\right) = \frac{X}{a}\frac{\partial P_{\xi\theta}}{\partial \xi} + \frac{X}{a}\frac{\partial P_{\theta\theta}}{\partial \theta} + \frac{\partial P_{z\theta}}{\partial z} + \frac{P_{\theta\theta} - P_{\xi\xi}}{a}\sin\theta + \frac{P_{\theta\xi} + P_{\xi\theta}}{a}\sinh\xi \qquad (2.36)$$

$$\rho\left(\frac{\partial^2 u_z}{\partial t^2}\right) = \frac{X}{a}\frac{\partial P_{\xi z}}{\partial \xi} + \frac{X}{a}\frac{\partial P_{\theta z}}{\partial \theta} + \frac{\partial P_{zz}}{\partial z} - \frac{P_{\xi z}}{a}\sinh\xi + \frac{P_{\theta z}}{a}\sin\theta$$

The stress-strain relation has a similar form for both rectangular and cylindrical coordinates:

Hence

$$\begin{aligned}
P_{\xi\xi} &= \lambda\phi + 2\mu E_{\xi\xi} \\
P_{\theta\theta} &= \lambda\phi + 2\mu E_{\theta\theta} \\
P_{zz} &= \lambda\phi + 2\mu E_{zz} \\
P_{\xi z} &= 2\mu E_{\xi z} \\
P_{\xi\theta} &= 2\mu E_{\xi\theta} \\
P_{\theta z} &= 2\mu E_{\theta z} \\
\phi &= E_{\xi\xi} + E_{\theta\theta} + E_{zz}
\end{aligned} \qquad (2.37)$$

where,

$$\begin{aligned}
E_{\xi\xi} &= \frac{X}{a}\frac{\partial u_\xi}{\partial \xi} + \frac{u_\theta}{a}\sin\theta \\
E_{\theta z} &= \frac{1}{2}\left[\frac{X}{a}\frac{\partial u_z}{\partial \theta} + \frac{\partial u_\theta}{\partial z}\right] \\
E_{\theta\theta} &= \frac{X}{a}\frac{\partial u_\theta}{\partial \theta} - \frac{u_\xi}{a}\sinh\xi \\
E_{\xi z} &= \frac{1}{2}\left[\frac{X}{a}\frac{\partial u_z}{\partial \xi} + \frac{\partial u_\xi}{\partial z}\right] \\
E_{zz} &= \frac{\partial u_z}{\partial z} \\
E_{\xi\theta} &= \frac{1}{2}\left[\frac{X}{a}\frac{\partial u_\theta}{\partial \xi} + \frac{X}{a}\frac{\partial u_\xi}{\partial \theta} - \frac{u_\xi}{a}\sin\theta + \frac{u_\theta}{a}\sinh\xi\right]
\end{aligned} \qquad (2.38)$$

In order to accommodate far field absorbing boundary conditions (to be discussed in chapter 3) we are required to set boundary values on lines ξ or θ as constant, which should reflect 'large' distances from the origin. Unfortunately, for this coordinate system such values reflect circles which approach near the origin, and we are led to the conclusion that these coordinates are unsuitable for this work, although the possibility remains that they may be used in the more flexible finite or boundary element approaches. However, for completeness, we include here the relevant equation information should a reader wish to pursue these coordinates further.

2.6 Summary

In this chapter, we provided more background information about the equations of motion before starting the research work proper of this thesis. The equations of motion were presented in general orthogonal coordinates, with particular attention paid to Cartesian, cylindrical and bipolar coordinates. We found the use of bipolar coordinates to model a two borehole geometry to be unsuitable for the FDM adopted for this work.

In the next chapter, we will solve the equations of motion to obtain the numerical solution for the seismic wave propagation problems.

CHAPTER 3

GENERAL NUMERICAL SEISMIC WAVE PROPAGATION MODELLING

3.1 Introduction

This chapter is based on the general numerical seismic wave propagation modelling. Various numerical methods for modelling wave propagation problems have been developed, including the FDM (Alterman and Karal [**3**]; Kelly et al. [**37**]), FEM (Chen [**15**]), Fourier or pseudospectral methods (Kosloff [**38**]), and Hybrid methods (Gazdag [**27**]). The FDM is a most powerful simple direct method, and well understood in solving the equations of motion widely used in seismic wave propagation problems. We are required to choose the correct grid parameters for the numerical solution so that unacceptable results can be avoided. We must pay attention to stability, consistency, and convergence and grid dispersion (Alford et al. [**2**]; Boore [**12**]; Virieux [**82**]). The seismic wave propagation problems are normally solved for an infinite medium, but because of the finite core of computers and finite time available the FDM solution can only be obtained at a finite number of points, thus it is necessary to introduce domain boundaries to obtain a finite model. We employ two different well known absorbing boundary conditions (ABCs) which are namely the Reynolds and Clayton-Engquist ABCs.

3.2 Finite Difference Methods

3.2.1 The Finite Difference Grid

In this section, we describe the FDM (Finite-Difference Method) (Alterman and Karal [3]; Kelly et al. [37], Ottaviani [55] which we employ to solve the equations of motion in 2-D. In solving the differential equations by the FDM, differential operators are replaced by difference expressions.

The whole geometry, with reference to the Cartesian coordinates (x, z), is divided into a finite number of mesh cells and bounded with a uniform rectangular grid. This division consist of M grid spaces of size Δx and N grid spaces of size Δz, in the x and z directions respectively. We therefore have M+1 grid points in the x-direction and N+1 grid points in the z-direction, so that

$$x_i = i\Delta x \qquad i = 0,1,\ldots,M \tag{3.1}$$

$$z_j = j\Delta z \qquad j = 0,1,\ldots,N \tag{3.2}$$

define grid lines see Figure (3.1).

Furthermore we set $t = n\Delta t$, $n = 0,1,\ldots$, with Δt as the time increment, where n is the number increments needed to reach some desired time $n\Delta t$. For convenience, we use the notation $\Delta x = h$ and $\Delta z = k$ and so $h = \frac{X_M}{M}$, $k = \frac{Z_N}{N}$, where X_M and Z_N represent the height and width of the geometry, respectively.

The point which lies at the intersection of the lines given by (3.1) and (3.2) is termed as the (i, j) grid point. The point vertically above (i, j) is the point (i, j+1) and that below (i, j) is the point (i, j-1). Similarly the points (i+1, j) and (i-1, j) lie to the

right and left of (i, j), (see Figure 3.1). If u is the dependent variable, the approximated value of the function u at the (i, j) th grid point is denoted by $u_{i,j}^{n}$ at time $n\Delta t$.

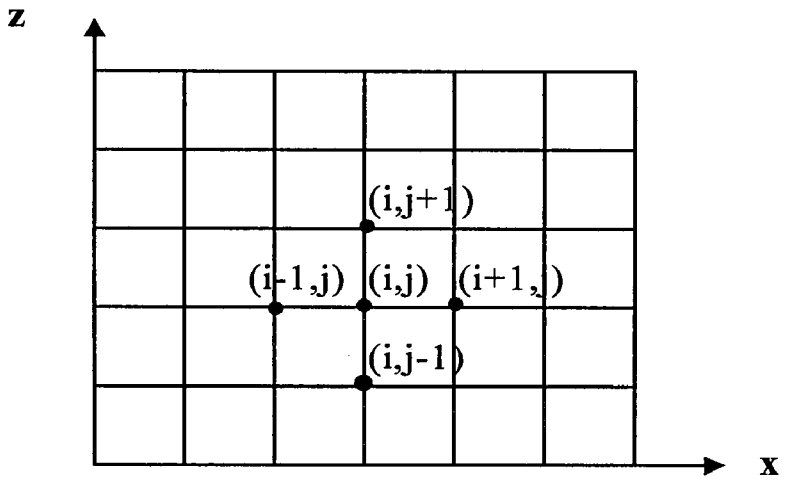

Figure 3.1 Finite difference mesh structure

3.2.2 Finite Difference Approximation to Derivatives

We assume the analytic solution u(x, z, t) possesses derivatives that are finite and continuous functions of x and z. The partial derivatives are approximated as finite differences by means of Taylor series.

The first order partial derivative of the function u, in the x-direction, can be approximated by one of the standard forms as follows:

I) Central difference approximation

$$\frac{\partial u_{i,j}^{n}}{\partial x} = \frac{u_{i+1,j}^{n} - u_{i-1,j}^{n}}{2h} + O(h^2) \qquad (3.3)$$

ii) Forward difference approximation

$$\frac{\partial u_{i,j}^{n}}{\partial x} = \frac{u_{i+1,j}^{n} - u_{i,j}^{n}}{h} + O(h) \qquad (3.4)$$

iii) Backward difference approximation

$$\frac{\partial u^{n}_{i,j}}{\partial x} = \frac{u^{n}_{i,j} - u^{n}_{i-1,j}}{h} + O(h) \tag{3.5}$$

The main source of error with the central approximation is the truncation error $O(h^2)$ associated with the approximation of the differential operator. The truncation error depends on grid size and can in theory be neglected as $h \to 0$.

The second order time derivative is approximated in a simple explicit method by using the central difference approximation in the increasing time direction as:

$$\frac{\partial^2 u^{n}{}_{i,j}}{\partial t^2} = \frac{u^{n+1}{}_{i,j} - 2u^{n}{}_{i,j} + u^{n-1}_{i,j}}{\Delta t^2} + O(\Delta t^2) \tag{3.6}$$

The second order and the 'cross' partial derivatives can be approximated to a second order using central differences;

$$\frac{\partial^2 u^{n}_{i,j}}{\partial x^2} = \frac{u^{n}_{i+1,j} - 2u^{n}_{i,j} + u^{n}_{i-1,j}}{h^2} + O(h^2) \tag{3.7}$$

$$\frac{\partial^2 u^{n}_{i,j}}{\partial x \partial z} = \frac{u^{n}_{i+1,j+1} - u^{n}_{i+1,j-1} - u^{n}_{i-1,j+1} + u^{n}_{i-1,j-1}}{4hk} + O(hk)\ . \tag{3.8}$$

Second order partial derivatives in the z-direction are approximated in a similar way as equation (3.2) to $O(k^2)$. The usual procedure for deriving an algorithm to simulate the changing displacements along the x and z axis as time moves forwards in steps is to start with the continuous differential equation describing the system and to discretise it. In this case, the equation is the 2-D scalar wave equation,

$$\frac{\partial^2 u}{\partial t^2} = v_p^2 \left(\frac{\partial^2 u}{\partial x^2} + \frac{\partial^2 u}{\partial z^2} \right) \tag{3.9}$$

where t is time, x, z are distance along horizontal and vertical direction and u is the magnitude of displacement. The parameter v_p is the wave speed.

The discretized equation is

$$\frac{\partial^2 u^n_{i,j}}{\partial t^2} \approx \frac{u^{n+1}{}_{i,j} - 2u^n_{i,j} + u^{n-I}_{i,j}}{\Delta t^2} \tag{3.10}$$

and

$$\frac{\partial^2 u^n_{i,j}}{\partial x^2} \approx \frac{u^n{}_{i+1,j} - 2u^n_{i,j} + u^n_{i-1,j}}{h^2} \tag{3.11}$$

similarly,

$$\frac{\partial^2 u^n_{i,j}}{\partial z^2} \approx \frac{u^n{}_{i,j+1} - 2u^n_{i,j} + u^n_{i,j-1}}{k^2} \tag{3.12}$$

where as before previously used Δt, h, k, are the spacing between samples in time and distance, respectively. Substitution of equations (3.10), (3.11) and (3.12) into (3.9) gives the equation,

$$u^{n+1}_{i,j} = 2u^n_{i,j} - u^{n-1}_{i,j} + \frac{v_p^2\Delta t^2}{h^2}(u^n_{i+1,j} - 2u^n_{i,j} + u^n_{i-1,j}) + \frac{v_p^2\Delta t^2}{k^2}(u^n_{i,j+1} - 2u^n_{i,j} + u^n_{i,j-1}) \tag{3.13}$$

from which it follows that;

$$u^{n+1}_{i,j} = a_0 u^n_{i,j} - u^{n-1}_{i,j} + a_1(u^n_{i+1,j} + u^n_{i-1,j}) + a_2(u^n_{i,j+1} + u^n_{i,j-1}) \tag{3.14}$$

with

$$a_1 = \frac{v_p^2\Delta t^2}{h^2}, \qquad a_2 = \frac{v_p^2\Delta t^2}{k^2} \tag{3.15}$$

and

$$a_0 = 2(1 - a_1 - a_2). \tag{3.16}$$

Equation (3.14) represents a direct simple finite-difference algorithm, since it describes how to calculate the value of u at a given point in space, one time-step Δt into the future, from values at that point and points nearby in the present and recent past.

3.3 Consistency, Stability and Convergence

We begin by investigating how to obtain the best results from the wave equation. We proceed with calculations based on two dimensional difference schemes, where we consider the convergence, consistency and stability of the schemes.

The mathematical foundations of the questions and stability of discretised finite-difference approximations of PDEs are well developed only for linear systems. Therefore the results from a linear system are used as a guideline for the non-linear problems to be encountered later. There are many techniques (Matrix, and Von Neumann) which are needed to investigate the stability and consistency of the difference equations, depending on whether 2-D or 3-D problems are involved.

Consistency is defined as follows. Let L(U) = 0 represent the PDE in independent variables x and t, with exact solution U. Let F(U) = 0 represent the approximating finite-difference equation with exact solution u. Let v be a continuous function of x and t with a sufficient number of continuous derivatives to enable L(v) to be evaluated at the point (ih, jk). Then the truncation error $T_{ij}(v)$ at the point (ih, jk) is defined by

$$T_{ij}(v) = F_{ij}(v) - L(v_{ij}).$$

If $T_{ij}(v) \rightarrow 0$ as $h \rightarrow 0$, $k \rightarrow 0$, the difference equation is said to be consistent or compatible with the PDE. With this definition T_{ij} gives an indication of the error resulting from the

replacement of $L(v_{ij})$ by $F_{ij}(v)$. Most authors let $v = U$ because $L(U) = 0$. It then follows that

$$T_{ij}(U) = F_{ij}(U),$$

and the truncation error coincides with the local truncation error. The difference equation is then consistent if the limiting value of the local truncation error for the differential equation becomes zero as $h \to 0$, $k \to 0$.

If U represents the exact solution of a PDE with independent variables x and t, and u the exact solution of the finite difference equations used the approximate the PDE, the finite difference approximation is convergent when u tends to U at a fixed point or along a fixed t-level as h and k both tend to zero. We examine both cases together.

When difference approximations are stable any computational errors can be made arbitrarily small, so that computational errors remain bounded. For a linear PDE the Lax theorem states consistency + stability => convergence. However, for non-linear PDEs, even if the difference approximations is stable, there is no general theorem in existence which guarantees convergence of the system.

In our case, the algebraic equations arising from finite-difference equations are solved by the simple explicit method equation (3.14). For the simple explicit case, the main and most commonly used stability method used is the Von-Neumann method.

A necessary condition for stability is that there exist a constant K such that

$$|\lambda(k)| \leq 1+K\Delta t \quad \forall k, \quad n\Delta t \leq t_F,$$

for every eigenvalue $\lambda(k)$ of the amplification matrix G(k).

The local truncation error for 2-D PDEs, such as the acoustic and elastic wave equations, is generally found to be $O(\Delta t^2, h^2, k^2)$, so if the mesh becomes more refined, $(h, k \to 0)$, and if the time increment vanishes, then the error due to discretisation

tends to zero. Therefore the finite-difference equations and PDEs are compatible in this limit. By applying the Von-Neumann (Lapidus and Pinder [41], Smith G.D. [65],Thomas [77], and Morton and Mayer [52]) analysis to the 2-D wave equation we see that it is stable as long as $\Delta t \le \frac{h}{\sqrt{2}v_p}$ (h=k) and the 2-D elastic wave equation is also stable provided that $\Delta t \le h\left[v_p^2 + v_s^2\right]^{-1/2}$ where v_p is a compressional wave velocity and v_s is a shear wave velocity. In general, it is easy to show that for the 3-D wave equation, the stability condition for the explicit difference equation is $\Delta t \le \frac{h}{\sqrt{3}v_p}$ where (h=k). We have not undertaken a detailed stability analysis of the heterogeneous formulation. Kelly et al. [37], Stephan et al. [72], and Virieux [82] suggested that minimising the homogeneous stability condition $\Delta t \le h\left[v_p^2 + v_s^2\right]^{-1/2}$ over all grid points is sufficient for the stability of heterogeneous case.

These methods are well examined in texts such as Thomas [77], Smith G. D. [65], Lapidus and Pinder [41] and Morton and Mayers [52].

3.4 Dispersion, and Dissipation

In this section we will deal with dispersion and dissipation and compare numerical results with the exact solutions when possible. Sometimes the results will help us choose the derivable parameters (Δx, Δt, etc.) for obtaining an appropriate solution, and sometimes the results will only tell us why our results are unsatisfactory. We now give some examples of mixed results, when equation (3.9) is solved for different grids in space and time space. The results are shown in Figure (3.2) (M=20 and

t=1.0, t=1.5, t=2.0) for Δx=24.4 m smoother but we have an unwanted oscillation behind the computed wave. When M is increased to 100, the solution is much smoother and is qualitative correct because of stability but the wave traces are rough (M=100, t=1.0, t=1.5, t=2.0) at Δx=4.88 m as a seen in Figure (3.3).

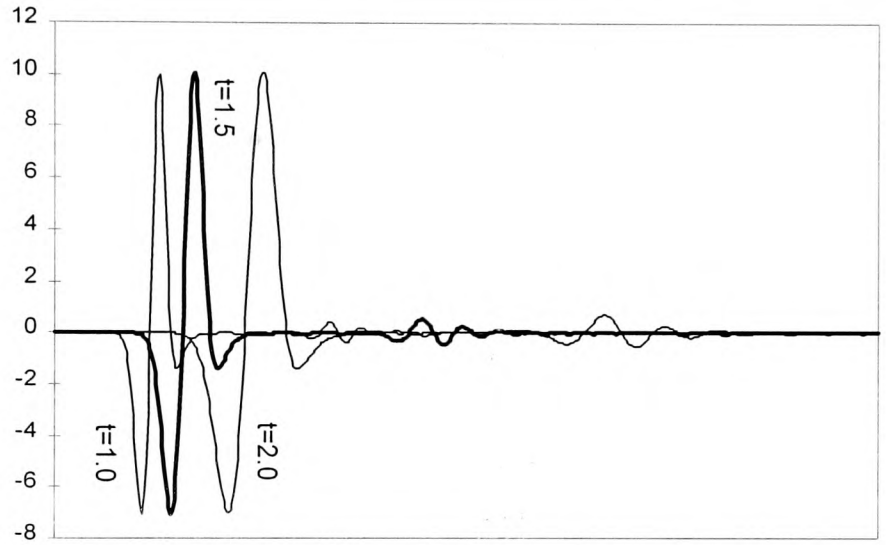

Figure (3.2) Approximate solutions to acoustic wave problem at times t=1.0, t=1.5 and t=2.0 obtained by using finite-difference methods with Δx=24.4 m.

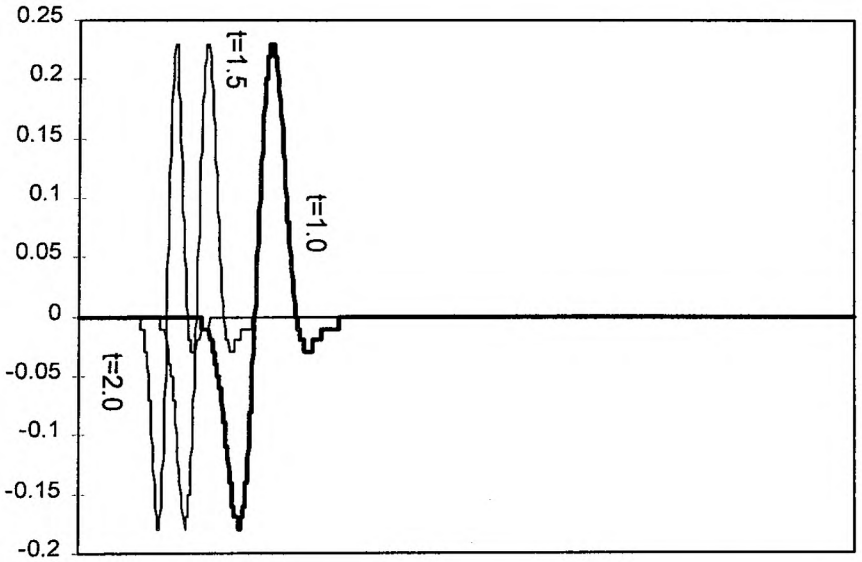

Figure (3.3) Approximate solutions to acoustic wave problem at times t=1.0, t=1.5 and t=2.0 obtained by using finite-difference methods with Δx=4.88 m.

Obviously, the oscillations are in some way due to the small time interval used (many time steps), but long time calculations will often be required when we tackle realistic applied problems. We must understand why a convergent scheme can give such undesirable results and would like to know how to correct these results. If we cannot explain how to correct these results, we must at least explain why these results are as they appear. More importantly, we must understand that if we are not careful, we can solve some problem numerically and the interesting results that appear could be due to numerical dissipation and /or dispersion. In both cases given above, we note that the results are not very good when we use M = 20 for long time calculations. Generally, M=100 does not generate a sufficiently fine grid to adequately resolve the solutions to 2-D PDEs.

When solving PDE's analytically, Fourier series or a Fourier transform are frequently used to give a solution type

$$u(x,z,t) = ue^{i(\omega n\Delta t - k\Delta x\cos\theta - k\Delta z\sin\theta)}, \qquad (3.17)$$

which describes a wave in space and time. In equation (3.17), ω is the frequency of the wave, k is the wave number and the wavelength, λ is given by $\lambda=2\pi/k$. We define the *dissipation* of solutions of PDEs when the Fourier amplitude modes in equation (3.17) do not grow with time, and at least one mode decays. Surely $\omega=\omega(k)$ is the dispersion relation and if ω independent of k then it is non-dissipative.

We chose $\omega=\omega(k)$ so that the solution equation (3.17) will satisfy our difference equation, and $\omega(k)$ is called the *discrete dispersion relation.* Considering $0< \beta\Delta x <\pi$ will give all of the modes contained in the finite Fourier series expansion of our solutions. In either case, to obtain dissipation and dispersion information for all modes associated with

either finite Fourier transform or finite series solutions of a FDM, we consider $\beta\Delta x$ in the range $0<\beta\Delta x<\pi$. Before we proceed, we claim that for finite-difference equations the discrete dispersion relation, $\omega=\omega(k)$, will generally be complex, the same situation if we considered PDE of the form

$$\frac{\partial^2 u}{\partial t^2} = v_p^2\left(\frac{\partial^2 u}{\partial x^2}+\frac{\partial^2 u}{\partial z^2}\right).$$

Consider a plane wave with wave number k, which makes an angle θ with the x-axis. Following Alfrod et al. **[2]**, and Virieux **[82]** the quantity γ given by

$$\gamma = \sqrt{2}v_p\frac{\Delta t}{\Delta x} \tag{3.18}$$

controls the numerical dispersion, and the quantity H defined as

$$H = \frac{\Delta x}{\lambda} \tag{3.19}$$

controls the number of nodes per wavelength of the plane wave. The resulting non-dimensional P-wave phase velocity (defined by the ratio of numerical P-wave phase velocity to true P-wave velocity) is:

$$q_p = \frac{\sqrt{2}}{\pi\gamma H}\sin^{-1}\left[\frac{\gamma}{\sqrt{2}}\sqrt{\sin^2(\pi H\cos\theta)+\sin^2(\pi H\sin\theta)}\right] \tag{3.20}$$

where q_p is independent of Poisson's ratio σ. Similarly the non-dimensional S-wave group velocity is:

$$q_s = \frac{\sqrt{2}v_p}{v_s\pi\gamma H}\sin^{-1}\left[\frac{v_s\gamma}{v_p\sqrt{2}}\sqrt{\sin^2(\pi H\cos\theta)+\sin^2(\pi H\sin\theta)}\right] \tag{3.21}$$

where q_s depends on the Poisson's ratio through v_s/v_p. The group velocity becomes zero when the wavelength becomes as short as twice the grid interval. The phase velocity is

shown in Figure (3.4) and group velocity is shown in Figure (3.5) as a function of H for several values $\Delta t/\Delta x$. Figure (3.4) and (3.5) indicate that $\Delta t/\Delta x$ should be made as large as possible to minimise dispersion. The maximum value is determined by the stability limit, $\Delta t/\Delta x = 2^{-1/2}$. Using values of $\Delta t/\Delta x$ near the stability limit is also desirable from the viewpoint of minimising computational time.

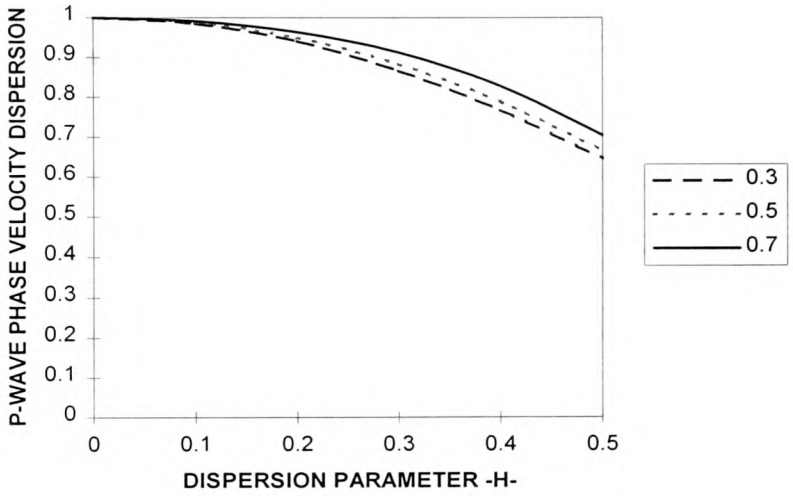

Figure (3.4) Normalised phase velocity for different stability ratios.

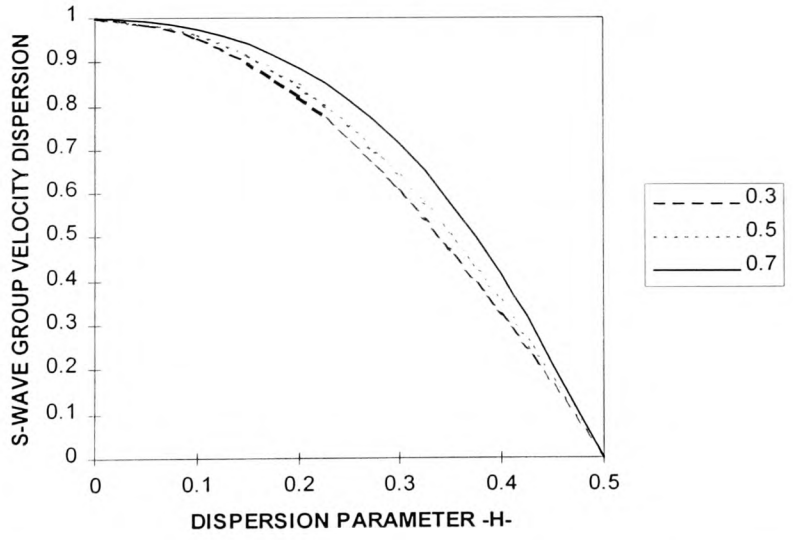

Figure (3.5) Normalised group velocity for different stability ratios.

The quantity q_p is always lower than unity and approaches one for small H. e.g. for $H \cong 0.1$, $q_p \cong 1$. $H \cong 0.1$ is the rule of thumb stating that a minimum of ten nodes is needed inside a wavelength for the correct modelling. In the case of usual FDM q_s may be found to be higher than unity, which means that the numerical S-wave propagates faster than the true S-wave. The quantity q_s approaches one for small H, giving the same rule thumb as for the P-wave modelling.

3.5 Absorbing Boundary Conditions

In this section Absorbing boundary conditions (ABCs) are examined for the wave equation. The wave propagation problems are normally solved for an infinite medium, but because of the finite core of computers and finite time available the FDM solution can only be obtained at a finite number of points, thus it is necessary to introduce boundaries to obtain a finite model. Traditional boundary conditions, such as Dirichlet and Neumann boundary conditions will generate reflecting waves, and pollute numerical wave solutions. When we solve our problem in a finite medium, we need ABC*s* due to edge reflection since ABC*s* reduce edge reflection. We give boundary conditions which greatly reduce this edge reflection and compare our boundary conditions with the Dirichlet and Neumann boundary conditions. Most of the ABCs developed are for use in FDM of the wave equation.

In the FDM, ABCs for the wave equation have been developed by several scientists such as Clayton & Engquist [**18**], with modifications by Fuyuki & Matsumoto [**26**], and by Emerman & Stephen [**23**]. Emerman & Stephen [**23**] found that Clayton & Engquist [**18**] ABCs are stable when $v_s/v_p > 0.46$. Whilst Emerman & Stephen [**23**] suggest $v_s/v_p > 0$. Numerical experimental evidence of this was shown by Higdon [**33**].

Lindman [**45**] who developed a remarkably effective solution for 2-D acoustic waves, based on a series expansion of $1/\cos\theta$. Randall [**59, 60**] decomposed the wavefield at the boundary into compressional and shear components by a potential method, and then applied Lindman's technique to each one separately. Long & Liow [**46**] also decomposed the incident wavefield into dilational and rotational strains and applied a one way equation to the two components independently. A wave-mechanical approach to the construction of ABCs is that proposed by Smith W.D. [**66**]. Kosloff et al. [**38**] used a viscous ABC which causes the wavefield to die away exponentially to zero at the boundaries, and thus to match all between opposite edges of the grid. The disadvantage of this approach is that, particularly in 2-D, a fairly large volume of the grid is wasted by the ABCs, which must typically be between ten and twenty wide.

The rigorous analysis of stability and accuracy for boundary conditions is very difficult, because of the many approximations typically involved in their formulation. Renaut & Peterson [**62**] have made some limited progress. Randall [**60**] indicates that his approach is applicable in 3-D but gives only 2-D examples. Chang and McMechan [**14**] studied 3-D problems. Also Stacey [**70**] was improved ABCs for the elastic wave equation. We concentrated on Reynolds and Clayton-Engquist ABCs. Reynolds [**64**] approaches have the advantages of being reliable, easy to understand, and fairly easy to implement. Reynolds's ABCs are ideal in a staggered grid approach because it uses only values on lines normal to the absorbing surface. We also used Clayton-Engquist ABCs in places.

3.5.1 Reynolds ABCs Approach

Below is an advancement of the Cartesian only approach of Reynolds [**64**]. Following Reynolds with $\tau = v_p t$ in orthogonal coordinates x_1, x_2, x_3 with line elements h_1, h_2, h_3 , and defining $H = h_1 h_2 h_3$ the 3-D wave equation is

$$\frac{\partial^2 u}{\partial \tau^2} = L[u] = L_1[u] + L_2[u] + L_3[u] \tag{3.22}$$

where,

$$L_i[u] = \frac{1}{h_i^2}\left(\frac{\partial^2 u}{\partial x_i^{\,2}} + \frac{\partial}{\partial x_i}\left(\ln\left(\frac{H}{h_i^2}\right)\right)\frac{\partial u}{\partial x_i}\right) \tag{3.23}$$

We shall "complete the square" on $L_i[u]$ with an operator

$$M_i[u] = \frac{1}{h_i}\left(\frac{\partial u}{\partial x_i} + A_i u\right)$$

so that

$$M_i^2[u] = \frac{1}{h_i^2}\left(\frac{\partial^2 u}{\partial x_i^2} + \left(2A_i - \frac{\partial}{\partial x_i}\left(\ln(h_i)\right)\right)\frac{\partial u}{\partial x_i}\right) + \frac{1}{h_i^2}\left(\frac{\partial A_i}{\partial x_i} + A_i^2 - A_i\frac{\partial}{\partial x_i}\left(\ln(h_i)\right)\right)$$

Writing $L_i[u] = M_i^2[u] + B_i u$ we obtain

$$2A_i - \frac{\partial}{\partial x_i}\left(\ln(h_i)\right) = \frac{\partial}{\partial x_i}\left(\ln\left(\frac{H}{h_i^2}\right)\right)$$

$$B_i = \frac{1}{h_i^2}\left(A_i\frac{\partial}{\partial x_i}\left(\ln(h_i)\right) - A_i^2 - \frac{\partial A_i}{\partial x_i}\right)$$

so $\quad A_i = \dfrac{\partial}{\partial x_i}\left(\ln\sqrt{\dfrac{H}{h_i}}\right)$,

The wave equation can be written as

$$\left(\frac{\partial}{\partial\tau}-\sqrt{L}\right)\cdot\left(\frac{\partial}{\partial\tau}+\sqrt{L}\right)[u]=0 \tag{3.24}$$

Thus an obvious boundary condition would be

$$\left(\frac{\partial}{\partial\tau}-\sqrt{L}\right)[u]=0 \text{ on } x_i=-a \quad \text{and} \quad \left(\frac{\partial}{\partial\tau}+\sqrt{L}\right)[u]=0 \text{ on } x_i=+a$$

We can use this equation to obtain relevant ABCs as follows. Consider

$$\left(\frac{\partial}{\partial\tau}\pm\sqrt{L}\right)[u]=0 \text{ on } x_i=\pm a \tag{3.25}$$

and pre-operate by M_i to obtain $\left(\frac{\partial M_i}{\partial\tau}\pm M_i\sqrt{L}\right)[u]=0$

In the spirit of Reynolds approximate, $M_i\sqrt{L}$ by $M_i^2+\frac{p}{p+1}B_i$ where p=1 is usual.

It is assumed , possibly incorrectly, that M_i and B_i , and M_i and $\sqrt{L}$ commute.

Since $\frac{\partial^2 u}{\partial\tau^2}=\left(M_i^2+B_i\right)[u]$ and $B_i[u]=\frac{\partial^2 u}{\partial\tau^2}-M_i^2[u]$

approximate $M_i\sqrt{L}$ by

$$M_i^2+\frac{p}{p+1}\left(\frac{\partial^2}{\partial\tau^2}-M_i^2\right)=\frac{p}{p+1}\frac{\partial^2}{\partial\tau^2}+\frac{1}{p+1}M_i^2$$

Then the boundary conditions are

$$\left(\frac{\partial M_i}{\partial\tau}\pm\frac{1}{p+1}\left(p\frac{\partial^2}{\partial\tau^2}+M_i^2\right)\right)[u]=0$$

or (3.26)

$$\left(p\frac{\partial}{\partial\tau}\pm M_i\right)\left(\frac{\partial}{\partial\tau}\pm M_i\right)[u]=0$$

Writing $\tau = v_p t$ in orthogonal co-ordinates the approximate boundary condition would be

$$\frac{p}{v_p^2}\frac{\partial^2 u}{\partial t^2} \pm \frac{p+1}{v_p}\frac{\partial}{\partial t} M_i[u] + M_i^2[u] = 0. \qquad (3.27)$$

i. ABCs for Cartesian coordinates

The Cartesian coordinate ABCs may be found from equation (3.27) by setting:

$$h_1 = h_2 = h_3 = 1 \quad \text{and} \quad H = 1$$

$$A_1 = A_2 = A_3 = 0 \quad , \quad M_1 = \frac{\partial u}{\partial x}, M_2 = \frac{\partial u}{\partial y}, M_3 = \frac{\partial u}{\partial z}$$

Thus at $x = \pm a$:

$$\frac{p}{v_p^2}\frac{\partial^2 u}{\partial t^2} \pm \frac{p+1}{v_p}\frac{\partial^2 u}{\partial t \partial x} + \frac{\partial^2 u}{\partial x^2} = 0 \qquad (3.28)$$

Whilst at $y = \pm a$:

$$\frac{p}{v_p^2}\frac{\partial^2 u}{\partial t^2} \pm \frac{p+1}{v_p}\frac{\partial^2 u}{\partial t \partial y} + \frac{\partial^2 u}{\partial y^2} = 0 \qquad (3.29)$$

and at $z = \pm a$:

$$\frac{p}{v_p^2}\frac{\partial^2 u}{\partial t^2} \pm \frac{p+1}{v_p}\frac{\partial^2 u}{\partial t \partial z} + \frac{\partial^2 u}{\partial z^2} = 0. \qquad (3.30)$$

There equations are given in Reynolds [**64**].

ii. ABCs for cylindrical coordinates

We now obtain cylindrical coordinates boundary conditions from equations (3.27). On setting

$$h_1 = h_3 = 1 \quad , h_2 = r \quad \text{and} \quad H = r$$

$$A_1 = \frac{1}{2r} \quad , A_2 = A_3 = 0 \quad , \quad M_1 = \frac{\partial u}{\partial r} + \frac{u}{2r}, M_2 = \frac{1}{r}\frac{\partial u}{\partial \theta}, M_3 = \frac{\partial u}{\partial z}$$

We find

At $r = a$

$$\frac{p}{v_p^2}\frac{\partial^2 u}{\partial t^2} \pm \frac{p+1}{v_p}\left(\frac{\partial^2 u}{\partial r \partial t} + \frac{1}{2r}\frac{\partial u}{\partial t}\right) + \frac{\partial^2 u}{\partial r^2} + \frac{1}{r}\frac{\partial u}{\partial r} - \frac{u}{4r^2} = 0 \qquad (3.31)$$

At $\theta = \pm a$

$$\frac{p}{v_p^2}\frac{\partial^2 u}{\partial t^2} \pm \frac{p+1}{v_p}\frac{1}{r}\frac{\partial^2 u}{\partial t \partial \theta} + \frac{1}{r^2}\frac{\partial^2 u}{\partial \theta^2} = 0 \qquad (3.32)$$

At $z = \pm a$

$$\frac{p}{v_p^2}\frac{\partial^2 u}{\partial t^2} \pm \frac{p+1}{v_p}\frac{\partial^2 u}{\partial t \partial z} + \frac{\partial^2 u}{\partial z^2} = 0 \qquad (3.33)$$

We have modified the Reynolds ABCs for cylindrical coordinates.

3.5.2 Clayton-Engquist ABCs Approach

In this section we present a set of Clayton-Engquist ABCs that are based on paraxial approximations of acoustic and elastic wave equations. The Clayton-Engquist ABCs for the acoustic case are given as

$x = \pm a$ $$u_{zt} + \frac{1}{v_p}u_{tt} - \frac{v_p}{2}u_{xx} = 0 \qquad (3.34)$$

$z = \pm a$ $$u_{xt} + \frac{1}{v_p}u_{tt} - \frac{v_p}{2}u_{zz} = 0 \qquad (3.35)$$

Derivatives in suffix notation $u_{zt} = \frac{\partial^2 u}{\partial z \partial t}$, $u_{tt} = \frac{\partial^2 u}{\partial t^2}$, and $u_{xx} = \frac{\partial^2 u}{\partial x^2}$.

The boundary condition formulas for the lower right-hand corner in acoustic case is

$$u_z + u_x + \frac{\sqrt{2}}{v_p}u_t = 0 \qquad (3.36)$$

For 2-D elastic problems Clayton-Engquist ABCs are given as

$x = a$ $$\mathbf{u}_{xt} + C_1\mathbf{u}_{tt} + C_2\mathbf{u}_{zt} + C_3\mathbf{u}_{zz} = 0 \quad (3.37)$$

$z = a$ $$\mathbf{u}_{zt} + C_1\mathbf{u}_{tt} + C_2\mathbf{u}_{xt} + C_3\mathbf{u}_{xx} = 0 \quad (3.38)$$

where $C_1 = \begin{pmatrix} \frac{1}{v_s} & 0 \\ 0 & \frac{1}{v_p} \end{pmatrix}$, $C_2 = (v_s - v_p)\begin{pmatrix} 0 & \frac{1}{v_s} \\ \frac{1}{v_p} & 0 \end{pmatrix}$, and $C_3 = \frac{1}{2}\begin{pmatrix} v_s - 2v_p & 0 \\ 0 & v_p - 2v_s \end{pmatrix}$.

For the lower right-hand corner in elastic case is

$$\mathbf{u}_z + \mathbf{u}_x + M\mathbf{u}_t = 0 \quad (3.39)$$

where $$M = \frac{1}{\sqrt{2}}\begin{pmatrix} \left(\frac{1}{v_s} + \frac{1}{v_p}\right) & \left(\frac{1}{v_s} - \frac{1}{v_p}\right) \\ \left(\frac{1}{v_s} - \frac{1}{v_p}\right) & \left(\frac{1}{v_s} + \frac{1}{v_p}\right) \end{pmatrix}.$$

3.6 Summary

In this chapter the FDM was presented for the numerical solution of wave propagation problems. Numerical solutions sometimes do not give the best results. We examined the requirements of consistency, stability, and convergence necessary to provide the required results along with the difficulties associated with numerical dispersion and dissipation. Subsequently we employed two different well known absorbing boundary conditions which are namely the Reynolds and Clayton-Engquist ABCs.

In the next chapter we will apply these approaches to the specific numerical seismic wave propagation modelling. We will introduce specific numerical methods which are namely the (ur + us), box, staggered grid and variable scale (VSM) methods, incorporating the work of this chapter.

CHAPTER 4

SPECIFIC NUMERICAL SEISMIC WAVE PROPAGATION MODELLING

4.1 Introduction

The FDM is a powerful and well established technique for studying the seismic wave propagation in layered rock media. Here we introduce the specific numerical schemes that will be employed for the numerical simulation of wave propagation problems. The methods apply to both acoustic wave propagation as well as to elastic displacement waves. These methods will be used extensively for the problems under consideration in future chapters.

Firstly, the FDM with the "(ur+us)" (details in the next section) model was employed by Ottaviani [**55**] who used a compressional line source in two evenly-welded quarter-spaces where he investigated diffraction of the source pulse. The approach was also employed by Stephen et al. [**72**] who presented an outline of the finite-difference method applied to the acoustic logging problem, including a boundary condition formulation for liquid-solid cylindrical interfaces. Absorbing boundaries based on the formulations of Reynolds [**64**] and Clayton and Engquist [**18**] were used to reduce reflections from the boundaries. They compared the sharp interface model with a discrete-wavenumber model.

Secondly, the FDM with a "Box" model was employed by Alterman & Karal [**3**] to accommodate source singularities that choose three different mesh sizes for the same

problem. They found sufficient accuracy for their theoretical seismograms and they subsequently examined the development of Rayleigh wave on the surface of a half-space.

Thirdly, staggered grid models were developed by Virieux [**82**] in 2-D, and used on Weathered-layer and Corner-edge problems to model P-SV waves in an inhomogeneous plane. Staggered grid algorithms are recognised as having better experimental stability and accuracy than centred ones as witnessed by Levander [**44**]. A further useful development of the staggered grid approach is given by Luo & Schuster [**47**] who introduced a 2-D formulation in which the stress-velocity, (p-v), fields are basically included as functions of a single field of vector displacement values. Improvement in accuracy and stability over a conventional centred scheme is demonstrated, but, a smaller number of values needs to be stored (at the expense of more calculation at each time-step) to make the numerical simulation more memory effective. A 3-D implementation of this "parsimonious" staggered grid scheme has recently been used successfully for modelling boreholes by Yoon & McMechan [**87**]. The parsimonious staggered grid algorithm is adopted here in preference to the (p-v) Virieux formulation because it is easier to perform the analysis and uses less computer memory.

4.2 (ur+us) Method

We used this method because the singularity at the source of seismic waves cannot be included in the finite-difference scheme. The displacement field is divided into two parts: the primary field of the source which is present only in the medium where the source is located, and the secondary field which includes the displacements

due to reflection, conversion, and diffraction at the boundaries and at the corners. We rewrite the horizontal and vertical displacements of equation (2.25) with this method. We write u=(ur+us) and w=(wr+ws) instead of the horizontal and vertical displacements u and w. These terms ur, wr include the horizontal, vertical reflection etc. components, and us, ws represent the horizontal and vertical source displacements which are analytic solutions for the compressive wave source in an infinite medium. We have

$$\begin{aligned}\frac{\partial^2(ur+us)}{\partial t^2} &= v_p^{\,2}\frac{\partial^2(ur+us)}{\partial x^2} + v_s^{\,2}\frac{\partial^2(ur+us)}{\partial z^2} + \left(v_p^{\,2}-v_s^{\,2}\right)\frac{\partial^2(wr+ws)}{\partial x\partial z}\\ \frac{\partial^2(wr+ws)}{\partial t^2} &= v_s^{\,2}\frac{\partial^2(wr+ws)}{\partial x^2} + v_p^{\,2}\frac{\partial^2(wr+ws)}{\partial z^2} + \left(v_p^{\,2}-v_s^{\,2}\right)\frac{\partial^2(ur+us)}{\partial x\partial z}\end{aligned} \tag{4.1}$$

The values of ur and wr, representing reflections, are always assumed bounded. Similarly, we can rewrite the all boundary condition equations (3.28) and (3.30) using the decomposition into ur+us. In this form "subtracting out" us and ws allows us to solve only for the bounded ur, wr within the computational domain. The complete solution at the geophones can be determined by "adding in" us, ws at those points. This method is primarily restricted to one medium. There are more details in Ottaviani [**55**].

4.3 Box Method

This method is adopted to take account of multimedia geometries. Suppose the source is surrounded by a rectangular region, a cross section of which is shown in Figure (4.1). Denote the interior region, including the inner doted boundary, by **I**. Denote the exterior region (one grid line removed from **I**), including the outer dotted boundary, by **II**. In both regions we can always express the horizontal and vertical displacements u and w as

$$u = us + ur$$
$$w = ws + wr \qquad (4.2)$$

Here us and ws are the horizontal and vertical displacements due to the source alone and can always be determined exactly. Again ur and wr are the remaining parts of the horizontal and vertical displacements due to all other causes. (i.e., such as reflections and are always bounded).

1. Calculate values of ur and wr in **I** using the finite-difference equation scheme.

2. Calculate values of u and w in **II** using the finite-difference equation scheme.

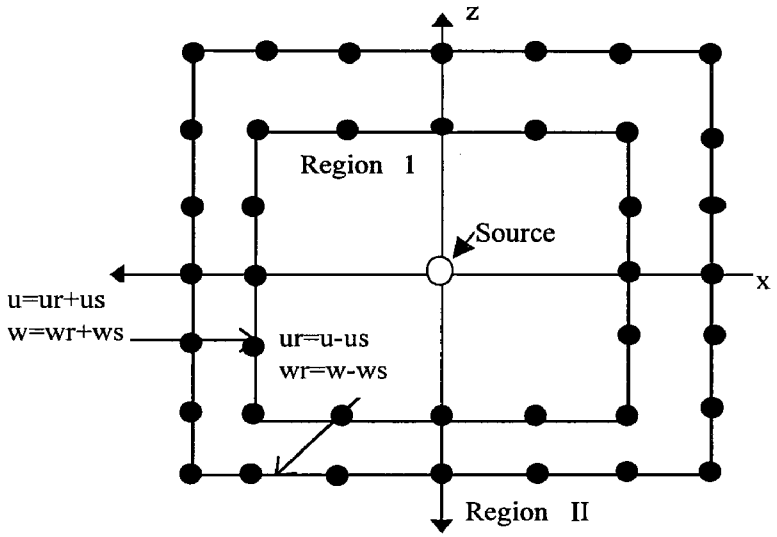

Figure (4.1) Box method geometry

3. From the calculation of ur and wr in **I**, calculate u and w along the inner dotted line using equation (4.2). These values provide the boundary values needed to calculate u and w in using the finite-difference equation scheme.

4. Similarly, from the calculation of u and w in **II**, calculate ur and wr along the outer dotted line using equation (4.2). These values provide the boundary values needed to calculate ur and wr in **I** using finite-difference equation scheme. The initial values for

ur and wr in region **I**, and for u and w in region **II**, are easily obtained. As long as the wave has not reached the boundaries, ur = 0, wr = 0 and these are the initial values for calculating ur and wr subsequently in region **I**. Similarly, as long as the pulse has not reached the boundaries, u = us, w = ws and these are the initial values for calculating u and w subsequently in region II. There are more details in Alterman and Karal [**3**].

4.4 Staggered Grid Method

The standard FDM is not stable for large contrasts in Poisson's ratio, such as at fluid-solid contacts (Stephen [**71**]). This stability problem may be overcome by using a staggered grid. This method gives stable and accurate results for step discontinuities in media properties enabling multimedia geometries to be essentially treated as for one domain. For 2-D, the conservation of momentum equation are

$$\rho\frac{\partial^2 u}{\partial t^2} = \frac{\partial P_{xx}}{\partial x} + \frac{\partial P_{xz}}{\partial z}$$
$$\rho\frac{\partial^2 w}{\partial t^2} = \frac{\partial P_{xz}}{\partial x} + \frac{\partial P_{zz}}{\partial z} \qquad (4.3)$$

and the stress-strain relations are

$$P_{xx} = \lambda\phi + 2\mu\frac{\partial u}{\partial x}$$
$$P_{zz} = \lambda\phi + 2\mu\frac{\partial w}{\partial z}$$
$$P_{xz} = \mu\left(\frac{\partial u}{\partial z} + \frac{\partial w}{\partial x}\right) \qquad (4.4)$$
$$\phi = \frac{\partial u}{\partial x} + \frac{\partial w}{\partial z}$$

where λ and μ are Lame's parameters, ρ is density, and u and w are displacement components relating to one particular medium. Now each material particle displacement will have a bearing on the displacement of the particles surrounding it. With reference to Figures (4.2) and (4.3) consider derivatives in the x direction at P, let L & R be points left and right of P at a distance Δx away. For a quantity T we have to second order accuracy from Taylor series

$$\frac{T^R - T^L}{2\Delta x} \approx \frac{\partial T}{\partial x} \quad , \quad \frac{T^T - T^B}{2\Delta z} \approx \frac{\partial T}{\partial z} \tag{4.5}$$

The displacement at the one time and place will have a direct effect on displacement in another time and place. In a similar way we can write for the time derivative.

$$\left(\frac{\partial^2 T}{\partial t^2}\right)_P^n = \frac{T_P^{n+1} - 2T_P^n + T_P^{n-1}}{\Delta t^2} \tag{4.6}$$

where

T_P^n is the value of T at P at time n (present)
T_P^{n+1} is the value of T at P at time n + 1 (future)
T_P^{n-1} is the value of T at P at time n − 1 (past)

If we now substitute equations (4.5) and (4.6) into (4.3) we get on the full line grid

$$\rho\left[\frac{u^{n+1} - 2u^n + u^{n-1}}{\Delta t^2}\right]_P = \frac{(P_{xx})_R^n - (P_{xx})_L^n}{2\Delta x} + \frac{(P_{xz})_T^n - (P_{xz})_B^n}{2\Delta z}$$

and similarly, (4.7)

$$\rho\left[\frac{w^{n+1} - 2w^n + w^{n-1}}{\Delta t^2}\right]_P = \frac{(P_{xz})_R^n - (P_{xz})_L^n}{2\Delta x} + \frac{(P_{zz})_T^n - (P_{zz})_B^n}{2\Delta z}$$

Therefore from equation (4.4), and for the present time we get on the dashed line grid

$$\left(P_{xx}\right)_P^n = \lambda_P^n \phi_P^n + 2\mu_P^n \left(\frac{u_R^n - u_L^n}{2\Delta x} \right)$$

$$\left(P_{zz}\right)_P^n = \lambda_P^n \phi_P^n + 2\mu_P^n \left(\frac{w_T^n - w_B^n}{2\Delta z} \right)$$

$$\left(P_{xz}\right)_P^n = \mu_P^n \left[\frac{u_T^n - u_B^n}{2\Delta z} + \frac{w_R^n - w_L^n}{2\Delta x} \right]$$

$$\phi_P^n = \frac{u_R^n - u_L^n}{2\Delta x} + \frac{w_T^n - w_B^n}{2\Delta z}$$

All this means that we take u and w as two interlinked meshes (see Figures (4.2), (4.3)); implementation is by second-order, central finite-differences.

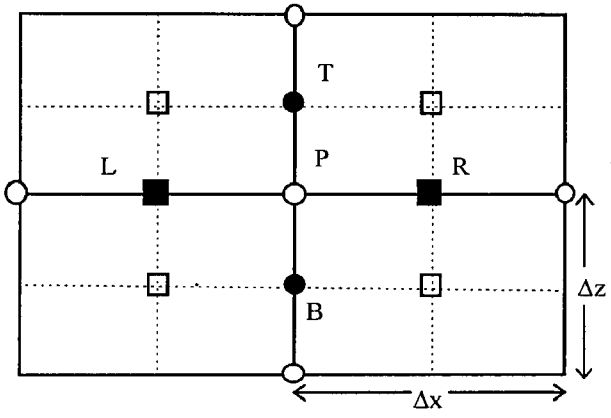

Figure (4.2) Full line grid discretisation

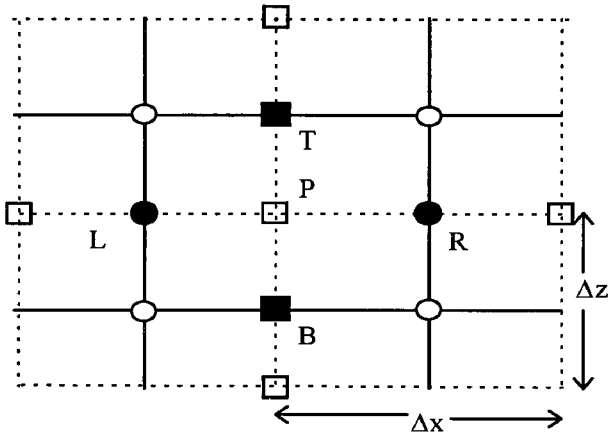

Figure (4.3) Dashed line grid discretisation

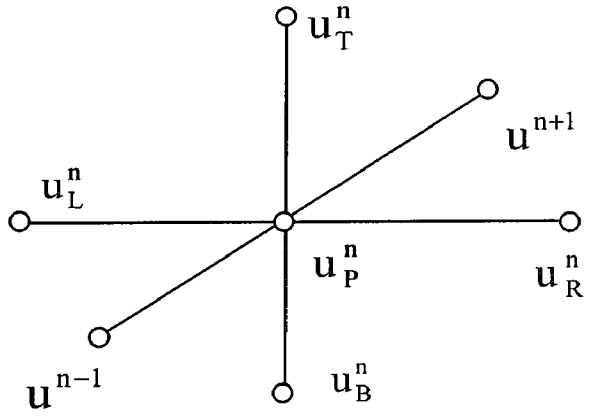

Figure (4.4) 3-D time discretisation for u

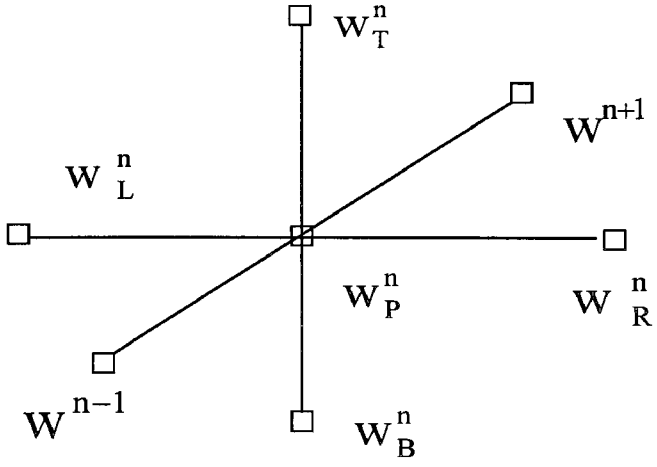

Figure (4.5) 3-D time discretisation for w

The u equation is based on full line grid at symbol O and the w equation is based on the dashed line grid at symbol □ perpendicular to the paper (see Figures (4.4) and (4.5)). This ultimately means that we have six arrays; past, present and future arrays for horizontal displacement; past, present and future arrays for the vertical displacement.

4.5 Variable Scale Method

In this section we employ a new method for the FDM which is useful for boreholes in Cartesian coordinates and cylindrical coordinates. It is inconvenient to solve the borehole problems with the standard FDM, because the borehole radius is very small. Therefore, we develop the variable scale method (VSM) that is superior to all other methods in terms of taking a small grid interval near the borehole and larger grids further from it. We obtained satisfactory results using this method for standard problems. We employ the variable function as follows.

$$\xi=\alpha\tanh(\beta x)$$

where α, β positive constants.

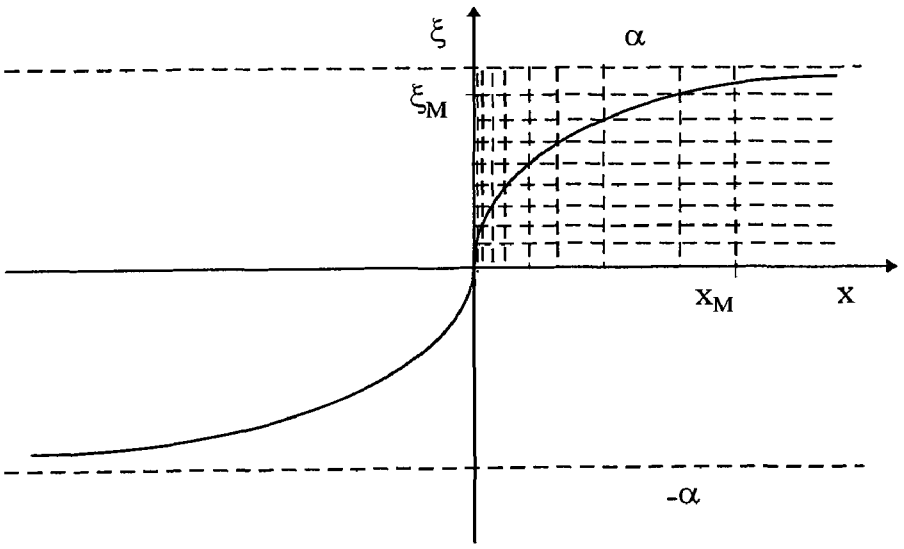

Figure (4.6) Variable scale geometry

The 2-D wave equation is converted to the scaling coordinates and is now given as

$$\rho\frac{\partial^2 u}{\partial t^2} = v_p^2\frac{\partial}{\partial\xi}\left(A(\xi)\frac{\partial u}{\partial\xi}\right) + v_s^2\frac{\partial^2 u}{\partial z^2} + \left(v_p^2 - v_s^2\right)A(\xi)\frac{\partial}{\partial\xi}\frac{\partial w}{\partial z} \tag{4.8}$$

where

$$A(\xi) = dx/d\xi = (\beta/\alpha)(\alpha^2-\xi^2)$$

In this method the stability condition is given by

$$\Delta t \le \frac{h}{\sqrt{2}A(\xi)v_p}$$

based on an approximate von Neumann stability and assuming $A(\xi)$ is locally constant. One borehole can be dealt with easily but two boreholes can not easily be accommodated.

4.6 Seismic Sources

In order to solve the seismic wave equations we need a source term for us and ws, and receivers to record seismic waves. The compressional point source was used with the box model and the impulsive line source was used with the (ur+us) model. A source term is located inside the medium along the axis at point (x_s, z_s) as in Figure(4.7). Receivers are located inside the medium along the axis at line (x_r, z_r) which these are very close to surface. e.g. Reynolds [**64**].

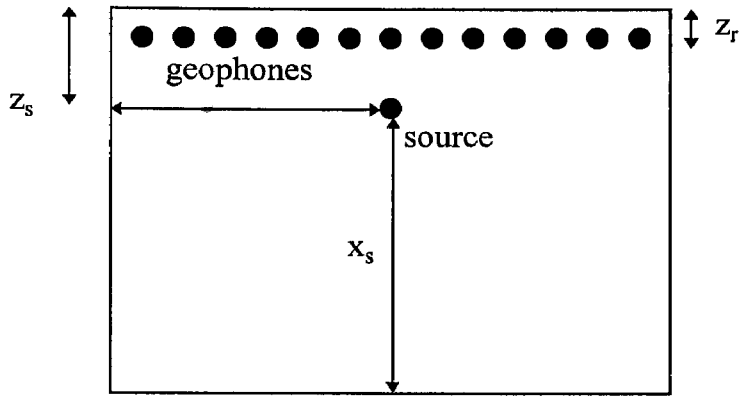

Figure (4.7) The geometry is shown source and receivers in medium.

Seismic detectors designed to transform seismic energy into electrical voltage are generally geophones on land and hydrophones at sea. **Geophones** transform the movement of the ground into a particle velocities. With the geophone placed on the ground, the magnet follows the vertical movements of the ground, and the coil tends to remain stationary by inertia. **Hydrophones** transform the pressure variations in the water into an electrical voltage.

Inclusion of the source term requires special consideration because of singularities at the source point and we used both the box model and (ur+us) model for avoiding this difficulty. Seismic sources are of different types for land and marine surveys.

4.6.1 Land sources

Explosive sources were the standard method formerly used for the seismic emission on land. It is still employed today in areas where its use is feasible. Dynamite charges from 100 g to a few kg are buried in holes 3 to 15 m deep, and 10 to 15 cm in diameter, at the base of the weathered zone. Explosive offers the advantage of being an energy source transmitting in a wide band of seismic frequencies. The most widely used

source in land surveying for seismic prospecting, is the hydraulically **driven vibrator,** in which a radiating plate is preloaded by the weight of the vehicle. **Other land sources** are simple impactors and coded impactors. They are often employed for fine seismic investigations with high resolution and medium penetration. Other systems employ metal plates thrust against the ground by the explosion of a gas mixture or a compressed air discharge into small water tanks placed on the ground surface (Bolt **air guns**). More details in Lavergne [**42**].

4.6.2 Marine sources

Explosives, formerly used for offshore seismic emissions, have almost completely disappeared today, mainly because of the damage, often inflicted on the marine fauna. **Air guns** are the most widely used sources today. The principle consists of the injection of a few litres of highly-compressed air into the water, causing the emission of a high-intensity pressure wave. **Steam guns** are sources that inject a quantity of superheated steam under high pressure into the water. The steam is heated by a shipboard boiler. The energy of steam guns is comparable to that of air guns. **Water guns** are marine sources which also generate pulses without bubble effect. Several water guns can be grouped to obtain directional effects, with energies comparable to those of air gun arrays. **Sparkers** emit acoustic energy by an electrical discharge in the sea-water. Sparkers are ideal sources for the fine analysis of shallow horizons. More details in Lavergne [**42**].

4.6.3 Compressional Point Source in 3-D Problems

The solution to the wave equation for the compressional point source in a homogeneous medium in Cartesian coordinates (x,y,z) is given by Stephen [72]. Suppose that the source time function is a Gaussian curve (Kelly et al. [37]). Then

$$g(t) = -2\alpha T e^{-\alpha T^2} \qquad , T = t - t_s ,$$

where α is a pulse width parameter and t_s is a time shift parameter. Since the horizontal displacements (refers to equations (4.1, 4.2)) *us*, *vs*, and vertical displacement *ws* are the gradient of the potential,

$$us(x,y,z,t) = \left[\frac{x - x_s}{R}\right]\frac{(-A)}{4\pi\rho v_p^2}\left[\frac{g\left(t - R/v_p^2\right)}{R^2} + \frac{g'\left(t - R/v_p^2\right)}{Rv_p^2}\right], \tag{4.9}$$

$$vs(x,y,z,t) = \left[\frac{y - y_s}{R}\right]\frac{(-A)}{4\pi\rho v_p^2}\left[\frac{g\left(t - R/v_p^2\right)}{R^2} + \frac{g'\left(t - R/v_p^2\right)}{Rv_p^2}\right] \tag{4.10}$$

and similarly

$$ws(x,y,z,t) = \left[\frac{z - z_s}{R}\right]\frac{(-A)}{4\pi\rho v_p^2}\left[\frac{g\left(t - R/v_p^2\right)}{R^2} + \frac{g'\left(t - R/v_p^2\right)}{Rv_p^2}\right] \tag{4.11}$$

where $$g'(t) = -2\alpha\left(1 - 2\alpha T^2\right)e^{-\alpha T^2}$$

where $R = \left(x^2 + y^2 + z^2\right)^{1/2}$ is the distance between the source and observation point, v_p is the compressional wave velocity in the medium, ρ is the density of the medium and A is a unit constant with dimensions of $\left(mass \times length^2 / time\right)$.

4.6.4 An Impulsive Line Source in 2-D Problems

The source is taken to be a compressional line pulse which is a solution of equations (2.25) in a geometry Figure (4.7). Horizontal and vertical displacements due to such a source are given as by Ottaviani [55]

$$us(x,z,t) = \frac{x-x_s}{R^2}\frac{v_p t}{\sqrt{v_p^2 t^2 - R^2}} H(v_p t - R)$$
$$ws(x,z,t) = \frac{z-z_s}{R^2}\frac{v_p^2 t}{\sqrt{v_p^2 t^2 - R^2}} H(v_p t - R) \qquad (4.12)$$

where x_s and z_s are the source position in the geometry , $R = \sqrt{(x-x_s)^2 + (z-z_s)^2}$ and H(t) is the Heaviside function. The impulsive line source as given by equations (4.12) has two singularities: one at R=0 and the other at $R = v_p t$. The former singularity does not affect our solution, but to avoid the later singularity, we employ the same procedure described by Alterman and Rotenberg [5]. Integrating equations (4.12) twice with respect to time and then computing their second order finite difference also with respect to time, one obtains

$$us(x,z,t) = \frac{1}{\Delta^2}\left[u_s(x,z,t) - 2u_s(x,z,t-\Delta) + u_s(x,z,t-2\Delta)\right]$$
$$ws(x,z,t) = \frac{1}{\Delta^2}\left[w_s(x,z,t) - 2w_s(x,z,t-\Delta) + w_s(x,z,t-2\Delta)\right] \qquad (4.13)$$

where Δ is a constant measuring the sharpness of the pulse and u_s and w_s are given by

$$u_s(x,z,t) = \frac{x-x_s}{v_p}\left[\frac{v_p t}{R}\sqrt{\left(\frac{v_p t}{R}\right)^2 - 1} - \ln\left(\frac{v_p t}{R} + \sqrt{\left(\frac{v_p t}{R}\right)^2 - 1}\right)\right]\cdot H\left(\frac{v_p t}{R} - 1\right)$$
$$w_s(x,z,t) = \frac{x-x_s}{v_p}\left[\frac{v_p t}{R}\sqrt{\left(\frac{v_p t}{R}\right)^2 - 1} - \ln\left(\frac{v_p t}{R} + \sqrt{\left(\frac{v_p t}{R}\right)^2 - 1}\right)\right]\cdot H\left(\frac{v_p t}{R} - 1\right) \qquad (4.14)$$

4.7 Seismic Receivers

An ideal receiver would provide an electrical output corresponding exactly to some feature of the seismic wave, without disturbing the wave field. A device small compared to all wavelengths, matching the density and elastic properties of the solid, would be expected to disturb the wave very little. The objective is to obtain an output proportional to some feature like particle displacement (or velocity, or acceleration); normal or tangential stress; pressure; elongation or shear strain; dilatation; rotation; or perhaps some non-linear combination like intensity. We shall consider briefly some of the attempts to observe these features of seismic waves. Seismic receivers designed to transform seismic energy into electrical voltage are generally geophones on land and hydrophones at sea. More details in Lavergne [**42**].

4.7.1 Geophones

The most widely used receivers in seismic prospecting and engineering geophysics are geophones. Geophones transform the movement of the ground into an electrical voltage. They are usually moving coil electomagnetic sensors. A moving coil with a large number of very fine wire turns is suspended in the slit by light, flat springs. With the geophone placed on the ground, the magnet follows the vertical movements of the ground, and the coil tends to remain stationary by inertia. The geophones' "responses" are expressed in volts per centimeter per second. It depends on the frequency, displays a plateau up to around 300 Hz, resonates around 20 Hz, and drops at the low frequencies. The value of the plateau is generally about 100 mV/cm/s, and shunt resistance is selected to achieve damping close to the critical damping. This produces an

electrical voltage proportional to the velocity of the ground particles, in a frequency band from 20 to 300 Hz, which normally covers the useful band in land surveys.

4.7.2 Hydrophones

Hydrophones transform the pressure variations in the water into an electrical voltage. They are generally piezoelectric sensors consisting of two piezoelectric ceremics mounted symmetrically on the two bases of a small cylindrical drum. Hydrophone response is expressed in volts per bar and depends on the frequency, the response displays a plateau at the high frequencies and drops at the low frequencies. The value of the plateau is a few volts per bar, and the electrical voltages obtained are proportional to the pressure, in a frequency band of about 20 to 300 Hz, which generally covers the useful band for marine surveys.

For modelling purposes we use selected grid points at which the wave signals received can be stored for display.

4.8 Summary

In this chapter we found that many researchers had studied the standard FDM almost exclusively in seismic wave modelling with comparatively little use of other FDM. The traditional approaches used are as follows; Alterman & Karal [**3**] used the "Box" method, Ottaviani [**55**] employed to the "(ur+us)" method and Reynolds[**64**], and Stephen [**72**] just used the traditional FDM. The staggered grid method was first employed by Virieux [**82**]. Building on this we have developed the new VSM approach. A compressional point source was used for 3-D cylindrical coordinates by Stephen [**72**] and an impulsive line source used for 2-D Cartesian coordinates as in Ottoviani [**55**],

and these formed the basis for our work. We believe our approach of combined box and staggered grid method to be novel, as is the VSM method.

In the next chapter we will present 2-D acoustic wave simulation results for various rock structures based on the above approaches.

CHAPTER 5

2-D ACOUSTIC WAVE MODELLING

5.1. Introduction

We now present the results of the 2-D acoustic wave propagation modelling in both Cartesian and cylindrical coordinates. We intend to compare our methods with those of others where possible (with standard FDM approaches), and in particular to examine our VSM.

Also examined will be the absorbing boundary conditions of Reynolds and Clayton-Engquist which will be compared with a view to finding which is the best for our purposes, and also to determine the effectiveness of the Reynolds ABCs in cylindrical coordinates which is believed to be a novel approach. Furthermore we shall determine the optimum grid / wavelength analyses to satisfy the requisite stability, convergence, dispersion, dissipation criteria for modelling purposes.

The possibility of observing the effects of multi layered media in the generated waveforms will also be examined.

5.2. 2-D Acoustic Wave Equation

In the two-dimensional case, the acoustic wave equation with a simple Gaussian source function is given by

$$\frac{1}{v_p^2}\frac{\partial^2 u}{\partial t^2} = \frac{\partial^2 u}{\partial x^2} + \frac{\partial^2 u}{\partial z^2} + \delta_{r,s} \cdot f(t) \qquad (5.1)$$

where v_p denotes the velocity sound of the medium and $\delta_{r,s}$ is the Kronecker delta function with source at x=rh, z=sk. For comparison with Reynolds [**64**]. The physical problem of interest consists of solving an equation of the form (5.1) for one medium, and multimedia, in the domain $D=\{(x, z, t)|\ -\infty<x<\infty,\ 0\le z<\infty,\ t\ge 0\}$

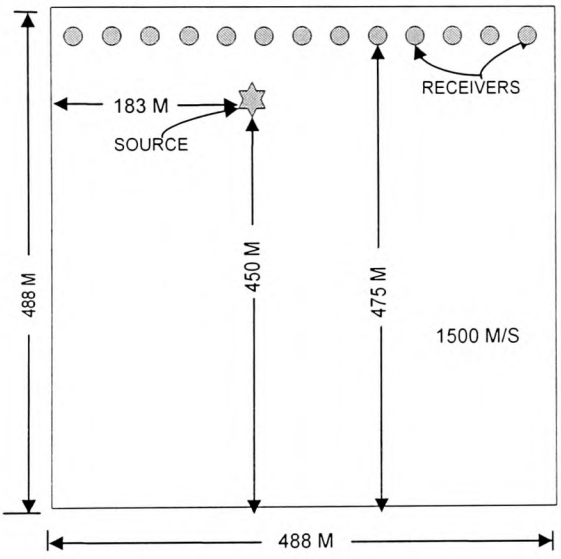

Figure (5.1) Physical model showing receiver geometry used to generate seismograms in the acoustic finite-difference program for one medium.

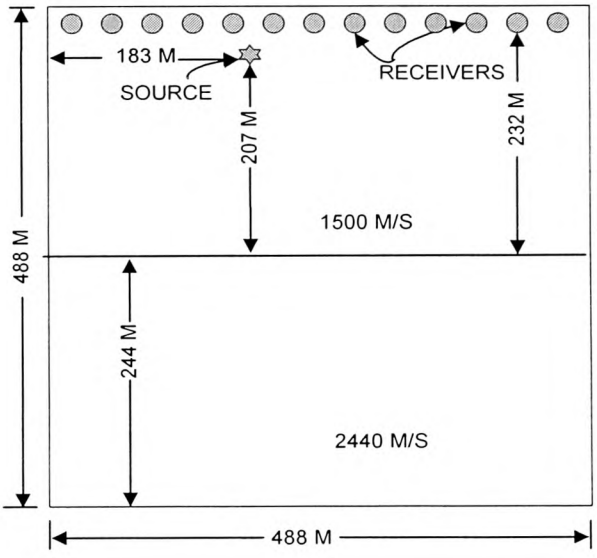

Figure (5.2) Physical model showing receiver geometry used to generate seismograms in the acoustic finite-difference program for two media.

However we solve the problem for $D'=\{(x, z, t)|\ 0\le x\le 488,\ 0\le z\le 488,\ 0\le t\le 1\}$ for a finite working domain. Figure (5.1) shows a one medium geometry and Figure (5.2) shows a two media geometry that we consider for comparison with the work of

Reynolds [64]. Figure (5.3) shows the multimedia geometry. We obtain traces determined at geophone receiver points.

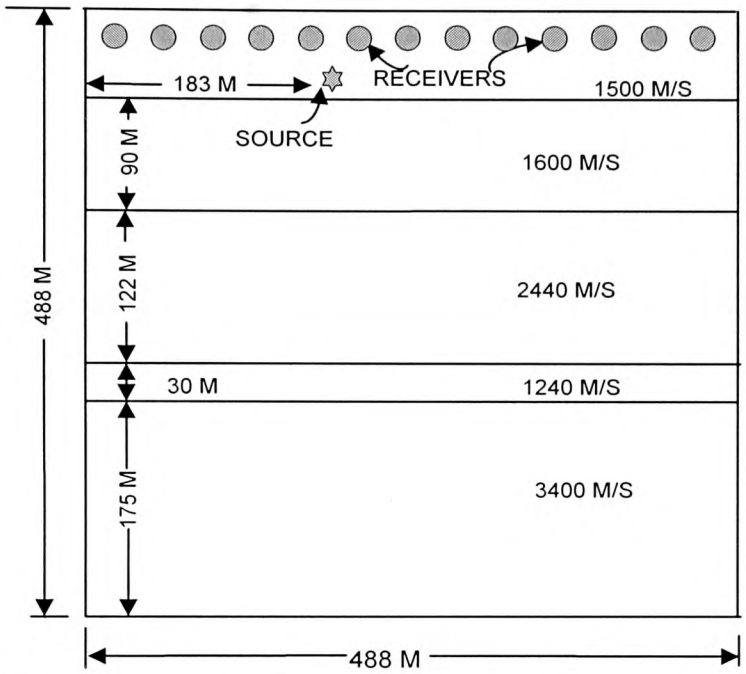

Figure (5.3) Physical model showing receiver geometry used to generate seismograms in the acoustic finite-difference program for multimedia

5.3 Discretisation of 2-D Acoustic Wave Equations

As mentioned in Chapter 3, some choice is available as to how to discretise equation (5.1) so as to construct a 2-D finite difference model.

To solve the partial differential equations we set up a grid over the domain. The partial differential equation is approximated using finite differences. Returning to the Cauchy problem involving the wave equation (5.1), the standard difference replacement of equation (5.1) on a rectangular grid is

$$\frac{1}{v_p^2 \Delta t^2}\left(u_{i,j}^{n+1} - 2u_{i,j}^{n} + u_{i,j}^{n-1}\right) - \frac{1}{h^2}\left[\left(u_{i+1,j}^{n} - 2u_{i,j}^{n} + u_{i-1,j}^{n}\right) + \left(u_{i,j+1}^{n} - 2u_{i,j}^{n} + u_{i,j-1}^{n}\right)\right] \quad (5.2)$$
$$-\delta_{r,s} \cdot f(t) = 0$$

where Δt and h are the grid sizes in the time and distance coordinates respectively, and the difference formula equation (5.2) refers to the grid point $x = i \cdot h$, $z = j \cdot h$, and $t = n \cdot \Delta t$, where i, j and n are integers. The above formula can be rewritten in the explicit form

$$u_{i,j}^{n+1} = 2u_{i,j}^{n} - u_{i,j}^{n-1} + q^2\left[\left(u_{i+1,j}^{n} - 2u_{i,j}^{n} + u_{i-1,j}^{n}\right) + \left(u_{i,j+1}^{n} - 2u_{i,j}^{n} + u_{i,j-1}^{n}\right)\right] + v_p^2 \Delta t^2 \delta_{r,s} \cdot f(t_n) \tag{5.3}$$

where $q = \dfrac{v_p \Delta t}{h}$ is the mesh ratio. The stability condition for the method is $q < 1/\sqrt{2}$.

5.4 Boundary conditions

Two different boundary conditions were considered, and the initial displacement and velocity conditions are specified as zero at $t = 0$. i. e

$$u(x,z,0) = 0$$
$$\frac{\partial u}{\partial t}(x,z,0) = 0$$

If we use boundary conditions of the following form, the boundary condition is called *Dirichlet or Neumann boundary* condition according to whether u or $\dfrac{\partial u}{\partial x_n}$ is specified, respectively on the boundary where n is the outward normal. Specifically

$$u(0,z,t) = 0\,,\ u(x_M,z,t) = 0\,,\ u(x,z_N,t) = 0$$
or
$$\frac{\partial u}{\partial x}(0,z,t) = 0\,,\ \frac{\partial u}{\partial x}(x_M,z,t) = 0 \text{ and } \frac{\partial u}{\partial z}(x,z_N,t) = 0\,, \tag{5.4}$$

Here x_M, and z_N, are shown boundary points (x_M & z_N = 488 m). We observe strong reflections from the sides (x = 0, M) and the top (z = N) of the model using these boundary conditions as will be shown later.

The Dirichlet boundary conditions of the finite-difference formulation are as below

$$\begin{aligned} u_{i,0}^{n+1} &= 0, \quad 0 \le i \le M, 1 \le n \le S \\ u_{0,j}^{n+1} &= 0, \quad 0 \le j \le N, 1 \le n \le S \\ u_{M,j}^{n+1} &= 0, \quad 0 \le j \le N, 1 \le n \le S \\ u_{i,N}^{n+1} &= 0, \quad 0 \le i \le M, 1 \le n \le S \end{aligned} \quad , \tag{5.5}$$

where time is shown S is typically one second. We obtained the ABCs which are called Transparent boundary conditions (reducing or absorbing boundary reflections) (see Chapter 3 Cartesian equations (3.28) and (3.30)) as follows.

$$\frac{\partial}{\partial x}\left(\frac{1}{v_p}\frac{\partial u}{\partial t}\right) - \frac{\partial^2 u}{\partial x^2} - \frac{1}{2}\frac{\partial^2 u}{\partial z^2} = 0 \quad , x = 0 \tag{5.6}$$

$$\frac{\partial}{\partial x}\left(\frac{1}{v_p}\frac{\partial u}{\partial t}\right) + \frac{\partial^2 u}{\partial x^2} + \frac{1}{2}\frac{\partial^2 u}{\partial z^2} = 0 \quad , x = 488M \tag{5.7}$$

Reynolds could not find the finite-difference approximations to equations (5.6) and (5.7) such that these approximations coupled with the standard second-order explicit finite difference scheme for the wave equation on the interior of D′ yielded a stable finite-difference scheme.

Following the approach of Reynolds for the purposes of illustration we note that equation (5.7) is equivalent to

$$\frac{1}{v_p}\frac{\partial^2 u}{\partial t \partial x} + \frac{\partial^2 u}{\partial x^2} + \left(\frac{q}{q+1}\right)\frac{\partial^2 u}{\partial z^2} = 0 \tag{5.8}$$

with $q=v_p\Delta t/\Delta x=1$ where we have treated v_p as a constant. We note that the von Neumann stability condition for the standard second-order explicit finite-difference scheme for the wave equation is $q= v_p\Delta t/\Delta x \le 1/\sqrt{2}$. The boundary condition equation

(5.8) is easier to implement in an explicit, finite-difference program if we transform the $\frac{\partial^2 u}{\partial z^2}$ term. From the wave equation (5.1), we have

$$\frac{\partial^2 u}{\partial z^2} = \frac{1}{v_p^2}\frac{\partial^2 u}{\partial t^2} - \frac{\partial^2 u}{\partial x^2} \tag{5.9}$$

and substituting equation (5.9) into equation (5.8) and multiplying the result by (1+q) gives

$$\frac{1}{v_p}\frac{\partial^2 u}{\partial t \partial x} + \frac{\partial^2 u}{\partial x^2} + q\left(\frac{1}{v_p}\frac{\partial^2 u}{\partial x \partial t} + \frac{1}{v_p^2}\frac{\partial^2 u}{\partial t^2}\right) = 0$$

or

$$\left(\frac{1}{v_p}\frac{\partial}{\partial t} + \frac{\partial}{\partial x}\right)\left(\frac{q}{v_p}\frac{\partial}{\partial t} + \frac{\partial}{\partial x}\right)u = 0 \quad , \quad x = X_M \tag{5.10}$$

$$\left(\frac{1}{v_p}\frac{\partial}{\partial t} - \frac{\partial}{\partial x}\right)\left(\frac{q}{v_p}\frac{\partial}{\partial t} - \frac{\partial}{\partial x}\right)u = 0 \quad , \quad x = 0 \tag{5.11}$$

Using finite-differences we obtain top and bottom boundary conditions

$$\begin{aligned} &u_{0,j}^{n+1} = u_{0,j}^{n} + u_{1,j}^{n} - u_{1,j}^{n-1} + q\left(u_{1,j}^{n} - u_{0,j}^{n} - \left(u_{2,j}^{n-1} - u_{1,j}^{n-1}\right)\right) \\ &1 \le j \le N, 1 \le n \le J \\ &u_{M,j}^{n+1} = u_{M,j}^{n} + u_{M-1,j}^{n} - u_{M-1,j}^{n-1} - q\left(u_{M,j}^{n} - u_{M-1,j}^{n} - \left(u_{M-1,j}^{n-1} - u_{M-2,j}^{n-1}\right)\right) \\ &1 \le j \le N, 1 \le n \le J \end{aligned} \tag{5.12}$$

Similarly, we obtain left and right boundary conditions

$$\begin{aligned} &u_{i,0}^{n+1} = u_{i,0}^{n} + u_{i,1}^{n} - u_{i,1}^{n-1} + q\left(u_{i,1}^{n} - u_{i,0}^{n} - \left(u_{i,2}^{n-1} - u_{i,1}^{n-1}\right)\right) \\ &1 \le i \le M, 1 \le n \le J \\ &u_{i,N}^{n+1} = u_{i,N}^{n} + u_{i,N-1}^{n} - u_{i,N-1}^{n-1} - q\left(u_{i,Nj}^{n} - u_{i,N-1}^{n} - \left(u_{i,N-1}^{n-1} - u_{i,N-2}^{n-1}\right)\right) \\ &1 \le i \le M, 1 \le n \le J \end{aligned} \tag{5.13}$$

The corner points are given as below as special cases.

$$
\begin{aligned}
u_{0,0}^{n+1} &= u_{0,0}^{n} + q\left(u_{1,1}^{n} - u_{0,0}^{n}\right), \\
u_{M,0}^{n+1} &= u_{M,0}^{n} + q\left(u_{M-1,1}^{n} - u_{M,0}^{n}\right), \\
u_{0,N}^{n+1} &= u_{0,N}^{n} + q\left(u_{1,N-1}^{n} - u_{0,N}^{n}\right), \\
u_{M,N}^{n+1} &= u_{M,N}^{n} + q\left(u_{M-1,N-1}^{n} - u_{M,N}^{n}\right) \\
1 &\le n \le J
\end{aligned}
\tag{5.14}
$$

These forms will be used to simulate transparent boundaries as in Figures (5.4) and (5.5). There are modifications for the VSM boundary conditions. Using finite-difference we obtain top and bottom boundary conditions.

$$
\begin{aligned}
u_{0,j}^{n+1} &= u_{0,j}^{n} + u_{1,j}^{n} - u_{1,j}^{n-1} + A(0)q\left(u_{1,j}^{n} - u_{0,j}^{n} - \left(u_{2,j}^{n-1} - u_{1,j}^{n-1}\right)\right) \\
1 &\le j \le N,\ 1 \le n \le J,\ A(0) = 0.15963 \\
u_{M,j}^{n+1} &= u_{M,j}^{n} + u_{M-1,j}^{n} - u_{M-1,j}^{n-1} - A(M)q\left(u_{M,j}^{n} - u_{M-1,j}^{n} - \left(u_{M-1,j}^{n-1} - u_{M-2,j}^{n-1}\right)\right) \\
1 &\le j \le N,\ 1 \le n \le J,\ A(N) = 0.14966
\end{aligned}
\tag{5.15}
$$

Similarly, we obtain left and right boundary conditions

$$
\begin{aligned}
u_{i,0}^{n+1} &= u_{i,0}^{n} + u_{i,1}^{n} - u_{i,1}^{n-1} + A(0)q\left(u_{i,1}^{n} - u_{i,0}^{n} - \left(u_{i,2}^{n-1} - u_{i,1}^{n-1}\right)\right) \\
1 &\le i \le M,\ 1 \le n \le J,\ A(0) = 0.15963 \\
u_{i,N}^{n+1} &= u_{i,N}^{n} + u_{i,N-1}^{n} - u_{i,N-1}^{n-1} - A(N)q\left(u_{i,Nj}^{n} - u_{i,N-1}^{n} - \left(u_{i,N-1}^{n-1} - u_{i,N-2}^{n-1}\right)\right) \\
1 &\le i \le M,\ 1 \le n \le J,\ A(N) = 0.14966
\end{aligned}
\tag{5.16}
$$

The corner points are modification and given as below as special cases.

$$
\begin{aligned}
u_{0,0}^{n+1} &= u_{0,0}^{n} + A(0)q\left(u_{1,1}^{n} - u_{0,0}^{n}\right), \\
u_{M,0}^{n+1} &= u_{M,0}^{n} + A(M)q\left(u_{M-1,1}^{n} - u_{M,0}^{n}\right), \\
u_{0,N}^{n+1} &= u_{0,N}^{n} + A(0)q\left(u_{1,N-1}^{n} - u_{0,N}^{n}\right), \\
u_{M,N}^{n+1} &= u_{M,N}^{n} + A(M)q\left(u_{M-1,N-1}^{n} - u_{M,N}^{n}\right) \\
1 &\le n \le J,\ A(0) = 0.15963,\ A(M) = 0.14966
\end{aligned}
\tag{5.17}
$$

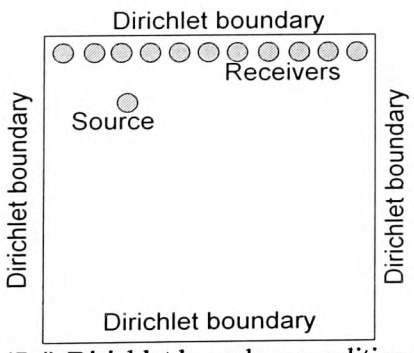

Figure (5.4) Dirichlet boundary conditions.

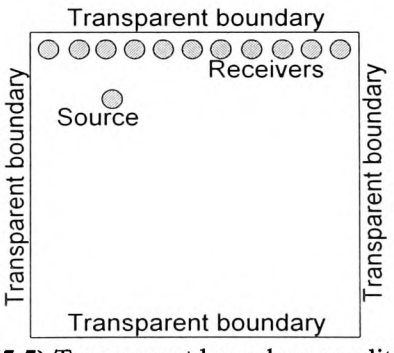

Figure (5.5) Transparent boundary conditions.

5.5 Accuracy of Numerical Solution in Cartesian Coordinates

In this section we present results for the seismograms patterns arising from the various types of seismograms configuration of the 2-D model. In order to demonstrate the accuracy and convergence of the FDM and VSM, we examine the 2-D acoustic wave problem and compare our program results with Reynolds's results. We normally produce results for one second of simulation time for a numerical solution and although the solutions are found to be consistent with grids ranging (M, N, S) from 16x16x1000 to 200x200x1000, we usually display results for 160x160x1000.

We consider the convergence of the solution by comparing calculations for various (equal) grid widths denoted by h, in both simple explicit FDM and VSM. All figures show results for the standard FDM, and VSM seismic wave u displacements evaluated near the top boundary (x = 244 m, z = 475 m, t = 0.5) denoted by u(244,475,0.5). Figure (5.6) shows results for the standard FDM with Dirichlet boundary conditions, for one medium, two media and multimedia. As seen in Figure (5.6) while h decreases the displacement exhibits convergence at h=3 m. Grid dispersion is kept down to an acceptable level by maintaining a minimum of 20 grid points per wavelength. Grid size is approximately 3 m for all figures presented.

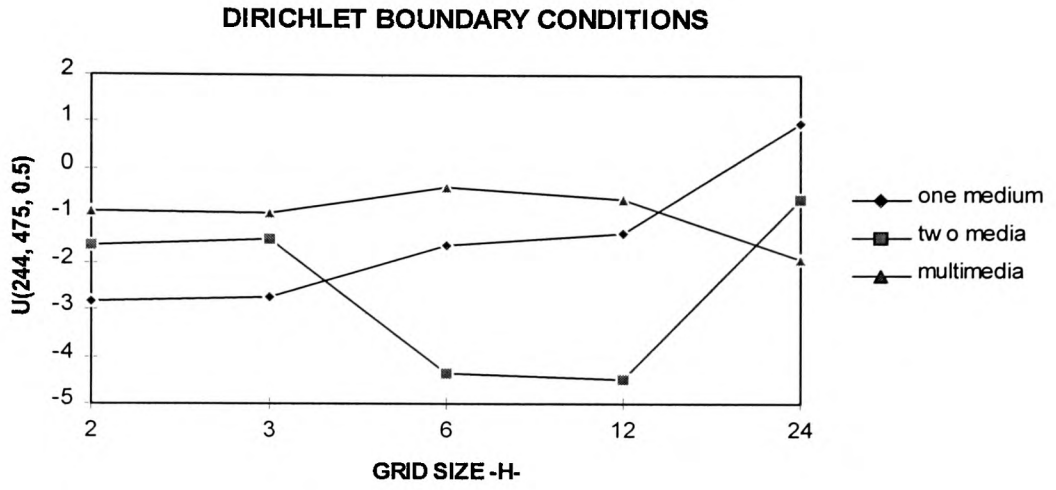

Figure (5.6) Convergence criterion for standard FDM solutions.

Figure (5.7) shows results for the seismic wave displacements at the same point for the standard FDM with the Reynolds ABCs in which convergence is found point at h=3 m for all figures.

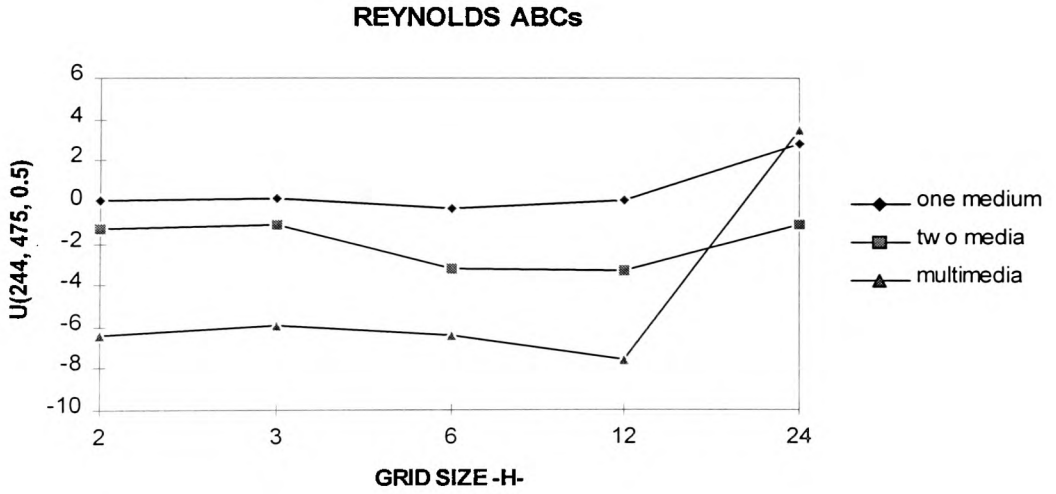

Figure (5.7) Convergence criterion for standard FDM solutions.

The VSM solution is given with Dirichlet boundary conditions in Figure (5.8). In Figure (5.9) results are illustrated for the VSM solution with Reynolds ABCs. Finally, the ABC

results of Clayton-Engquist are shown in Figure (5.10). All figures show that while h decreases the displacement exhibits convergence at h=3 m.

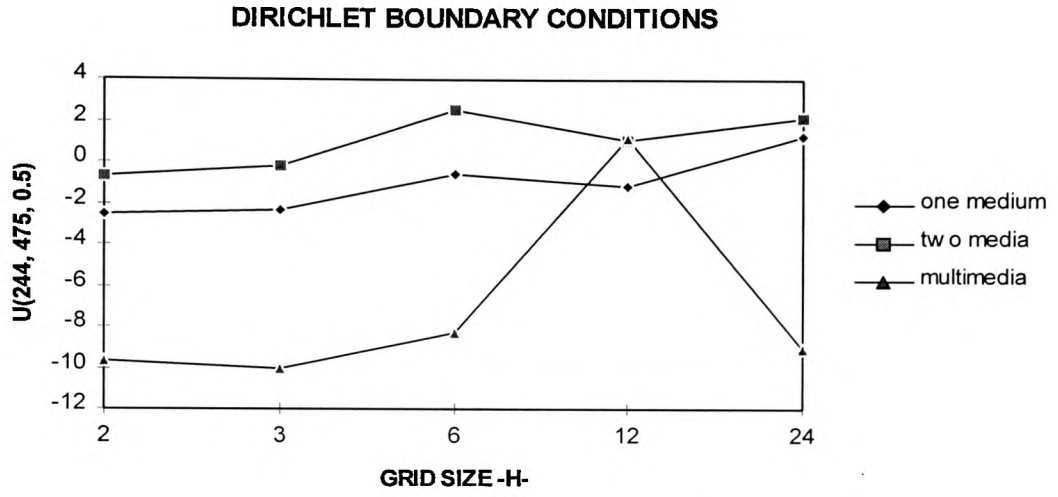

Figure (5.8) Convergence criterion for VSM solution.

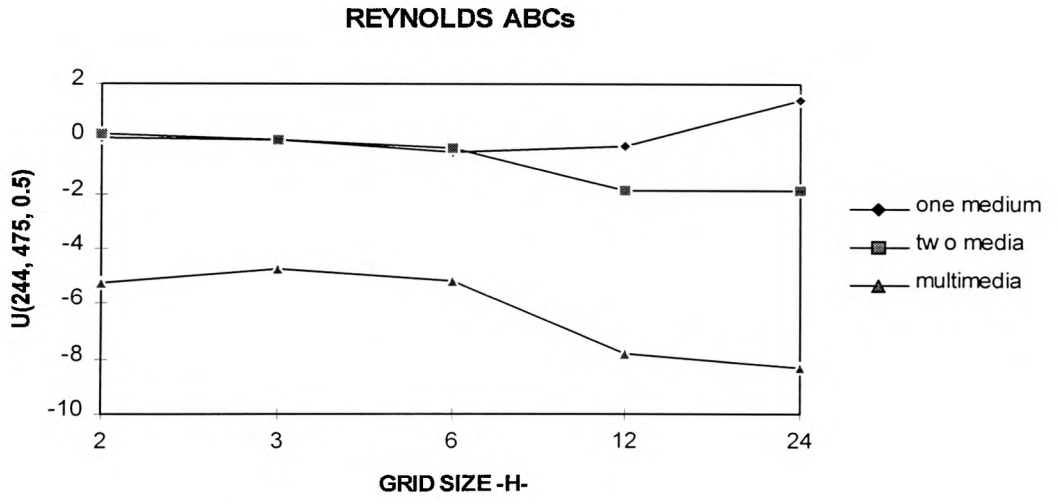

Figure (5.9) Convergence criterion for VSM solution.

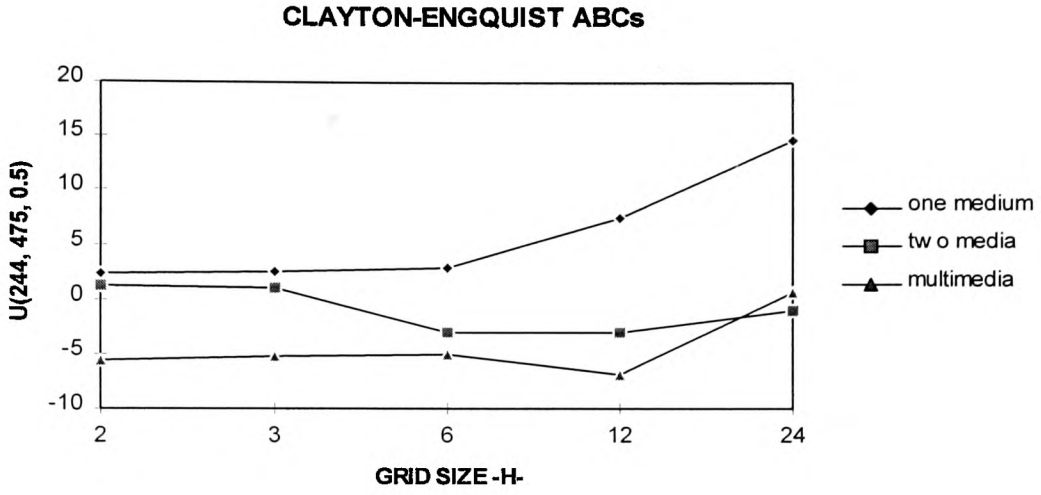

Figure (5.10) Convergence criterion for standard FDM solution.

The standard finite-difference solution and the VSM solutions were obtained using FORTRAN programs on the University of Glamorgan research computer system.

5.5.1 Single Medium Results for Cartesian Coordinates

In this section we will consider two models: one of standard (simple explicit) finite-difference method and our new method (VSM). Both models have v_p, of 1500 m/s from Reynolds [**64**], typical for sea-water. For the source term in equation (5.1), the first derivative of the Gaussian function (Alford et al. [**2**], Reynolds [**64**]), is used

$$f(t)= (t - t_s)e^{-\alpha(t-t_s)^2} \tag{5.18}$$

where the parameter α, which controls the wavelength content of the excition, is equal to 1000, and t_s is delay time parameter, is chosen as to 0.13 sec. The source is located 30 m below the surface. The receivers are accommodated at 13 m below the surface. The grid size and time increment are 3 m and 0.001 sec respectively, which ensure accurate calculation for frequencies up to 10 Hz. As the wave must travel through sea-water before it hits any solid structures, this would be the most logical medium to use.

The seismograms correspond to the geometry of Figure (5.1) with time on the horizontal axis and all displacements from receivers on the vertical axis. With Dirichlet boundary conditions as shown in Figure (5.11) the results contain large reflections from all the boundaries as evident by the criss-cross pattern. The VSM results with Dirichlet boundary conditions are shown in Figure (5.12). Figure (5.13) (plotted sideways) shows Reynolds's results with Dirichlet boundary conditions. The results obtained from the FDM and the VSM are most favourable on comparison with those found by the Reynolds and exhibit a level of agreement that implies that both methods are generating acceptable solutions which are in qualitative agreement with Reynolds.

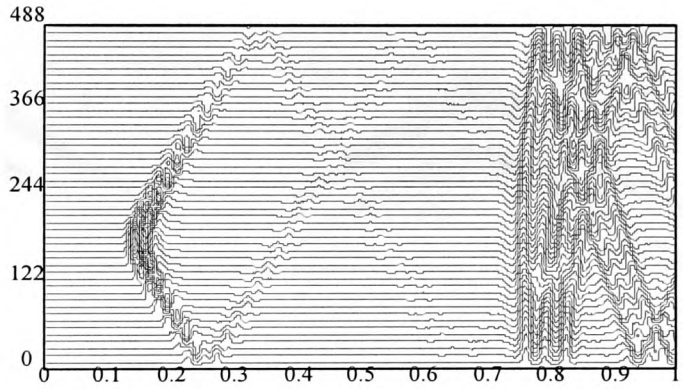

Figure (5.11) Synthetic seismograms generated from the finite-difference solution of the 2D acoustic wave equation with Dirichlet boundary conditions.

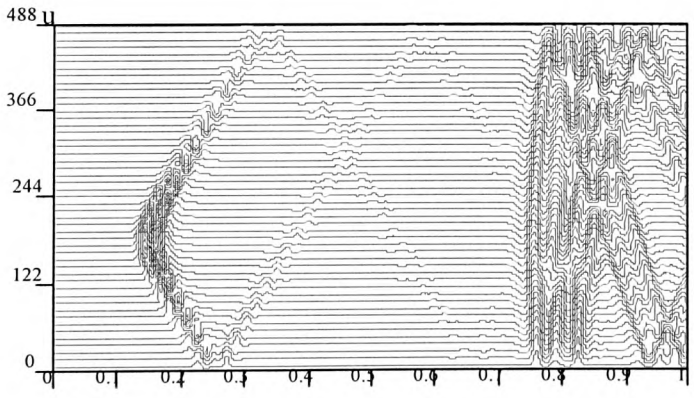

Figure (5.12) Synthetic seismograms generated from the VSM solution of the 2D acoustic wave equation with Dirichlet boundary conditions.

The finite-difference solutions using the transparent boundary conditions equations (5.12), (5.13) and (5.14) show no reflections. The standard FDM results with transparent boundary conditions using equations (5.15), (5.16) and (5.17) are shown in Figure (5.15). With the VSM result are shown with transparent boundary conditions in Figure (5.16). Figure (5.14) shows Reynolds's results with transparent boundary conditions. The corresponding VSM results are compared with those found with standard FDM results in Figure (5.15), and (5.16), respectively. The standard FDM and VSM results are in agreement qualitatively. Figures (5.15), (5.14) and (5.16) show qualitative agreement with the Reynolds results as well.

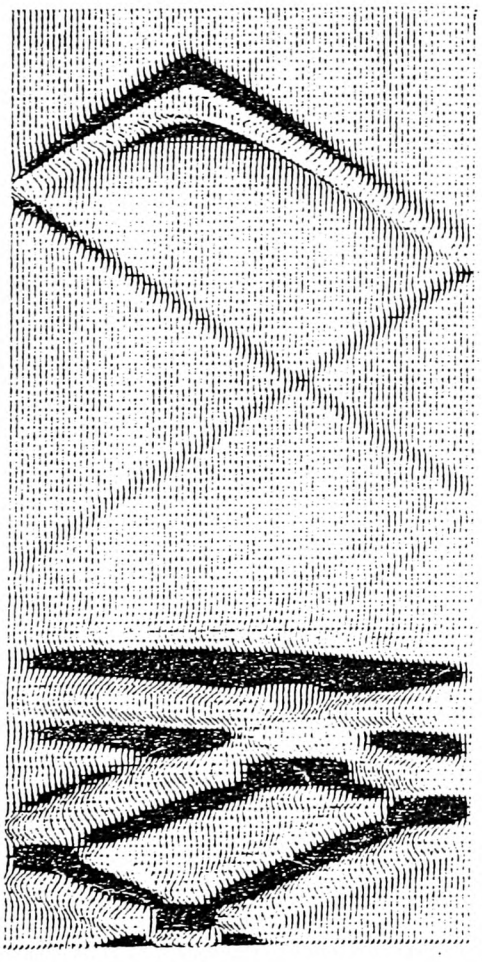

Figure (5.13) Reynolds results with Dirichlet boundary conditions.

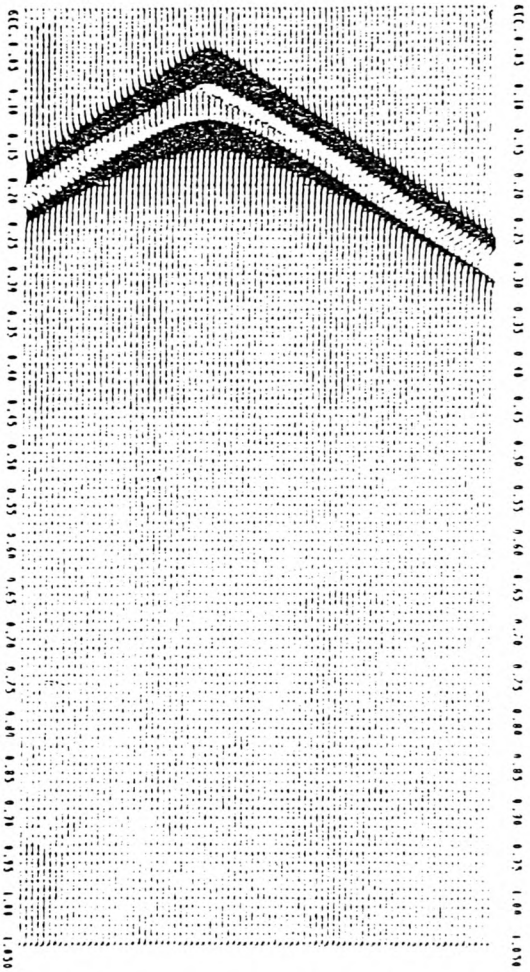

Figure (5.14) Reynolds results with transparent boundary conditions

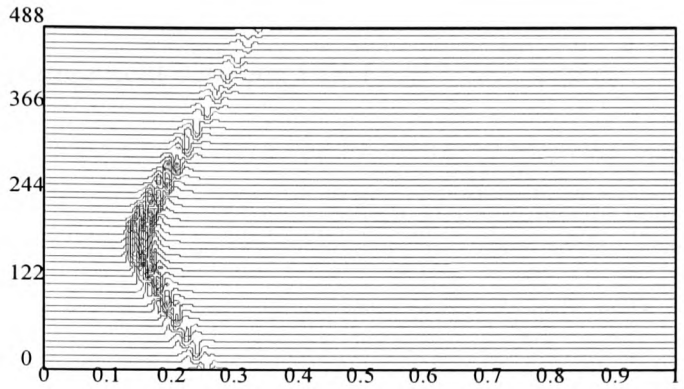

Figure (5.15) Synthetic seismograms generated from the finite-difference solution of the 2D acoustic wave equation with transparent boundary conditions.

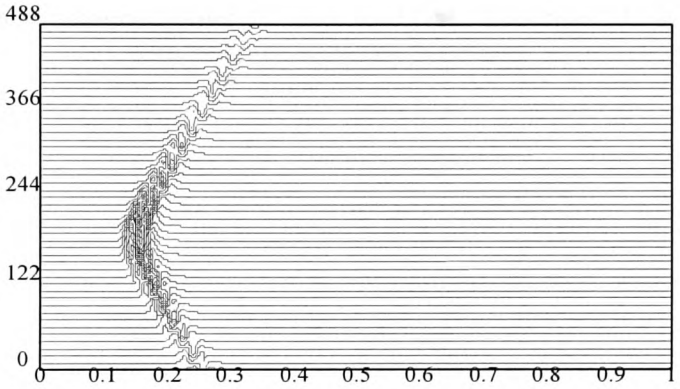

Figure (5.16) Synthetic seismograms generated from the VSM solution of the 2D acoustic wave equation with transparent boundary conditions.

5.5.2 Two media results for Cartesian coordinates

So far, a single medium problem has been considered but now we consider what happens when the wave hits the next medium? In this section, the algorithm was developed to incorporate simple flat layers. The material velocities v_P are 1500 m/s and 2400 m/s respectively as given by Reynolds [**64**]. If the basic array is taken and divided in two, by defining the velocities over these two regions, then two media effectively have been created (see Figure (5.2)), which for our case simulate sea-water and shale media. Figure (5.17) represents two media seismograms corresponding to the geometry

There is an excellent agreement between FDM and VSM results.

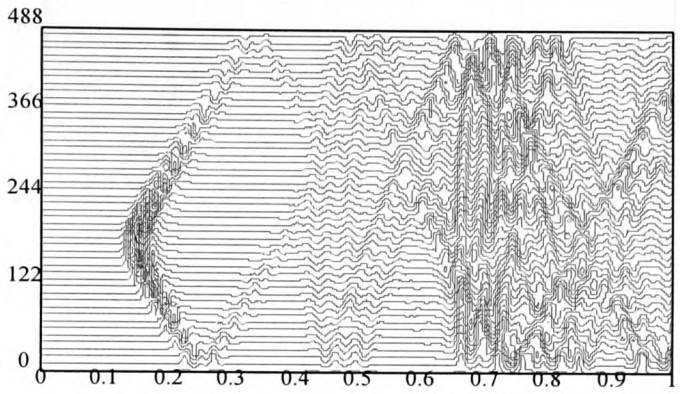

Figure (5.17) Synthetic seismogram generated from the FDM solutions of 2D acoustic wave equation with Dirichlet boundary condition.

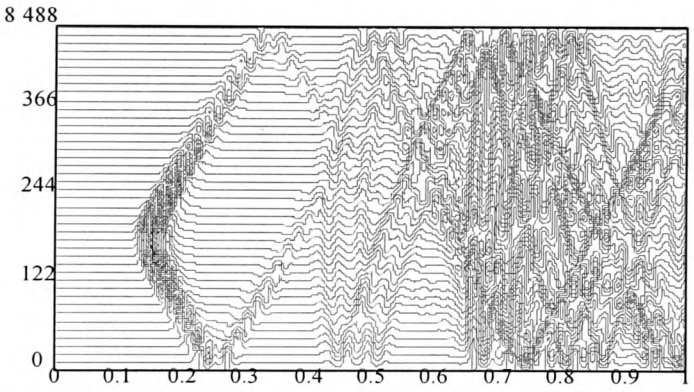

Figure (5.18) Synthetic seismogram generated from the VSM solutions of 2D acoustic wave equation with Dirichlet boundary condition.

It should be noted that, the finite-difference solution obtained with Dirichlet boundary conditions contains large reflections from the boundaries, whilst the finite-difference solution using the Reynolds transparent boundary conditions will show no reflections. Figure (5.19) shows the FDM results with transparent boundary conditions and Figure (5.20) shows the VSM results with Reynolds transparent boundary conditions. There is an excellent agreement between FDM and VSM results.

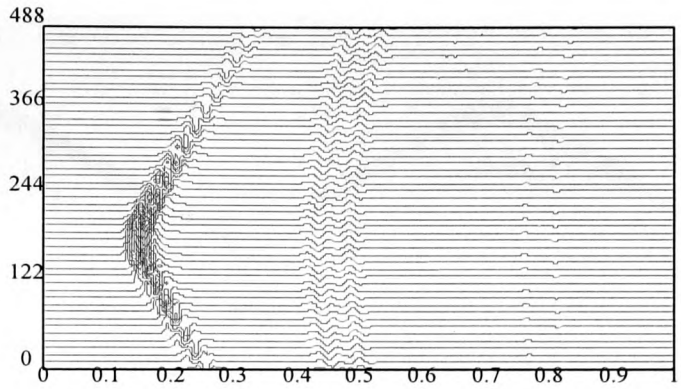

Figure (5.19) Synthetic seismogram generated from the FDM solutions of 2D acoustic wave equation with Reynolds transparent boundary condition.

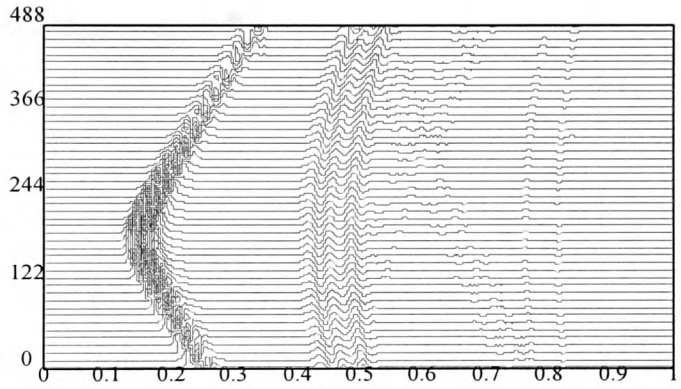

Figure (5.20) Synthetic seismogram generated from the VSM solutions of 2D acoustic wave equation with Reynolds transparent boundary condition.

The seismograms are shown for Reynolds's results with Dirichlet and transparent boundary conditions in Figures (5.21), (5.22). Comparison of Reynolds's results with our results (see Figures (5.17), (5.18), (5.19), (5.20), (5.21), and (5.22) respectively) indicates that two methods are in very good qualitative agreement. There are small unwanted oscillations after the interface waves in Figure 5.20. Two media interface waves are visible.

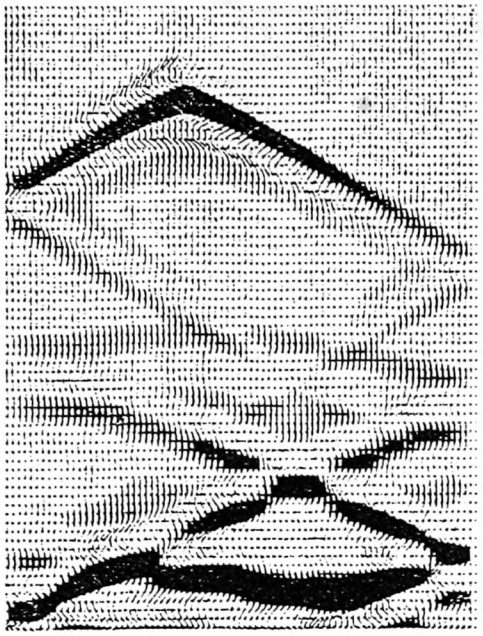

Figure (5.21) Reynolds's results with Dirichlet boundary conditions.

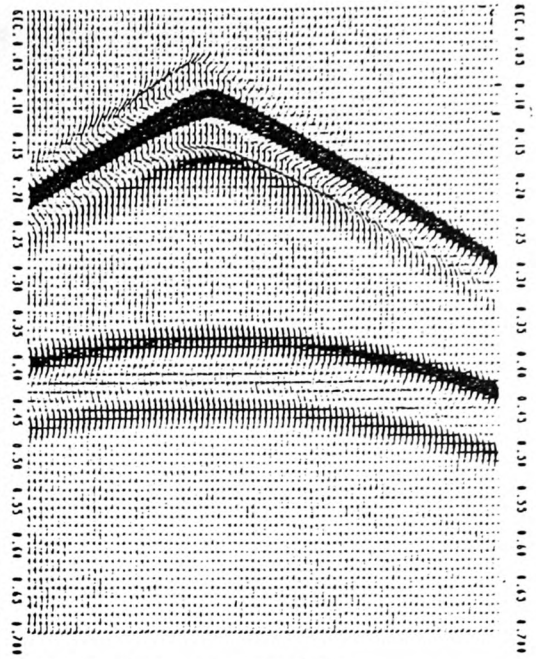

Figure(5.22) Reynolds's results with transparent boundary conditions.

5.5.3 Multimedia results for Cartesian coordinates

In this section a multimedia problem is considered. We employ the previously described numerical methods, FDM and VSM, to solve this multimedia problem. We have five layers: sea-water, mud, shale, oil and limestone, respectively. The velocities are given from top layer to bottom layer respectively: 1500 m/s, 1600 m/s, 2440 m/s, 1240 m/s and 3400 m/s and the multimedia geometry is shown in Figure (5.3). We also use the same source and parameters in this problem as previously. The usual rule of using at least twenty grid points for the wavelength of the source is respected for this problem.

The results are depicted in a seismogram representation of the numerical solution. The Figure (5.23) shows the large reflections by the boundaries and interface of the media whilst Figure (5.24) shows ABCs results.

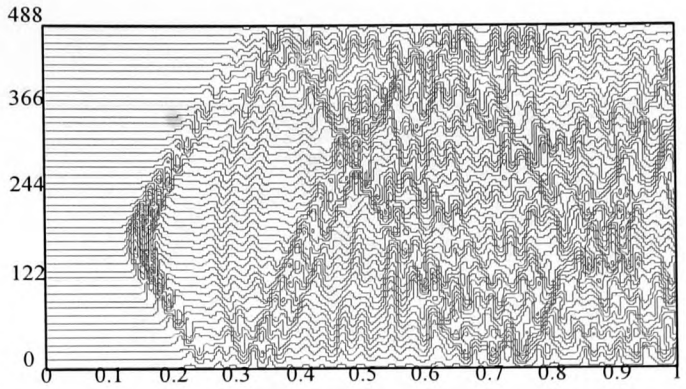

Figure (5.23) Synthetic seismogram generated from the FDM solutions of 2D acoustic wave equation with Dirichlet boundary condition.

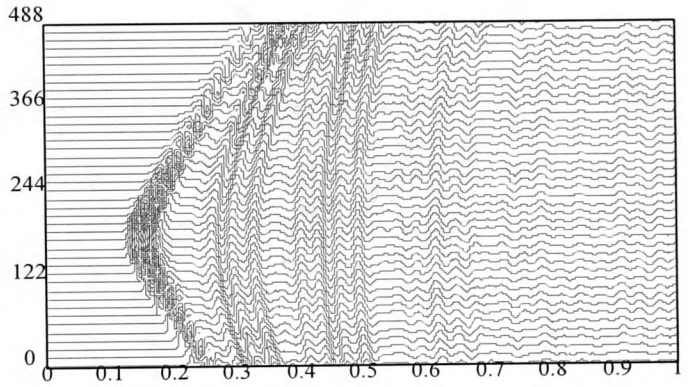

Figure (5.24) Synthetic seismogram generated from the FDM solutions of 2D acoustic wave equation with Reynolds transparent boundary condition.

The VSM results are given in Figures (5.25) and (5.26). With Figure (5.25) showing results with Dirichlet boundary conditions, and transparent boundary conditions results are given in Figure (5.26). Comparison of the standard FDM results with VSM results, shows good agreement.

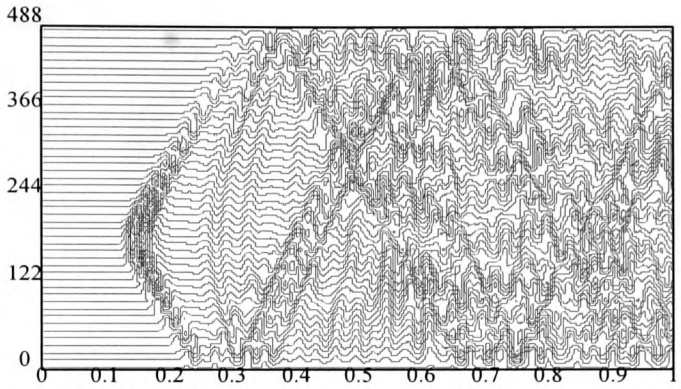

Figure (5.25) Synthetic seismogram generated from the VSM solutions of 2D acoustic wave equation with Dirichlet boundary condition.

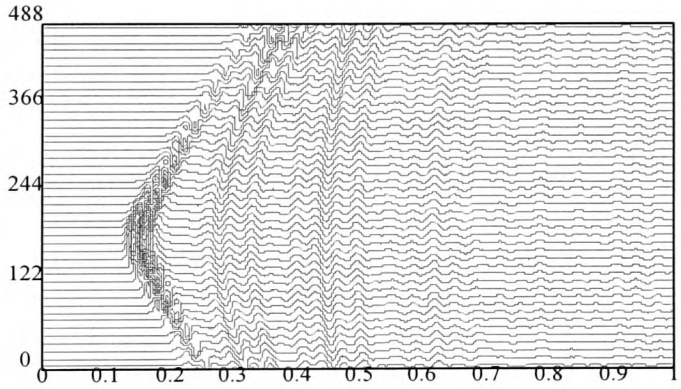

Figure (5.26) Synthetic seismogram generated from the VSM solutions of 2D acoustic wave equation with Reynolds transparent boundary condition.

5.5.4 Clayton-Engquist ABCs results in Cartesian coordinates

In this section, we consider a Clayton-Engquist ABC problem where the boundary conditions are more complicated than the Reynolds ABCs. The Clayton-Engquist ABC results for one medium are given in Figure (5.27).

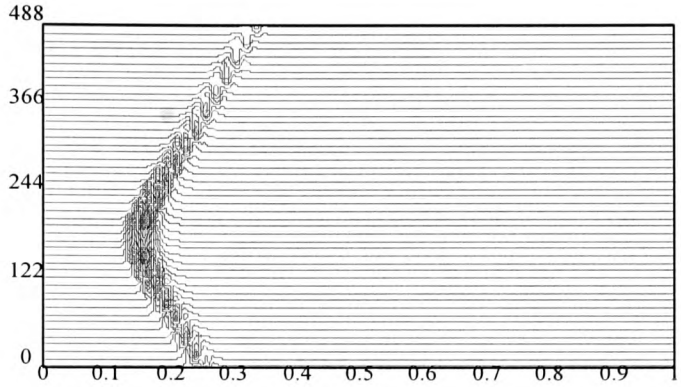

Figure (5.27) Synthetic seismogram generated from the FDM solutions of 2D acoustic wave equation with Clayton-Engquist ABCs one medium.

Figure (5.28) shows results for two media and, the seismogram in Figure (5.29) shows Clayton-Engquist results with multimedia. Clayton-Engquist ABCs results are now compared with Reynolds ABCs results in the next section.

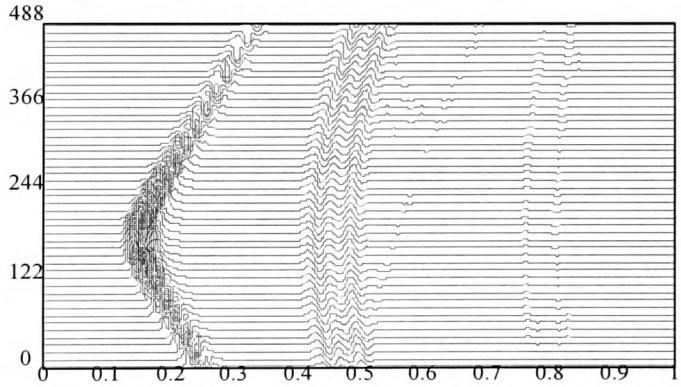

Figure (5.28) Synthetic seismogram generated from the FDM solutions of 2D acoustic wave equation with Clayton-Engquist ABCs two media.

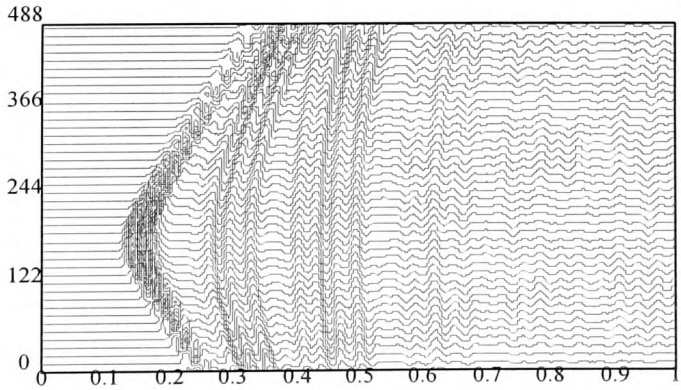

Figure (5.29) Synthetic seismogram generated from the FDM solutions of 2D acoustic wave equation with Clayton-Engquist ABCs multimedia.

5.5.4 Comparison of the FDM and VSM Results

In this section, we compare directly the FDM, VSM, Reynolds and Clayton-Engquist ABCs. Accuracy of the FDM seismograms is mainly affected by grid dispersion. Figure (5.30) shows the synthetic seismogram with Dirichlet boundary conditions calculated by the FDM and VSM for single layer model. There is a close match of the two waveforms; wave traces are nearly identical, and there is overall good agreement between the two results. Figure (5.31) presents the synthetic seismogram calculated for Reynolds and Clayton-Engquist ABCs by the FDM and VSM. There is an excellent match between the two methods, with only significant difference being a slight amplitude difference in the direct wave pulses in the Clayton-Engquist ABCs.

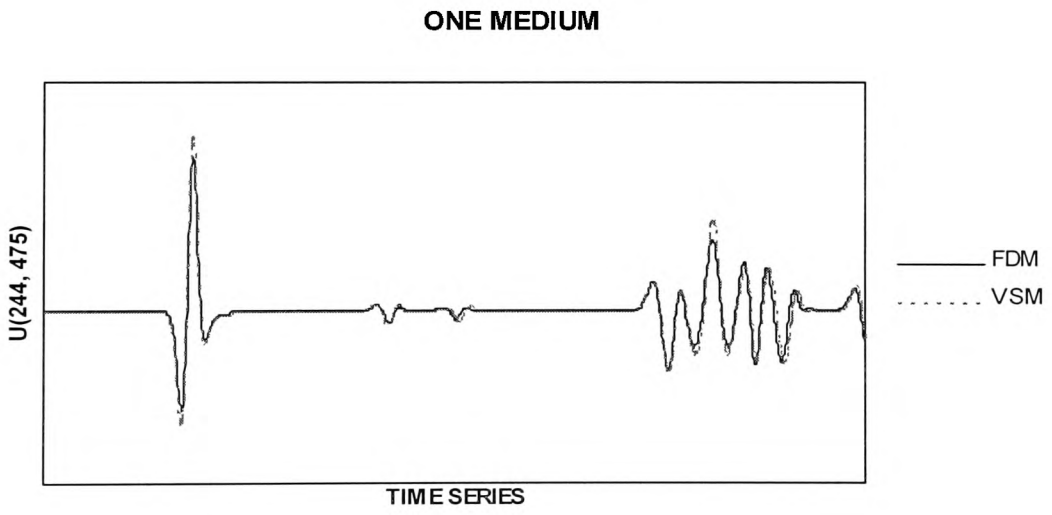

Figure (5.30) Synthetic seismograms obtained from the standard FDM and VSM with Dirichlet boundary conditions solutions for single medium.

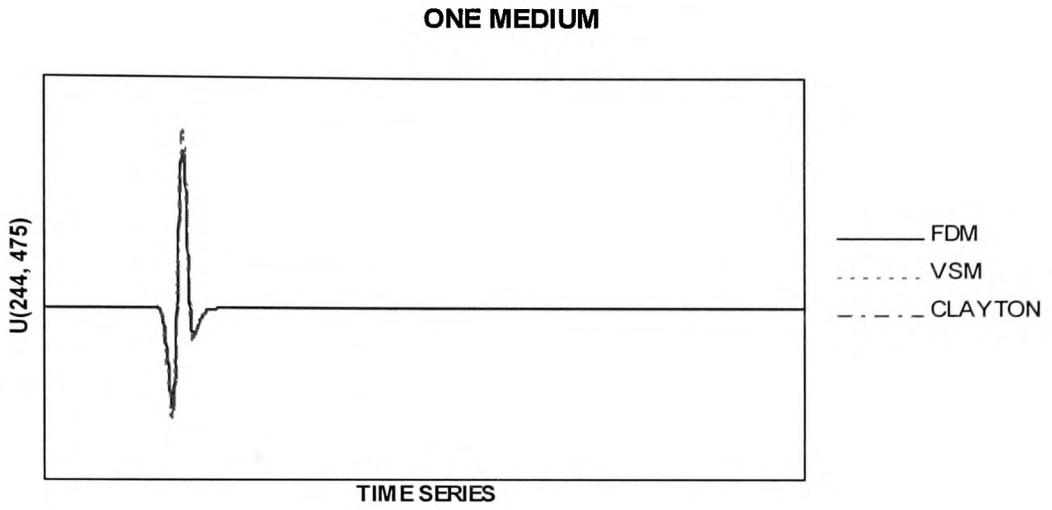

Figure (5.31) Synthetic seismograms obtained from the standard FDM and VSM with ABCs solutions for single medium.

Figure (5.32) shows the synthetic seismograms calculated by the standard FDM and VSM with Dirichlet boundary conditions for two media. There is good agreement again between the seismograms generated by the two different methods. We now compare with the standard FDM, VSM for ABCs in Figure (5.33). We find there is a good agreement between FDM, VSM and Clayton-Engquist ABCs but the amplitude difference exhibits the main contrast.

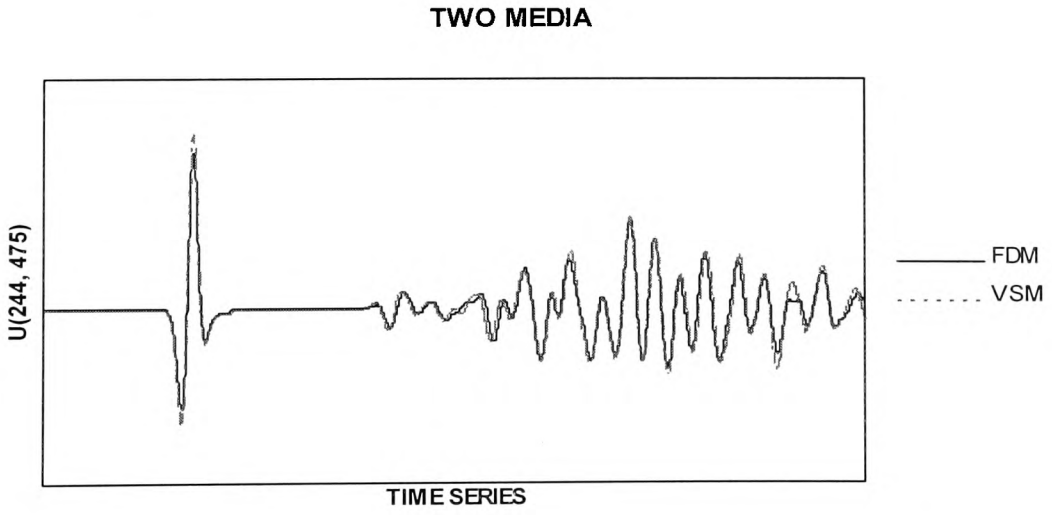

Figure (5.32) Synthetic seismograms obtained from the standard FDM and VSM with Dirichlet boundary condition solutions for two media.

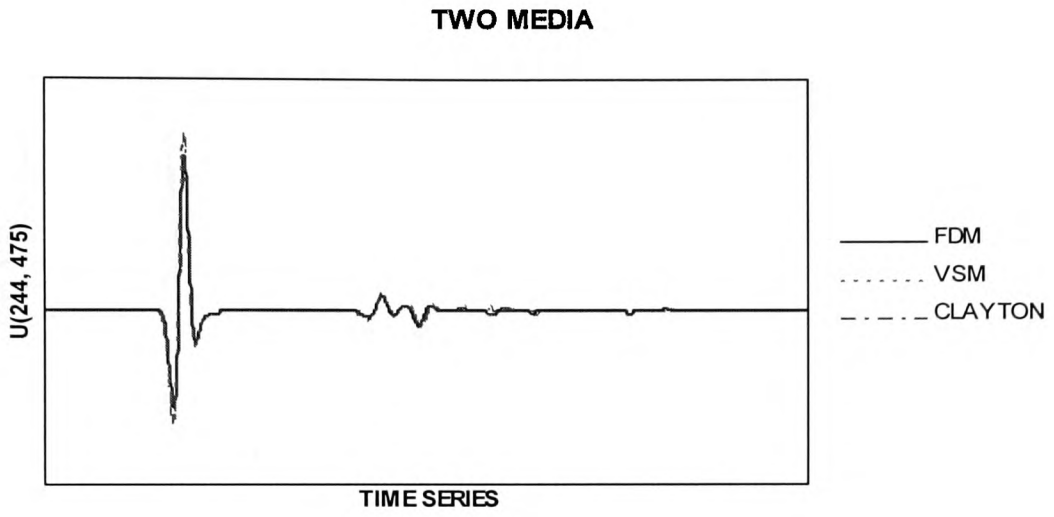

Figure (5.33) Synthetic seismograms obtained from the standard FDM and VSM with ABCs solutions for two media.

Figure (5.34) shows a comparison of the synthetic seismograms generated by the standard FDM and VSM for Dirichlet boundary conditions for multimedia.

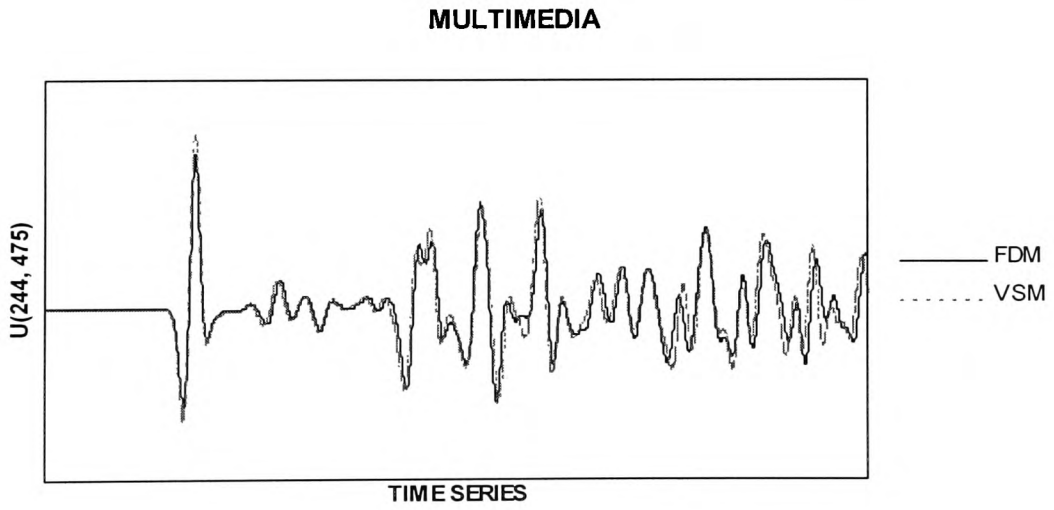

Figure (5.34) Synthetic seismograms obtained from the standard FDM and VSM with Dirichlet boundary conditions solutions for multimedia.

The comparison, in Figure (5.35) shows the FDM, VSM for ABCs for the multimedia. There is excellent agreement between the FDM and VSM and Clayton-Engquist ABCs apart from amplitude difference.

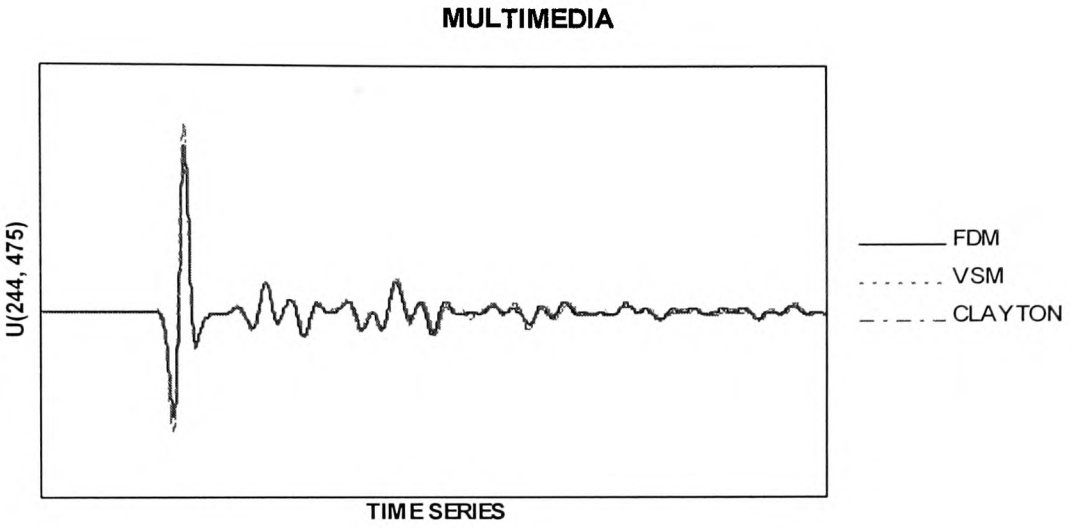

Figure (5.35) Synthetic seismograms obtained from the standard FDM and VSM with ABCs solutions for multimedia.

5.5.5 Conclusion of the Cartesian Results

Our results compare well with those of others based on the determined grid / wavelength criteria for best effects. Also the VSM results are found to be as good as those for the standard FDM. The Clayton-Engquist ABCs are generally found to be less effective as those of Reynolds. It is pleasing to note that multimedia reflected waves are visible in Cartesian coordinates.

5.6 Accuracy of Numerical Solution in Cylindrical Coordinates

In this section the 2-D acoustic wave equation in cylindrical coordinates is used with notational symmetry to model with a source term given for the case of axial symmetry by

$$\frac{1}{v_p^2}\frac{\partial^2 u}{\partial t^2} = \frac{\partial^2 u}{\partial r^2} + \frac{1}{r}\frac{\partial u}{\partial r} + \frac{\partial^2 u}{\partial z^2} + \delta_{a,b} \cdot f(t) \qquad (5.19)$$

where v_p denotes the velocity of the medium and $\delta_{a,b}$ is the Kronecker delta function with source at r=ah, z=bk (usually a=0). We solve the our problem for $D' = \{(r,z,t) \mid 0 \le r \le 244,\ 0 \le z \le 488,\ 0 \le t \le 1\}$ for a finite domain. Equation (5.19) is solved in 2-D cylindrical coordinates (r, z) with a source located in a sea-water on the axis of symmetry (r=0). Receivers are located in a horizontal line 12 m below the surface. Figure (5.36) is a half section though the cylindrical domain with the source on the axis of symmetry and shows the one medium geometry used Figure (5.37) shows the corresponding two media geometry. Also Figure (5.38) shows the multimedia geometry considered. Left side of the each figure shows the radial symmetry.

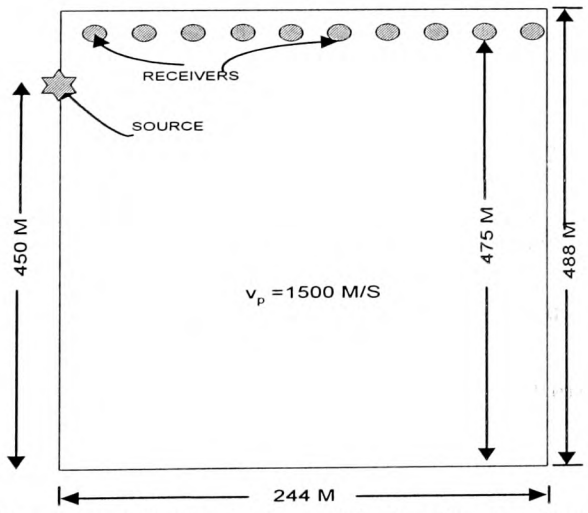

Figure (5.36) Physical model showing receiver geometry used to generate seismograms in the acoustic finite-difference program for one medium.

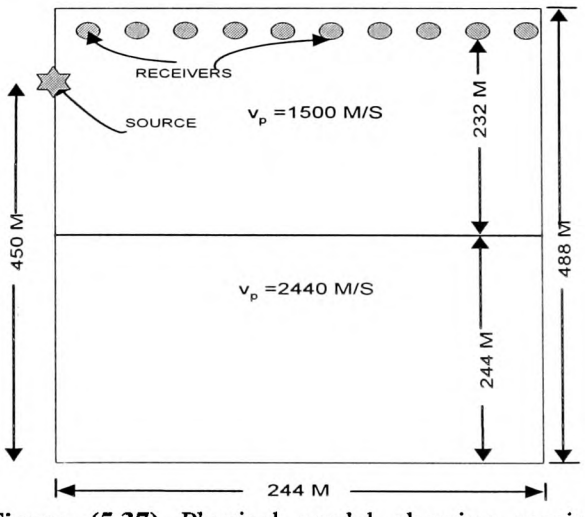

Figure (5.37) Physical model showing receiver geometry used to generate seismograms in the acoustic finite-difference program for two media.

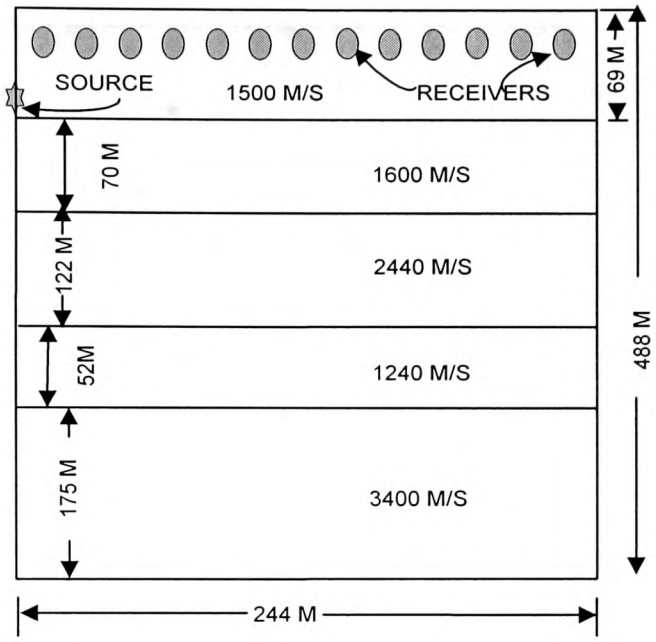

Figure (5.38) Physical model showing receiver geometry used to generate seismograms in the acoustic finite-difference program for multimedia.

When we obtain numerical solutions they are found to be consistent with grids ranging from 8x16 to 100x200. We usually display results for 100x200x1000 (100 grid points by 200 grid points at 2 m per grid point) and time series are generated up to 1 s (1000 time steps at 0.001 s for one medium and 2000 time steps at 0.0005 s for two media and multimedia). In FDM calculations there are two fundamental considerations: stability, which affects the possibility of a solution, and grid dispersion which affects the accuracy of a solution. In the standard FDM, stability requires that $\Delta t<h/(v_p\sqrt{2})$ holds. We consider the convergence of the solution by comparing calculations for various grid widths denoted by h, in both simple explicit FDM and VSM cases. All figures show results for the standard FDM and VSM seismic wave displacements with u evaluated near the top boundary (r = 122 m, z = 475 m, t=0.5 s). Figure (5.39) show results for the standard FDM with Dirichlet boundary conditions. Figure (5.40) show results for the Reynolds ABCs. One medium both boundary conditions results show convergence at

h=6 m. Two media and multimedia results exhibit convergence at h=3 m. The standard FDM seems to produce accurate results at ten or more grid points per wavelength.

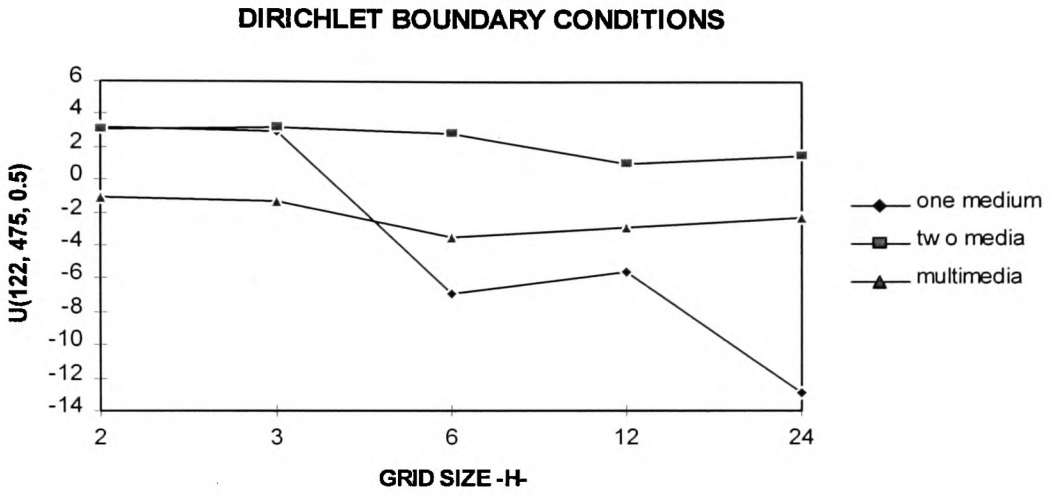

Figure (5.39) Convergence criterion for standard FDM solution with Dirichlet boundary conditions.

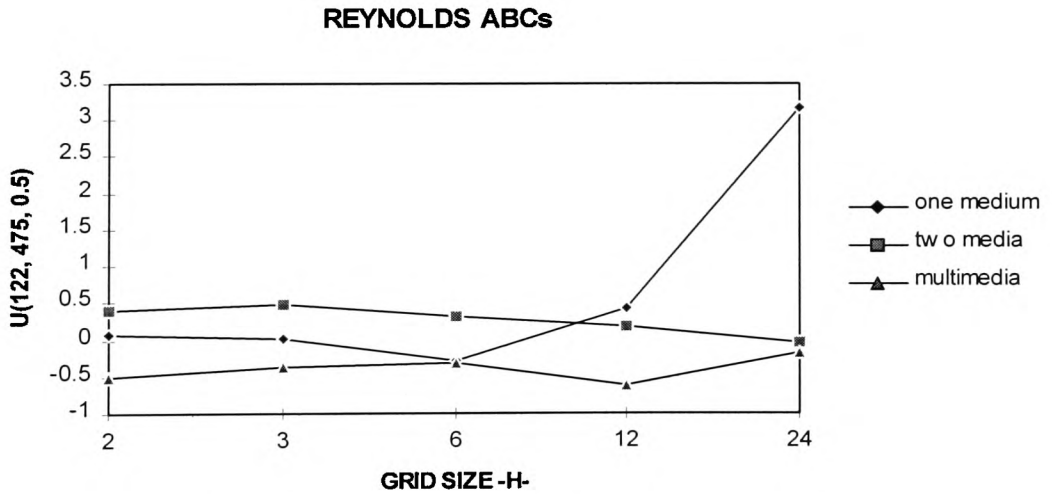

Figure (5.40) Convergence criterion for standard FDM solution with Reynolds ABCs.

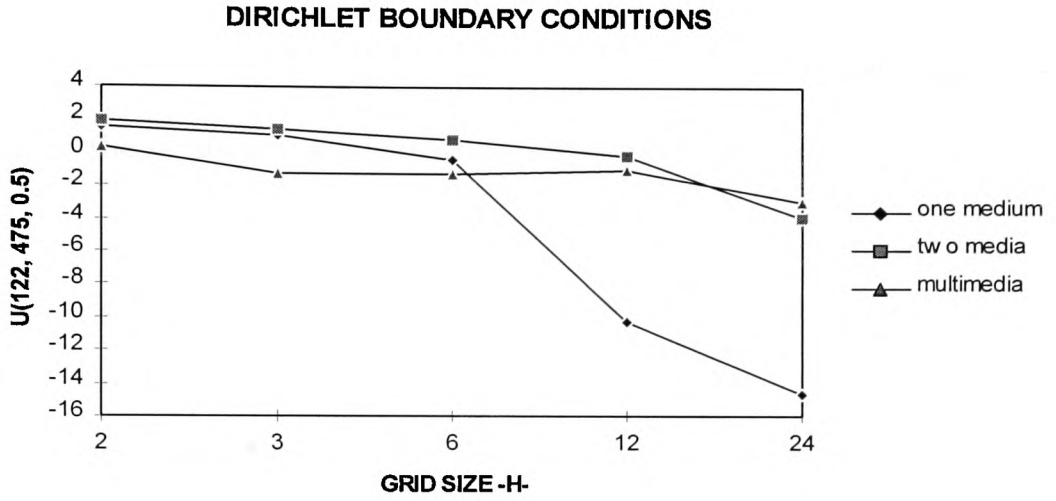

Figure (5.41) Convergence criterion for standard VSM solution with Dirichlet boundary conditions.

The VSM with Dirichlet boundary conditions results is shown in Figure (5.41). Figure (5.42) show results for the VSM with Reynolds ABCs. One medium results seem to show converge when the grid size is close to 6 m. Two media and multimedia results seem to show converge when the grid sizes close to 3 m.

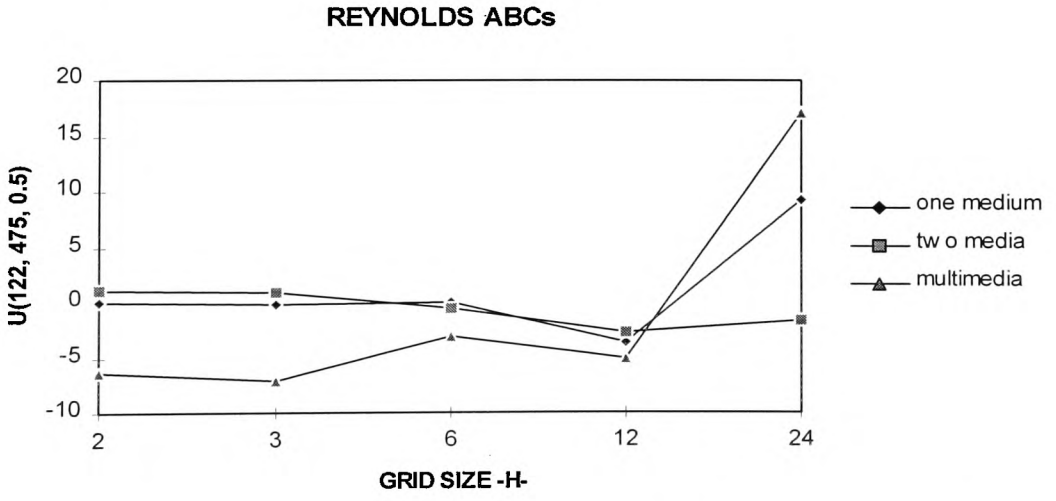

Figure (5.42) Convergence criterion for standard VSM solution with Reynolds ABCs.

5.6.1 Single medium results in cylindrical coordinates

In this section, a single layer model is chosen for which the velocity in the layer is 1500 m/s. The synthetic seismograms are generated by the standard FDM and VSM with the Reynolds ABCs. Usually, ground motion at a number of different receivers recorded by plotting this motion as a function of time and as a function of the distance from the source. In this case, time runs along the horizontal axis and distance from the source along the vertical axis. Radial symmetry is used to provide a left boundary condition (r=0). The Reynolds ABCs is used for the other boundaries. In all cases, the time shift, t_s, is 0.13 s and the pulse width parameter, α, is 1000. These values of t_s and α are found by trial and error to show results to best effect, and are realistic values. The synthetic seismogram obtained by using the standard FDM with the Dirichlet boundary conditions in Figure (5.43). The synthetic seismogram obtained by using the VSM with the Dirichlet boundary conditions in Figure (5.44). Both figures show strong similarities. Figure (5.45) contains the synthetic seismogram obtained by the FDM with the Reynolds ABCs which are more effective at eliminating reflections from the outgoing wave. The synthetic seismogram obtained by using the VSM with the Reynolds ABCs is shown in Figure (5.46). There is no significant difference between Figures (5.45) and (5.46).

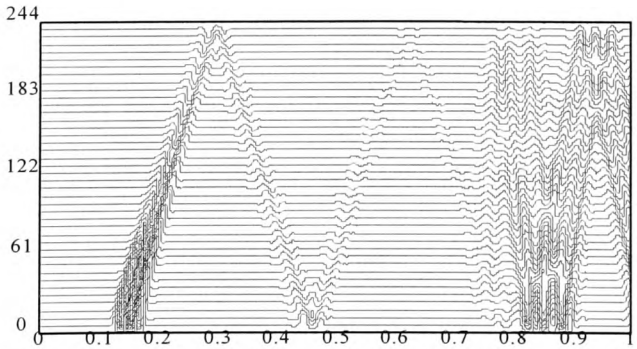

Figure (5.43) Synthetic seismogram generated from the FDM solution of 2-D acoustic wave equation in cylindrical coordinates.

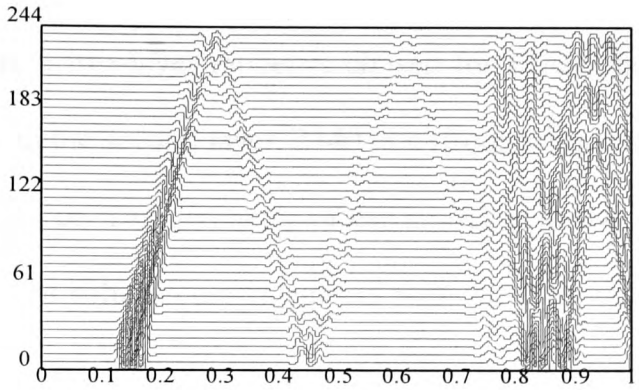

Figure (5.44) Synthetic seismogram generated from the VSM solution of 2-D acoustic wave equation in cylindrical coordinates.

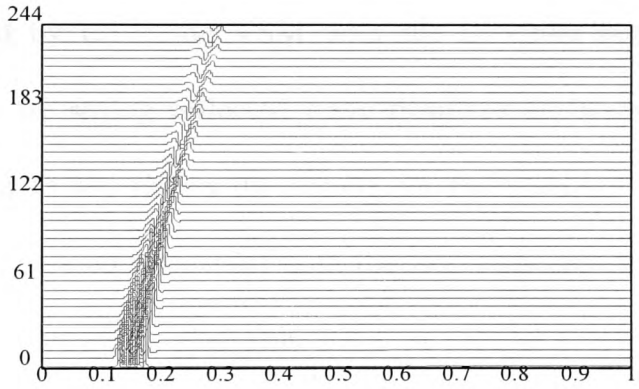

Figure (5.45) Synthetic seismogram generated from the FDMs solution of 2-D acoustic wave equation in cylindrical coordinates.

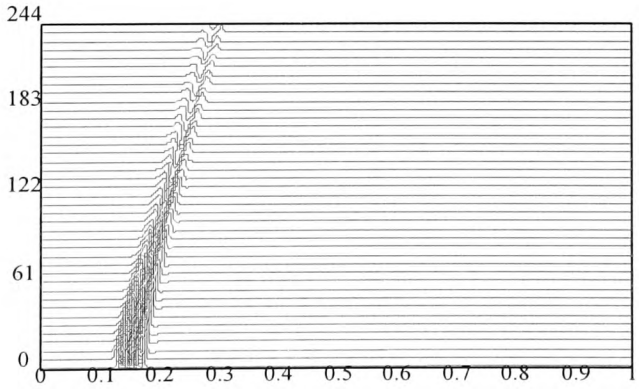

Figure (5.46) Synthetic seismogram generated from the VSM solution of 2-D acoustic wave equation in cylindrical coordinates.

5.6.2 Two media results in cylindrical coordinates

In this section, a two-layer model is chosen for which the velocity in the first layer is 1500 m/s and in the second layer, 2440 m/s (from Reynolds [**64**]). The thickness of the each layer is 244 m. The geometry of the model is shown in Figure (5.37). The standard FDM and VSM solution are calculated with the Reynolds ABCs for right and bottom boundary and Dirichlet boundary conditions for the top boundary and radial symmetry for left boundary. The synthetic seismogram obtained by using the standard FDM with the Dirichlet boundary conditions in Figure (5.47). The synthetic seismogram obtained by using the VSM with the Dirichlet boundary conditions in Figure (5.48). There are strong reflected wave from the all boundary in both Figures (5.47), (5.48). Figure (5.49) shows the results for the standard FDM. The synthetic seismogram obtained by using the VSM with the Reynolds ABCs in Figure (5.50). The mild interface reflection can be seen after 0.4 s in Figures (5.49), (5.50). The bottom reflection appears at about 0.65 s without significant distortion from the interface reflection. There are strong similarities between Figures (5.49) and (5.50).

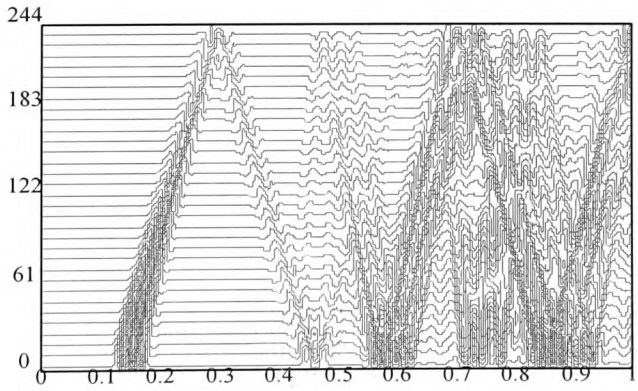

Figure (5.47) Synthetic seismogram generated from the FDM solution of 2-D acoustic wave equation in cylindrical coordinates.

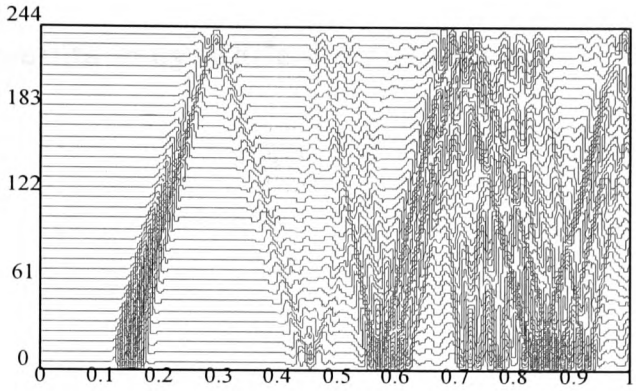

Figure (5.48) Synthetic seismogram generated from the VSM solution of 2-D acoustic wave equation in cylindrical coordinates.

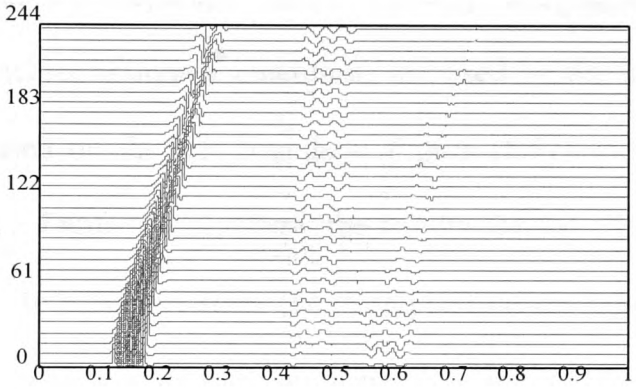

Figure (5.49) Synthetic seismogram generated from the FDM solution of 2-D acoustic wave equation in cylindrical coordinates.

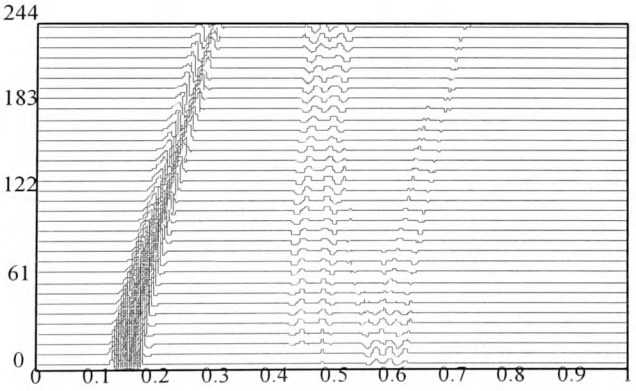

Figure (5.50) Synthetic seismogram generated from the VSM solution of 2-D acoustic wave equation in cylindrical coordinates.

5.6.3 Multimedia results in cylindrical coordinates

In this section, a multimedia model is chosen for which the velocity in the first layer is 1500 m/s, in the second layer 1600 m/s, in the third layer 2440 m/s, in the fourth layer 1240 m/s and in the last layer is 3400 m/s (from Reynolds [**64**] and Yoon and McMechan [**87**]).The geometry of the model is shown in Figure (5.38) displaying layer thickness. In this case, the synthetic seismograms are obtained by using the standard FDM and VSM with the Reynolds ABCs. The top and right boundaries use the Reynolds ABCs. Dirichlet boundary conditions are used on the bottom boundary, and radial symmetry is used on the left boundary. Figure (5.51) show the results for the standard FDM. Whilst Figure (5.52) show the results for the VSM with the Dirichlet boundary conditions. Both Figures show the strong reflections from the boundaries. The synthetic seismogram which is obtained by using the standard FDM is shown in Figure (5.53) and Figure (5.54) show the results for the VSM with the Reynolds ABCs. In Figures (5.53) and (5.54), the weak reflection from the first interface, and the other interface respectively, which arrive after 0.22, 0.3, 0.4 and 0.55 s, are almost entirely obscured by the interface reflection. This interface reflection is a multiple reflection from the artificial and axial boundaries. Figure (5.54) show similar behaviour to that shown in Figure (5.53).

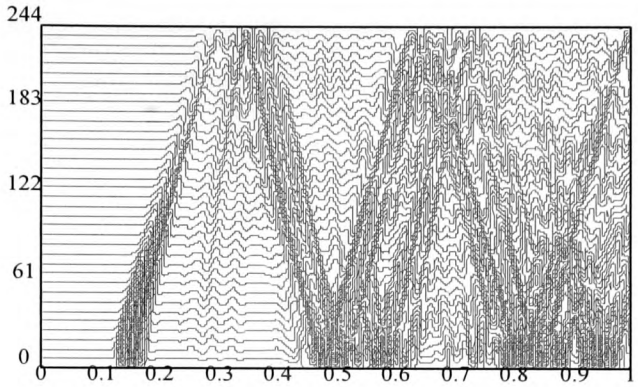

Figure (5.51) Synthetic seismogram generated from the FDM solution of 2-D acoustic wave equation in cylindrical coordinates.

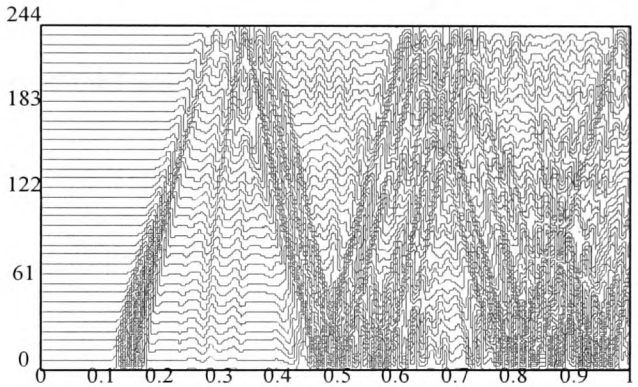

Figure (5.52) Synthetic seismogram generated from the VSM solution of 2-D acoustic wave equation in cylindrical coordinates.

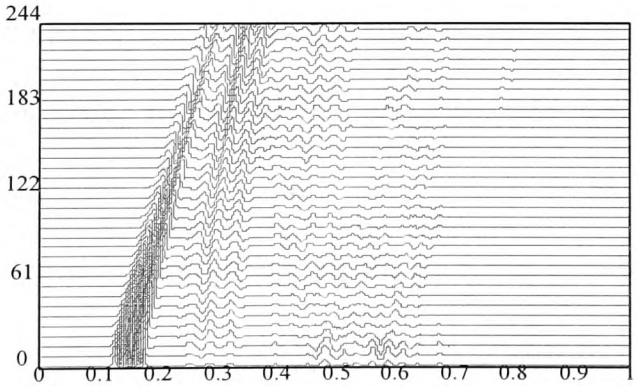

Figure (5.53) Synthetic seismogram generated from the FDM solution of 2-D acoustic wave equation in cylindrical coordinates.

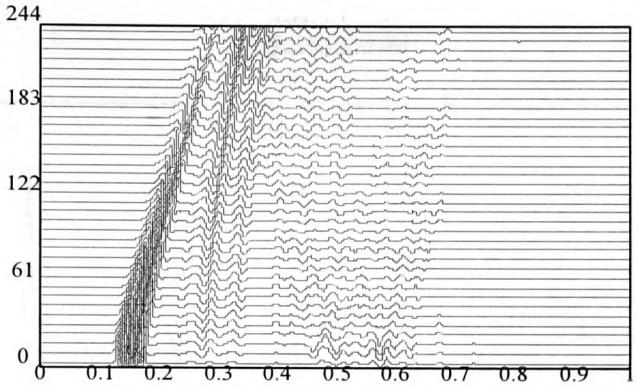

Figure (5.54) Synthetic seismogram generated from the VSM solution of 2-D acoustic wave equation in cylindrical coordinates.

5.6.4 Comparison of FDM and VSM results

In the following seismograms we present the numerical results from single layer, two layer and multi layer 2-D models. Figure (5.55) shows a comparison of the standard FDM and VSM with the Dirichlet boundary conditions. The small amplitude differences are due to the numerical dispersion of the FDM and VSM. Figure (5.56) shows a comparison of the time series with the FDM and VSM solutions for Reynolds ABCs. In the third comparison in Figure (5.57), we compute the seismograms for the FDM and VSM with the Dirichlet boundary conditions. In the fourth comparison in Figure (5.58), we compute the seismograms for the FDM and VSM with the Reynolds ABCs. The good agreement between the both methods can be seen on the seismogram. Figure (5.59) shows a comparison of the standard FDM and VSM with the Dirichlet boundary conditions. The last comparison of the FDM with VSM with Reynolds ABCs is shown in Figure (5.60). There is again good agreement between the two methods.

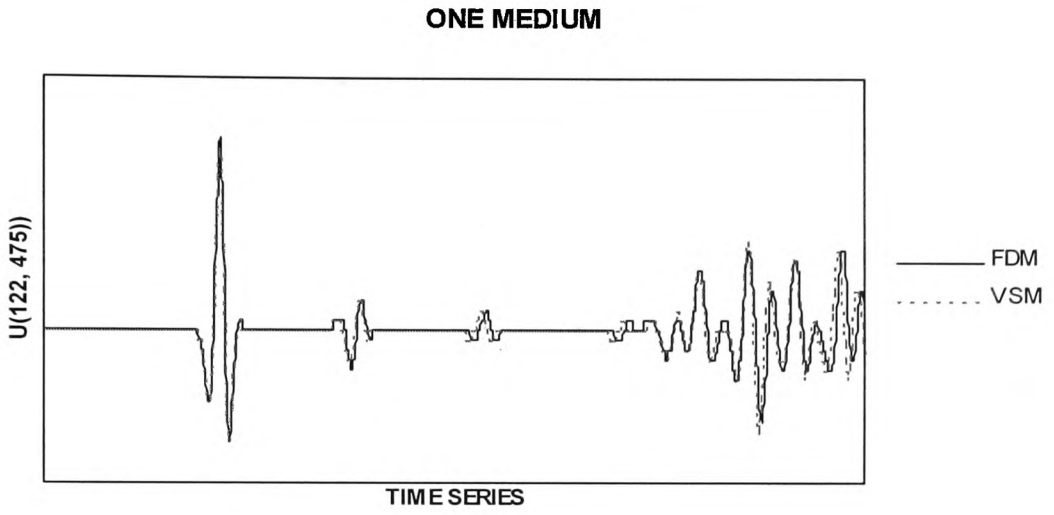

Figure (5.55) Numerical results with the standard FDM and VSM solutions for Dirichlet boundary conditions.

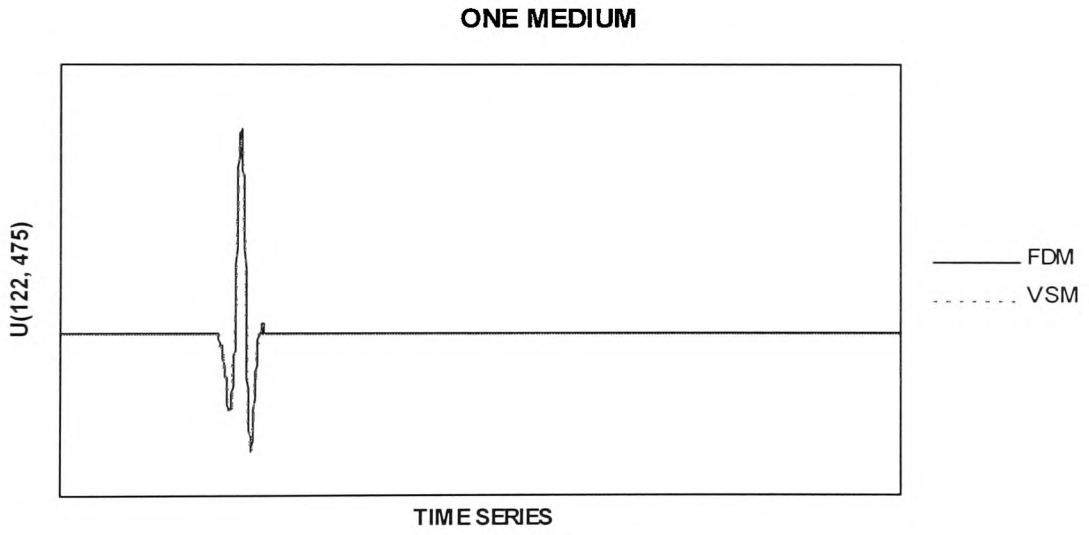

Figure (5.56) Numerical results with the standard FDM and VSM solutions for Reynolds ABCs.

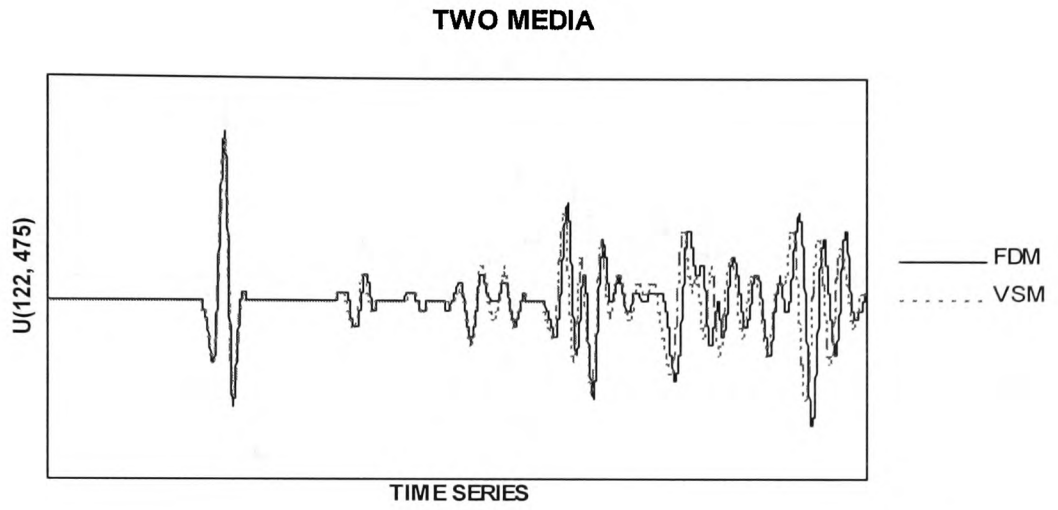

Figure (5.57) Numerical results with the standard FDM and VSM solutions for Dirichlet boundary conditions.

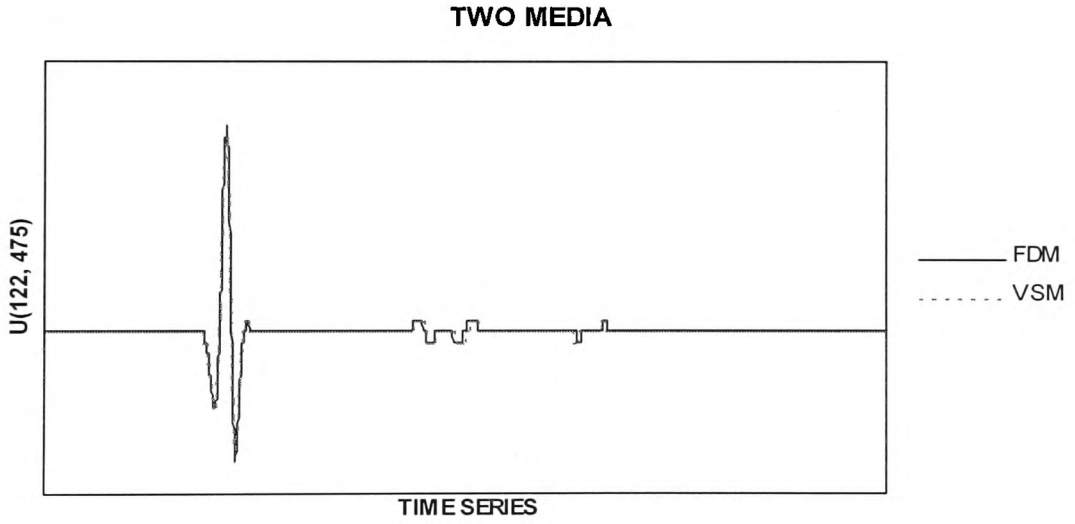

Figure (5.58) Numerical results with the standard FDM and VSM solutions for Reynolds ABCs.

MULTIMEDIA

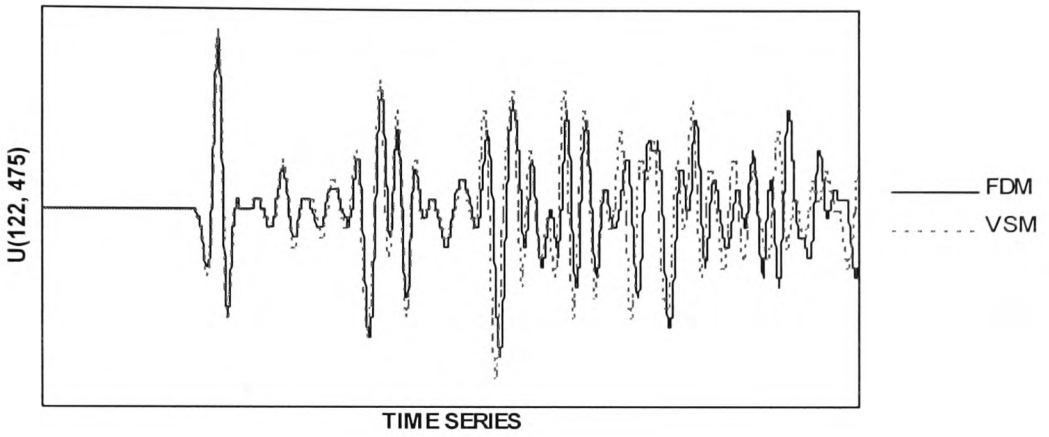

Figure (5.59) Numerical results with the standard FDM and VSM solutions for Dirichlet boundary conditions.

MULTIMEDIA

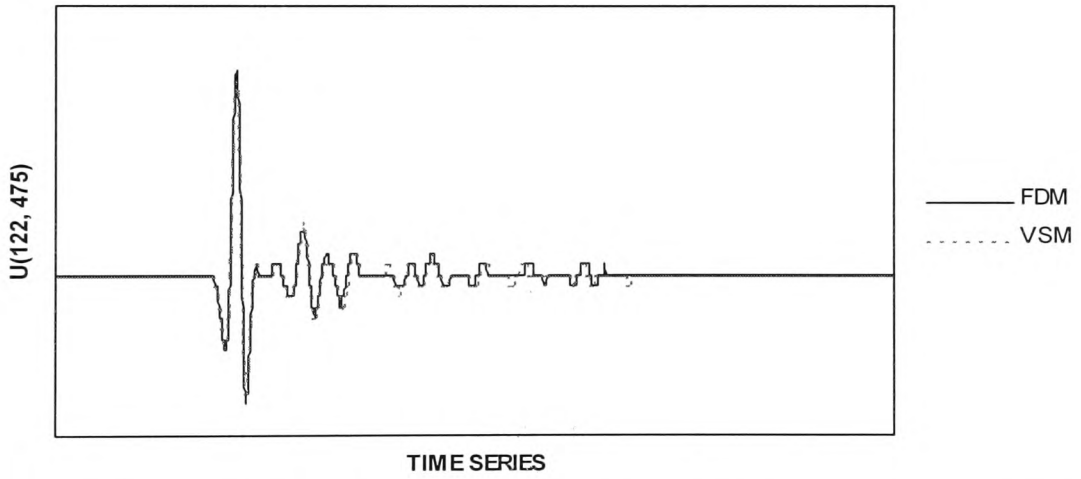

Figure (5.60) Numerical results with the standard FDM and VSM solutions for Reynolds ABCs.

5.6.5 Conclusion of Cylindrical Results

We believe the results presented previously to be novel ones. We solved the 2-D acoustic wave propagation problem numerically with Dirichlet and absorbing boundary conditions in cylindrical coordinates for single layer, two layered, and multi layered media based on the grid / wavelength criteria for best effect. The VSM results were

found to be as good as those from the standard FDM results. The Reynolds ABCs were modified for cylindrical coordinates and was found to be most effective. The interface waves are not as strongly present as for the Cartesian results.

We now have confidence in the numerical approaches adopted for later modelling exercises.

In the next chapter we will present the 2-D elastic wave propagation problem which is an extension of the work developed in this and the previous chapter.

CHAPTER 6

2-D ELASTIC WAVE MODELLING

6.1 Introduction

In this chapter we introduce the numerical solution of the 2-D elastic wave equation in Cartesian and cylindrical coordinates. For more realistic simulation of wave propagation in rock media we need to consider more fully the elastic properties of rocks. This requires the elastic wave propagation equation (2.22 - 2.25, 2.28 - 2.31). As in chapter 5 we shall examine the effectiviness of the optimal grid / wavelength parameters. Also we shall analyse our box & staggered grid model results with the work of others, as well examining the appropriations of the Reynolds and Clayton-Engquist ABCs for modelling purposes. Also cylindrical coordinates models will be considered as a basis for future boreholes models.

The FDM has been studied by Alterman & Karal [**3**], Ottaviani [**55**], Alford et al [**2**], and Stephen [**72,73**]. Much of effort expended on seismic FDM has been directed toward the generation of 2-D synthetic seismograms, mostly because of the utility of their output as interpretational aids (Dai et al. [**19**], Daudt et al. [**21**], Zahradnik et al. [**90**]). The staggered grids were developed by Virieux in 2-D, and used to model both SH-waves [**81**] and P, and SV waves [**82**] in an inhomogeneous plane. The staggered grid method is known as having better numerical stability and accuracy than the

standard FDM, as studied by Levander [44]. A further development of the staggered grid method is given by Luo & Schuster [47] who succeed in a 2-D formulation in which the wavefield in the grid is stored as a set of stresses and velocities.

6.2 2-D Elastic Wave Equations

For 2-D in the x-z plane, the Cartesian elastic wave equations are given as follows:

$$\rho\frac{\partial^2 u}{\partial t^2} = \frac{\partial P_{11}}{\partial x} + \frac{\partial P_{13}}{\partial z}$$
$$\rho\frac{\partial^2 w}{\partial t^2} = \frac{\partial P_{31}}{\partial x} + \frac{\partial P_{33}}{\partial z} \qquad (6.1)$$

and the stress-strain relations are

$$P_{11} = (\lambda + 2\mu)\frac{\partial u}{\partial x} + \lambda\frac{\partial w}{\partial z}$$
$$P_{33} = (\lambda + 2\mu)\frac{\partial w}{\partial z} + \lambda\frac{\partial u}{\partial x} \qquad (6.2)$$
$$P_{13} = P_{31} = \mu(\frac{\partial u}{\partial z} + \frac{\partial w}{\partial x})$$

where λ and μ are Lame's parameters, ρ is density, and u and w are displacement components in the x and z directions respectively.

From equations (6.1) & (6.2) second-order partial differential equations can be used to describe the motion of P-waves and SV-waves in a medium. The equations of motion in a homogeneous isotropic elastic medium are given by

$$\frac{\partial^2 u}{\partial t^2} = v_p^2\frac{\partial^2 u}{\partial x^2} + v_s^2\frac{\partial^2 u}{\partial z^2} + \left(v_p^2 - v_s^2\right)\frac{\partial^2 w}{\partial x \partial z} \qquad (6.3)$$

$$\frac{\partial^2 w}{\partial t^2} = v_p^2\frac{\partial^2 w}{\partial z^2} + v_s^2\frac{\partial^2 w}{\partial x^2} + \left(v_p^2 - v_s^2\right)\frac{\partial^2 u}{\partial x \partial z} \qquad (6.4)$$

where v_p and v_s are the compressional and shear-wave velocities, respectively and $v_p = \sqrt{\frac{\lambda + 2\mu}{\rho}}$, $v_s = \sqrt{\frac{\mu}{\rho}}$ where ρ is a density, t is the time. The source is taken to be a purely compressional pulse, which is a solution of equations (6.3) and (6.4) in the geometry of Figure(6.1). A compressional point source is located inside the layer along the axis at the point (427m, 305m). In this chapter we examine the three models: single medium, two media and multimedia models. The single medium contains shale only, and the two media contain sea-water and shale, like Reynolds [**64**].

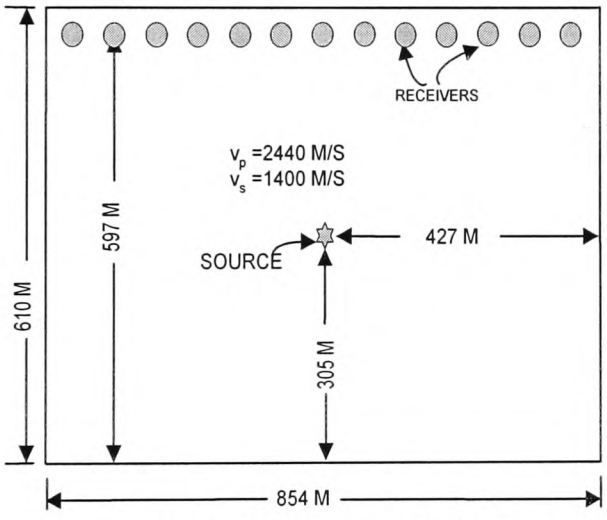

Figure (6.1) Physical model showing receiver geometry used to generate seismograms in the elastic finite-difference program for one medium.

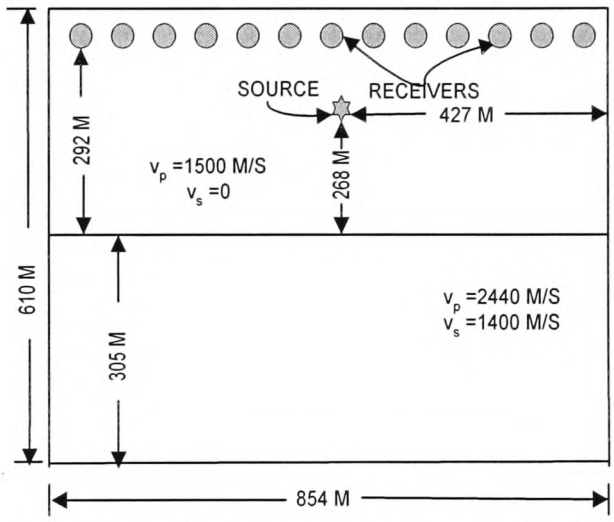

Figure (6.2) Physical model showing receiver geometry used to generate seismograms in the elastic finite-difference program for two media

The third model contains sea-water, mud, shale, oil and limestone respectively.

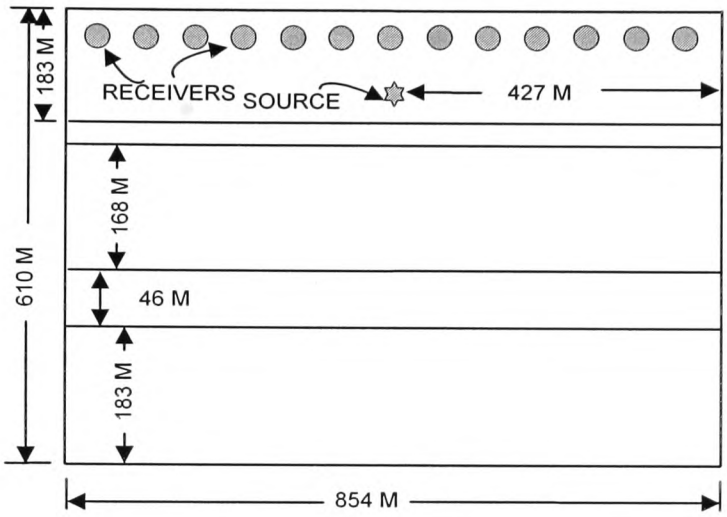

Figure (6.3) Physical model showing receiver geometry used to generate seismograms in the elastic finite-difference program for multimedia.

6.3 Discretisation of 2-D Elastic Wave Equation

These equations of motion can be written in the FDM form by replacing the various derivatives by their centred finite difference approximations. The FDM formulation corresponding to Equations (6.3) and (6.4) has been derived by Ottaviani [**55**] and Kelly et al. [**37**], and given as follows:

$$u_{i,j}^{n+1} = 2u_{i,j}^{n} - u_{i,j}^{n-1} + q_1\left(u_{i+1,j}^{n} - 2u_{i,j}^{n} + u_{i-1,j}^{n}\right) + q_2\left(w_{i+1,j+1}^{n} - w_{i+1,j-1}^{n} - w_{i-1,j+1}^{n} + w_{i-1,j-1}^{n}\right)$$

$$+ q_3\left(u_{i,j+1}^{n} - u_{i,j}^{n} + u_{i,j-1}^{n}\right) \qquad (6.5)$$

$$w_{i,j}^{n+1} = 2w_{i,j}^{n} - w_{i,j}^{n-1} + q_3\left(w_{i+1,j}^{n} - 2w_{i,j}^{n} + w_{i-1,j}^{n}\right) + q_2\left(u_{i+1,j+1}^{n} - u_{i+1,j-1}^{n} - u_{i-1,j+1}^{n} + u_{i-1,j-1}^{n}\right)$$

$$+ q_1\left(w_{i,j+1}^{n} - w_{i,j}^{n} + w_{i,j-1}^{n}\right) \qquad (6.6)$$

The terms $u_{i,j}^{n+1}$ and $w_{i,j}^{n+1}$ represent the horizontal and vertical displacement at the point (ih, jh) for the time (n+1)Δt, h is the grid interval in both the x and z directions, and i, j, and n are defined to be integers. Finally q_1, q_2, and q_3 are parameters given by

$q_1=(v_p\Delta t/h)^2$, $q_2=[(v_p-v_s)\Delta t/h]^2$ and $q_3=(v_s\Delta t/h)^2$ and the x, z grid width are both equal to h. Equations (6.5) and (6.6) form an simple explicit system since they enable one to compute the displacement u and w at each spatial grid point at time step (n+1) exclusively in terms of the motion at the two previous time steps n and (n-1).

The stability conditions for the explicit FDM are discussed in detail by Kelly [37], Alterman & Loewenthal [4] and Mitchell [49]. The following is the Von Neumann stability condition for the numerical method:

$$\Delta t \le \frac{h}{\left(v_p^2 + v_s^2\right)^{1/2}} \tag{6.7}$$

for all v_p and v_s.

6.4 Boundary Conditions

The boundary conditions at the free surface require the normal and shear stresses as to vanish, that is (Grant and West [28]),

$$\begin{aligned} \left(v_p^2 - 2v_s^2\right)\frac{\partial u}{\partial x} + v_p^2\frac{\partial w}{\partial z} &= 0 \\ \frac{\partial u}{\partial z} + \frac{\partial w}{\partial x} &= 0 \end{aligned} \tag{6.8}$$

We employ all boundary conditions in a similar way as for the previously examined acoustic wave equation. The side boundary conditions are given in the previous chapter 3, and here we only employ the finite difference approximation from the Reynolds ABCs namely.

$$\begin{aligned} u_{0,j}^{n+1} &= u_{0,j}^{n} + u_{1,j}^{n} - u_{1,j}^{n-1} + q_1\left(u_{1,j}^{n} - u_{0,j}^{n} - u_{2,j}^{n-1} + u_{1,j}^{n-1}\right) \\ w_{0,j}^{n+1} &= w_{0,j}^{n} + w_{1,j}^{n} - w_{1,j}^{n-1} + q_1\left(w_{1,j}^{n} - w_{0,j}^{n} - w_{2,j}^{n-1} + w_{1,j}^{n-1}\right) \end{aligned} \tag{6.9}$$

$$\begin{aligned} u_{M,j}^{n+1} &= u_{M,j}^{n} + u_{M-1,j}^{n} - u_{M-1,j}^{n-1} - q_1\left(u_{M,j}^{n} - u_{M-1,j}^{n} - u_{M-1,j}^{n-1} + u_{M-2,j}^{n-1}\right) \\ w_{M,j}^{n+1} &= w_{M,j}^{n} + w_{M-1,j}^{n} - w_{M-1,j}^{n-1} - q_1\left(w_{M,j}^{n} - w_{M-1,j}^{n} - w_{M-1,j}^{n-1} + w_{M-2,j}^{n-1}\right) \end{aligned} \tag{6.10}$$

We also need to consider the corner point boundary conditions at the geometry vertices. The u displacement was obtained by using the following Reynolds corner point boundary conditions.

$$\begin{aligned} u_{0,0}^{n+1} &= u_{0,0}^{n} + q_1\left(u_{1,1}^{n} - u_{0,0}^{n}\right) \\ u_{0,N}^{n+1} &= u_{0,N}^{n} + q_1\left(u_{1,N-1}^{n} - u_{0,N}^{n}\right) \\ u_{M,0}^{n+1} &= u_{M,0}^{n} + q_1\left(u_{M-1,1}^{n} - u_{M,0}^{n}\right) \\ u_{M,N}^{n+1} &= u_{M,N}^{n} + q_1\left(u_{M-1,N-1}^{n} - u_{M,N}^{n}\right) \end{aligned} \tag{6.11}$$

Similarly for w at the corners.

$$\begin{aligned} w_{0,0}^{n+1} &= w_{0,0}^{n} + q_1\left(w_{1,1}^{n} - w_{0,0}^{n}\right) \\ w_{0,N}^{n+1} &= w_{0,N}^{n} + q_1\left(w_{1,N-1}^{n} - w_{0,N}^{n}\right) \\ w_{M,0}^{n+1} &= w_{M,0}^{n} + q_1\left(w_{M-1,1}^{n} - w_{M,0}^{n}\right) \\ w_{M,N}^{n+1} &= w_{M,N}^{n} + q_1\left(w_{M-1,N-1}^{n} - w_{M,N}^{n}\right) \end{aligned} \tag{6.12}$$

We use the absorbing boundary conditions for the left and right geometry sides. Also the top and bottom boundary are taken to be free surfaces.

6.5 Accuracy of the Numerical Solution of the 2-D Elastic Wave

In this section we present results for the seismogram patterns arising from the various types of seismograms configuration of the 2-D elastic model. We consider the convergence of the solution by comparing calculations for various equal grid widths denoted by h. We have produced results for one second of simulation time to obtain a numerical solution, and the solutions are found to be consistent with grids ranging from

28x20x1000 to 280x200x1000. We will compare the three methods for one medium which are namely (ur+us), box, and staggered grid. Figure (6.4a) shows the results for (ur+us), box, and staggered grid values evaluated near the boundary (x=210 m, z=12 m, t=0.5 s) and display the u horizontal displacement. Figure(6.4b) shows the results for the vertical w displacements at the same point. Figure (6.4a) and (6.4b) exhibit the results with Dirichlet boundary conditions. All the methods show convergence at the h=6 m. The ABCs results are shown in Figure (6.5a) with (ur+us), box, staggered grid and the Clayton-Engquist ABCs for horizontal u displacement, whilst Figure (6.5b) show results for vertical w displacement with the ABCs. Also Figure (6.5a) and (6.5b) show convergence at the h=6 m.

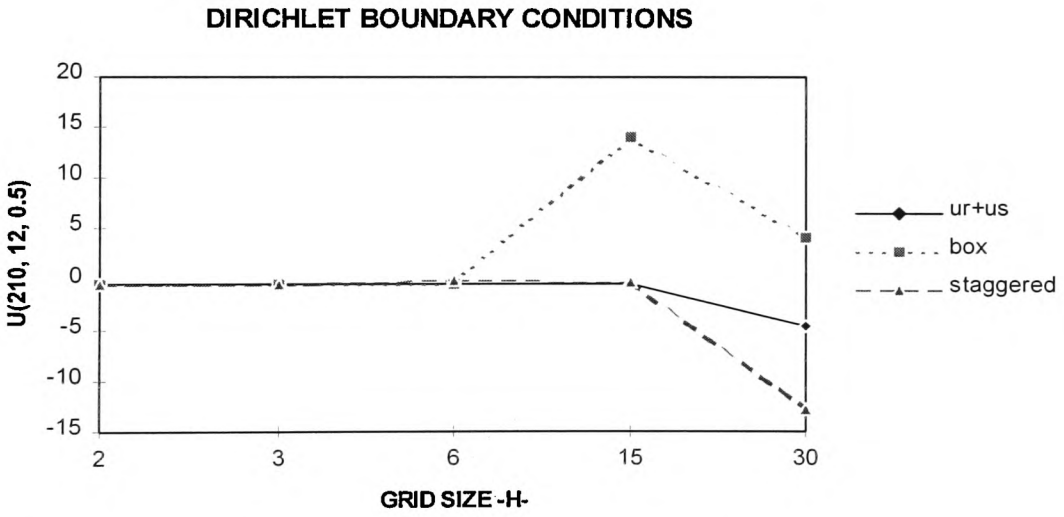

Figure (6.4a) Convergence criterion with horizontal displacement for (ur+us), box and staggered grid methods.

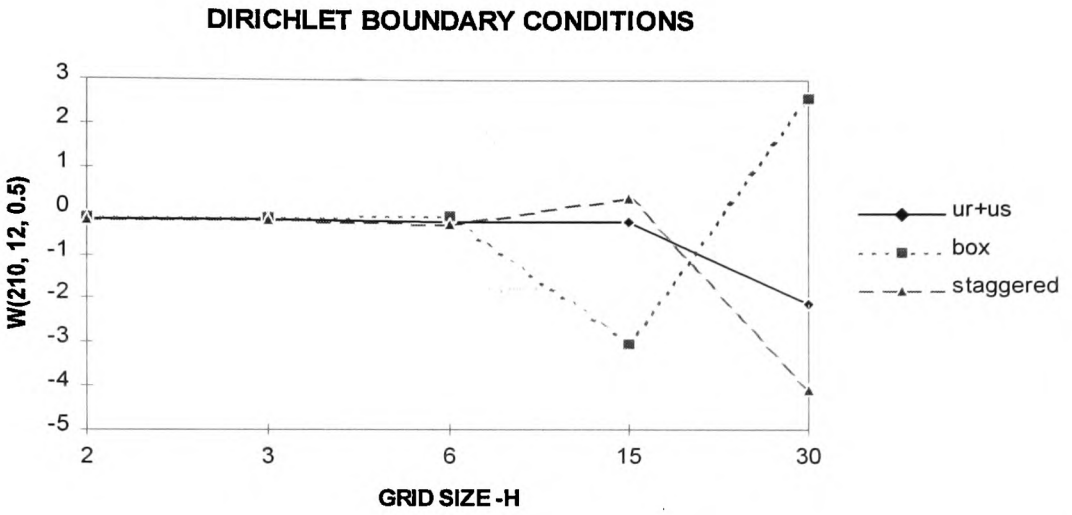

Figure (6.4b) Convergence criterion with vertical displacement for (ur+us), box and staggered grid methods.

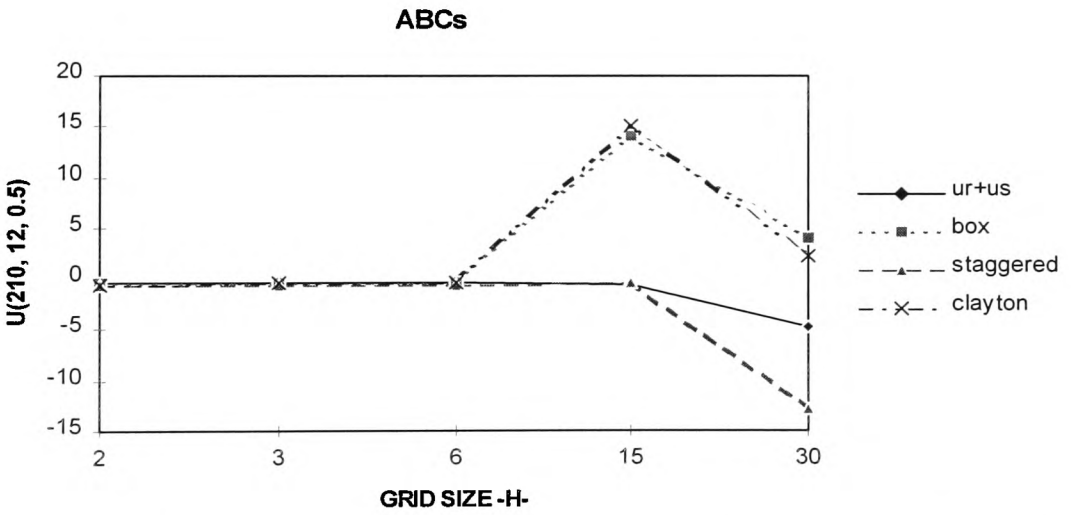

Figure (6.5a) Convergence criterion with horizontal displacement for (ur+us), box, staggered grid and Clayton-Engquist ABCs methods.

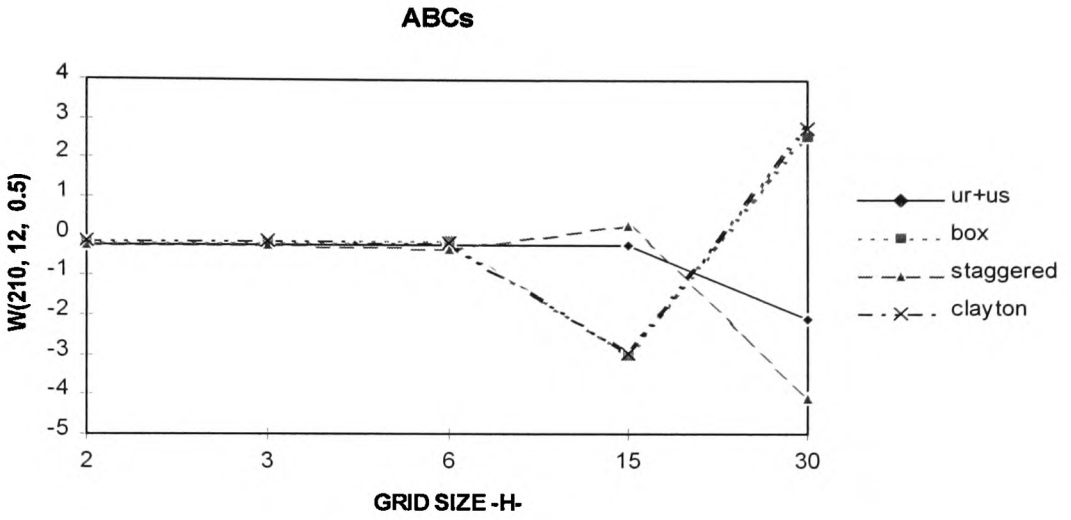

Figure (6.5b) Convergence criterion with vertical displacement for (ur+us), box, staggered grid and Clayton-Engquist ABCs methods.

Figures (6.6a), and (6.6b) show results for horizontal and vertical displacements with ABCs for two media.

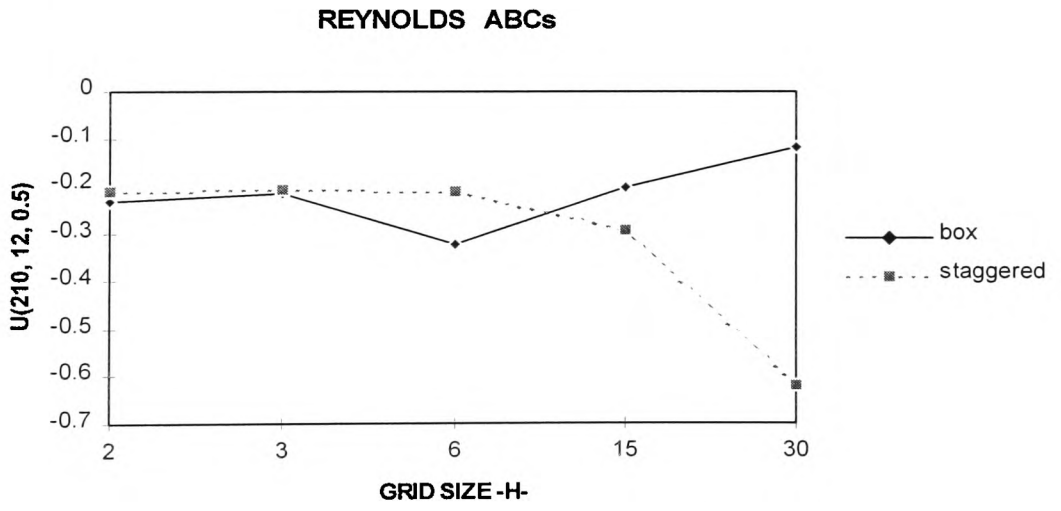

Figure (6.6a) Convergence criterion with horizontal displacement for (ur+us), box, and staggered grid methods.

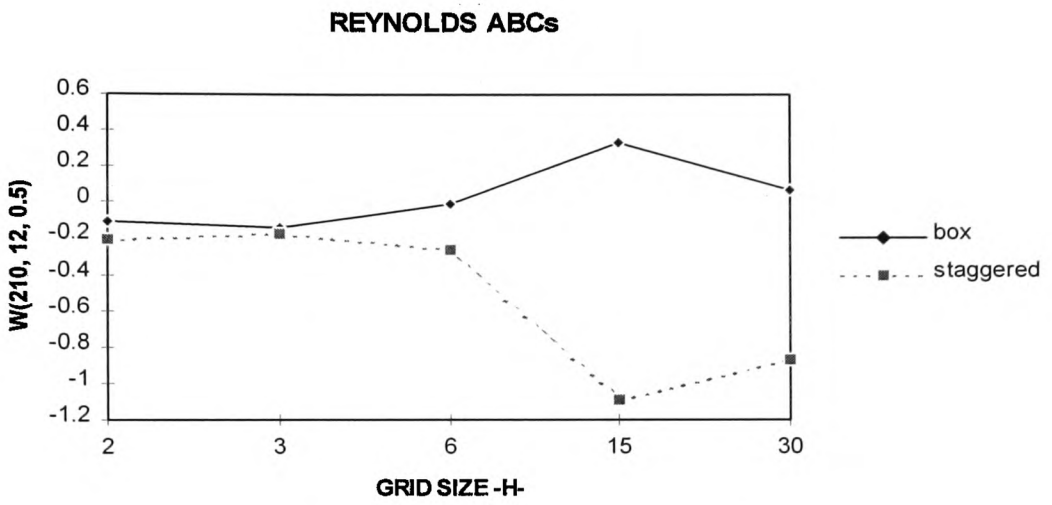

Figure (6.6b) Convergence criterion with vertical displacement for (ur+us), box, and staggered grid methods.

All methods exhibit converge at h=3 m. Emerman and Stephen [**23**] found the Clayton-Engquist [**18**] ABCs were only stable when v_s/v_p was greater than 0.46. Our two media model includes sea-water and shale and since the sea-water shear velocity is zero then that ratio is equal to zero. Our version of the Clayton-Engquist ABCs program did not produce acceptable results because of this difficulty. The program exhibited overflow due to the Clayton-Engquist absorbing boundary conditions used. Figure (6.7a) and (6.7b) show results the horizontal and vertical displacements with the Reynolds ABCs for multimedia.

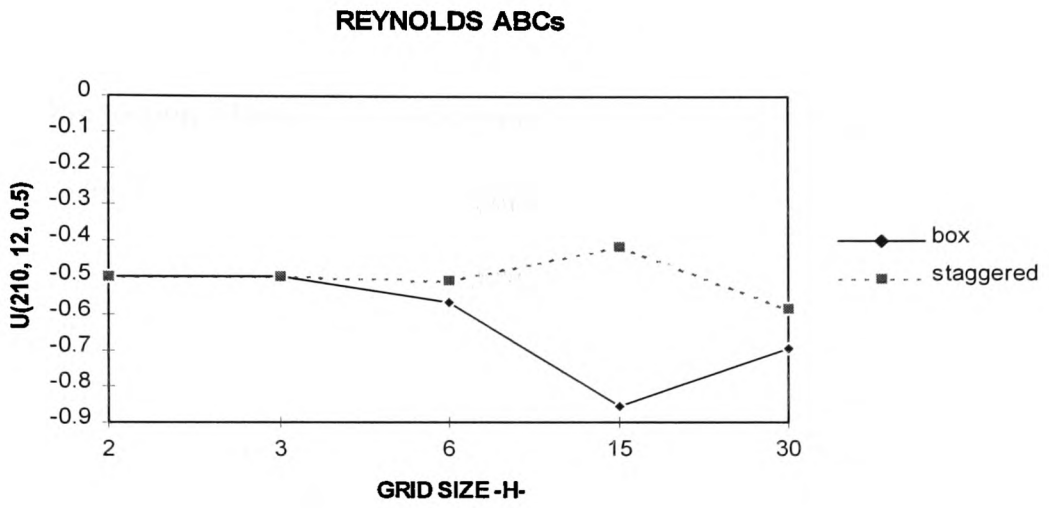

Figure (6.7a) Convergence criterion with horizontal displacement for (ur+us), box, and staggered grid methods.

The multimedia results show similarity with the two media results with convergence near h=3 m. The staggered grid method exhibits convergence before the box method.

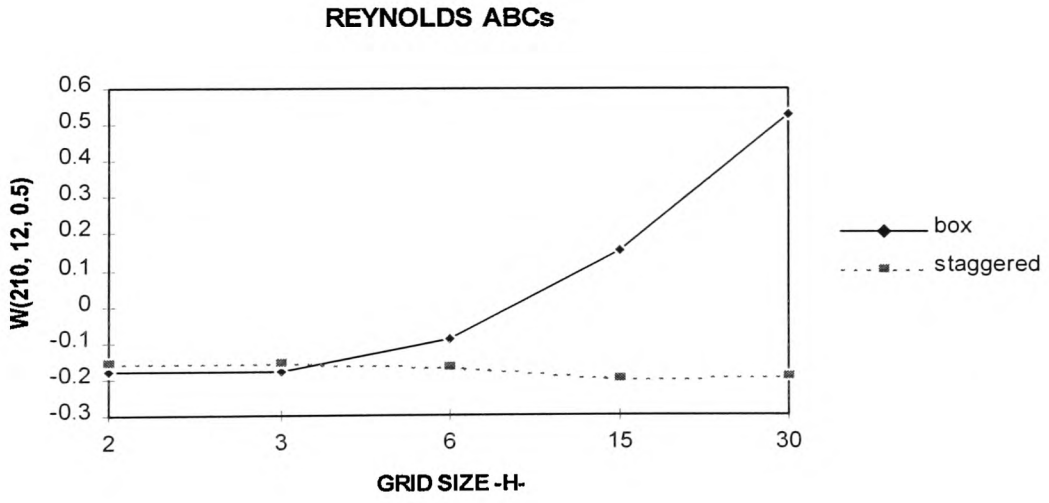

Figure (6.7b) Convergence criterion with vertical displacement for (ur+us), box, and staggered grid methods.

6.5.1 Single medium results in Cartesian coordinates

In this section, elastic wave equations are solved by different numerical methods which are namely (ur+us), box, and staggered grid methods. Figure (6.1) shows a simplified 2-D elastic homogeneous medium with the compressional wave velocity 2440 m/s, and the shear wave velocity 1400 m/s which were obtained from Reynolds [64]. A source was located at a point 427 m from each side boundary, at a depth of 305 m. Receivers were positioned in a horizontal row 12 m below the free surface. The grid size and time increment are 6 m and 0.001 s respectively. The single medium model was solved with two different boundary conditions for the artificial boundaries that are Reynolds ABCs and Clayton-Engquist ABCs.

We tested the FDM on numerical methods and compared the results with those of three methods: (ur+us), box and staggered grid method. We give the seismograms of one medium (ur+us) results with the Dirichlet boundary conditions in Figure (6.8) with u displacement on the left and w on the right. Figure (6.9) shows results obtained by the box method with Dirichlet boundary conditions. Figure (6.10) presents the results obtained by the staggered grid method with Dirichlet boundary conditions.

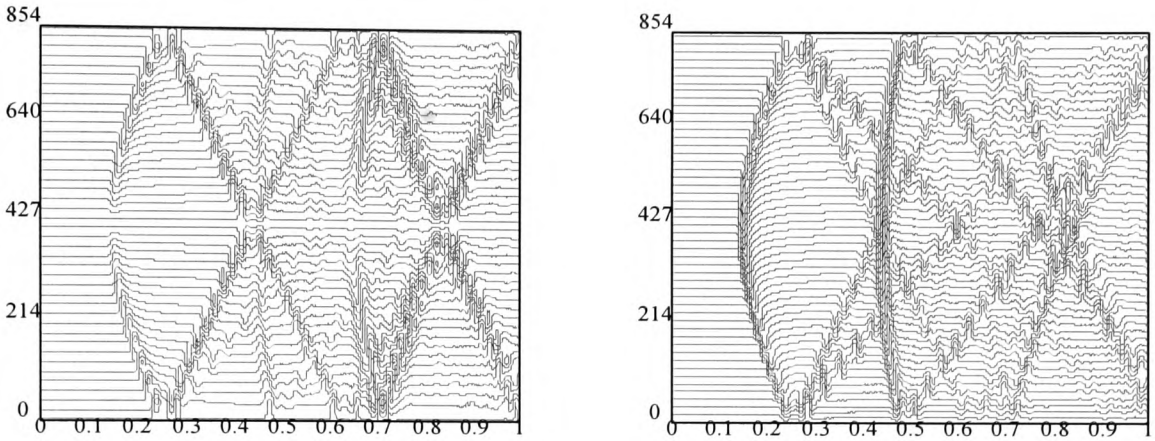

Figure (6.8) Synthetic horizontal and vertical seismograms from the elastic (ur+us) method program with Dirichlet boundary conditions.

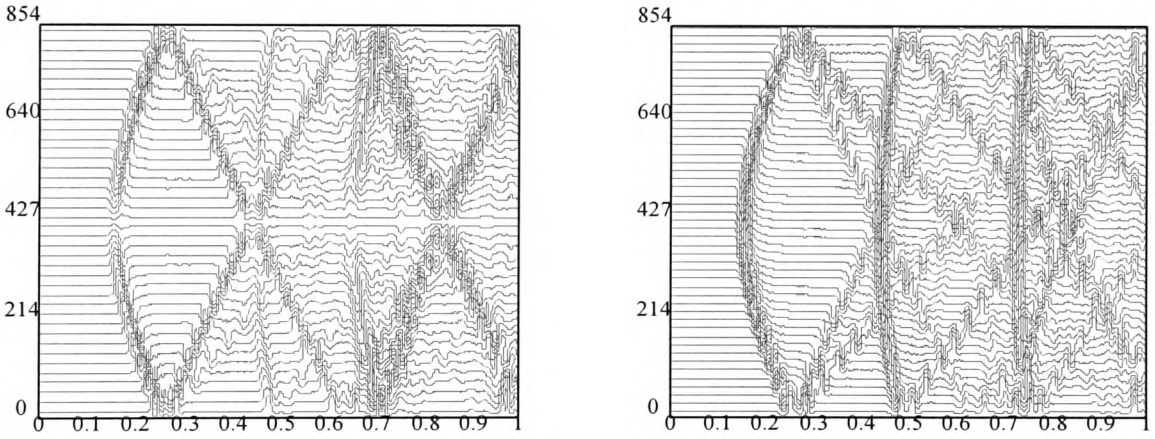

Figure (6.9) Synthetic horizontal and vertical seismograms from the elastic box method program with Dirichlet boundary conditions.

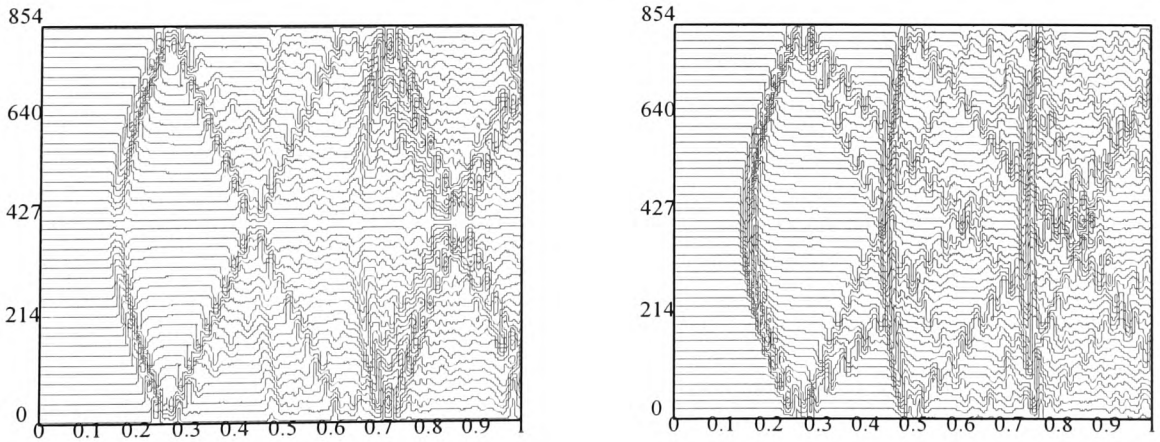

Figure (6.10) Synthetic horizontal and vertical seismograms from the elastic staggered grid method program with Dirichlet boundary conditions.

Figure (6.11) shows results of the (ur+us) method with horizontal and vertical seismograms for the Reynolds ABCs. The box method results are shown in Figure (6.12) for the Reynolds ABCs. Figure (6.13) show results from the staggered grid method with horizontal and vertical seismograms using the Reynolds ABCs. Finally, Figure (6.14) shows the box method results with the Clayton-Engquist ABCs which exhibit parasitic reflections. Figure (6.15a) shows horizontal displacement for the Reynolds's results with both boundary conditions. Figure (6.15b) shows vertical displacement for Reynolds's results with the Dirichlet and absorbing boundary conditions. On comparism of Reynolds's results with our results, we obtain excellent qualitative agreement in all cases except Clayton-Engquist results which exhibit small unwanted reflection from the side boundaries.

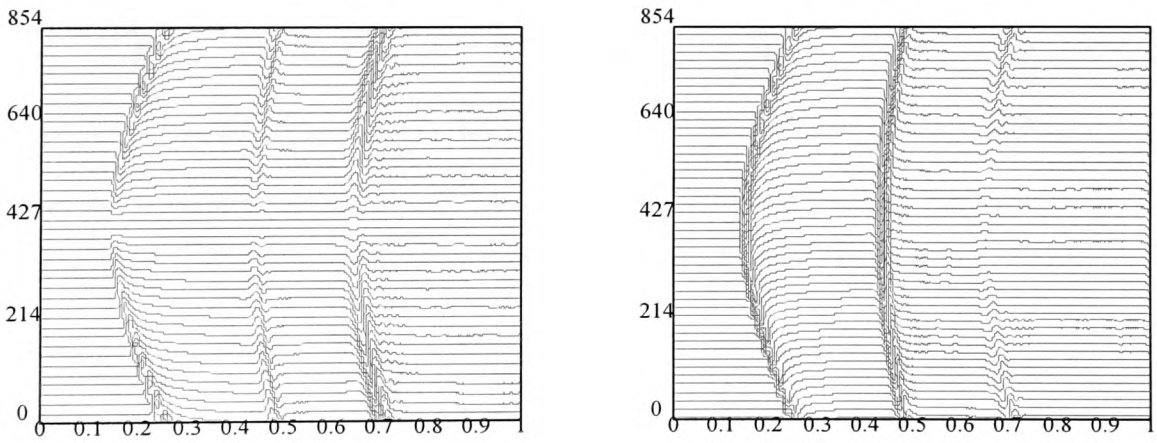

Figure (6.11) Synthetic horizontal and vertical displacement seismograms from the elastic (ur+us) method program with Reynolds ABCs.

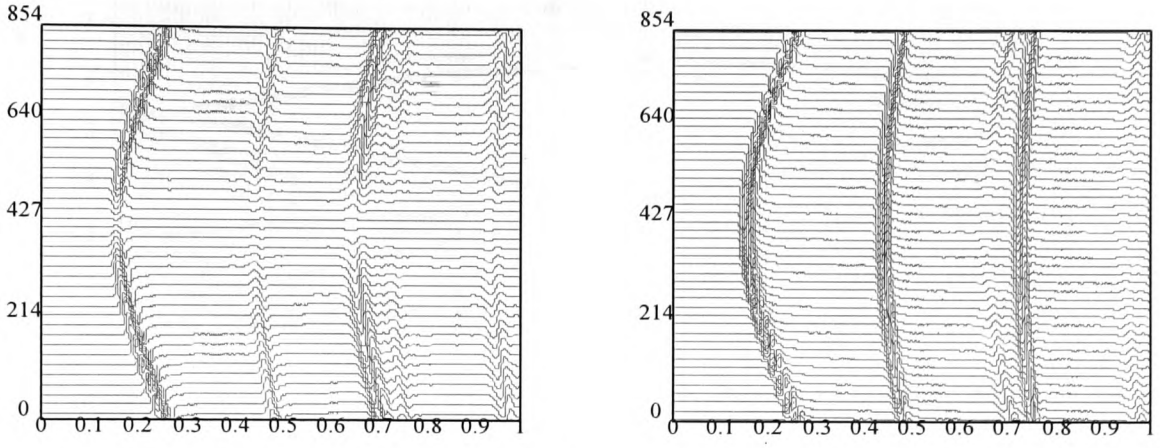

Figure (6.12) Synthetic horizontal and vertical displacement seismograms from the elastic box method program with Reynolds ABCs.

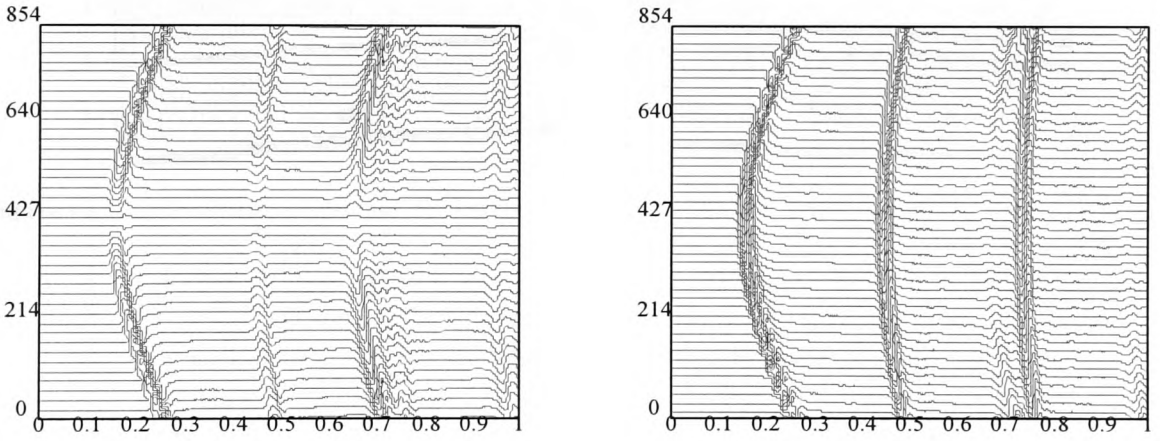

Figure (6.13) Synthetic horizontal and vertical displacement seismograms from the elastic staggered grid method program with Reynolds ABCs.

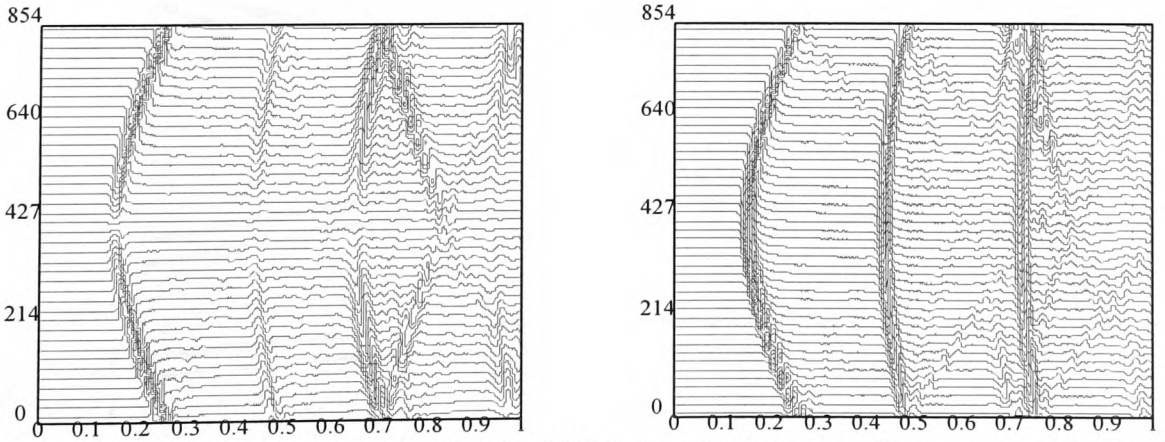

Figure (6.14) Synthetic horizontal and vertical displacement seismograms from the elastic box method program with Clayton-Engquist ABCs.

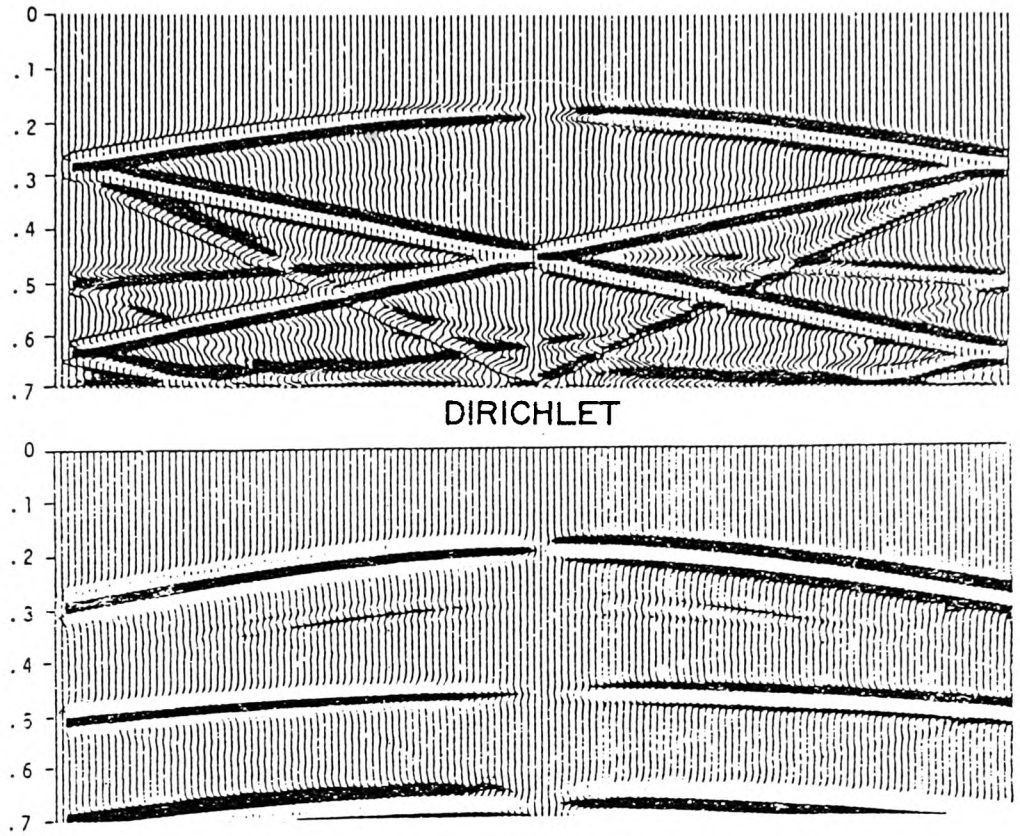

Figure (6.15a) Synthetic horizontal displacement with Dirichlet and Transparent boundary conditions for Reynolds's results.

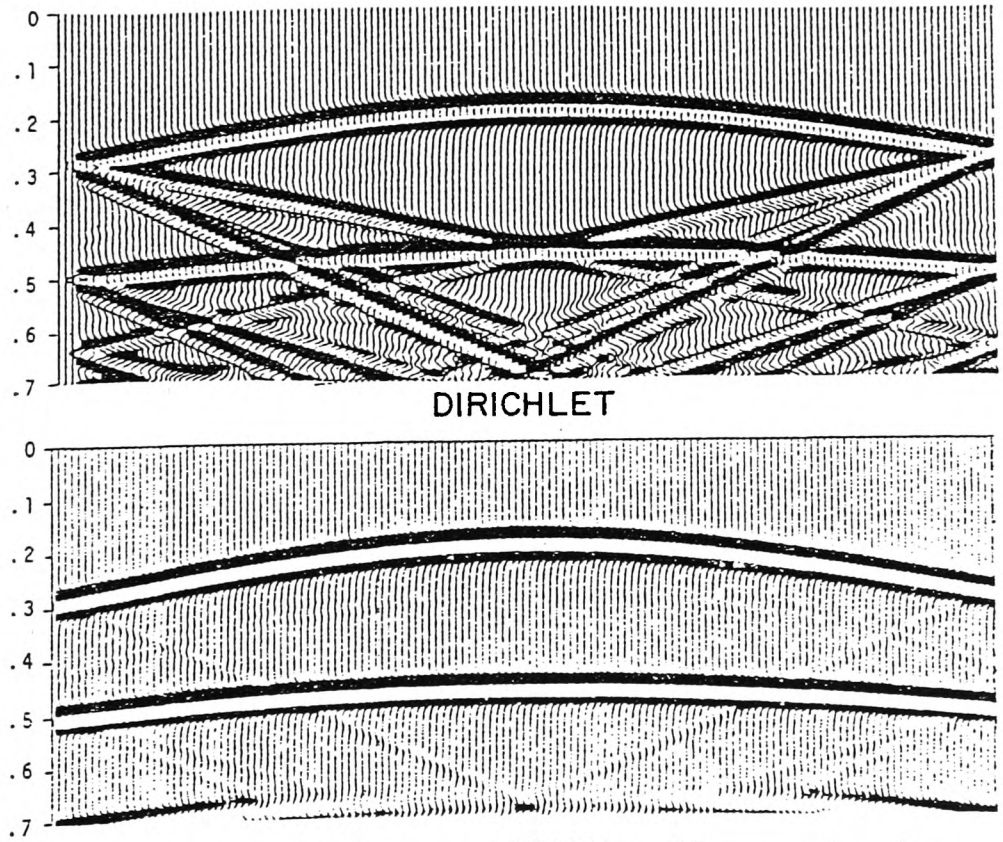

Figure (6.15b) Synthetic vertical displacement with Dirichlet and Transparent boundary conditions for Reynolds's results.

6.5.2 Two media results in Cartesian coordinates

In this section to illustrate the results of numerical modelling in 2-D elastic case, we computed seismograms for two methods which are the box and staggered grid method. The physical parameters are given in table (6.1). The interface is located 305 m below the free surface and a line source is located 61 m below the free surface. The receiver line is parallel to the interface at the a depth of 12 m. An acoustic upper layer is bounded by a free surface. The free surface causes total reflection of the wavefield while the acoustic-elastic interface causes angle dependent reflections and transmissions, including interface waves.

Table (6.1). Physical Parameters of a Two Layer Elastic Model.

Layers	λ(Pa)	μ(Pa)	ρ(kg/m^3)	v_p(m/s)	v_s(m/s)
sea-water	2.32E9	0.0	1030	1500	0.0
shale	4.99E9	4.80E9	2450	2440	1400

The size of the model grid is 140x200 in the x, z axis directions, respectively, and the grid increment is 3 m. In this case, receivers are located at 30 m distance intervals. Figure (6.16) shows horizontal and vertical displacement with Reynolds ABCs for the box method. Figure (6.17) shows horizontal and vertical displacement with Reynolds ABCs for the staggered grid method. For both seismograms, time runs along the horizontal axis and distance from the source along the vertical axis. In both Figures (6.16) and (6.17), the direct wave arrives after approximately 0.04 s, with the interface and reflected waves arriving after 0.355, and 0.436 s. The bottom reflected wave arrives after 0.76, and 0.84 s for the vertical w displacement. The horizontal wave seismogram shows the direct and interface reflected wave arriving at 0.04, 0.35, and 0.43 s,

respectively. Figures (6.16) and (6.17) horizontal seismograms show that the interface waves are weaker than vertical seismograms interface waves.

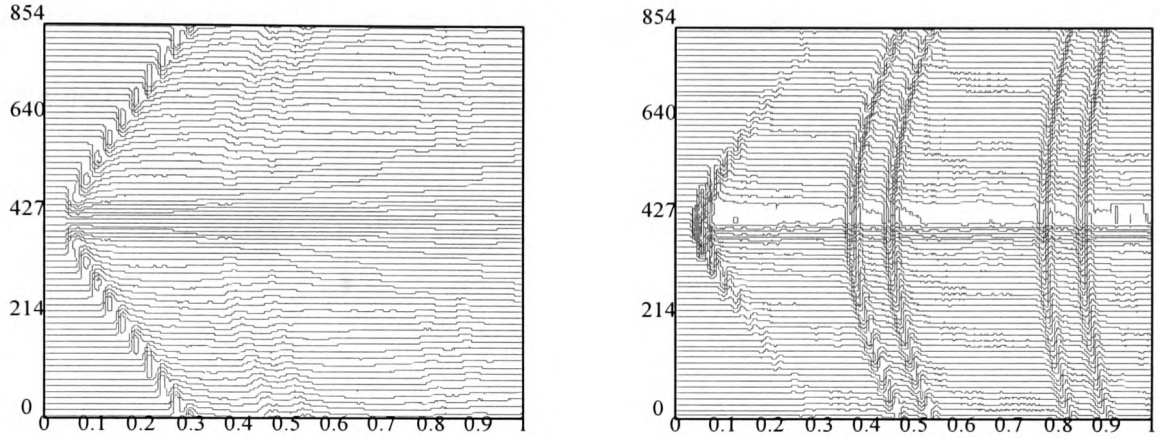

Figure (6.16) Synthetic horizontal and vertical seismograms from the elastic box method program with Reynolds ABCs.

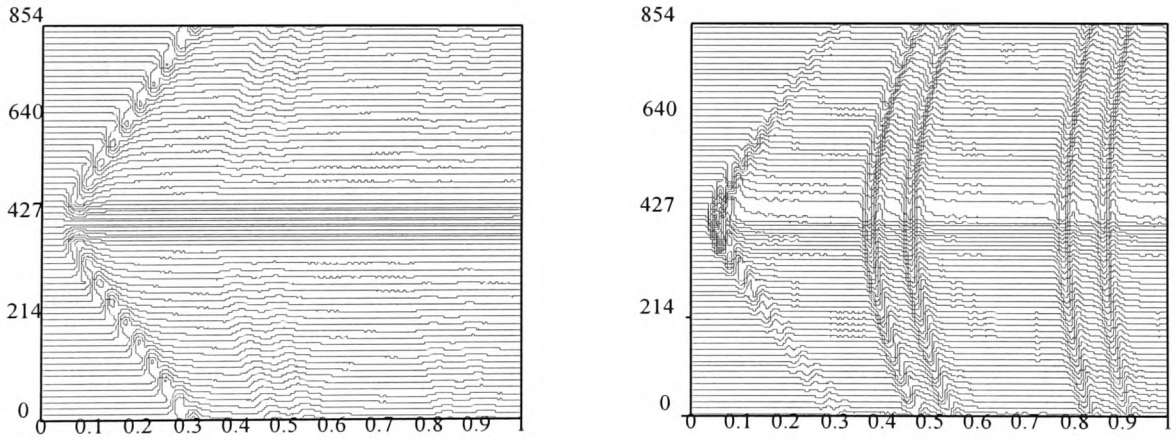

Figure (6.17) Synthetic horizontal and vertical seismograms from the elastic staggered grid method program with Reynolds ABCs.

6.5.3 Multimedia Results in Cartesian Coordinates

In this section the synthetic seismograms were generated for the multimedia model of Figure (6.3) with the elastic physical parameters of table (6.2) which are obtained from Yoon & McMechan [87].

Table (6.2). Physical Parameters of a Multimedia Elastic Model.

Layers	λ(Pa)	μ(Pa)	ρ(kg/m^3)	v_p(m/s)	v_s(m/s)
sea-water	2.32E9	0.0	1030	1500	0.0
mud	3.71E9	0.0	1450	1600	0.0
shale	4.99E9	4.80E9	2450	2440	1400
oil	1.37E9	0.0	890	1240	0.0
limestone	13.38E9	7.18E9	2400	3400	1730

An upper layer and lower layer are bounded by free surfaces with all other sides bounded by the ABCs. The synthetic seismograms were generated using a grid size of 3 m in x, and z with time increment was 0.0005 s. The wavefield is recorded at 12 m below the free surface by 20 receivers and the source is located 61 m below the free surface. The synthetic seismograms computed for two methods which are the box and staggered grid methods. Both methods generated similar seismograms. We will compare the two methods in the following section. Figure (6.18) shows the horizontal and vertical seismograms with the Reynolds ABCs for the box method. The next seismograms show the staggered grid method results with the Reynolds ABCs in Figure (6.19). Agreement between both figures is acceptable.

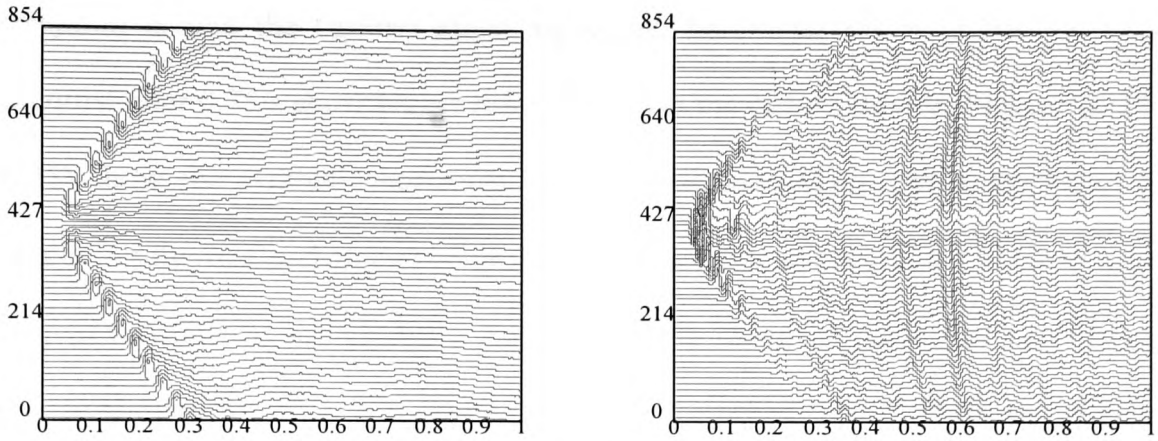

Figure (6.18) The synthetic horizontal and vertical seismograms from the elastic box method program with Reynolds ABCs.

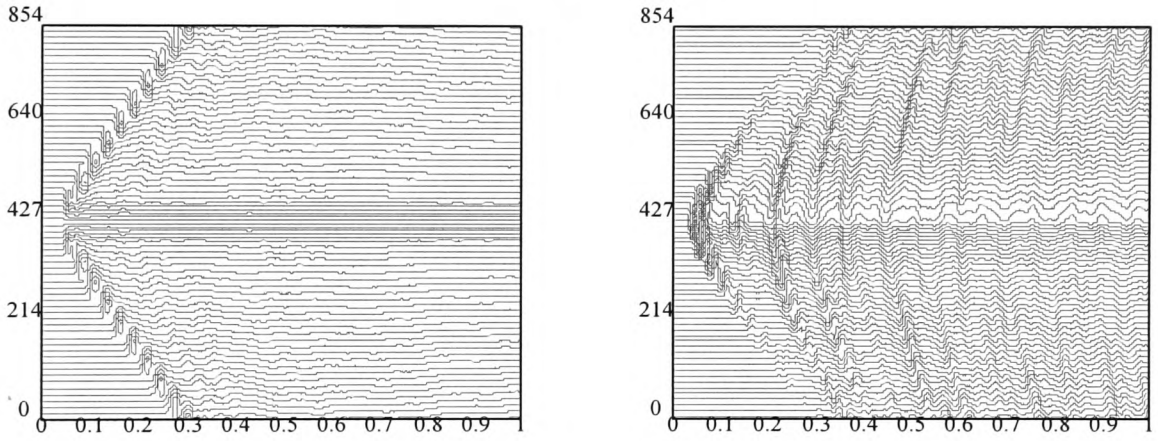

Figure (6.19) The synthetic horizontal and vertical seismograms from the elastic staggered grid method program with Reynolds ABCs.

6.5.4 Comparison of Numerical Results

In this section, we compare the (ur+us), box, and staggered grid methods in Figure (6.20) and (6.21) with the Dirichlet boundary conditions. We find good agreement between the three methods but there are differences between the (ur+us) method and the other two methods. Figure (6.22) and (6.23) show a comparison of the synthetic horizontal and vertical seismograms generated by the (ur+us), box, and staggered grid methods for Reynolds and Clayton-Engquist ABCs a for single medium. Excellent agreement is seen generally in both figures for the three methods. The

exception is that the (ur+us) direct wave and horizontal seismograms for Clayton-Engquist after 0.75 s show bigger reflections than the other methods. Figures (6.24) and (6.25) show the synthetic horizontal and vertical seismograms with Reynolds ABCs employing the box and staggered grid methods for two media. There is close match of the two waveforms; vertical wave traces are nearly identical, horizontal wave traces are closely similar but there is a small difference after direct wave. There is good overall agreement between the two methods. For display purposes we have purposely displaced the wave traces on the figures.

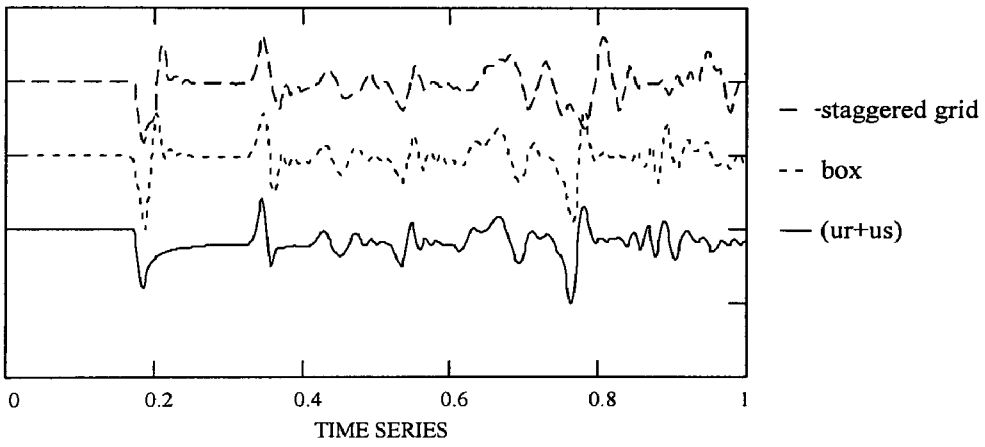

Figure (6.20) Synthetic horizontal displacement seismograms obtained from the (ur+us), box, and staggered grid methods with Dirichlet boundary conditions solutions for single medium.

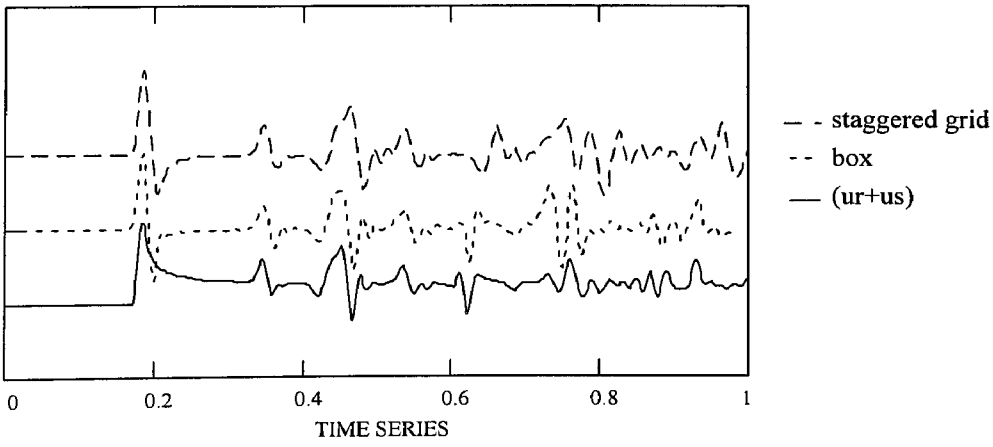

Figure (6.21) Synthetic vertical displacement seismograms obtained from the (ur+us), box, and staggered grid methods with Dirichlet boundary conditions solutions for single medium.

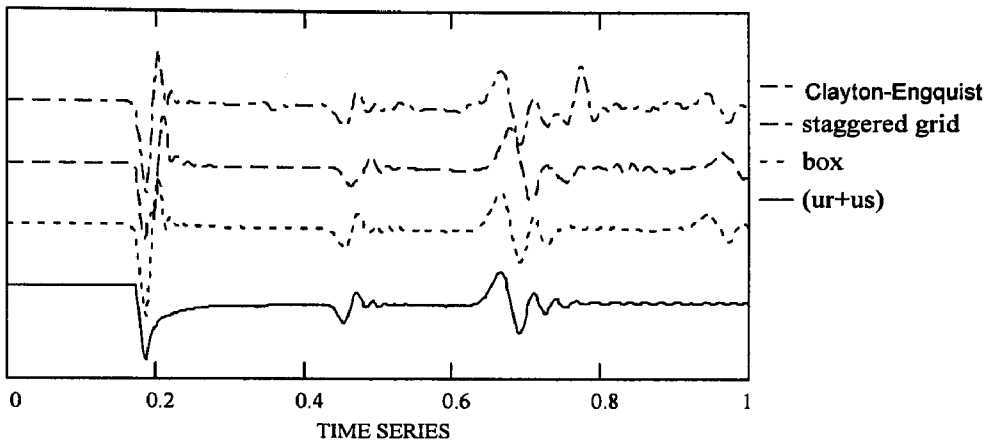

Figure (6.22) Synthetic horizontal displacement seismograms obtained from the (ur+us), box, and staggered grid methods with Reynolds and Clayton-Engquist ABCs solutions for single medium.

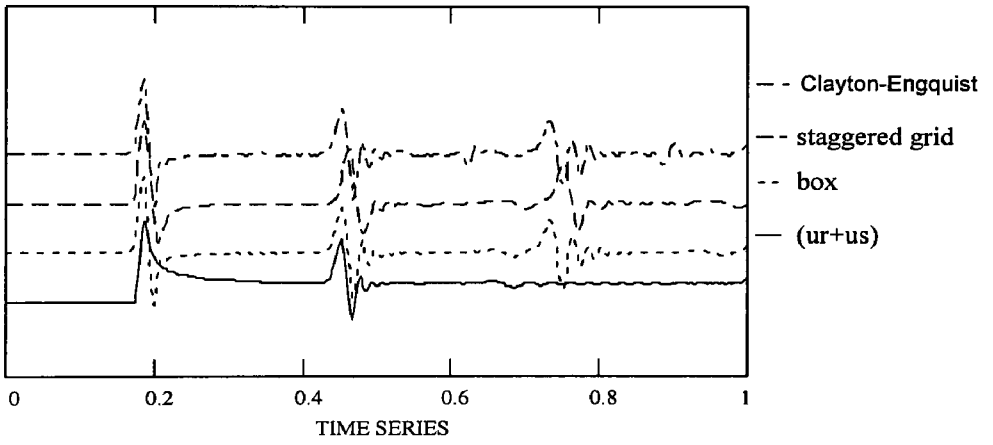

Figure (6.23) Synthetic vertical displacement seismograms obtained from the (ur+us), box, and staggered grid methods with Reynolds and Clayton-Engquist ABCs solutions for single medium.

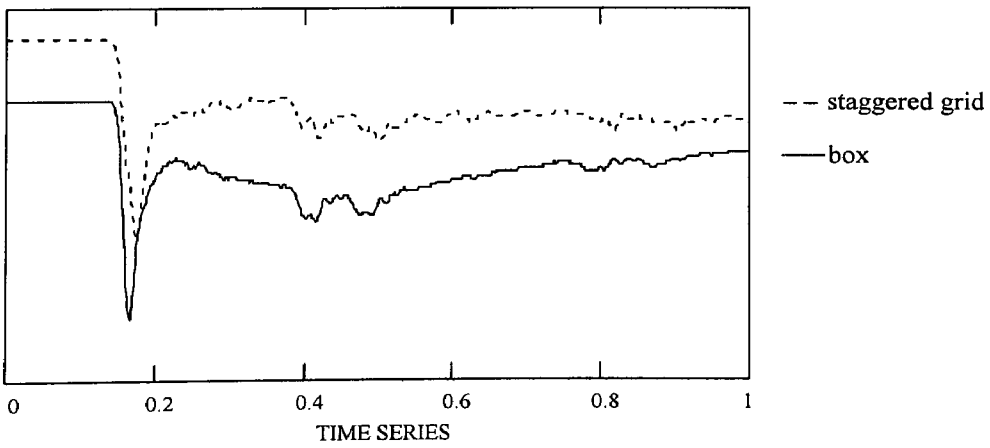

Figure (6.24) Synthetic horizontal displacement seismograms obtained from the box, and staggered grid methods with Reynolds ABCs solutions for two media.

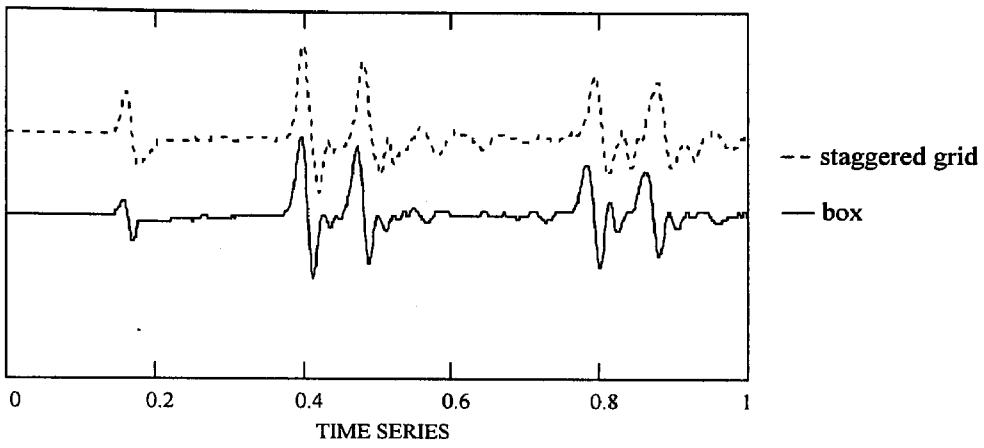

Figure (6.25) Synthetic vertical displacement seismograms obtained from the box, and staggered grid methods with Reynolds ABCs solutions for two media.

Figures (6.26) and (6.27) show the synthetic horizontal and vertical seismograms calculated for Reynolds ABCs by the box and staggered grid methods. The horizontal wave traces show a similarity between the two methods. The vertical wave traces show a similarity only for the direct wave as there are slight differences after the direct wave.

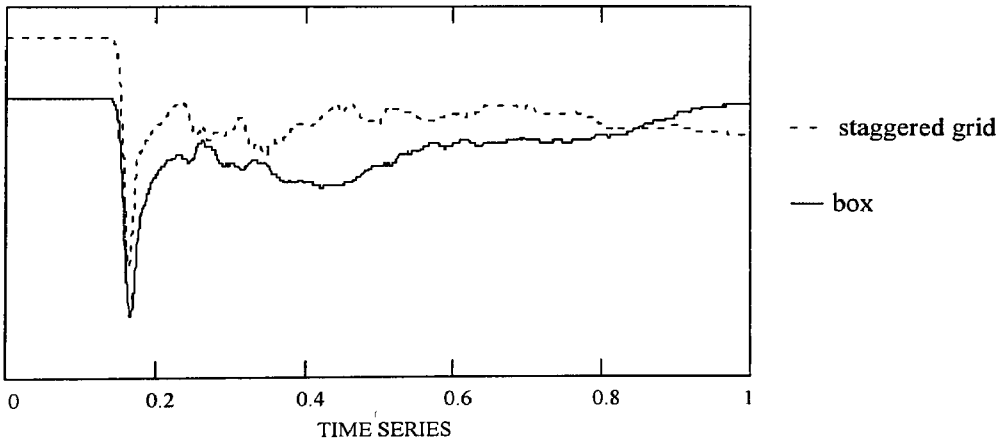

Figure (6.26) Synthetic horizontal displacement seismograms obtained from the box, and staggered grid methods with Reynolds ABCs solutions for multimedia.

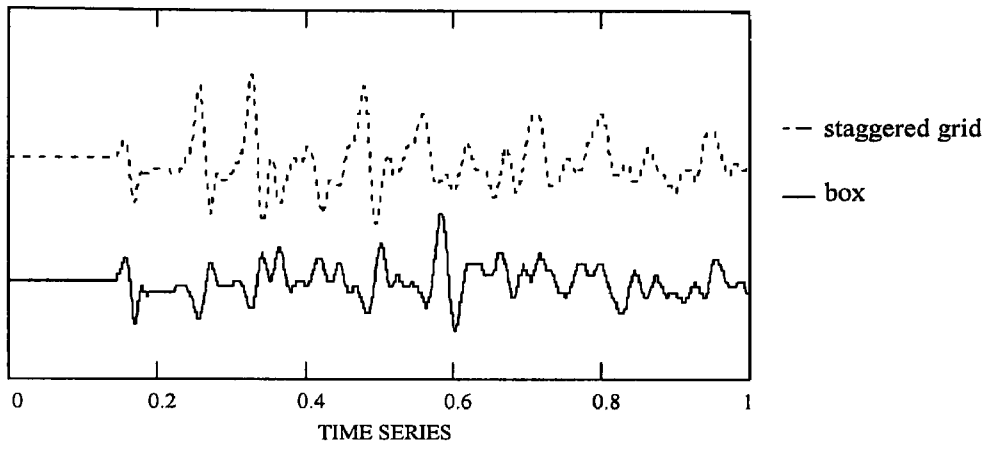

Figure (6.27) Synthetic vertical displacement seismograms obtained from the box, and staggered grid methods with Reynolds ABCs solutions for multimedia.

6.5.5 Conclusion of Cartesian Results

In this chapter we employed two different methods in combination, namely the staggered grid and box methods. We obtained the optimal grid parameters and found our work compared well with that of others. The Clayton-Engquist ABCs were again found not to be generally as good as the Reynolds ABCs. Again multimedia reflected waves were clearly observable.

6.6 Elastic Wave in the Cylindrical Coordinates

In this section we consider a 2-D elastic medium in which the (axially symmetric) equations are given by

$$\rho\frac{\partial^2 u}{\partial t^2} = \frac{\partial P_{rr}}{\partial r} + \frac{P_{rr} - P_{\theta\theta}}{r} + \frac{\partial P_{rz}}{\partial z}$$
$$\rho\frac{\partial^2 w}{\partial t^2} = \frac{\partial P_{rz}}{\partial r} + \frac{P_{rz}}{r} + \frac{\partial P_{zz}}{\partial z} \qquad (6.13)$$

where u and w are the radial and normal components of the displacement, ρ is the density, P_{rr}, P_{rz}, $P_{\theta\theta}$, and P_{zz} are the normal and tangential stresses. Using the usual stress | strain relation equation (6.13) may be written as

$$\frac{\partial^2 u}{\partial t^2} = v_p^2\left[\frac{\partial^2 u}{\partial r^2} + \frac{1}{r}\frac{\partial u}{\partial r} - \frac{u}{r^2} + \frac{\partial^2 w}{\partial r \partial z}\right] + v_s^2\left[\frac{\partial^2 u}{\partial z^2} - \frac{\partial^2 w}{\partial r \partial z}\right]$$
$$\frac{\partial^2 w}{\partial t^2} = v_p^2\left[\frac{\partial^2 w}{\partial z^2} + \frac{1}{r}\frac{\partial u}{\partial z} + \frac{\partial^2 u}{\partial r \partial z}\right] + v_s^2\left[\frac{\partial^2 u}{\partial r^2} - \frac{\partial^2 u}{\partial r \partial z} - \frac{1}{r}\frac{\partial u}{\partial z} + \frac{1}{r}\frac{\partial w}{\partial r}\right] \qquad (6.14)$$

where $$v_p = \sqrt{\frac{\lambda + 2\mu}{\rho}}, \quad v_s = \sqrt{\frac{\mu}{\rho}}$$

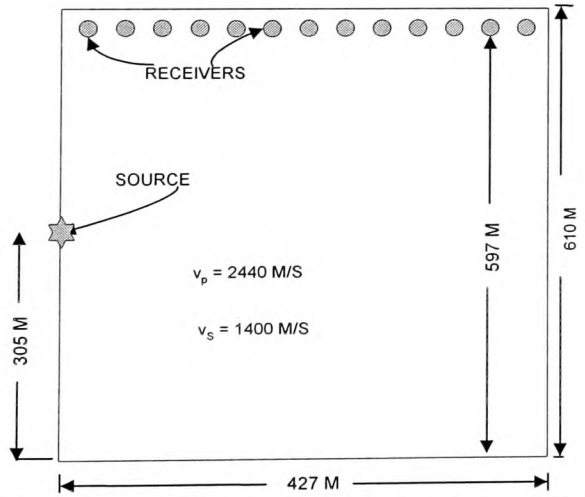

Figure (6.28) Physical model showing receiver one medium geometry used to generate seismograms in the 2-D elastic finite-difference program.

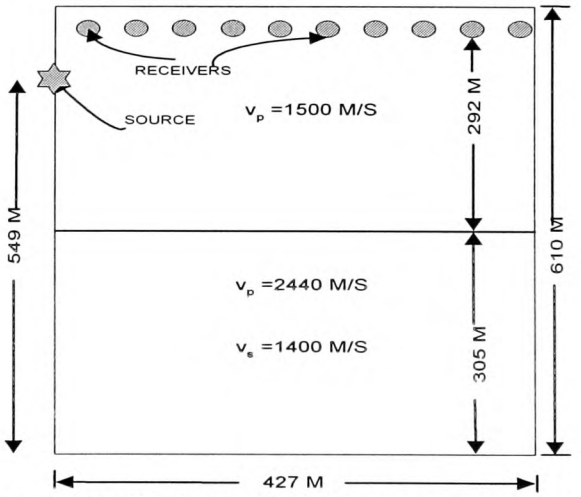

Figure (6.29) Physical model showing receiver two media geometry used to generate seismograms in the 2-D elastic finite-difference program.

Now we present the boundary conditions for 2-D r-z case. The cylindrical coordinates for boundary conditions at the right wall are given by equation (3.31) (see Chapter 3). The boundary conditions at the top and bottom walls are given by the free surface. Figures (6.28) and (6.29) show the cylinder domain in this section. Transparent boundary conditions are

$$\frac{q}{c^2}\frac{\partial^2 u}{\partial t^2} \pm \frac{q+1}{c}\left(\frac{\partial^2 u}{\partial r \partial t} + \frac{1}{2r}\frac{\partial u}{\partial t}\right) + \frac{\partial^2 u}{\partial r^2} + \frac{1}{r}\frac{\partial u}{\partial r} - \frac{u}{4r^2} = 0 \qquad (6.15)$$

where $q = v_p \cdot \Delta t/\Delta r$ and $\Delta r = \Delta z$ at the right boundary.

6.6.1 Discretisation of 2-D Elastic Wave in Cylindrical Coordinates

The equations of motion may be written in finite-difference form by replacing the various derivatives by their centred finite-difference approximations. If we let $r = i.\Delta r$ and $z = j.\Delta z$, where Δr and Δz are incremental lengths along the r and z axes and equal to h, and let $t = n.\Delta t$, where Δt is an increment in time. Equations (6.14) may now be written as follows:

$$\begin{aligned} u_{i,j}^{n+1} &= 2u_{i,j}^{n} - u_{i,j}^{n-1} + \left(\frac{v_p \Delta t}{h}\right)^2 \left[u_{i+1,j}^{n} - 2u_{i,j}^{n} + u_{i-1,j}^{n}\right] - \left(\frac{v_p \Delta t}{h}\right)^2 \frac{1}{i} u_{i,j}^{n} \\ &+ \frac{1}{2\cdot i}\left(\frac{v_p \Delta t}{h}\right)^2 \left[u_{i+1,j}^{n} - u_{i-1,j}^{n}\right] + \left(\frac{v_s \Delta t}{h}\right)^2 \left[u_{i,j+1}^{n} - 2u_{i,j}^{n} + u_{i,j-1}^{n}\right] \\ &+ \frac{\left(v_p^2 - v_s^2\right)\Delta t^2}{4h^2}\left[w_{i+1,j+1}^{n} - w_{i+1,j-1}^{n} - w_{i-1,j+1}^{n} + w_{i-1,j-1}^{n}\right] \end{aligned} \qquad (6.16)$$

Similarly,

$$\begin{aligned} w_{i,j}^{n+1} &= \left(\frac{v_p \Delta t}{h}\right)^2 \left[w_{i,j+1}^{n} - 2w_{i,j}^{n} + w_{i,j-1}^{n}\right] + \frac{1}{2\cdot i}\left(\frac{v_s \Delta t}{h}\right)^2 \left[w_{i+1,j}^{n} - w_{i-1,j}^{n}\right] \\ &+ \frac{1}{2\cdot i}\left(\frac{(v_p^2 - v_s^2)\Delta t}{h^2}\right)\left[u_{i,j+1}^{n} - u_{i,j-1}^{n}\right] + \frac{v_s^2 \Delta t^2}{h^2}\left[w_{i+1,j}^{n} - 2w_{i,j}^{n} + w_{i-1,j}^{n}\right] \\ &+ \frac{\left(v_p^2 - v_s^2\right)\Delta t^2}{4h\Delta t}\left[u_{i+1,j+1}^{n} - u_{i+1,j-1}^{n} - u_{i-1,j+1}^{n} + u_{i-1,j-1}^{n}\right] + 2w_{i,j}^{n} - w_{i,j}^{n-1} \end{aligned} \qquad (6.17)$$

In the above equations the notation $u_{i,j}^{n+1}$ means the value of the radial displacement at the point ($i\Delta r$, $j\Delta z$) for the time $(n+1)\,\Delta t$. Similar meanings apply to other subscripts attached to the displacement components u and w. Following Alterman & Karal [3] along the axis of symmetry (i=0) , equations (6.16) and (6.17) are undefined because of the presence of r in the denominator. Valid equations along the axis of symmetry are easily derived, however, by using independent arguments. Due to continuity of the elastic media, the radial displacement u is zero along the axis of symmetry, hence

$$u_{0,j}^{n+1} = 0. \tag{6.18}$$

The normal displacement w is more complicated. The terms causing trouble in the equation for w are $(1/r)(\partial u/\partial z)$ and $(1/r)(\partial w/\partial r)$. By using L'Hôpital's rule, the term $(1/r)(\partial u/\partial z)$ can be replaced by $\partial^2 u/\partial r\partial z$, and $(1/r)(\partial w/\partial r)$ can be replaced by $\partial^2 w/\partial r^2$. These, in turn, can be replaced by their finite-difference approximations. We have u and w defined for $r\geq 0$ only, However due to their regularity near r = 0, they can be continued to $r<0$ by using the symmetry conditions

$$\begin{aligned} u_{-1,j}^{n} &= -u_{1,j}^{n} \\ w_{-1,j}^{n} &= +w_{1,j}^{n} \end{aligned} \tag{6.19}$$

If we make these new substitutions in the equation of motion for w, then

$$\begin{aligned} w_{0,j}^{n+1} = 2w_{0,j}^{n} - w_{0,j}^{n-1} + \left(\frac{v_p \Delta t}{h}\right)^2 \left[w_{0,j+1}^{n} - 2w_{0,j}^{n} + w_{0,j-1}^{n}\right] \\ + 4\left(\frac{v_s \Delta t}{h}\right)^2 \left[w_{1,j}^{n} - w_{0,j}^{n}\right] + \frac{\left(v_p^2 - v_s^2\right)\Delta t^2}{h^2}\left[u_{1,j+1}^{n} - u_{1,j-1}^{n}\right] \end{aligned} \tag{6.20}$$

If we write Equation (6.15) with the finite-difference formulation we obtain the appropriate boundary equations.

$$u_{M,j}^{n+1} = u_{M,j}^{n} + u_{M-1,j}^{n} - u_{M-1,j}^{n-1} - \frac{v_p^2 \Delta t^2}{h^2}\left[u_{M,j}^{n} - u_{M-1,j}^{n} - u_{M-1,j}^{n-1} + u_{M-2,j}^{n-1}\right]$$
$$-\left(2+\left(\frac{h}{\Delta t v_p}\right)^2 - \frac{1}{2m}\right)\left(\left(\frac{h}{\Delta t v_p}\right)^2 \frac{1}{2m} u_{M,j}^{n} - u_{M-1,j}^{n-1} - u_{M-1,j}^{n} - \left(\frac{h}{\Delta t v_p}\right)^2 u_{M,j}^{n-1}\right) \quad (6.21)$$

Similarly,

$$w_{M,j}^{n+1} = w_{M,j}^{n} + w_{M-1,j}^{n} - w_{M-1,j}^{n-1} - \frac{v_p^2 \Delta t^2}{h^2}\left[w_{M,j}^{n} - w_{M-1,j}^{n} - w_{M-1,j}^{n-1} + w_{M-2,j}^{n-1}\right]$$
$$-\left(2+\left(\frac{h}{\Delta t v_p}\right)^2 - \frac{1}{2m}\right)\left(\left(\frac{h}{\Delta t v_p}\right)^2 \frac{1}{2m} w_{M,j}^{n} - w_{M-1,j}^{n-1} - w_{M-1,j}^{n} - \left(\frac{h}{\Delta t v_p}\right)^2 w_{M,j}^{n-1}\right) \quad (6.22)$$

where M is the right boundary point.

Equations (6.16) , (6.18) , (6.20) , (6.21) and (6.22) are the basic formulae used in our computations.

Alterman & Karal [3] carried out a standard stability study and find the approximate stability criterion to be given by

$$\left(\frac{v_p \Delta t}{h}\right) < \left[1+\left(v_s/v_p\right)^2\right]^{-1/2} \quad (6.23)$$

The finite difference equations (6.16)-(6.18) and (6.20) cannot be applied at the free surface z = 0 because the equations involve indefinite quantities. In order to calculate the displacements on these special surfaces, it is necessary to use the boundary conditions that must be satisfied there. Consider first the case of the free surface. The boundary conditions that must hold on these surface are given by $P_{zz} = 0$ and $P_{rz} = 0$ as before. The free surface boundary conditions are then found to be

$$u_{i,-1}^{n} = u_{i,1}^{n} + \left(\frac{\Delta z}{\Delta r}\right)\left(w_{i+1,0}^{n} - w_{i-1,0}^{n}\right) \quad (6.24)$$

and

$$w^n_{i,-1} = w^n_{i,1} + \left(\frac{\Delta z}{\Delta r}\right)^2 \left[1 - 2\left(\frac{v_s}{v_p}\right)^2\right]\left(u^n_{i+1,0} - u^n_{i-1,0}\right) + 2\left(\frac{\Delta z}{\Delta r}\right)\left[1 - 2\left(\frac{v_s}{v_p}\right)^2\right]\frac{1}{i}u^n_{i,0} \qquad (6.25)$$

Note that the values of u and w given on the left hand side of equations (6.24)-(6.25) are for j = -1, and therefore correspond to a fictitious line one grid point above and below the actual physical surface at j = 0 (see Figure (6.30)).

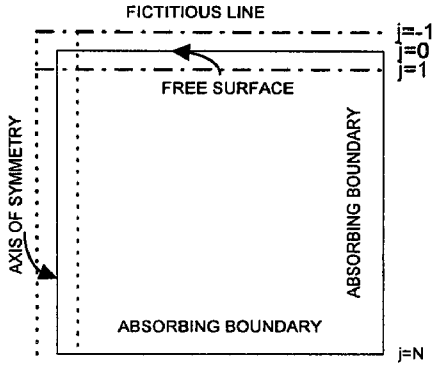

Figure (6.30) Grid arrangement at the surface z = 0 showing the fictitious line and free boundary.

A complication arises on the axis of symmetry (i =0) and special treatment is required. Due to continuity and cylindrical symmetry,

$$u^n_{0,-1} = 0 \qquad (6.28)$$

and

$$w^n_{0,-1} = w^n_{0,1} + 4\left(\frac{\Delta z}{\Delta r}\right)\left[1 - 2\left(\frac{v_s}{v_p}\right)^2\right]u^n_{1,0}. \qquad (6.29)$$

Equations (6.24)-(6.29) make it possible at any given time level to compute values of u and w on the fictitious line i = -1. Knowing values on these line, it is then possible to use the equations of motion (6.16)-(6.18) and (6.20) up to and on the actual physical surface i = 0. For staggered grid we use $P_{rz} = P_{zz} = 0$ directly. Free surface conditions often require careful consideration in FDM because of concerns related to numerical

stability and accuracy of the computed response (Alterman and Rotenberg [**5**]; Ilan et al. [**36**]; Bayliss et al. [**9**]; Vidale and Clayton [**78**]; Kosloff et al. [**38**]; Zahradnik et al. [**90**]).

6.6.2 Accuracy of the Numerical Solution in 2-D Cylindrical Coordinates

In this section we consider the convergence of the solution by comparing calculations for various grid widths denoted by h. The solutions are found to be consistent with grid ranging from 14x20x1000 to 140x200x1000. We will compare two methods for the models. Figure (6.31) shows the results for the box and staggered grid methods values evaluated near the boundary (r = 210 m, z = 12 m, and t = 0.5 s) that is the u horizontal displacement. Figure (6.32) shows the results for same methods with the w displacement.

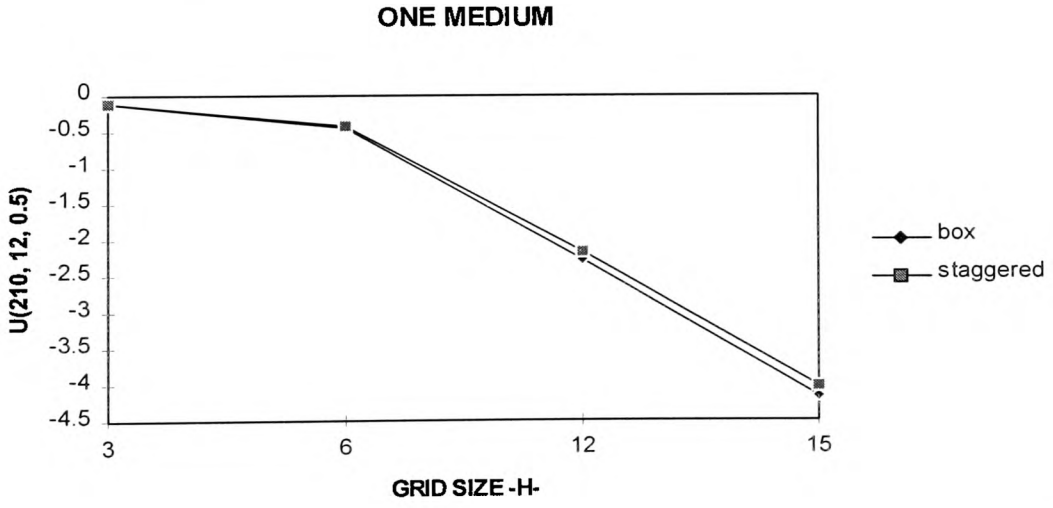

Figure (6.31) Convergence criterion with horizontal displacement for the box and staggered grid methods for single medium.

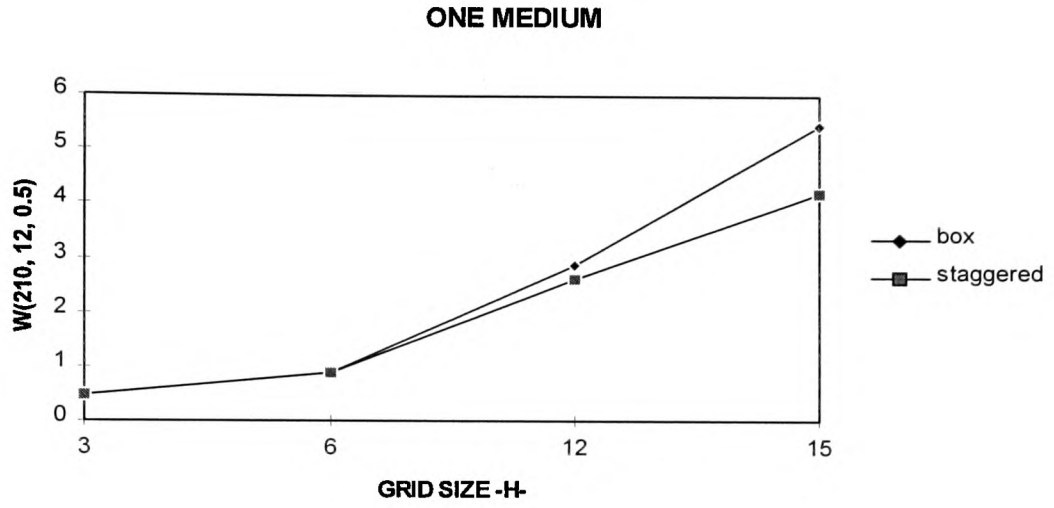

Figure (6.32) Convergence criterion with vertical displacement for the box and staggered grid methods for single medium.

Figure (6.33) and (6.34) show the results for two media by the box and staggered grid methods. As seen in all figures while h decreases the displacement exhibits convergence at h= 3 m.

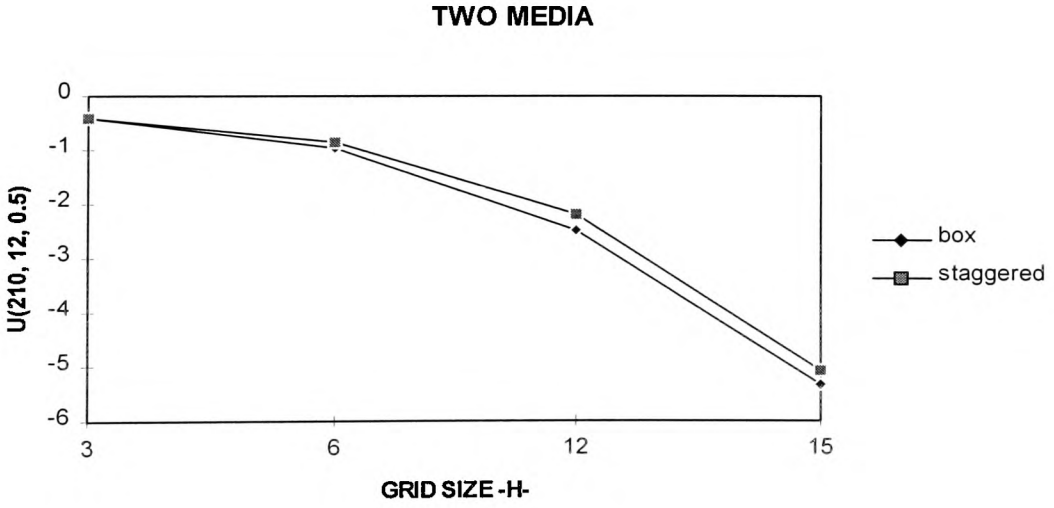

Figure (6.33) Convergence criterion with horizontal displacement for the box and staggered grid methods for two media.

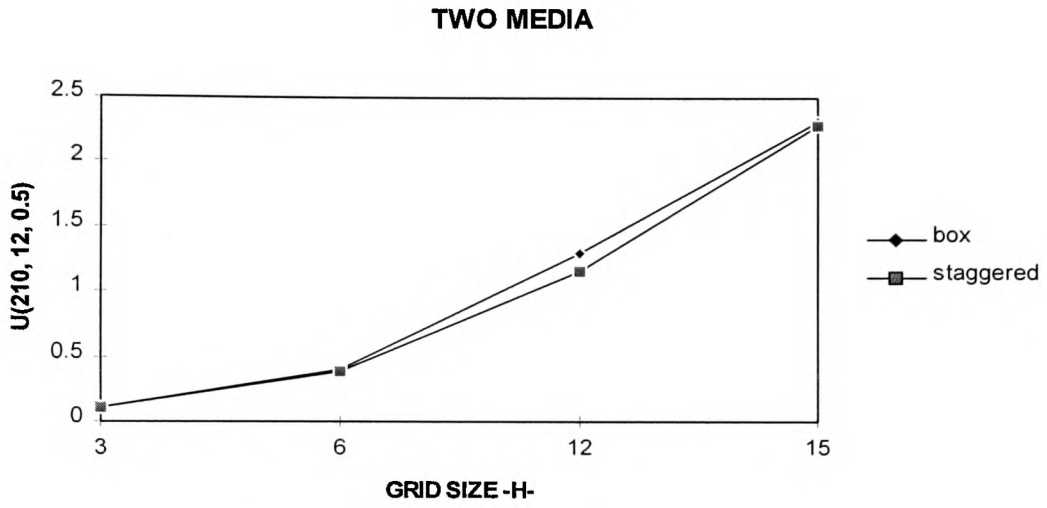

Figure (6.34) Convergence criterion with vertical displacement for the box and staggered grid methods for two media.

The number of grid points per wavelength at the upper half-power frequency of the source should be approximately ten or more (Kelly [**37**], Alford [**2**], Virieux [**82**] and Yoon & McMechan [**87**]) in order to satisfactorily limit the grid dispersion. Grid dispersion is minimised when the time increment is near the stability limit (Alford [**2**]).

6.6.3 Results in Cylindrical Coordinates

In this section we will consider two models: single medium and two media models where the physical properties v_p, and v_s, are 2440 m/s, and 1400 m/s for shale and v_p, and v_s are 3400 m/s, and 1730 m/s for limestone (from Yoon & McMechan [**87**]). The source was located at a depth of 200 m and the receivers were located in a horizontal row 12 m below the free surface which are located at twenty metre distance intervals. The geometry of the models are shown in Figures (6.28) and (6.29). In all programs the time shift, t_s, is 0.13 s and the pulse width parameter, α, is 657 which demonstrate results to best effect. The synthetic seismograms show the time runs along

the horizontal axis and distance along the vertical axis. The box, and staggered grid methods are employed with the Reynolds ABCs. The horizontal (left) and vertical (right) synthetic seismograms are obtained with the Reynolds ABCs using the box method which are shown in Figure (6.35). In this case synthetic seismograms are obtain by using the staggered grid method in Figure (6.36).

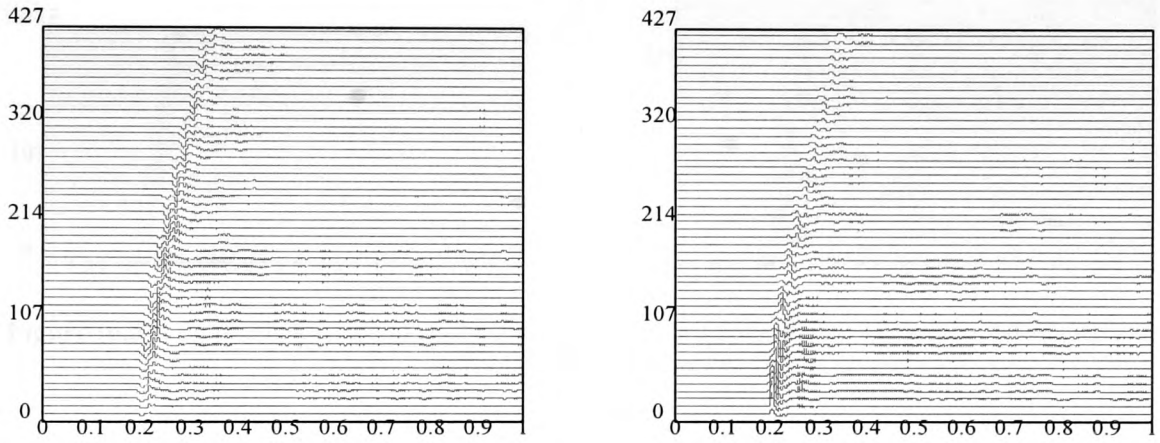

Figure (6.35) Synthetic horizontal and vertical seismograms from the elastic box method program with Reynolds ABCs for one medium.

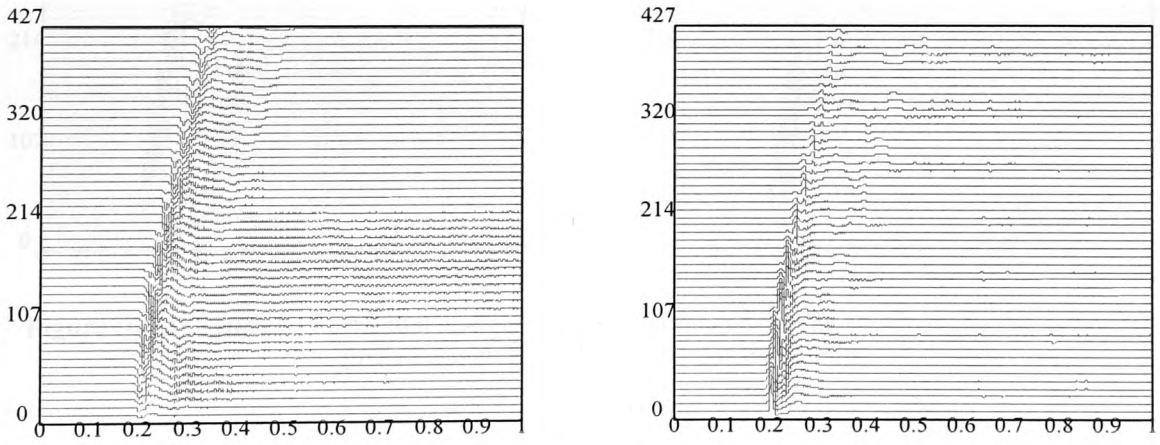

Figure (6.36) Synthetic horizontal and vertical seismograms from the elastic staggered grid method program with Reynolds ABCs for one medium.

Figure (6.37) shows the results box method with the horizontal and vertical seismograms for the two media. The staggered grid method results are shown in Figure (6.38) for the two media.

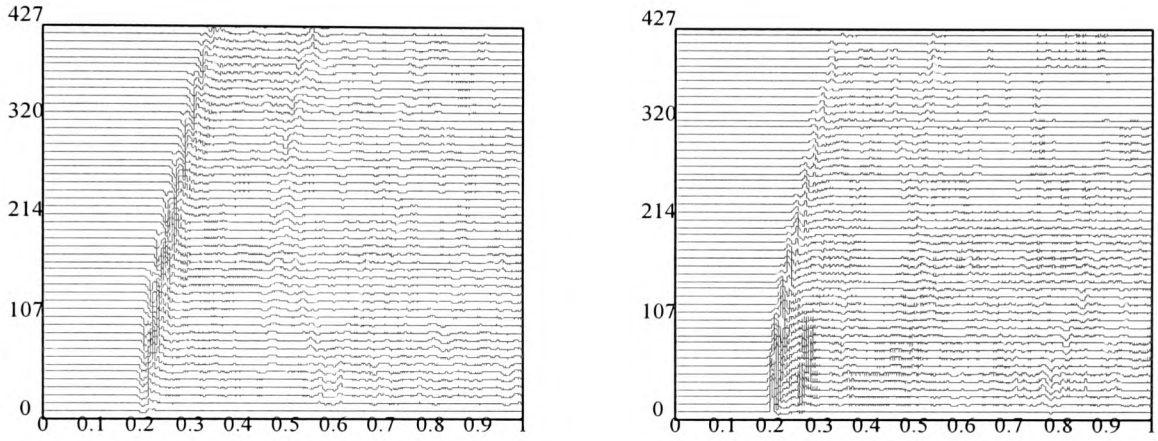

Figure (6.37) Synthetic horizontal and vertical seismograms from the elastic box method program with Reynolds ABCs for two media.

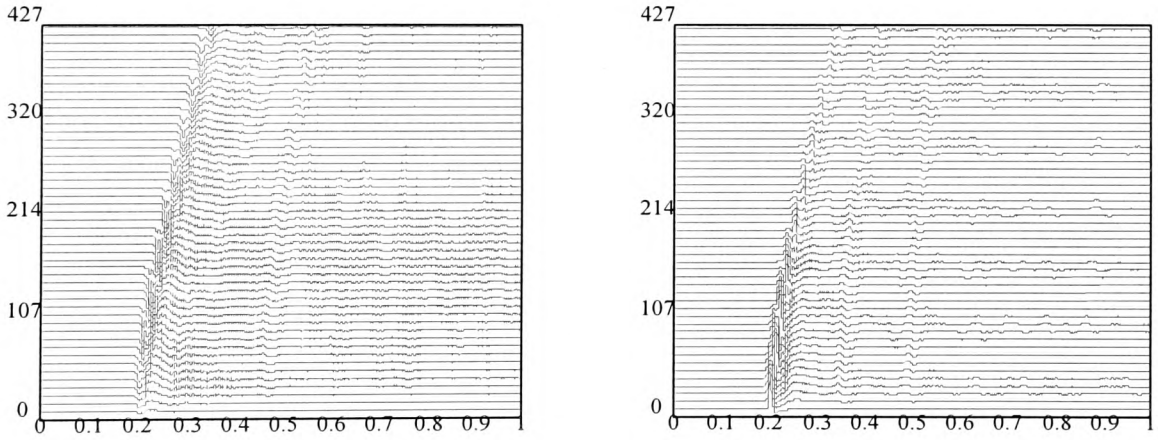

Figure (6.38) Synthetic horizontal and vertical seismograms from the elastic staggered grid method program with Reynolds ABCs for two media.

6.6.4 Comparison of Numerical Results

Computer programs have been implemented for the box and staggered grid methods. Both synthetic seismic wave traces are chosen at the point (210m, 12m). Time runs along the horizontal axis, amplitude of the ground motion runs along the vertical

axis. The synthetic horizontal and vertical seismic wave traces obtained using the box and staggered grid methods for the single medium shown in Figures (6.39) and (6.40), show good overall agreement between the two methods for direct wave arrival. Both methods also show unwanted oscillations. Figures (6.41) and (6.42) shows a comparison between the synthetic horizontal and vertical seismic wave traces employing the box and staggered grid methods for two media. There is good agreement between both methods as can be seen on the direct wave, but not for the reflected wave. The staggered grid method wave trace is much clearer than the box method wave trace. For display purposes we have purposely displaced the wave traces on the figures.

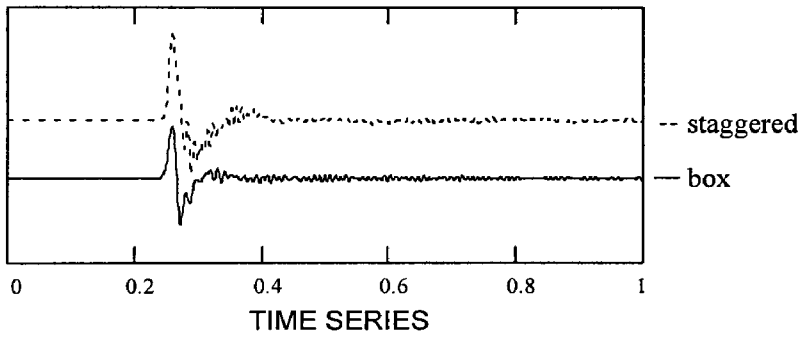

Figure(6.39) Synthetic horizontal displacement wave traces obtained from the box and staggered grid methods with Reynolds ABCs for single medium.

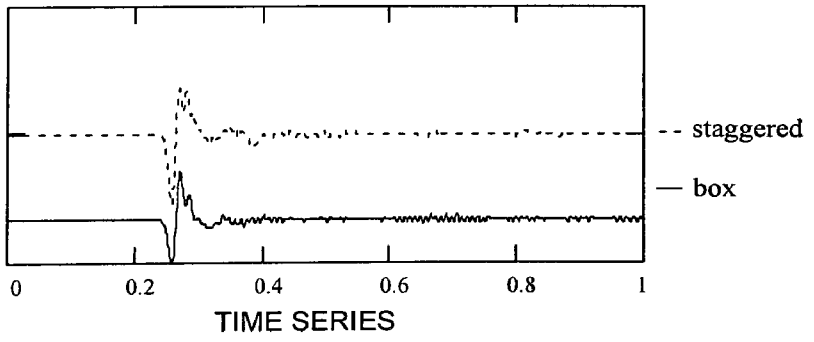

Figure(6.40) Synthetic vertical displacement wave traces obtained from the box and staggered grid methods with Reynolds ABCs for single medium.

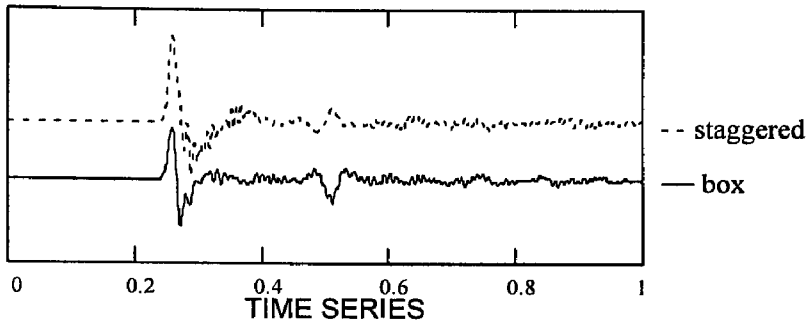

Figure (6.41) Synthetic horizontal displacement wave traces obtained from the box and staggered grid methods with Reynolds ABCs for two media.

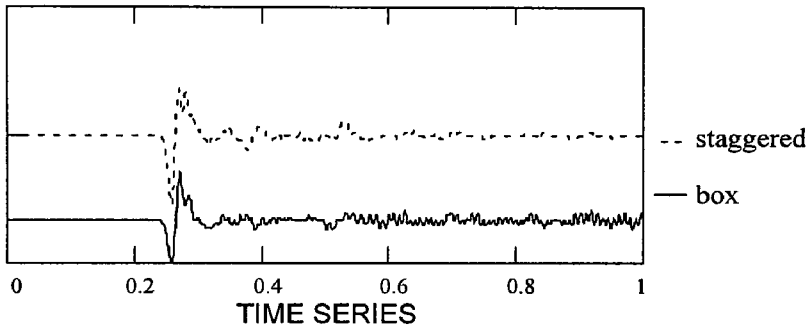

Figure (6.42) Synthetic vertical displacement wave traces obtained from the box and staggered grid methods with Reynolds ABCs for two media.

6.6.5 Conclusion of cylindrical results

We solved numerically the 2-D elastic wave propagation problem in cylindrical coordinates, based on optimal grid parameters. The Reynolds ABCs again gave good results and interface waves were visible, but much weaker than for Cartesian results. We believe the results in cylindrical coordinates to be new.

We now have confidence in the numerical wave modelling approaches adopted here for later wave simulation purposes. In the next chapter, we will present the 3-D wave propagation problem which is an extension of the work presented in this chapter.

CHAPTER 7

3-D ACOUSTIC & ELASTIC WAVE MODELLING

7.1 Introduction

In this chapter, having gained confidence in our 2-D modelling exercises we move on to the more realistic case of 3-D geometries. We shall adopt the approaches of chapters 5 and 6 in our examination of 3-D wave propagation. Again the staggered grid and box approach is believed to be a new approach. Also again the Reynolds and Clayton-Engquist ABCs for 3-D situations will be examined to find the "best" ABCs. Where possible we shall compare our work with that of others.

The 3-D numerical FDM solutions have been obtained for the acoustic (Chen & McMechan [**16**], Villarreal et al. [**80**]), and elastic problems (Chang & McMechan [**14**], Yoon & McMechan [**87**], Graves & Clayton [**29**], Graves [**30**]). There exist a number of numerical representations of 3-D seismic sources (Archuleta et al. [**6**], Quin et al. [**58**], and Miyatake [**50**], Vidale [**79**]). There are also a number of numerical 3-D wave propagation solutions (Reshef et al. [**63**], Mora [**51**], Yoon & McMechan [**88,89**], Igel et al. [**34,35**], Chen & McMechan [**16**], Dang & McMechan [**20**]). The 3-D elastic wave equation can be formulated into second-order hyperbolic equations by using displacement and stress, and are discretised on a staggered grid. We use the FDM for

acoustic and elastic models with the staggered grid method employed in the elastic case. Both these methods are used in Cartesian coordinates.

7.2 3-D Acoustic and Elastic Wave Equation

In this chapter 3-D acoustic and elastic wave equations are considered in Cartesian coordinates systems. Firstly, the acoustic wave equation is given in Cartesian coordinates as

$$\frac{1}{v_p^2}\frac{\partial^2 u}{\partial t^2}=\frac{\partial^2 u}{\partial x^2}+\frac{\partial^2 u}{\partial y^2}+\frac{\partial^2 u}{\partial z^2} \tag{7.1}$$

where u is the displacement, v_p is the velocity, x and y are the horizontal coordinates, z is the vertical coordinates, t is time. Secondly, the elastic wave equations are given in Cartesian coordinates as

$$\begin{aligned}
\rho\frac{\partial^2 u}{\partial t^2}&=\frac{\partial P_{11}}{\partial x}+\frac{\partial P_{12}}{\partial y}+\frac{\partial P_{13}}{\partial z}\\
\rho\frac{\partial^2 v}{\partial t^2}&=\frac{\partial P_{12}}{\partial x}+\frac{\partial P_{22}}{\partial y}+\frac{\partial P_{23}}{\partial z}\\
\rho\frac{\partial^2 w}{\partial t^2}&=\frac{\partial P_{13}}{\partial x}+\frac{\partial P_{23}}{\partial y}+\frac{\partial P_{33}}{\partial z}
\end{aligned} \tag{7.2}$$

In the above equations (7.2) when we substitute for the stresses in terms of strains, the equations of motion in terms of displacement are:

$$\begin{aligned}
\rho\frac{\partial^2 u}{\partial t^2}&=(\lambda+2\mu)\frac{\partial^2 u}{\partial x^2}+\mu\left(\frac{\partial^2 u}{\partial y^2}+\frac{\partial^2 u}{\partial z^2}\right)+(\lambda+\mu)\left(\frac{\partial^2 v}{\partial x\partial y}+\frac{\partial^2 w}{\partial x\partial z}\right)\\
\rho\frac{\partial^2 v}{\partial t^2}&=(\lambda+2\mu)\frac{\partial^2 v}{\partial y^2}+\mu\left(\frac{\partial^2 v}{\partial x^2}+\frac{\partial^2 v}{\partial z^2}\right)+(\lambda+\mu)\left(\frac{\partial^2 u}{\partial x\partial y}+\frac{\partial^2 w}{\partial y\partial z}\right)\\
\rho\frac{\partial^2 w}{\partial t^2}&=(\lambda+2\mu)\frac{\partial^2 w}{\partial z^2}+\mu\left(\frac{\partial^2 w}{\partial x^2}+\frac{\partial^2 w}{\partial y^2}\right)+(\lambda+\mu)\left(\frac{\partial^2 u}{\partial x\partial z}+\frac{\partial^2 v}{\partial y\partial z}\right)
\end{aligned} \tag{7.3}$$

where λ and μ are the Lame parameters, u and v are displacements in the two horizontal (x and y) directions and w is displacement in the vertical (z) direction respectively; ρ is density, and t is time. The compressional wave velocity v_p and the shear wave velocity v_s are

$$v_p = \sqrt{(\lambda+2\mu)/\rho}$$

$$v_s = \sqrt{\mu/\rho}\ .$$

The free surface conditions (Grant & West [**28**] and Chang & McMechan [**14**]) are that the normal stress on z = constant is zero namely:

$$(v_p^2 - v_s^2)\left(\frac{\partial u}{\partial x}+\frac{\partial v}{\partial y}\right)+v_p^2\frac{\partial w}{\partial z}=0 \qquad (7.4)$$

where v_p and v_s are the compressional (P) and shear (S) velocities, respectively, and the tangential stresses are zero: i.e.

$$\frac{\partial v}{\partial z}+\frac{\partial w}{\partial y}=0$$

and

$$\frac{\partial u}{\partial z}+\frac{\partial w}{\partial x}=0 \qquad (7.5)$$

Now we present the remaining boundary conditions used in 3-D simulations. The Cartesian coordinates ABC boundary conditions at the right, left and front, back walls are given by

$$\begin{aligned}\frac{p}{v_p^2}\frac{\partial^2 u}{\partial t^2}\pm\frac{p+1}{v_p}\frac{\partial^2 u}{\partial t\partial x}+\frac{\partial^2 u}{\partial x^2}=0\\ \frac{p}{v_p^2}\frac{\partial^2 u}{\partial t^2}\pm\frac{p+1}{v_p}\frac{\partial^2 u}{\partial t\partial y}+\frac{\partial^2 u}{\partial y^2}=0\end{aligned} \qquad (7.6)$$

The bottom wall ABC boundary condition is given by

$$\frac{p}{v_p^2}\frac{\partial^2 u}{\partial t^2} \pm \frac{p+1}{v_p}\frac{\partial^2 u}{\partial t \partial z} + \frac{\partial^2 u}{\partial z^2} = 0 \tag{7.7}$$

7.3 Discretisation of 3-D Acoustic and Elastic Wave Equations

The 3-D equation of motion can be written in the FDM form by replacing the various derivatives by their centred finite-difference approximations. The FDM formulation corresponding to equations (7.1) has been derived by Wild [**86**], for equation (7.1) and is given as follows:

$$\begin{aligned} u_{i,j,k}^{n+1} = q^2\{(u_{i+1,j,k}^n - 2u_{i,j,k}^n + u_{i-1,j,k}^n) + (u_{i,j+1,k}^n - 2u_{i,j,k}^n + u_{i,j-1,k}^n) \\ + (u_{i,j,k+1}^n - 2u_{i,j,k}^n + u_{i,j,k-1}^n)\} + 2u_{i,j,k}^n - u_{i,j,k}^{n-1} \end{aligned} \tag{7.8}$$

The "parsimonious" staggered grid algorithm is constructed in two stages. Firstly, equation (7.2) is discretised, to give the equation,

$$\begin{aligned} \frac{\rho}{\Delta t^2}\left(u_i(t+\Delta t) + u_i(t-\Delta t) - u_i(t)\right) = \frac{P_{ii}(x_i + \Delta x_i) - P_{ii}(x_i - \Delta x_i)}{2\Delta x_i} + \\ \frac{P_{ij}(x_j + \Delta x_j) - P_{ij}(x_j - \Delta x_j)}{2\Delta x_j} + \frac{P_{ik}(x_k + \Delta x_k) - P_{ik}(x_k - \Delta x_k)}{2\Delta x_k} \end{aligned} \tag{7.9}$$

with no implied summation, and arguments of terms are given only where they differ from x, y, z, t. Secondly, the P terms in this equation are expressed in terms of the equations,

$$P_{ii} = (\lambda + 2\mu)\frac{\partial u_i}{\partial x_i} + \lambda\frac{\partial u_j}{\partial x_j} + \lambda\frac{\partial u_k}{\partial x_k}, \tag{7.10}$$

and,

$$P_{ij} = \mu\left(\frac{\partial u_i}{\partial x_j} + \frac{\partial u_j}{\partial x_i}\right) \tag{7.11}$$

where i = 1, 2, 3 indicates displacement and stresses component. The displacements component (u_1, u_2, u_3) are equal to (u, v, w). The unit cell for the 3-D implementation of this "parsimonious" staggered grid scheme is shown in Figure (7.1).

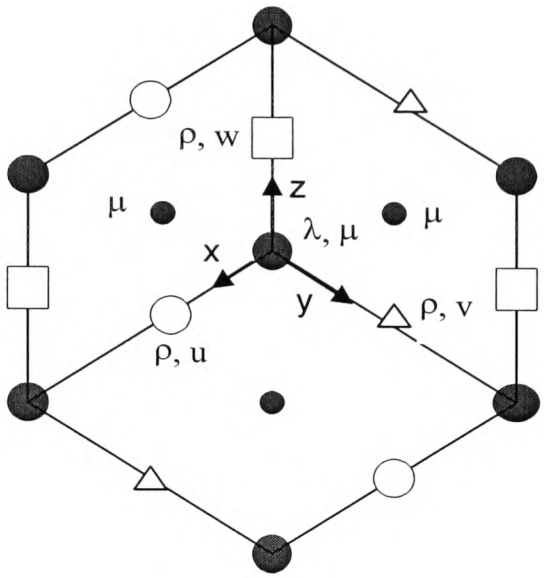

Figure (7.1) Spatial repeat cell for 3-D Parsimonious staggered grid.

The FDM formulation corresponding to equations (7.3) has been derived by Wild **[86]**, for equation (7.3) and are given as follows:

$$\begin{aligned} u_{i,j,k}^{n+1} &= q_1^2(u_{i+1,j,k}^n - 2u_{i,j,k}^n + u_{i-1,j,k}^n) + q_2^2\{(u_{i,j+1,k}^n - 2u_{i,j,k}^n + u_{i,j-1,k}^n) \\ &+ (u_{i,j,k+1}^n - 2u_{i,j,k}^n + u_{i,j,k-1}^n)\} + q_3^2\{(v_{i+1,j+1,k}^n - v_{i+1,j-1,k}^n - v_{i-1,j+1,k}^n \\ &+ v_{i-1,j-1,k}^n) + (w_{i+1,j+1,k}^n - w_{i+1,j-1,k}^n - w_{i-1,j+1,k}^n + w_{i-1,j-1,k}^n)\} + 2u_{i,j,k}^n - u_{i,j,k}^{n-1} \end{aligned}$$

$$\begin{aligned} v_{i,j,k}^{n+1} &= q_1^2(v_{i,j+1,k}^n - 2v_{i,j,k}^n + v_{i,j-1,k}^n) + q_2^2\{(v_{i+1,j,k}^n - 2v_{i,j,k}^n + v_{i-1,j,k}^n) \\ &+ (v_{i,j,k+1}^n - 2v_{i,j,k}^n + v_{i,j,k-1}^n)\} + q_3^2\{(u_{i+1,j+1,k}^n - u_{i+1,j-1,k}^n - u_{i-1,j+1,k}^n \\ &+ u_{i-1,j-1,k}^n) + (w_{i,j+1,k+1}^n - w_{i,j-1,k+1}^n - w_{i,j+1,k-1}^n + w_{i,j-1,k-1}^n)\} + 2v_{i,j,k}^n - v_{i,j,k}^{n-1} \end{aligned} \tag{7.12}$$

$$\begin{aligned} w_{i,j,k}^{n+1} &= q_1^2(w_{i,j,k+1}^n - 2w_{i,j,k}^n + w_{i,j,k-1}^n) + q_2^2\{(w_{i+1,j,k}^n - 2w_{i,j,k}^n + w_{i-1,j,k}^n) \\ &+ (w_{i,j+1,k}^n - 2w_{i,j,k}^n + w_{i,j-1,k}^n)\} + q_3^2\{(u_{i+1,j,k+1}^n - u_{i+1,j,k-1}^n - u_{i-1,j,k+1}^n \\ &+ u_{i-1,j,k-1}^n) + (v_{i,j+1,k+1}^n - v_{i,j-1,k+1}^n - v_{i,j+1,k-1}^n + v_{i,j-1,k-1}^n)\} + 2w_{i,j,k}^n - w_{i,j,k}^{n-1} \end{aligned}$$

The notation $u_{i,j,k}^{n+1}, v_{i,j,k}^{n+1}$ show the horizontal displacements, and $w_{i,j,k}^{n+1}$ shows the vertical displacement at the point (ih, jh, kh) for time $(n+1)\Delta t$, h is the grid interval in all the x, y and z directions, and i, j, k and n are defined to be (grid line) integers. Finally q_1, q_2, and q_3 are a parameters given by $q_1 = v_p\Delta t/h$, $q_2 = v_s\Delta t/h$, and $q_3 = (v_p - v_s)\Delta t/h$. Equations (7.12) form an simple explicit system since they enable one to compute the displacement u, v and w at each spatial grid point at time step (n+1) exclusively in terms of the motion at the two previous time steps n and (n-1).

The numerical stability conditions are ensured by taking time steps $\Delta t < h/(v_p 3^{1/2})$ (Yoon & McMechan [**87**]) and v_p is the highest compressional wave velocity in the model.

7.4 Accuracy of the FDM Calculation in 3-D Acoustic Case

In this section we consider the convergence of the solution by comparing calculations for various equal grid widths denoted by h. We employ the 3-D acoustic wave propagation compare Reynolds ABCs and Clayton-Engquist ABCs results. We have produced results for two second of simulation time for a numerical solution. The solutions are found to be consistent with grids ranging (M, N, K) from (20x20x20 to 100x100x100), and we display results for 100x100x100 and for 750 time steps. All figures show results for the standard FDM seismic wave u displacements evaluated near the top boundary (x = 1000 m, y = 1000 m, z = 40 m, and t = 0.5 s). Figure (7.2) shows results for the standard FDM with the Dirichlet boundary conditions, for one medium, two media and multimedia. Figure (7.3) shows results for the acoustic seismic wave u displacements at the same point for the standard FDM using the Reynolds ABCs. The

last Figure (7.4) shows results for the Clayton-Engquist ABCs. As seen in all figures show that while h decreases the displacement exhibits convergence near h=20m.

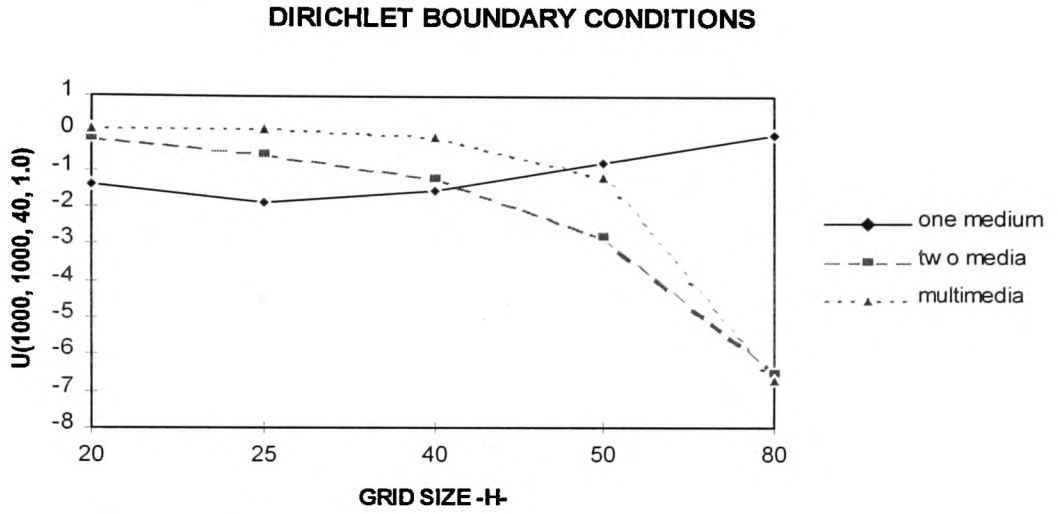

Figure (7.2) Convergence criterion for the standard FDM solution using the Dirichlet boundary conditions.

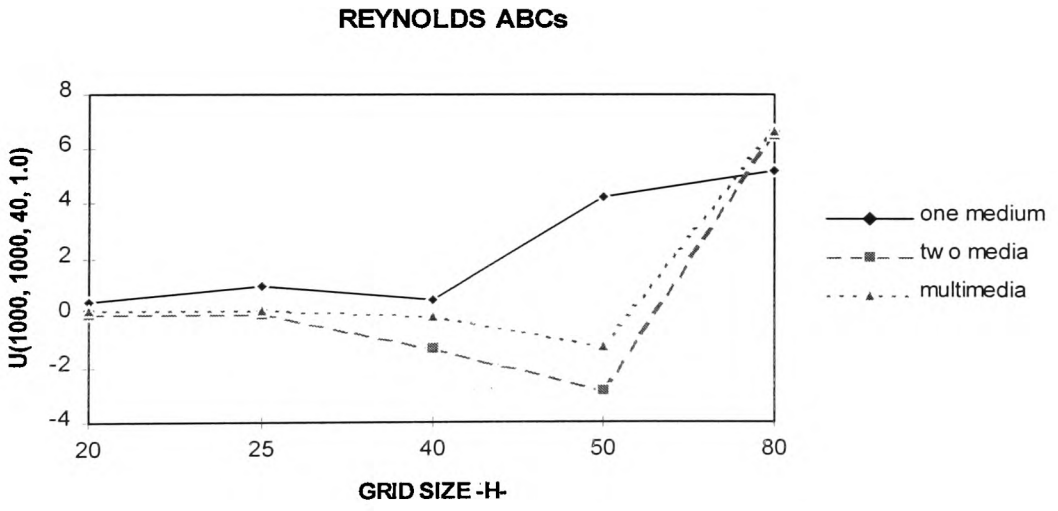

Figure (7.3) Convergence criterion for the standard FDM solution using the Reynolds ABCs.

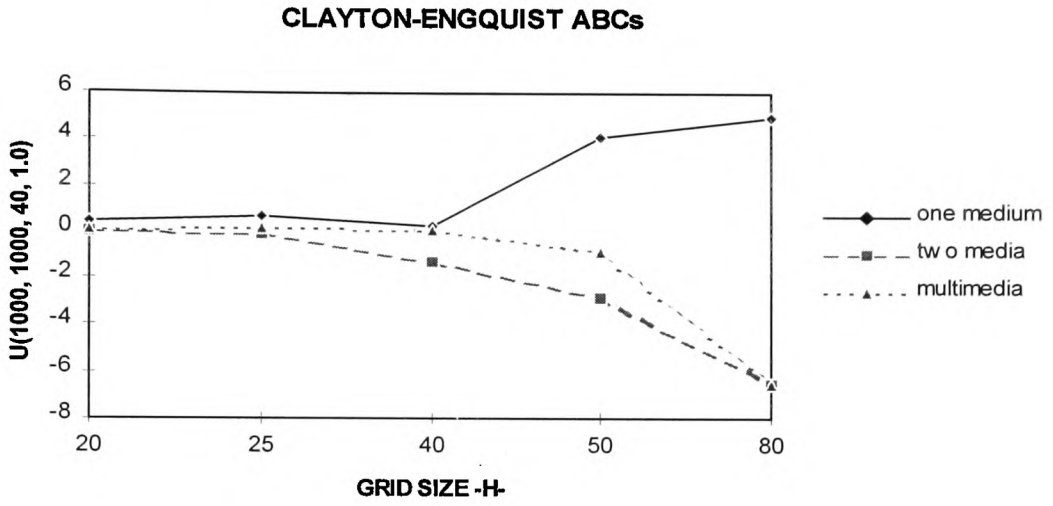

Figure (7.4) Convergence criterion for the standard FDM solution using Clayton-Engquist ABCs.

7.4.1 Results in 3-D Acoustic Case

The 3-D modelling algorithm described above enables synthesis of the seismic response of a realistic media. We consider single medium, two media and multimedia models where the physical properties are given in Table (7.1) (from Yoon & McMechan [87]).

Table (7.1). Properties of media used in 3-D Model.

Layers	λ(Pa)	μ(Pa)	ρ(kg/m^3)	v_p(m/s)	v_s(m/s)
sea-water	2.32E9	0.0	1030	1500	0.0
mud	3.71E9	0.0	1450	1600	0.0
shale	4.99E9	4.80E9	2450	2440	1400
oil	1.37E9	0.0	890	1240	0.0
sandstone	11.35E9	2.61E9	2160	2770	1100
limestone	13.38E9	7.18E9	2400	3400	1730
basalt	3.50E9	23.85E9	3200	4000	2730
granite	34.30E9	25.20E9	2800	5500	3000

The one medium layer contains a shale, and the two media contains sea-water and shale whilst the multimedia contains sea-water, shale, limestone, oil and granite. The Gaussian source was located at a depth of 500 m and the receivers were located in a horizontal row 40 m below the free surface which are located at hundred meter distance intervals. The geometry of models are shown in Figures (7.5), (7.6),and (7.7).

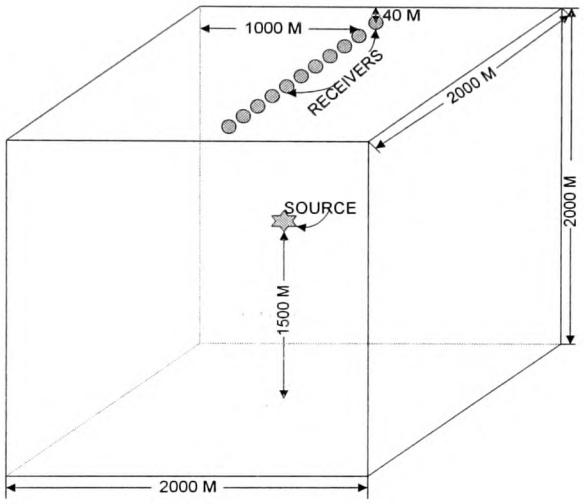

Figure (7.5) Physical model showing receiver one medium geometry used to generate seismograms in the 3-D FDM program.

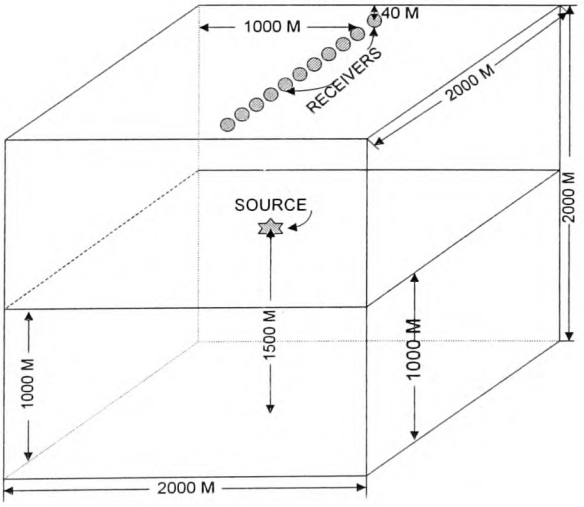

Figure(7.6) Physical model showing receiver two media geometry used to generate seismograms in the 3-D FDM program.

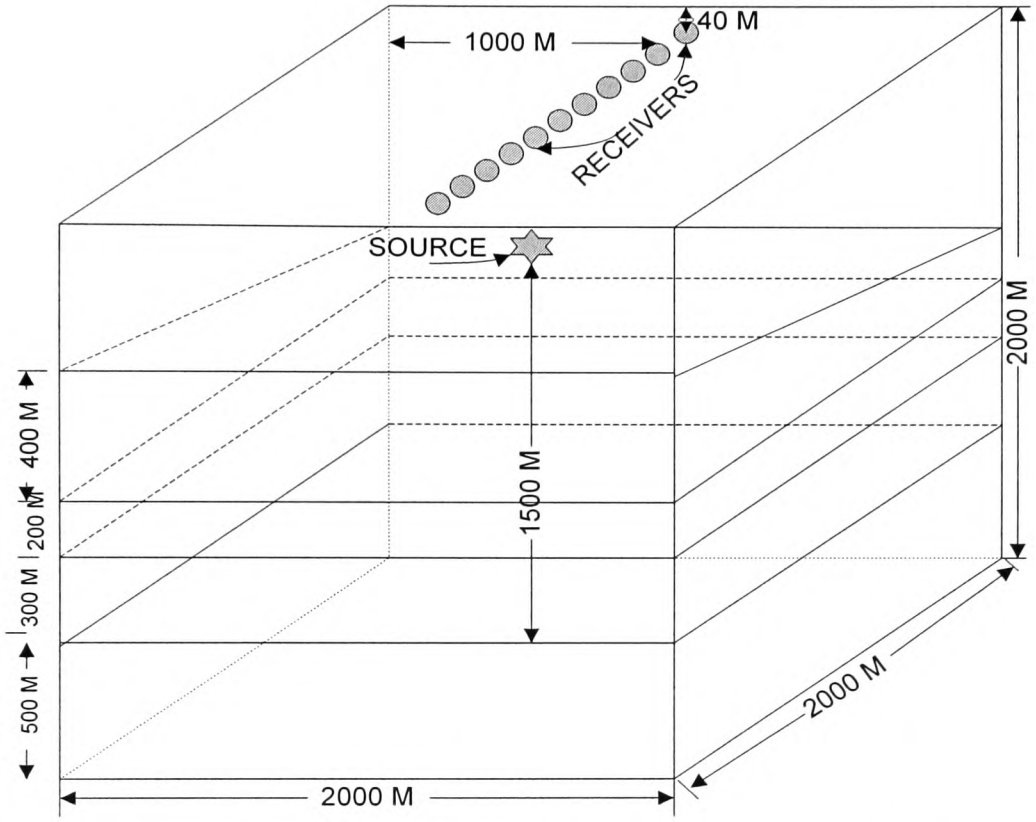

Figure (7.7) Physical model showing receiver multimedia geometry used to generate seismograms in the 3-D FDM program.

In all programs the time shift, t_s, is 0.13 s and the pulse width parameter , α, is 1000. The size of the model grid is 100x100x100 in the x, y, and z-axis directions, respectively, and the grid increment is 20 m. We normally produced results for a two second period of simulation time for a numerical solution. The simple explicit FDM is employed with the Dirichlet boundary conditions and Reynolds and Clayton-Engquist ABCs. The FDM results with the Dirichlet boundary conditions are shown in Figure (7.8) and results contain large reflections from the all boundaries. The synthetic seismogram obtain by using the FDM with the Reynolds ABCs are shown in Figure (7.9). Time runs along the horizontal axis and distance from the source along the

vertical axis. Figure (7.10) shows the result for the Clayton-Engquist ABCs for one medium.

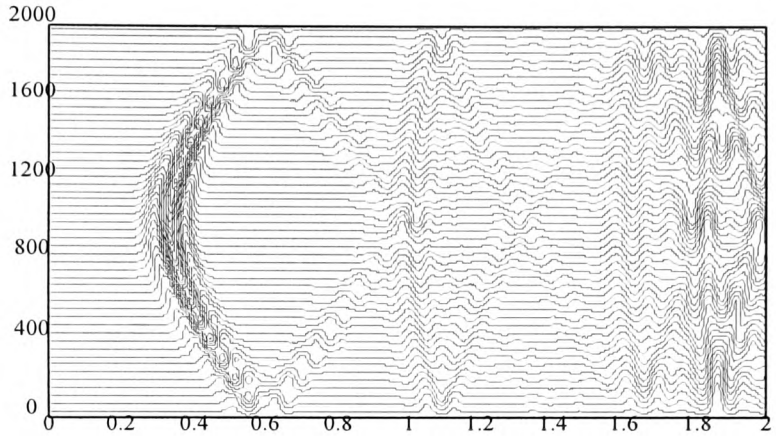

Figure (7.8) Synthetic seismograms from the FDM program with the Dirichlet boundary conditions.

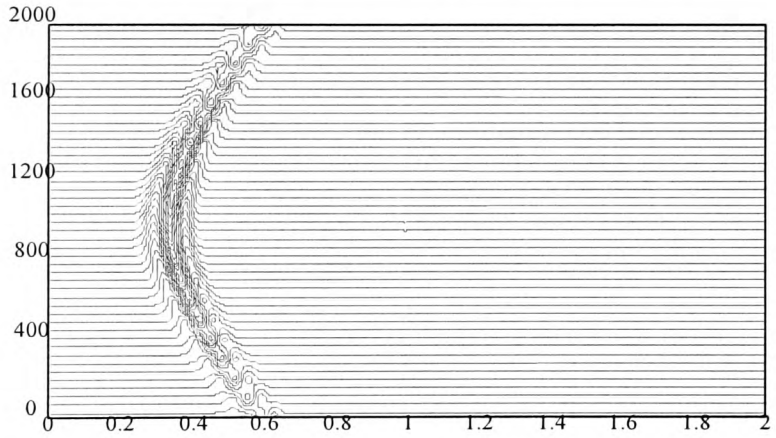

Figure (7.9) Synthetic seismograms from the FDM program with the Reynolds ABCs.

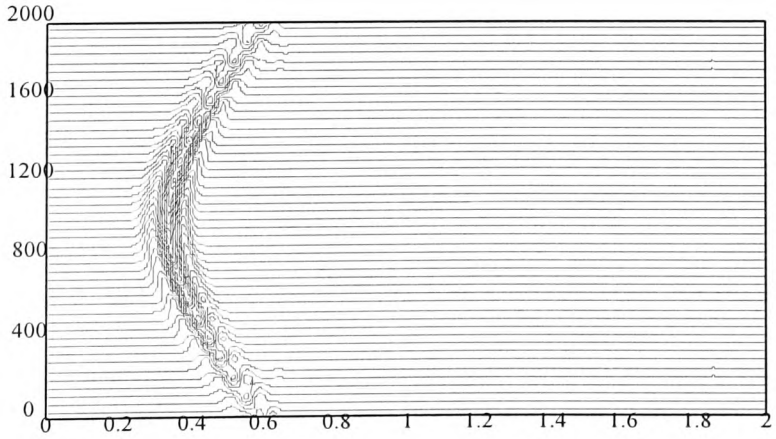

Figure (7.10) Synthetic seismograms from the FDM program with the Clayton-Engquist ABCs.

Two media results are given in Figures (7.11), (7.12), and (7.13). Figure (7.11) shows results with Dirichlet boundary conditions and shows large reflections from all boundaries and mild reflection from the interface. Figure (7.12) shows results with the Reynolds ABCs and the Clayton-Engquist ABCs results are shown in Figure (7.13). The mild interface reflection can be seen after 1.1 s in Figures (7.12) and (7.13). The small side reflection can be seen after 1.4 s in Figure (7.12), and Figure (7.13) shows the large side reflection after 1.4 s.

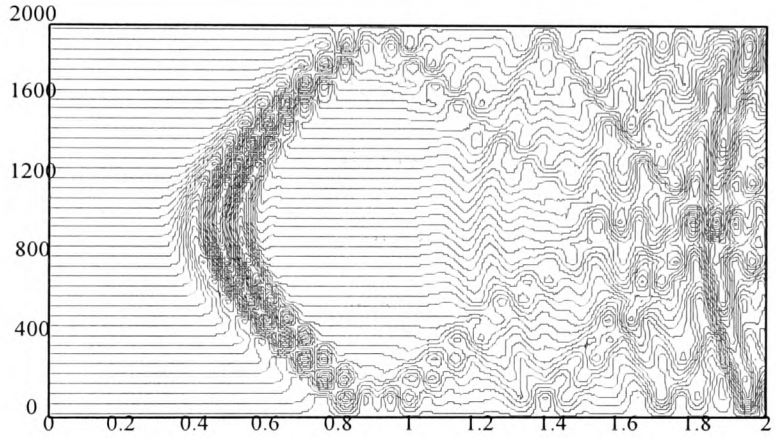

Figure (7.11) Synthetic seismograms from the FDM program with the Dirichlet boundary conditions for two media.

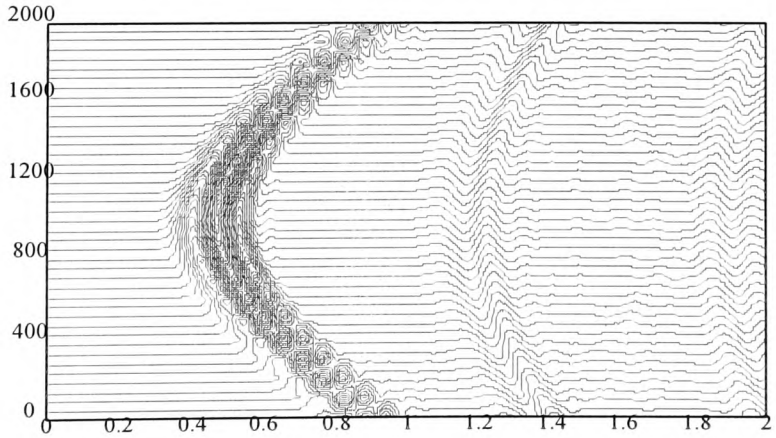

Figure (7.12) Synthetic seismograms from the FDM program with the Reynolds ABCs for two media.

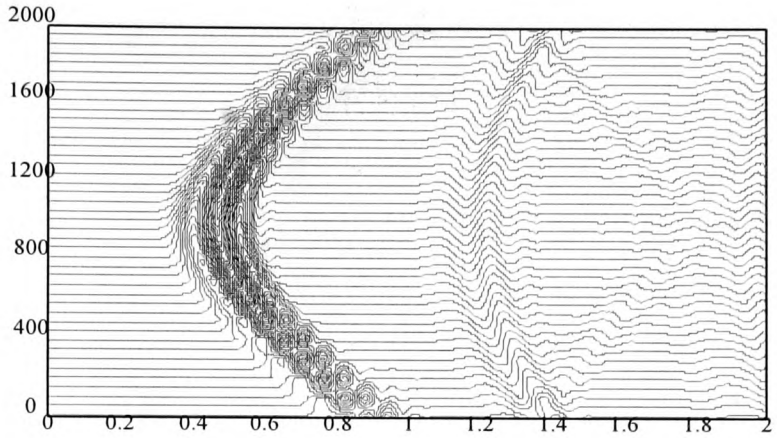

Figure (7.13) Synthetic seismograms from the FDM program with the Clayton-Engquist ABCs for two media.

The synthetic multimedia seismograms show the results for the standard FDM using the Dirichlet boundary conditions in Figure (7.14) with Figure (7.15) showing the seismograms using Reynolds ABCs, and the Clayton-Engquist ABCs results are shown in Figure (7.16). All Figures (7.14), (7.15), and (7.16) show similarities for the first and secondary wave. The Reynolds and Clayton-Engquist ABCs results show good agreement.

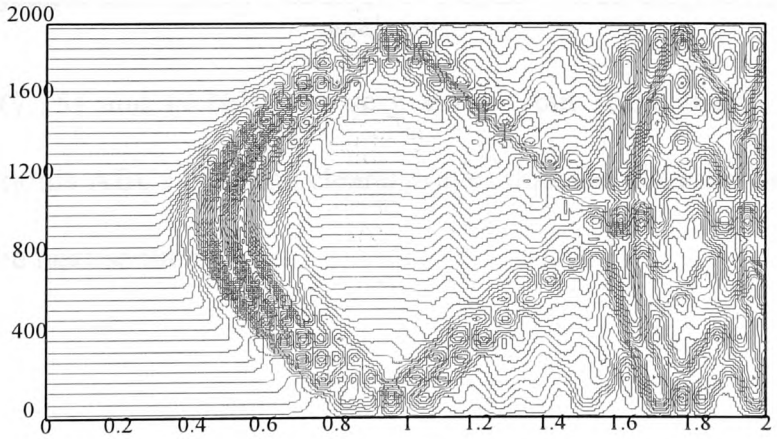

Figure (7.14) Synthetic seismograms from the FDM program with the Dirichlet boundary conditions for multimedia.

The multiple interface waves can be seen that after 1.0 s.

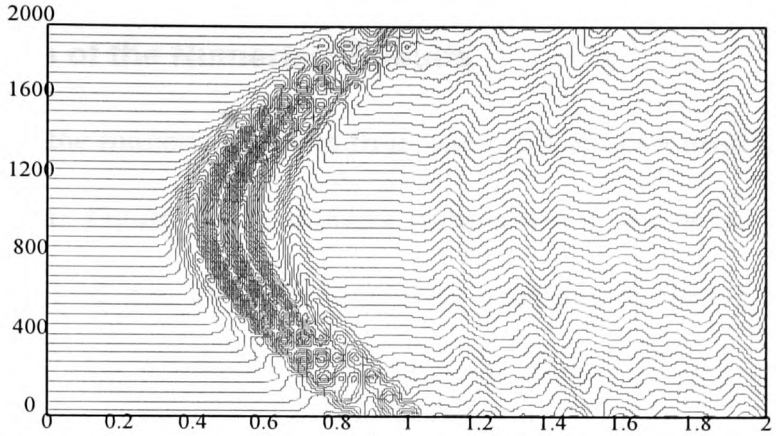

Figure (7.15) Synthetic seismograms from the FDM program with the Reynolds ABCs for multimedia.

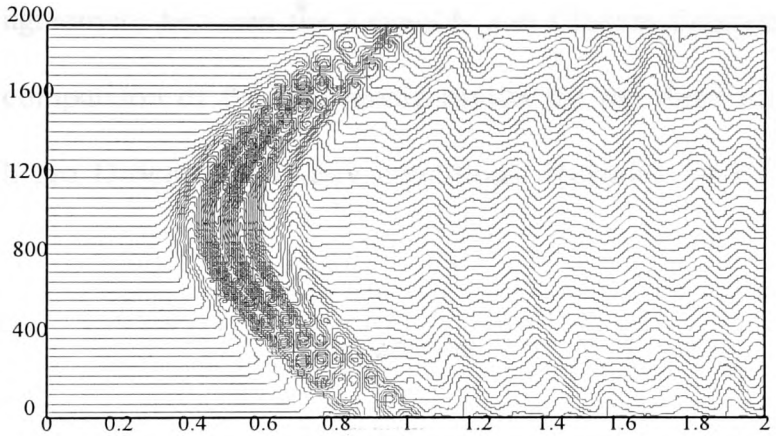

Figure (7.16) Synthetic seismograms from the FDM program with the Clayton-Engquist ABCs for multimedia.

Figures (7.15) and (7.16) look very similar but wave traces show the small differences. Reynolds ABCs generate clearer waves than the Clayton-Engquist ABCs as will be seen in the next section.

7.4.2 Comparison of the Numerical Results

We present the numerical results from one medium, two media, and multimedia in 3-D acoustic case. Figure (7.17) shows a comparison of the seismograms generated by the standard FDM for Dirichlet boundary conditions, Reynolds and Clayton-Engquist ABCs for one medium at (x=1000m, y=1000m, z=1960m). Reynolds and Clayton-Engquist results show a flat line after the direct wave. There is a close match between the three waveforms for the direct wave pulse; wave traces are identical and there is a good agreement between the Reynolds and Clayton-Engquist ABCs. Figure (7.18) shows a comparison of the two media results for the three different boundary conditions which are Dirichlet boundary conditions, Reynolds and Clayton-Engquist ABCs.

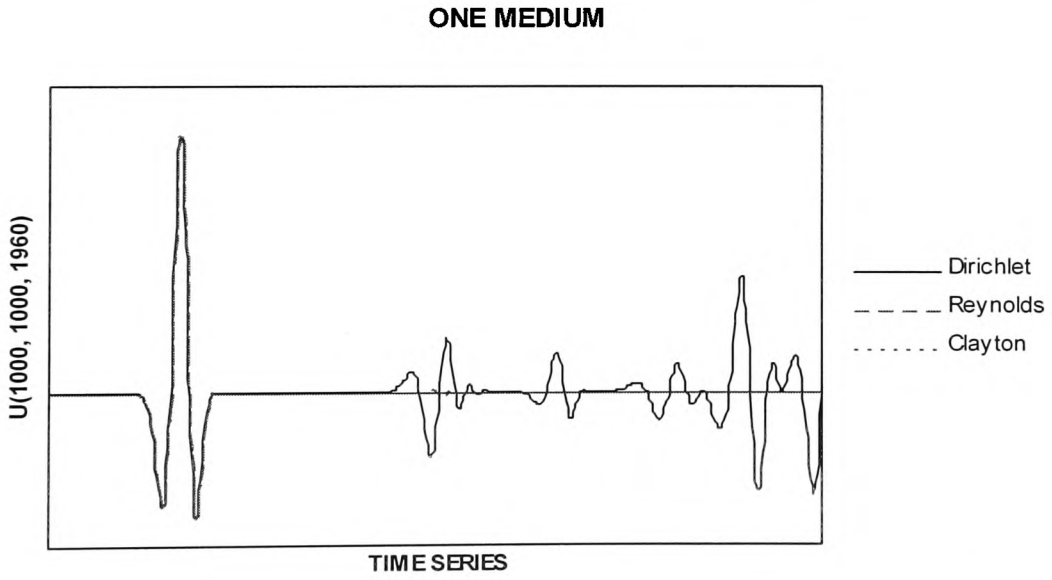

Figure (7.17) Numerical results with the standard FDM for Dirichlet boundary conditions, Reynolds and Clayton-Engquist ABCs.

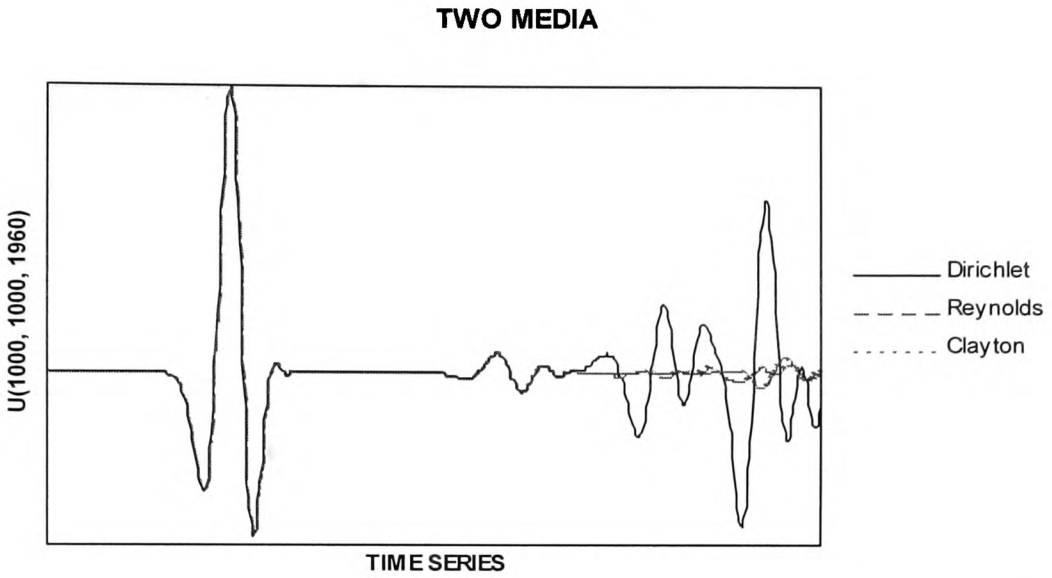

Figure (7.18) Numerical results with the standard FDM for Dirichlet boundary conditions, Reynolds and Clayton-Engquist ABCs.

The direct wave pulses are identical; Reynolds and Clayton-Engquist ABCs results show a difference as can be seen near the end of the trace. Figure (7.19) shows the seismograms calculated by the standard FDM for multimedia. There is good agreement for the direct wave pulse. There are slight differences between the Reynolds and Clayton-Engquist ABCs as can be seen after the interface waves. The Reynolds ABCs are found better than the Clayton-Engquist ABCs. The Reynolds ABCs were also found to be better by Zahradnik et al. [**90**], and Yoon & McMechan [**87**].

MULTIMEDIA

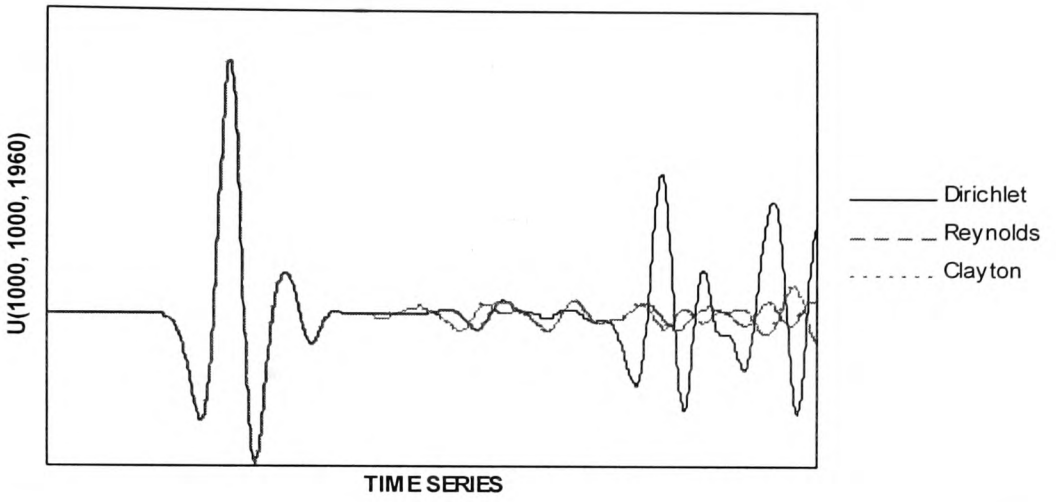

Figure (7.19) Numerical results with the standard FDM for Dirichlet boundary conditions, Reynolds and Clayton-Engquist ABCs.

7.5. Accuracy of the FDM Calculation in 3-D Elastic case

In this section we consider the convergence of the solution for the 3-D elastic case. We have produced results for two seconds of simulation time for a numerical solution. The numerical solutions are found to be consistent with grids ranging (M, N, K) from (25x25x25 to 100x100x100), and for 500 and 700 time steps. All figures show the results for the box method, and staggered grid method. The seismic wave u, w displacements evaluated near the top boundary (x = 1000 m, y = 1000 m, z = 40 m, and t = 1.0 s). Figure (7.20a) shows the results for box method values display the u horizontal displacement. Figure (7.20b) shows the results for the vertical w displacements at the same point. Figures (7.20a) and (7.20b) exhibit the results with Dirichlet boundary conditions. Figures (7.21a) and (7.21b) show the results for the staggered grid using the Dirichlet boundary conditions for horizontal u and vertical w displacement.

The Reynolds ABCs results are shown in Figure (7.22a) with the box method for horizontal u displacement, whilst Figure (7.22b) show the results for vertical w displacement with the Reynolds ABCs. Figures (7.23a) and (7.23b) show the results for the staggered grid method using the Reynolds ABCs display u and w displacement. The Clayton-Engquist ABCs convergence results are shown in Figures (7.24a) and (7.24b). All the one medium results show convergence near the h=20 m. Also two media results show convergence after the h = 20 m. Due to computer memory constants, we were restricted to running our program for an array size less than 200.

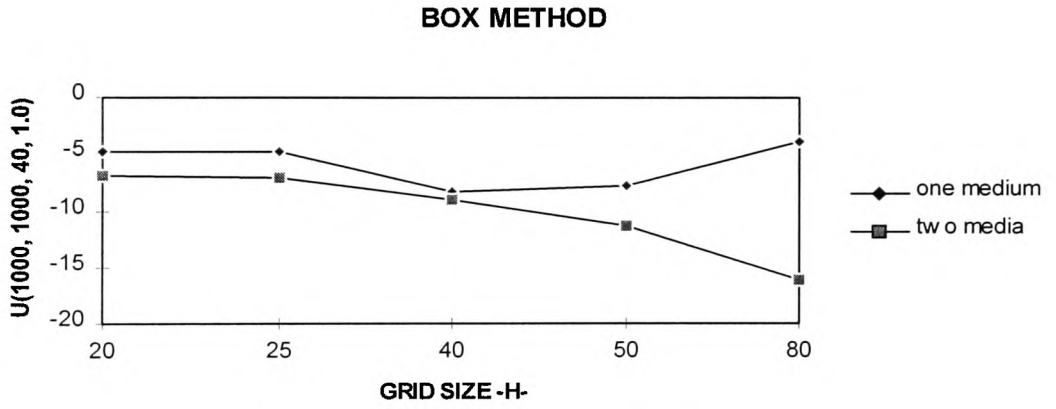

Figure (7.20a) Convergence criterion for the box method solution using the Dirichlet boundary conditions display horizontal displacement.

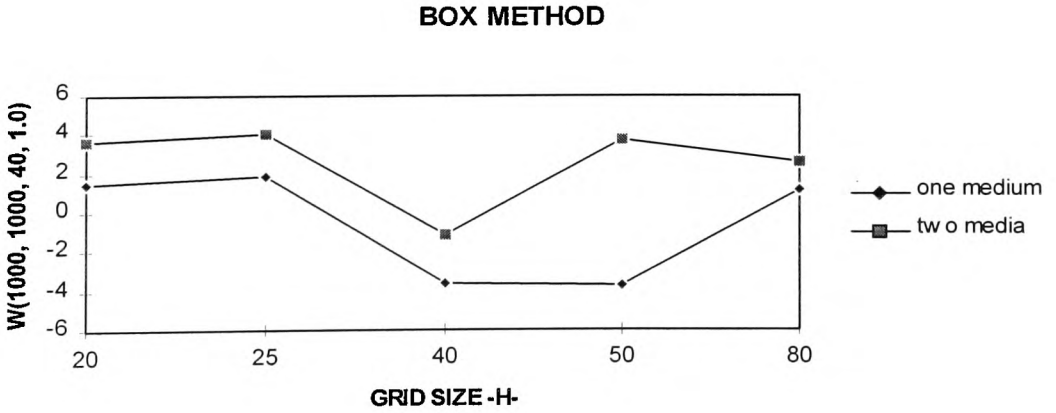

Figure (7.20b) Convergence criterion for the box method solution using the Dirichlet boundary conditions display vertical displacement.

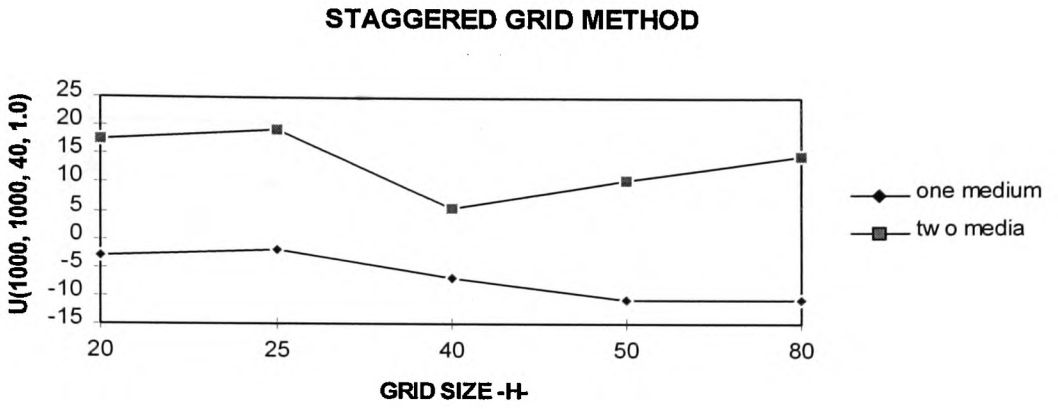

Figure (7.21a) Convergence criterion for the staggered grid method solution using the Dirichlet boundary conditions display horizontal displacement.

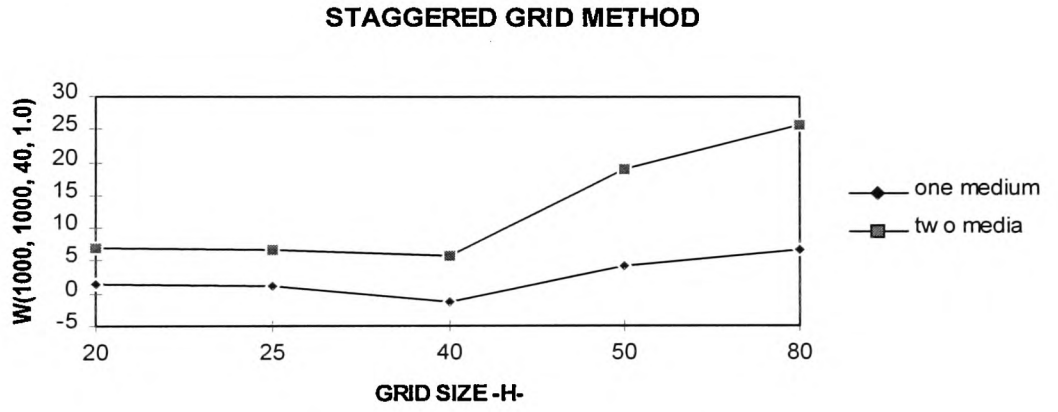

Figure (7.21b) Convergence criterion for the staggered grid method solution using the Dirichlet boundary conditions display vertical displacement.

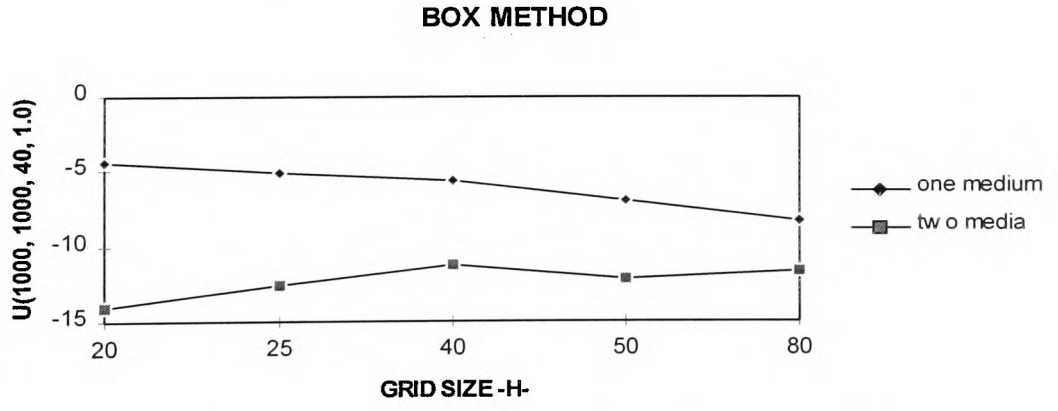

Figure (7.22a) Convergence criterion for the box method solution using the Reynolds ABCs display horizontal displacement.

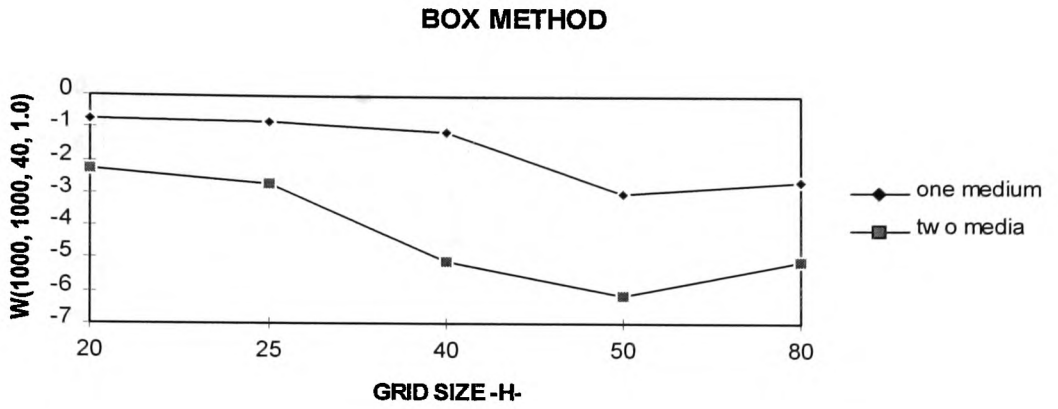

Figure (7.22b) Convergence criterion for the box method solution using the Reynolds ABCs display vertical displacement.

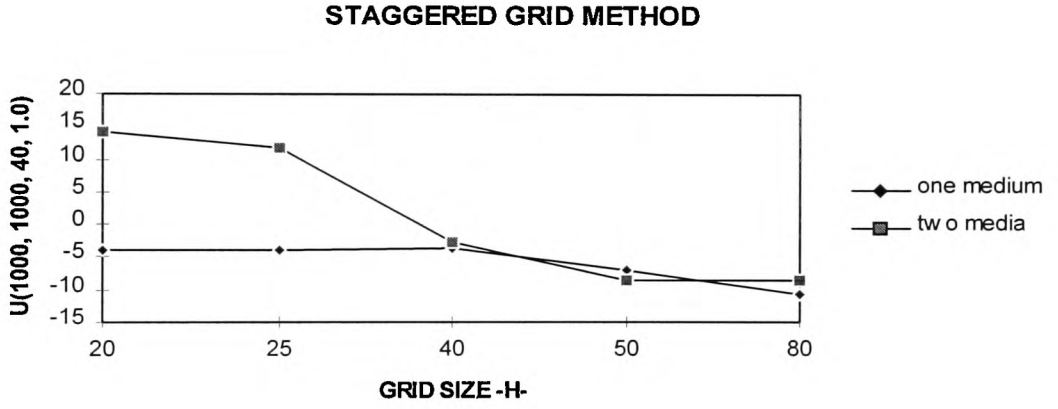

Figure (7.23a) Convergence criterion for the staggered grid method solution using the Reynolds ABCs display horizontal displacement.

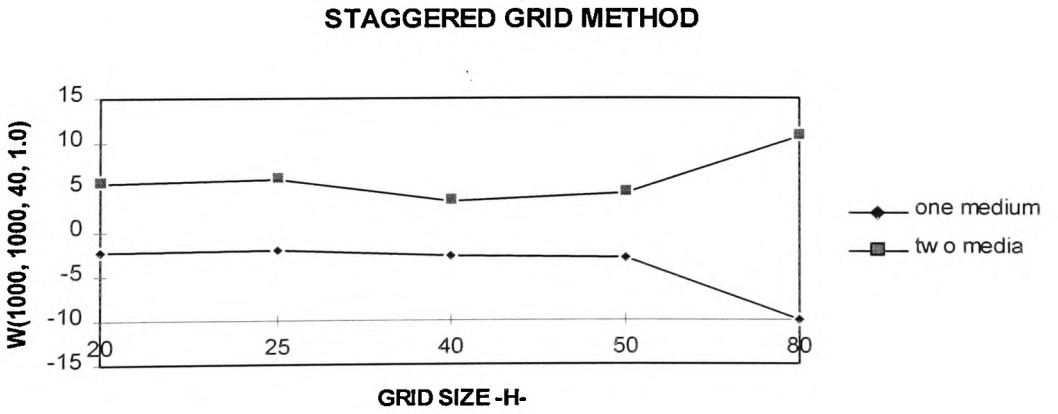

Figure (7.23b) Convergence criterion for the staggered grid method solution using the Reynolds ABCs display vertical displacement.

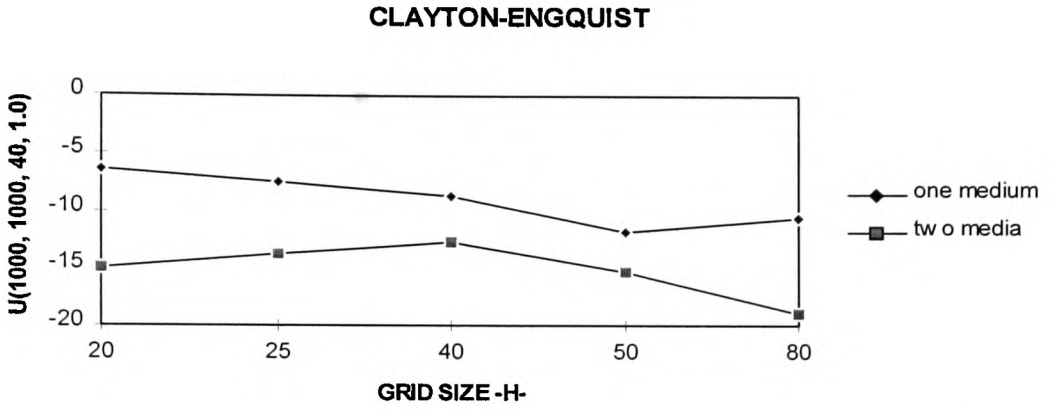

Figure (7.24a) Convergence criterion for the box method solution using the Clayton-Engquiat ABCs display horizontal displacement.

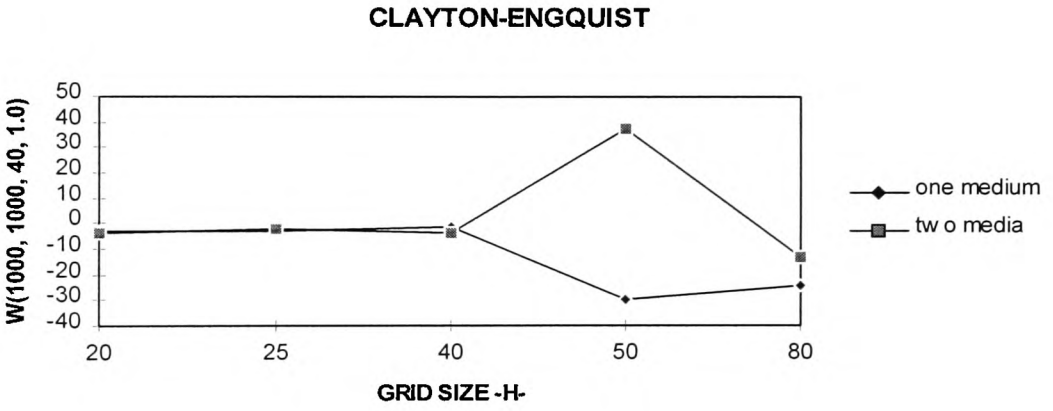

Figure (7.24b) Convergence criterion for the box method solution using the Clayton-Engquiat ABCs display vertical displacement.

7.5.1 Results in 3-D Elastic Case

In this section we consider one medium and two media models using two methods which are namely box and staggered grid methods. The Clayton-Engquist ABCs are used with the box method. The one medium model contains shale with P and S velocities 2440 m/s and 1400 m/s respectively from Yoon & McMechan [**87**]. The two media model contains shale and basalt with the physical properties obtained from Yoon & McMechan [**87**] and Sochacki et al. [**68**]. The basalt P and S velocities are 4000

m/s and 2730m/s, respectively. The source is taken to be a purely compressional pulse which is a solution of equations (4.14) and (4.15) in an elastic medium, Ottaviani [**55**]. In all programs the sharpness of the pulse parameter Δ is taken as 0.04. The source function is located at a depth of 500 m and the receivers are located in a horizontal row 40 m below the free surface which are located at two hundred metre distance intervals. The geometry of models are used in Figure (7.5) and (7.6). The finite-difference grid increment used in all three direction is 20 m, and time increment used is for one medium 0.004 s and two media 0.00285 s. The box method results using Dirichlet boundary conditions are shown in Figure (7.25a) and (7.25b) with u and w seismograms. Figure (7.26a) and (7.26b) show the results for staggered grid method using the Dirichlet boundary conditions with u and w seismograms. The horizontal and vertical seismograms obtain by using the box method with the Reynolds ABCs are shown in Figure (7.27a) and (7.27b). Figure (7.28a) and (7.28b) show the result for the staggered grid method using the Reynolds ABCs. The Clayton-Engquist ABCs for one medium results are shown in Figures (7.29a) and 7.29b).

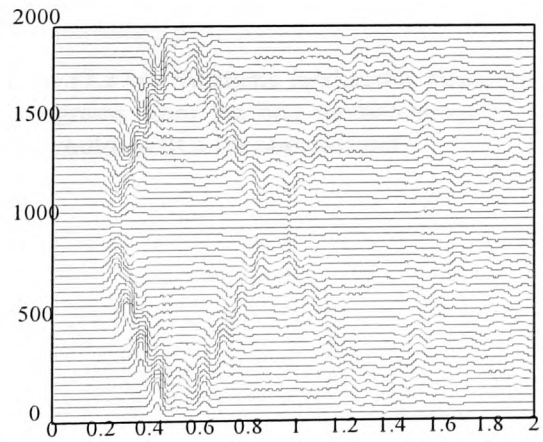

Figure (7.25a) Synthetic horizontal displacement seismograms from the box method program with the Dirichlet boundary conditions for one medium.

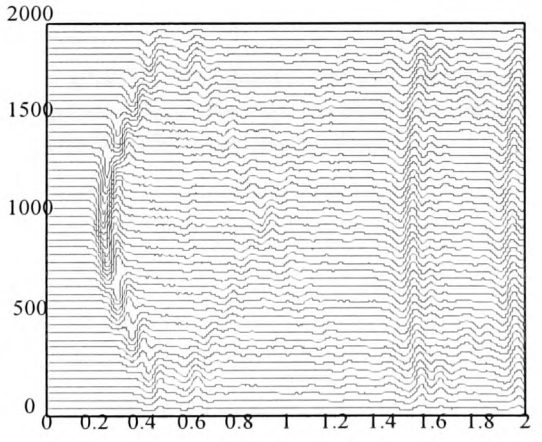

Figure (7.25b) Synthetic vertical displacement seismograms from the box method program with the Dirichlet boundary conditions for one medium.

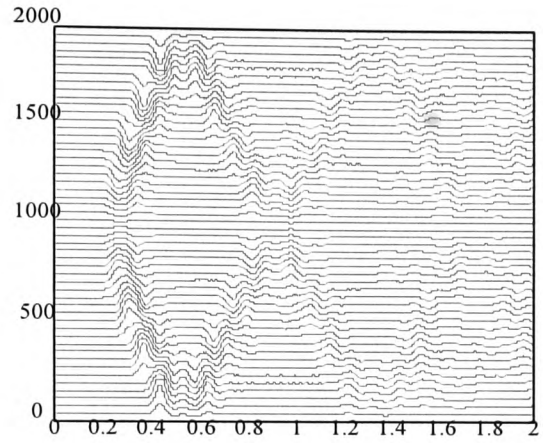

Figure (7.26a) Synthetic horizontal displacement seismograms from the staggered grid method program with the Dirichlet boundary conditions for one medium.

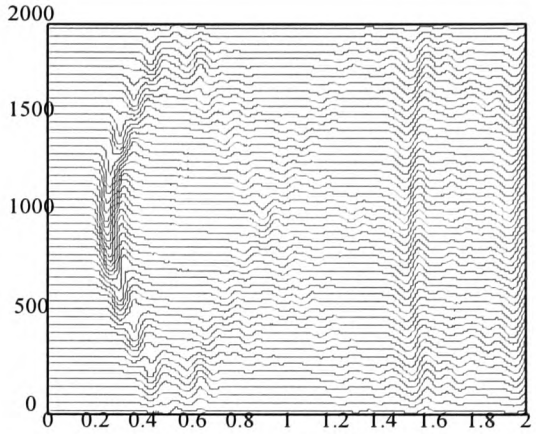

Figure (7.26b) Synthetic vertical displacement seismograms from the staggered grid method program with the Dirichlet boundary conditions for one medium.

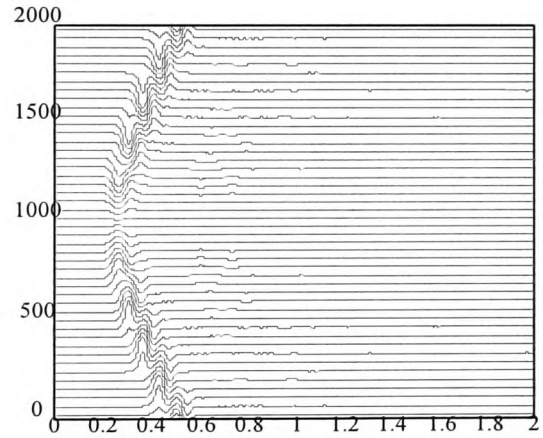

Figure (7.27a) Synthetic horizontal displacement seismograms from the box method program with the Reynolds ABCs for one medium.

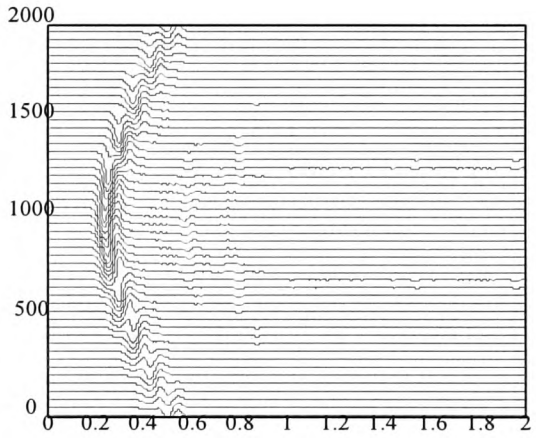

Figure (7.27b) Synthetic vertical displacement seismograms from the box method program with the Reynolds ABCs for one medium.

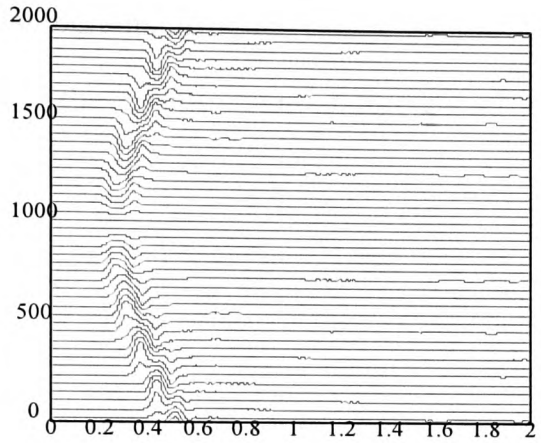

Figure (7.28a) Synthetic horizontal displacement seismograms from the staggered grid method program with the Reynolds ABCs for one medium.

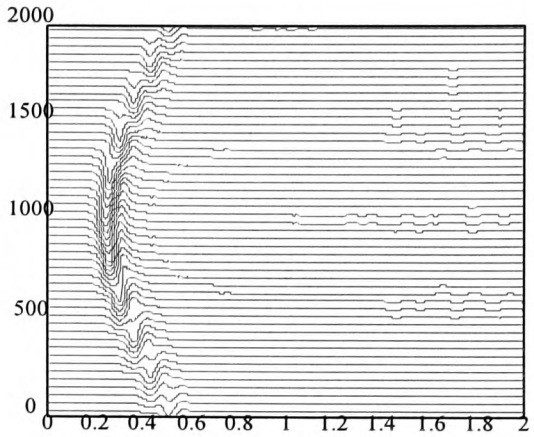

Figure (7.28b) Synthetic vertical displacement seismograms from the staggered grid method program with the Reynolds ABCs for one medium.

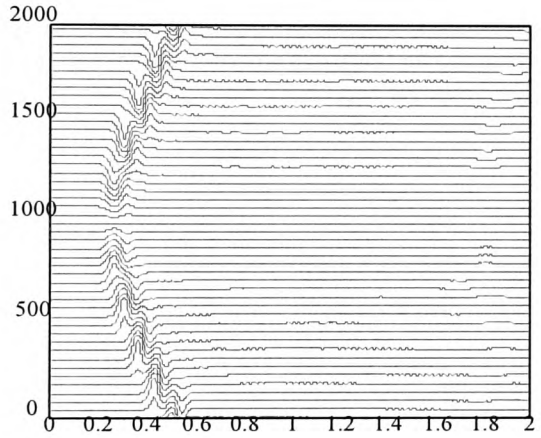

Figure (7.29a) Synthetic horizontal displacement seismograms from the box method program with the Clayton-Engquist ABCs for one medium

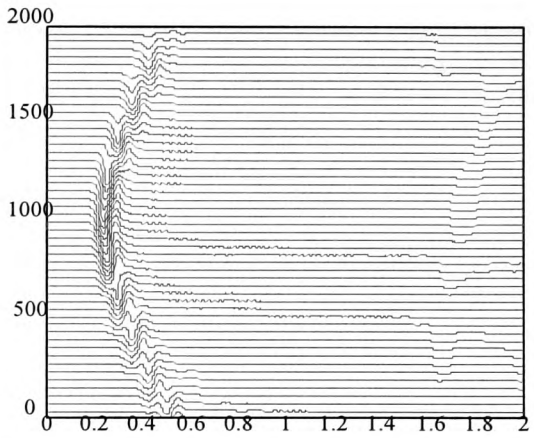

Figure (7.29b) Synthetic vertical displacement seismograms from the box method program with the Clayton-Engquist ABCs for one medium.

Figures (7.30a) and (7.30b) show the horizontal and vertical seismograms for the box method using Dirichlet boundary conditions. The horizontal and vertical seismograms are obtained by the staggered grid method using Dirichlet boundary conditions which are shown in Figures (7.31a) and (7.31b). The Reynolds ABCs results are shown in Figures (7.32a), (7.32b), (7.33a) and (7.33b), respectively. The horizontal and vertical seismograms are obtained using the box method that are shown in Figures (7.32a) and (7.32b). Figures (7.33a) and (7.33b) show the results the horizontal and vertical

seismograms using the staggered grid method. The last two Figures (7.34a) and (7.34b) show the results horizontal and vertical seismograms using the box method with the Clayton-Engquist ABCs.

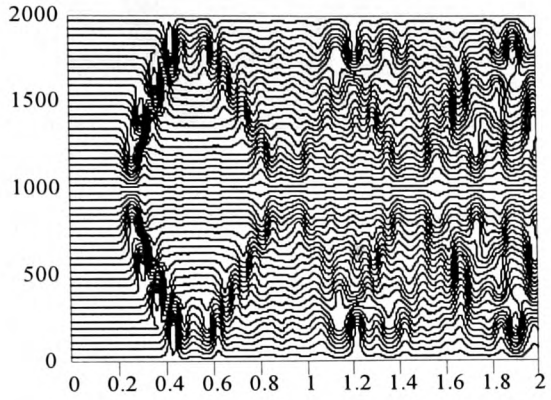

Figure (7.30a) Synthetic horizontal displacement seismograms from the box method program with the Dirichlet boundary conditions for two media.

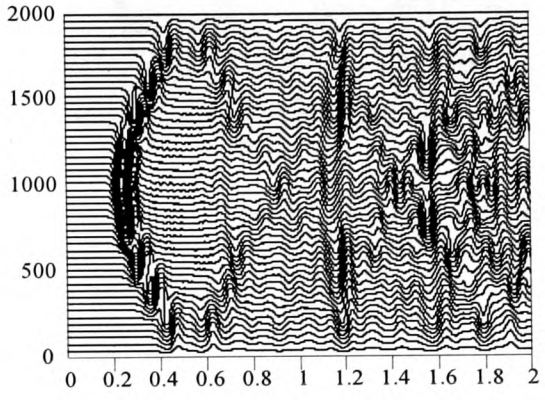

Figure (7.30b) Synthetic vertical displacement seismograms from the box method program with the Dirichlet boundary conditions for two media.

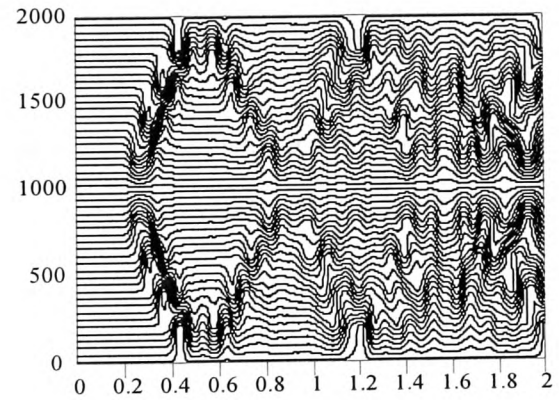

Figure (7.31a) Synthetic horizontal displacement seismograms from the staggered grid method program with the Dirichlet boundary conditions for two media.

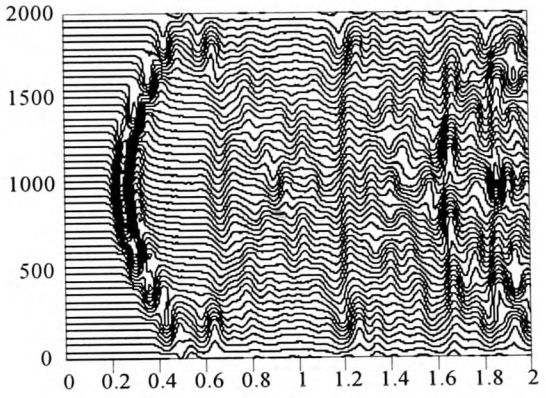

Figure (7.31b) Synthetic vertical displacement seismograms from the staggered grid method program with the Dirichlet boundary conditions for two media.

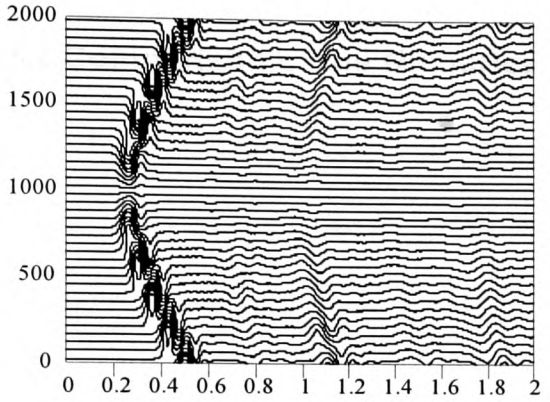

Figure (7.32a) Synthetic horizontal displacement seismograms from the box method program with the Reynolds ABCs for two media.

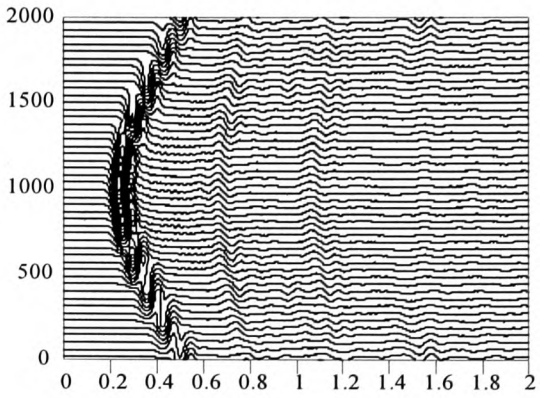

Figure (7.32b) Synthetic vertical displacement seismograms from the box method program with the Reynolds ABCs for two media.

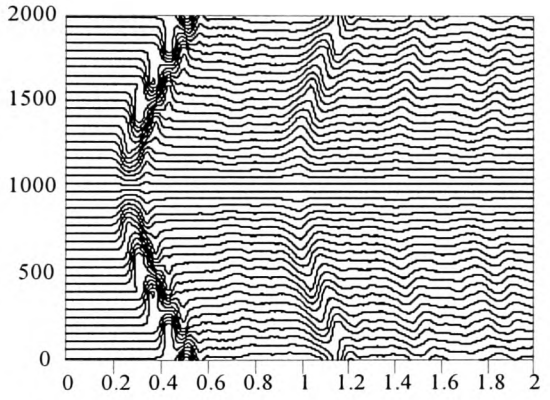

Figure (7.33a) Synthetic horizontal displacement seismograms from the staggered grid method program using the Reynolds ABCs for two media.

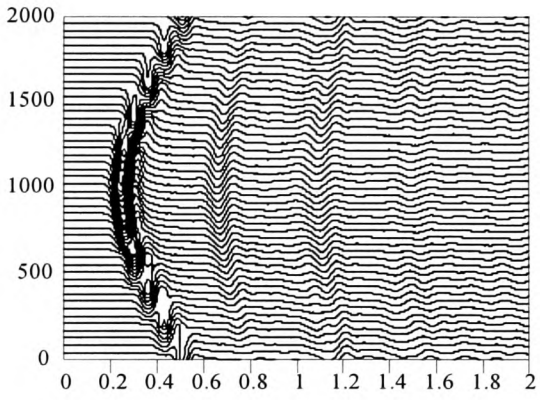

Figure (7.33b) Synthetic vertical displacement seismograms from the staggered grid method program with the Reynolds ABCs for two media.

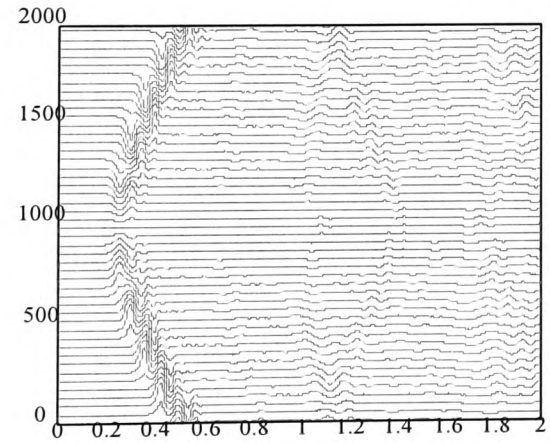

Figure (7.34a) Synthetic horizontal displacement seismograms from the box method program with the Clayton-Enguist ABCs for two media.

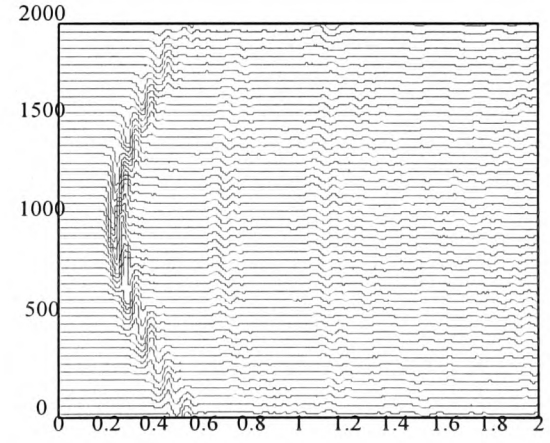

Figure (7.34b) Synthetic vertical displacement seismograms from the box method program with the Clayton-Enguist ABCs for two media.

7.5.2 Comparison of the Numerical Results in 3-D Elastic Case

In this section we present the numerical results for the one medium and two media in 3-D elastic case. Several comparisons of the box method with the staggered grid method are presented. The first comparison shows the two different numerical solutions for the one medium case. The compared solutions are obtained using the box and staggered grid methods with the Dirichlet boundary conditions and are shown in Figures (7.35a) and (7.35b) at (x=1000m, y=1000, z=1960). The second comparison of the numerical results are obtained using the box and staggered grid method with the Reynolds and Clayton-Engquist ABCs in Figures (7.36a) and (7.36b). The comparison of the synthetic seismograms are obtained for two media. Figures (7.37a) and (7.37b) show the comparison of the horizontal u and vertical w displacement seismograms for Dirichlet boundary conditions. The last comparison of the horizontal u and vertical w displacement seismograms are obtained using the Reynolds and Clayton-Engquist ABCs which are shown in Figures (7.38a) and (7.38b). Accuracy of the numerical solution is affected by grid dispersion. The staggered grid method results exhibit less dispersion than the box method results as can be seen in Figures (7.35a), (7.35b), (7.36a), and (7.36b). The two media results exhibit more dispersion than the one medium results because the two media model has larger wave velocities. Our approach was found to be better than the box method.

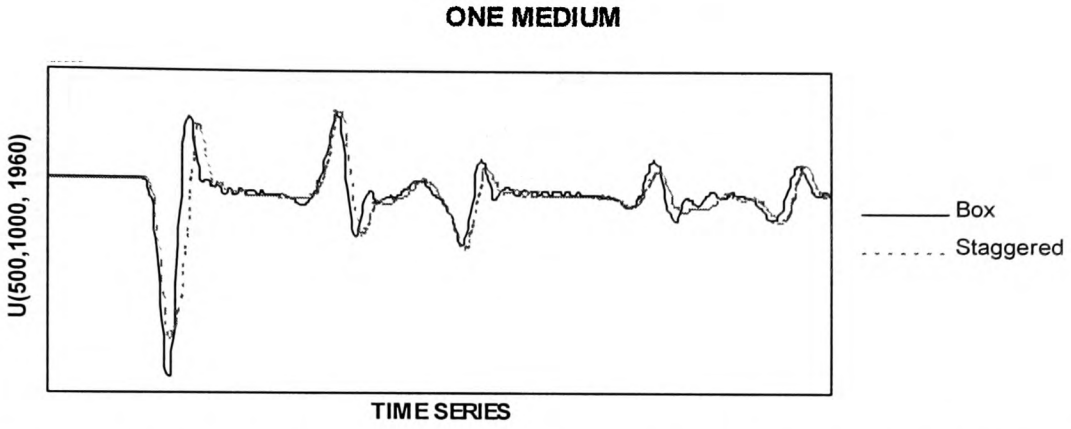

Figure (7.35a) The horizontal u displacement seismograms obtained from the box and staggered grid with Dirichlet boundary conditions for one medium.

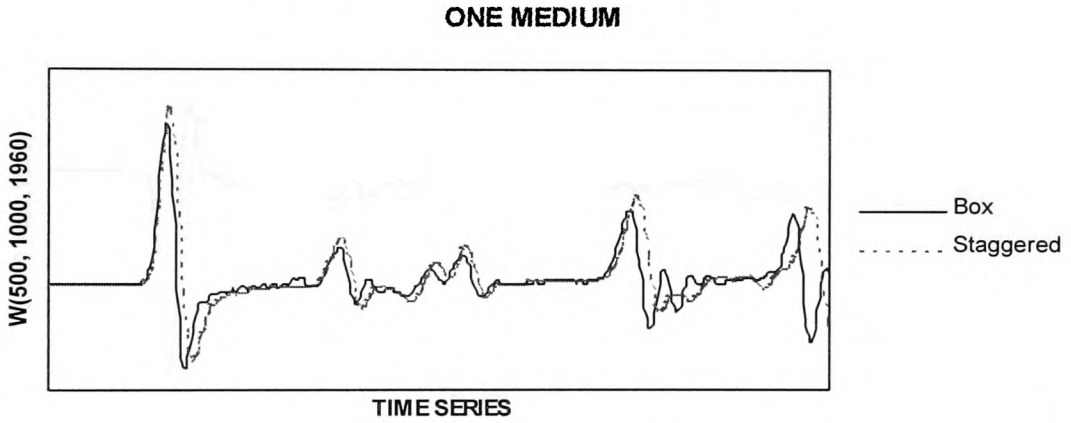

Figure (7.35b) The vertical w displacement seismograms obtained from the box and staggered grid with Dirichlet boundary conditions for one medium.

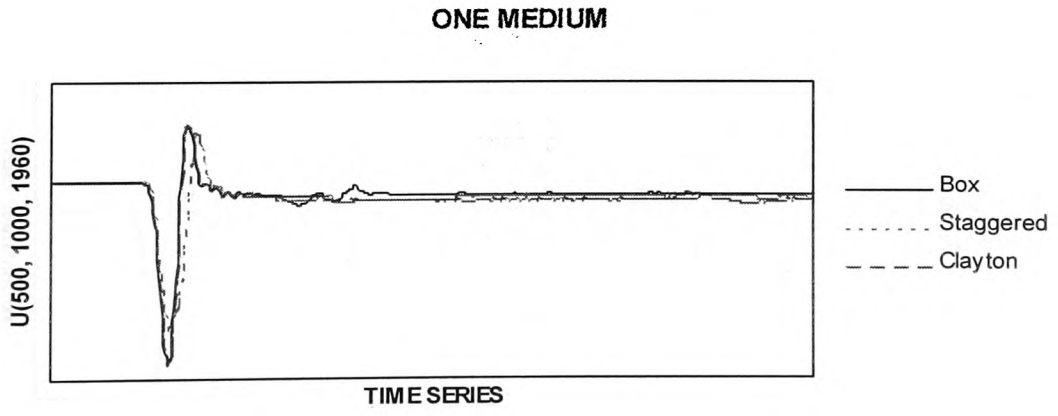

Figure (7.36a) The horizontal u displacement seismograms obtained from the box and staggered grid with Reynolds and Clayton-Engquist ABCs for one medium.

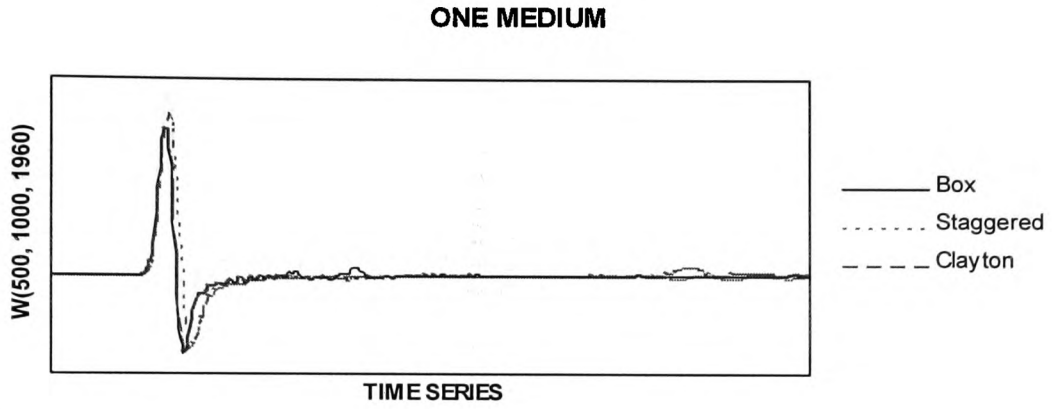

Figure (7.36b) The vertical w displacement seismograms obtained from the box and staggered grid with Reynolds and Clayton-Engquist ABCs for one medium.

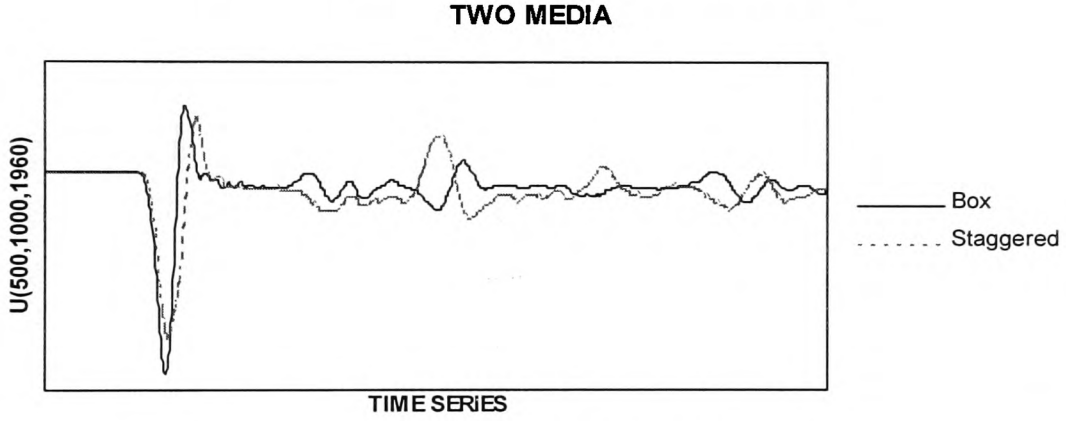

Figure (7.37a) The horizontal u displacement seismograms obtained from the box and staggered grid with Dirichlet boundary conditions for two media.

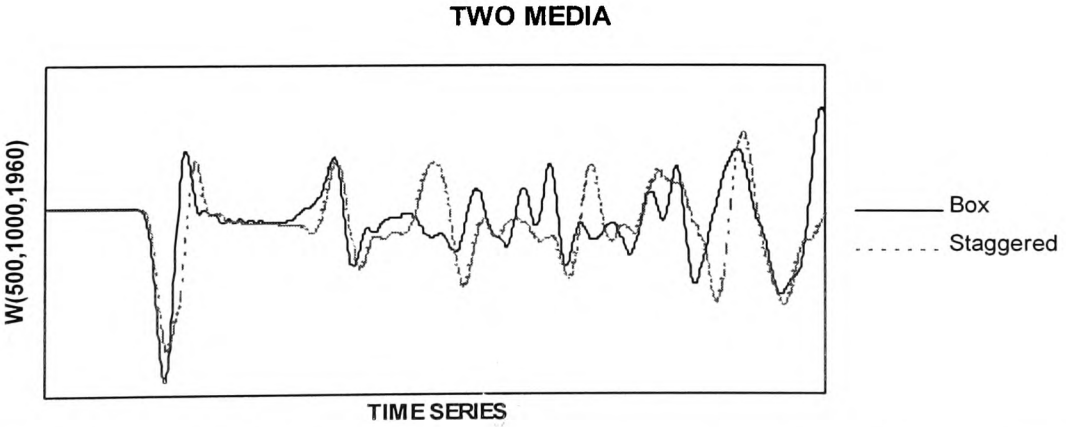

Figure (7.37b) The vertical w displacement seismograms obtained from the box and staggered grid with Dirichlet boundary conditions for two media.

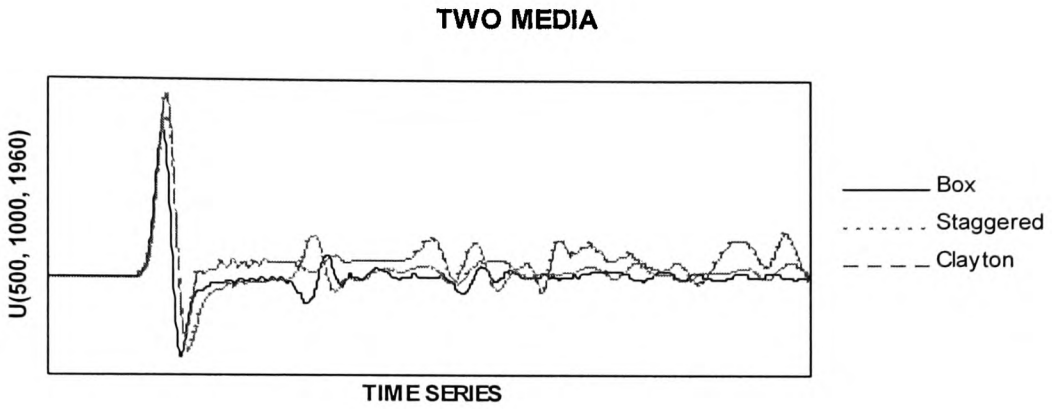

Figure (7.38a) The horizontal u displacement seismograms obtained from the box and staggered grid with Reynolds and Clayton-Engquist ABCs for two media.

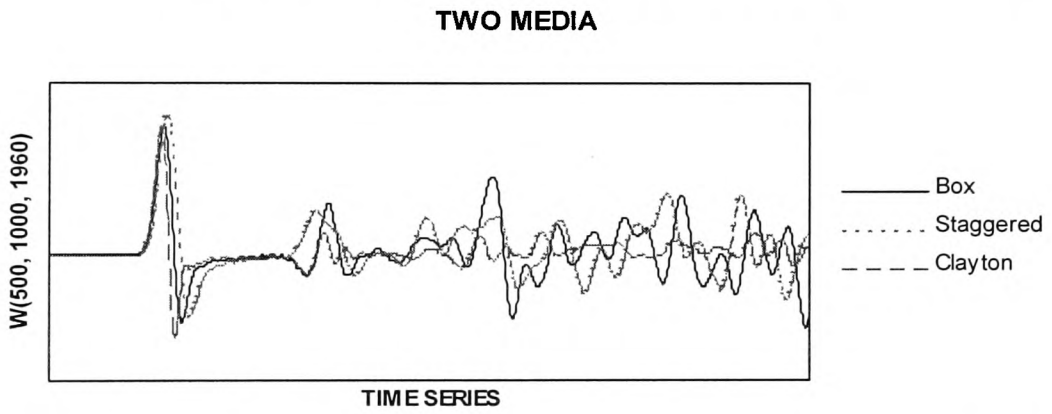

Figure (7.38b) The vertical w displacement seismograms obtained from the box and staggered grid with Reynolds and Clayton-Engquist ABCs for two media.

7.6 Conclusion

We have examined the 3-D acoustic and elastic wave propagation for a single layer, two layered, and multi layered rocks in Cartesian coordinates. We analysed the convergence criteria for all models and found optimal grid parameters. Generally the Reynolds ABCs performed better than those of Clayton-Engquist. Multimedia waves are clearly visible, but weaker than for the direct wave. Our new approach gave favourable results by comparison with the work of others.

CHAPTER 8

BOREHOLE MODELLING

8.1. Introduction

In this chapter we introduce the numerical results for borehole geometries in 2-D, and 3-D Cartesian and cylindrical coordinates. One of the main aims of this thesis is to detail how best to model the case of a borehole with a source. On the back of our successful previous simulations we now use the best combinations of methods to model a simple borehole with sources, in 2-D and then more realistically in 3-D. The VSM model will be used in same cases.

The Reynolds's ABCs are used throughout in the borehole modelling. We present results of the FDM applied to the surface seismograms and VSP (vertical seismic profiling). We demonstrate the applicability of the staggered grid synthetic VSP method by considering some useful models of borehole structure. We present results of the staggered grid method and VSM with the receivers are located at the horizontal axis on the surface. We employ two borehole models, and for both the source and receivers are located in the fluid-filled borehole and we also employ two borehole models in 3-D cylindrical coordinates. We follow a source box method (Alterman and Karal [**3**], Pitarka et al. [**57**]) as given in detail in Chapter 4. 2-D examples in Cartesian coordinates are studied by Sun and McMechan [**75**], 3-D examples in Cartesian coordinates are studied by Yoon and McMechan [**87**] and 3-D Cylindrical coordinates are studied by Stephen et al. [**72**].

The borehole tube wave is the low-frequency part of the Stoneley mode that is often observed on VSP data Hardage [**32**]. The Stoneley wave is an interface wave and its amplitude decreases exponentially as a function of the distance for the wall both in the fluid within the borehole and in the formation outside the borehole. The Stoneley wave is also a symmetrical mode and in axisymmetrical problem. Tube waves can be excited by body waves, surface waves or other tube waves (Ording et al. [**54**]; Hardage [**31,32**]). For vertically stratified media, avaible methods include reflectivity (Temme et al. [**76**] for acoustic waves and Dietrich et al. [**22**] for elastic waves). For laterally varying media, finite-difference (McMechan [**48**]) for acoustic waves. A number of studies of propagation in boreholes have been done; these include both numerical (Stephen et al. [**72**], Randall et al. [**61**]) and analytical (Biot [**10**], Lee et al. [**43**],White et al. [**84**], White [**83**], Nicoletis et al. [**53**], Peterson [**56**], Cheng et al. [**17**], Kurkjian et al. [**39**]) approaches. All these studies assume the borehole is in a homogeneous medium.

8.2 2-D and 3-D Elastic Wave Equation in Cartesian Coordinates

In this section we present the elastic wave equation in borehole modelling. The elastic wave equation is similar to that presented by Sun and McMechan [**74**], and is a solution of the 2-D elastic wave equation (Sun and McMechan [**75**]):

$$\begin{aligned} \rho u_{tt} &= \left[\lambda(u_x + w_z) + 2\mu u_x\right]_x + \left[\mu(w_x + u_z)\right]_z \\ \rho w_{tt} &= \left[\lambda(u_x + w_z) + 2\mu w_z\right]_z + \left[\mu(w_x + u_z)\right]_x \end{aligned} \tag{8.1}$$

and 3-D elastic wave propagation is given by Yoon and McMechan 1992 [**87**]

$$\begin{aligned} \rho u_{tt} &= (\lambda + 2\mu)u_{xx} + \lambda(v_{yx} + w_{zx}) + \mu(v_{xy} + u_{yy}) + \mu(w_{xz} + u_{zz}) \\ \rho v_{tt} &= (\lambda + 2\mu)v_{yy} + \lambda(u_{xy} + w_{zy}) + \mu(v_{zz} + w_{yz}) + \mu(v_{xx} + u_{yx}) \\ \rho w_{tt} &= (\lambda + 2\mu)w_{zz} + \lambda(u_{xz} + v_{yz}) + \mu(w_{xx} + u_{zx}) + \mu(w_{yy} + v_{zy}) \end{aligned} \tag{8.2}$$

where u is displacement in the x direction, and v is displacement in the y direction, and w is displacement in the z direction, ρ is density, and λ and μ are the Lame parameters and t is time. We have used here suffix notation to denote derivatives.

Waves are particularly difficult to synthesise in borehole environments because the standard FDM are not stable for large contrasts in Poisson's ratio, such as at fluid-solid interfaces (Stephen [**71**]). This stability problem may be overcome by using the staggered grid finite-difference formulation (Virieux [**82**]; Stephen [**73**]; Fornberg [**25**]. We solve equations (8.1) and (8.2) using the staggered grid finite-difference formulation described in Luo and Schuster [**47**], and Yoon and McMechan [**87**] extended from 2-D to 3-D. Implementation is by second-order, central finite differences. The free-surface boundary conditions are zero and tangential stress and the Reynolds's ABCs are used on the sides and bottom of the computational media. Reynolds's ABCs is ideal in staggered grid because it uses only values on lines normal to the absorbing surface (Yoon and McMechan [**87**]). A compressional point source is used in borehole modelling as in Stephen et al. [**72**].

8.3 2-D and 3-D Elastic Wave Equation in Cylindrical Coordinates

The 2-D elastic wave equation in cylindrical coordinates is given by Alterman and Karal [**3**] as

$$\rho u_{tt} = \frac{1}{r}\frac{\partial}{\partial r}(rP_{rr}) + \frac{\partial}{\partial z}(P_{rz}) - \frac{P_{\theta\theta}}{r}$$

$$\rho w_{tt} = \frac{1}{r}\frac{\partial}{\partial r}(rP_{rz}) + \frac{\partial}{\partial z}(P_{zz}) \qquad (8.3)$$

and we extend the 3-D elastic wave equations in cylindrical coordinates as given by

$$\rho u_{tt} = \frac{1}{r}\frac{\partial}{\partial r}(rP_{rr}) + \frac{1}{r}\frac{\partial}{\partial \theta}(P_{\theta r}) + \frac{\partial}{\partial z}(P_{rz}) - \frac{P_{\theta\theta}}{r}$$

$$\rho v_{tt} = \frac{1}{r^2}\frac{\partial}{\partial r}(r^2 P_{r\theta}) + \frac{1}{r}\frac{\partial}{\partial \theta}(P_{\theta\theta}) + \frac{\partial}{\partial z}(P_{z\theta}) + \frac{P_{\theta r} - P_{r\theta}}{r} \qquad (8.4)$$

$$\rho w_{tt} = \frac{1}{r}\frac{\partial}{\partial r}(rP_{rz}) + \frac{1}{r}\frac{\partial}{\partial \theta}(P_{\theta z}) + \frac{\partial}{\partial z}(P_{zz})$$

where ρ is the density, and t is time. We shall use the 3-D elastic wave equation in cylindrical coordinates in two borehole modelling.

8.4 Discretisation of the Elastic Wave Equation with VSM

In this section the wave equation is formulated into the second-order hyperbolic equations by using the FDM and discretised on a VSM. Equation (8.1) are given now as

$$\begin{aligned}
\rho u_{tt} &= a(\xi)\left[\lambda\left(a(\xi)u_{\xi} + b(\eta)w_{\eta}\right) + 2\mu a(\xi)u_{\xi}\right]_{\xi} + b(\eta)\left[\mu\left(a(\xi)w_x + b(\eta)u_z\right)\right]_z \\
\rho w_{tt} &= b(\eta)\left[\lambda\left(a(\xi)u_x + b(\eta)w_z\right) + 2\mu b(\eta)w_z\right]_z + a(\xi)\left[\mu\left(a(\xi)w_x + b(\eta)u_z\right)\right]_x
\end{aligned} \qquad (8.5)$$

where $b(\eta)$ is equal to $a(\xi)$. Also the finite-difference formulation for the horizontal and vertical displacements is obtained by solving equations (8.1) and replacing ξ, η, and t derivatives with centred finite-differences. Hence

$$\begin{aligned}
u_{i,j}^{n+1} &= 2u_{i,j}^{n} - u_{i,j}^{n-1} + q_1 a(i)\left(a(i+1)u_{i+1,j}^{n} - (a(i+1)+a(i))u_{i,j}^{n} + a(i)u_{i-1,j}^{n}\right) \\
&\quad + q_2 b(j)\left(b(j+1)u_{i,j+1}^{n} - (b(j+1)+b(j))u_{i,j}^{n} + b(j)u_{i,j-1}^{n}\right) + q_3 a(i) \\
&\quad \left(b(j+1)(w_{i+1,j+1}^{n} - w_{i-1,j+1}^{n}) - b(j)(w_{i+1,j-1}^{n} - w_{i-1,j-1}^{n})\right)
\end{aligned} \qquad (8.6)$$

and similarly

$$\begin{aligned}
w_{i,j}^{n+1} &= 2w_{i,j}^{n} - w_{i,j}^{n-1} + q_2 a(i)\left(a(i+1)w_{i+1,j}^{n} - (a(i+1)+a(i))w_{i,j}^{n} + a(i)w_{i-1,j}^{n}\right) \\
&\quad + q_1 b(j)\left(b(j+1)w_{i,j+1}^{n} - (b(j+1)+b(j))w_{i,j}^{n} + b(j)w_{i,j-1}^{n}\right) + q_3 b(j) \\
&\quad \left(a(i+1)(u_{i+1,j+1}^{n} - u_{i-1,j+1}^{n}) - a(i)(u_{i+1,j-1}^{n} - u_{i-1,j-1}^{n})\right)
\end{aligned} \qquad (8.7)$$

where $q_1 = (v_p.\Delta t/h)^2$, $q_2 = (v_s.\Delta t/h)^2$, and $q_3 = (v_p-v_s)^2.\Delta t^2 / h^2$ and a and b are variable functions.

The wave equation is now formulated for the VSM in cylindrical coordinates. Equation (8.3) is given by the VSM as

$$\begin{aligned} u_{tt} =& v_p^2\left(a(\xi)\frac{\partial}{\partial\xi}\left(a(\xi)\frac{\partial u}{\partial\xi}\right)+\frac{1}{\xi}a(\xi)\frac{\partial u}{\partial\xi}+a(\xi)\frac{\partial}{\partial\xi}\left(b(\eta)\frac{\partial w}{\partial\eta}\right)-u/\xi^2\right) \\ &+ v_s^2\left(b(\eta)\frac{\partial}{\partial\eta}\left(b(\eta)\frac{\partial u}{\partial\eta}\right)-a(\xi)\frac{\partial}{\partial\xi}\left(b(\eta)\frac{\partial w}{\partial\eta}\right)\right) \\ w_{tt} =& v_p^2\left(b(\eta)\frac{\partial}{\partial\eta}\left(b(\eta)\frac{\partial w}{\partial\eta}\right)+\frac{1}{\xi}b(\eta)\frac{\partial u}{\partial\eta}+a(\xi)\frac{\partial}{\partial\xi}\left(b(\eta)\frac{\partial u}{\partial\eta}\right)\right) \\ &+ v_s^2\left(a(\xi)\frac{\partial}{\partial\xi}\left(a(\xi)\frac{\partial w}{\partial\xi}\right)-a(\xi)\frac{\partial}{\partial\xi}\left(b(\eta)\frac{\partial u}{\partial\eta}\right)-\frac{1}{\xi}b(\eta)\frac{\partial u}{\partial\eta}+\frac{1}{\xi}a(\xi)\frac{\partial w}{\partial\xi}\right) \end{aligned} \tag{8.8}$$

The finite-difference formulation for radial and vertical displacements is obtained by solving equations (8.8) and discretised as

$$\begin{aligned} u_{i,j}^{n+1} =& 2u_{i,j}^n - u_{i,j}^{n-1} + q_1 a(i)\left(a(i+1)u_{i+1,j}^n - (a(i+1)+a(i))u_{i,j}^n + a(i)u_{i-1,j}^n\right) \\ &+ q_2 b(j)\left(b(j+1)u_{i,j+1}^n - (b(j+1)+b(j))u_{i,j}^n + b(j)u_{i,j-1}^n\right) + q_3 a(i) \\ &\left(b(j+1)(w_{i+1,j+1}^n - w_{i-1,j+1}^n) - b(j)(w_{i+1,j-1}^n - w_{i-1,j-1}^n)\right) - q_1 a(i)/i^2\, u_{i,j}^n \\ &+ q_1 a(i)/2i\left(a(i+1)u_{i+1,j}^n - a(i)u_{i-1,j}^n\right) \end{aligned} \tag{8.9}$$

and similarly

$$\begin{aligned} w_{i,j}^{n+1} =& 2w_{i,j}^n + q_2 a(i)\left(a(i+1)w_{i+1,j}^n - (a(i+1)+a(i))w_{i,j}^n + a(i)w_{i-1,j}^n\right) \\ &+ q_1 b(j)\left(b(j+1)w_{i,j+1}^n - (b(j+1)+b(j))w_{i,j}^n + b(j)w_{i,j-1}^n\right) + q_3 b(j) \\ &\left(a(i+1)(u_{i+1,j+1}^n - u_{i-1,j+1}^n) - a(i)(u_{i+1,j-1}^n - u_{i-1,j-1}^n) + 2(b(j+1)u_{i,j+1}^n\right. \\ &\left.-b(j)u_{i,j-1}^n)/i\right) + q_2 a(i)\left(a(i+1)w_{i+1,j}^n - a(i)w_{i-1,j}^n\right)/2i - w_{i,j}^{n-1} \end{aligned} \tag{8.10}$$

where $q_1 = (v_p.\Delta t/h)^2$, $q_2 = (v_s.\Delta t/h)^2$, and $q_3 = (v_p-v_s)^2.\Delta t^2 / h^2$ and a and b are variable functions.

8.5. Results in 2-D Cartesian Coordinates

In this section, numerical results are obtained by two different methods, which are the staggered grid and variable scale methods. The borehole used are uncased in all models. Two applications are considered: 1. One borehole results. 2. Vertical seismic profiling (VSP) with two boreholes.

8.5.1 One Borehole Results

Figure (8.1) shows a homogeneous medium with a borehole and Figure (8.2) shows two media with borehole. The sea-water velocity is 1500 m/s and density is 1030 kg/m^3 whilst the shale has a P-wave velocity of 2440 m/s, S-wave velocity of 1400 m/s and a density of 2450 kg/m^3. A source is located in middle of borehole with receivers located in a horizontal row 2 m below the free surface and every 0.2 m intervals. The grid and time increments are 0.2 m and 0.05 ms.

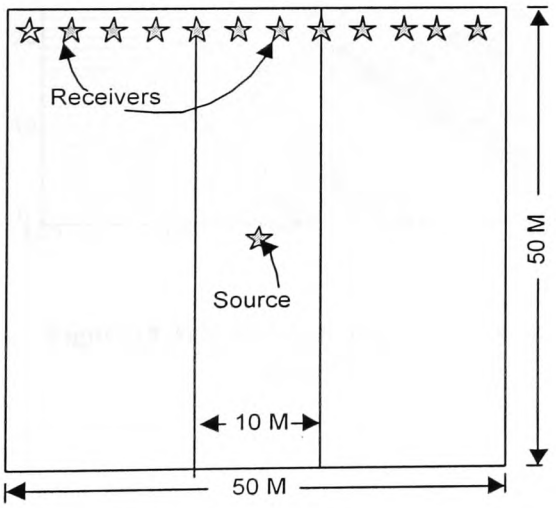

Figure (8.1) Physical model showing borehole geometry used to generate seismograms in the 2-D elastic FDM and VSM programs for one medium.

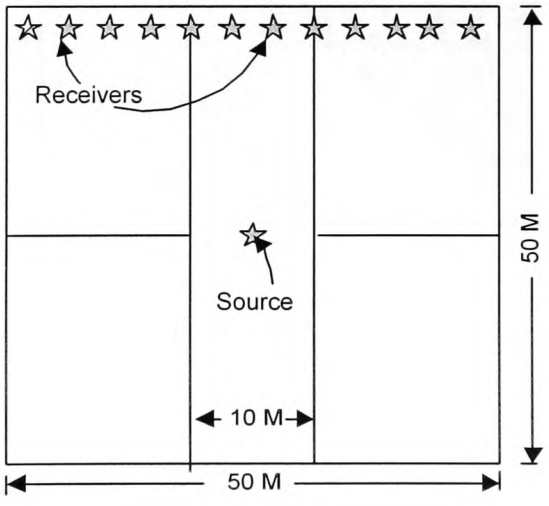

Figure (8.2) Physical model showing borehole geometry used to generate seismograms in the 2-D elastic FDM and VSM programs for multimedia.

The borehole contains sea-water with an outside layer of shale as for the one medium case as in Figure (8.1). The two media geometry contains shale, limestone and the borehole contains sea-water as shown in Figure (8.2).

Figure (8.3) shows the horizontal and vertical displacement with the Reynolds's ABCs for the staggered grid method. For both seismograms, time runs along the horizontal axis and distance from the source along the vertical axis. The VSM results are shown in Figure (8.4) with the horizontal and vertical displacements. Figure (8.5) shows the horizontal and vertical seismograms for the staggered grid method and Figure (8.6) shows the results for the VSM. Figures (8.5) and (8.6) show results for the multimedia geometry.

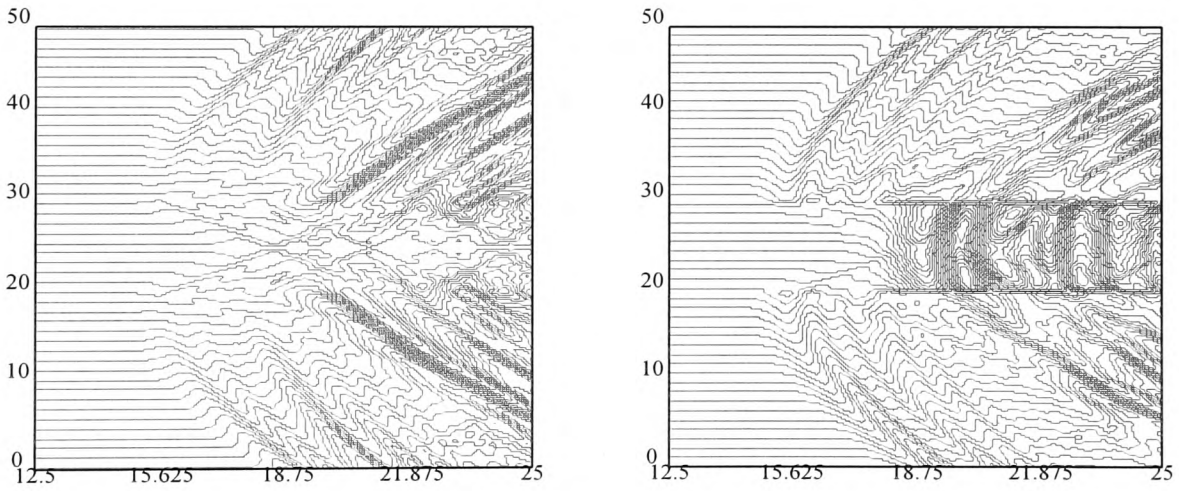

Figure (8.3) Synthetic horizontal and vertical seismograms generate the 2-D elastic staggered grid method program with the Reynolds's ABCs for one medium.

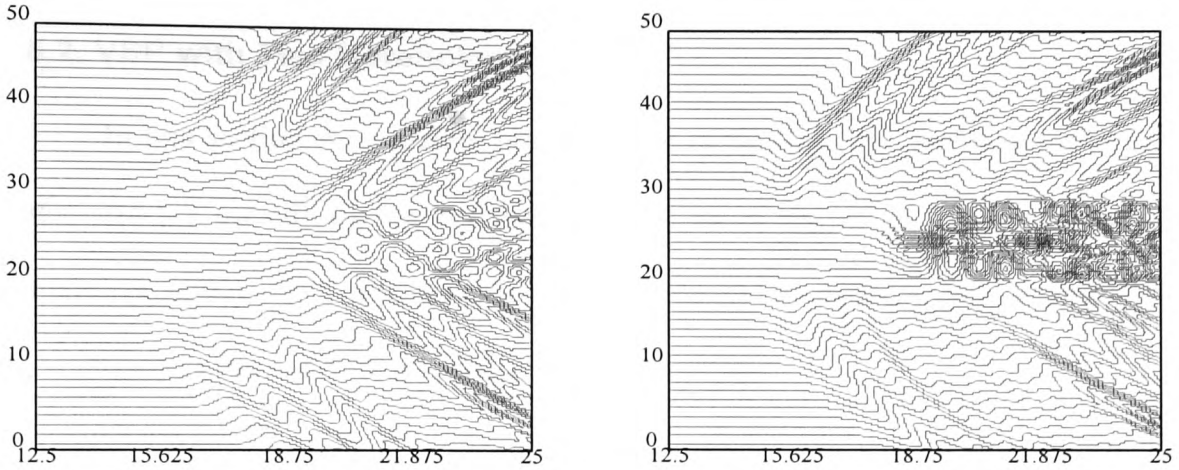

Figure (8.4) Synthetic horizontal and vertical seismograms generate the 2-D elastic VSM program with the Reynolds's ABCs for one medium.

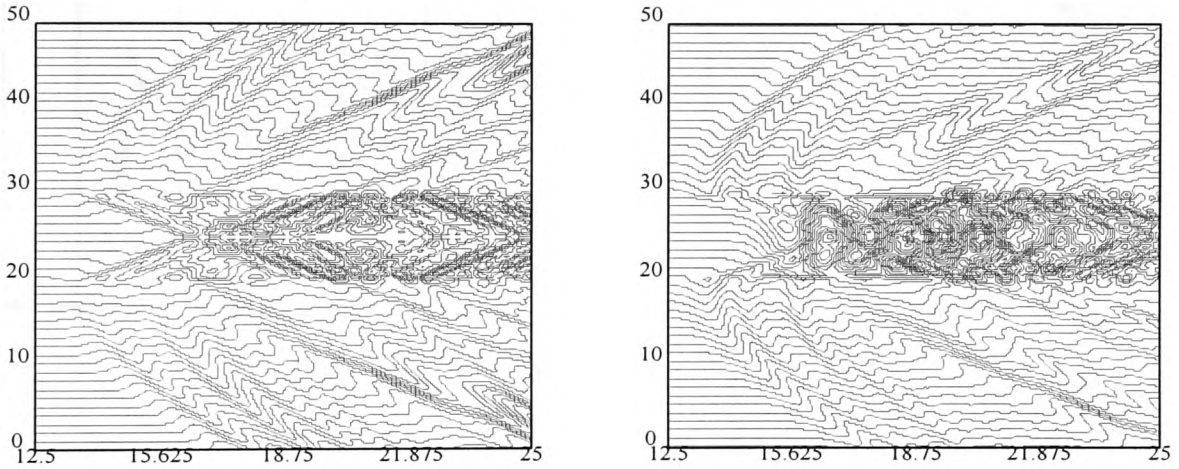

Figure (8.5) Synthetic horizontal and vertical seismograms generate the 2-D elastic staggered grid method program with the Reynolds's ABCs for two media.

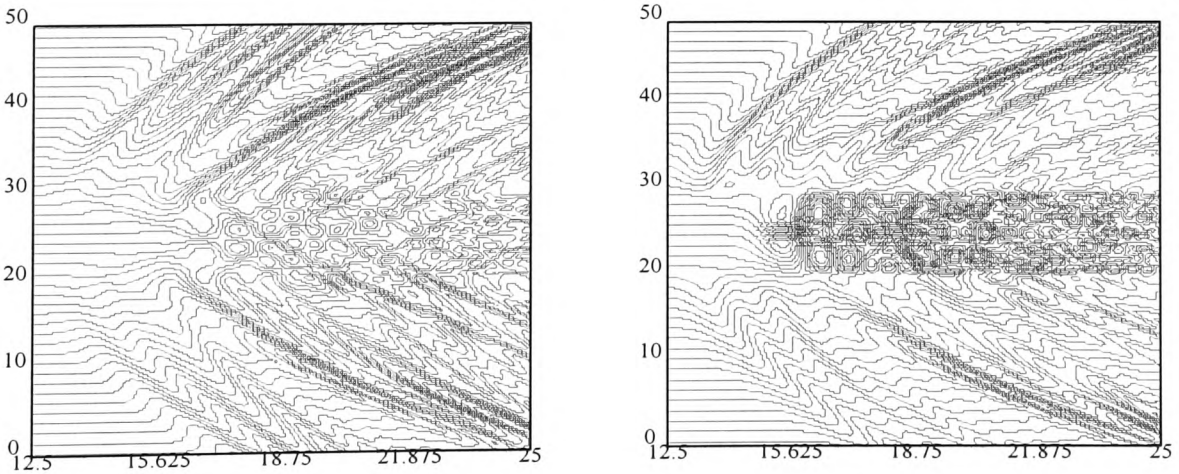

Figure (8.6) Synthetic horizontal and vertical seismograms generate the 2-D elastic VSM program with the Reynolds's ABCs for two media.

8.5.2. VSP with Two Boreholes

In this section we consider two borehole modelling. The boreholes contain sea-water and the outside of the borehole is shale as in Figure (8.7). The bottom layer contains limestone, and upper layer contains shale and boreholes contains sea-water for the multimedia geometry that is shown in Figure (8.8).

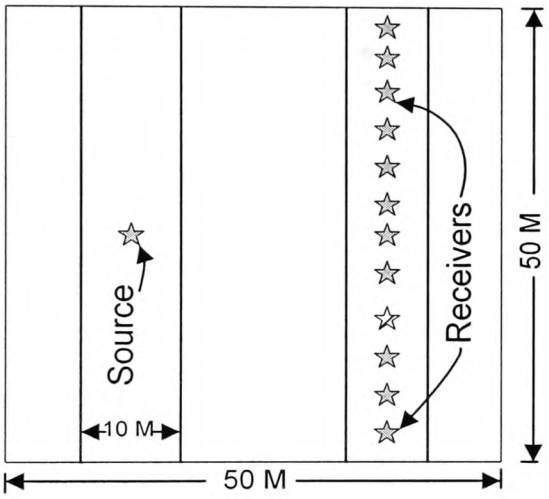

Figure (8.7) Physical model showing boreholes geometry used to generate seismograms in the 2-D elastic staggered grid and VSM programs for simple medium.

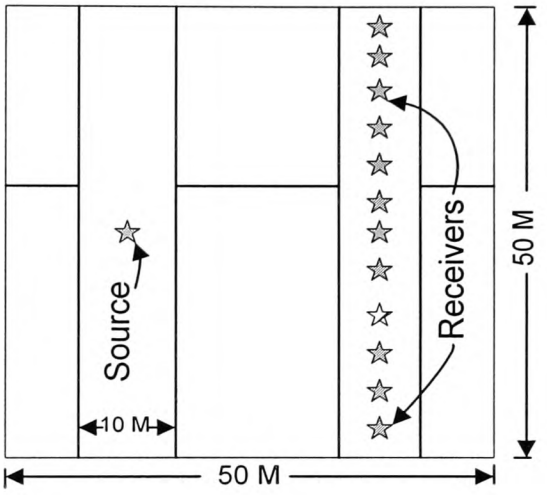

Figure (8.8) Physical model showing boreholes geometry used to generate seismograms in the 2-D elastic staggered grid and VSM programs for multimedia.

The two boreholes are located 25 m apart, and both are uncased with a 5 m radius and filled by sea-water (velocity 1500 m/s, density 1030 kg/m^3). Throughout the model, the exterior of the borehole has a compressional wave velocity of 2440 m/s and a shear wave velocity of 1400 m/s and density of 2450 kg/m^3 for shale, compressional wave velocity of 3400 m/s, shear wave velocity of 1730 m/s and density of 2400 kg/m^3 for limestone.

Figure (8.9) shows the results for the staggered grid method whilst Figure (8.10) shows the results for the VSM. These two seismograms exhibit VSP modelling.

Multimedia results are given for the staggered grid method in Figure (8.11) and for VSM in Figure (8.12).

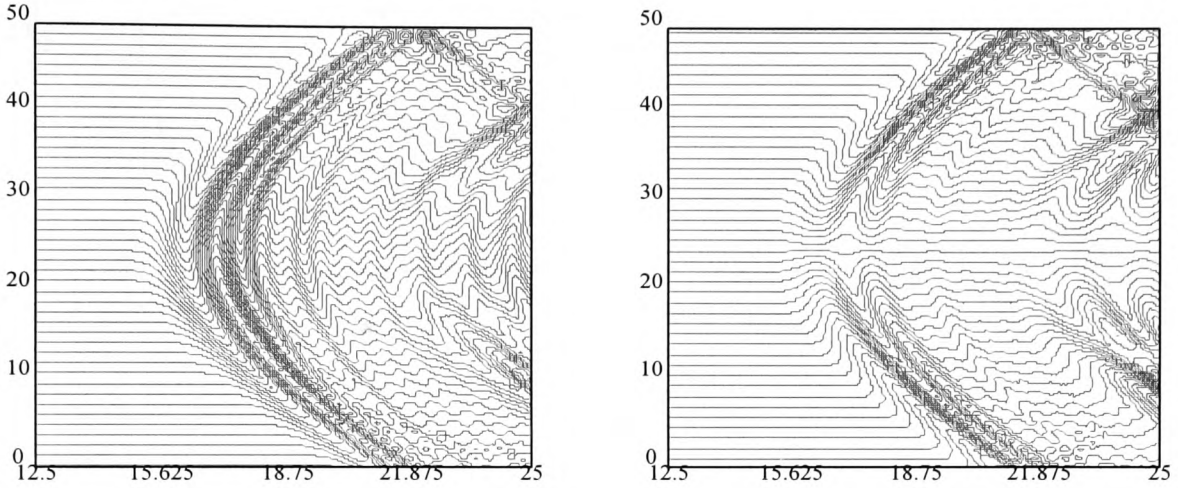

Figure (8.9) Synthetic horizontal and vertical seismograms generate the 2-D elastic staggered grid method program with the Reynolds's ABCs for simple media.

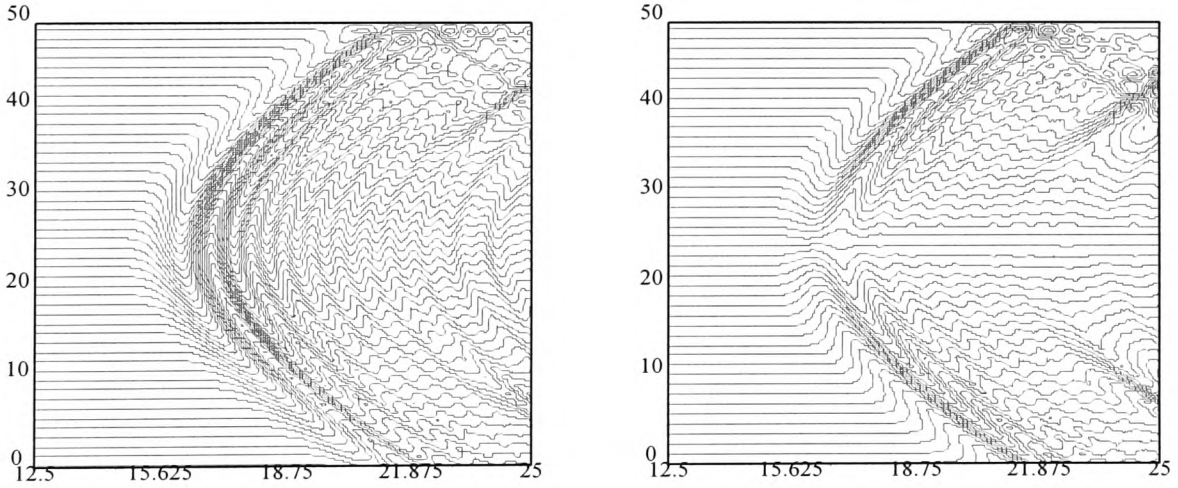

Figure (8.10) Synthetic horizontal and vertical seismograms generate the 2-D elastic VSM program with the Reynolds's ABCs for simple media.

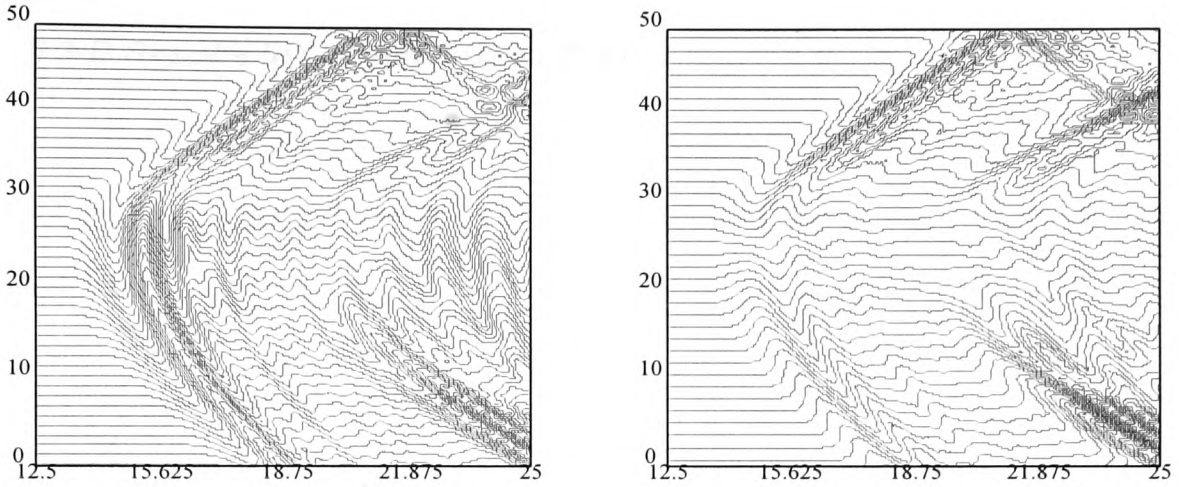

Figure (8.11) Synthetic horizontal and vertical seismograms generate the 2-D elastic staggered grid method program with the Reynolds's ABCs for multimedia.

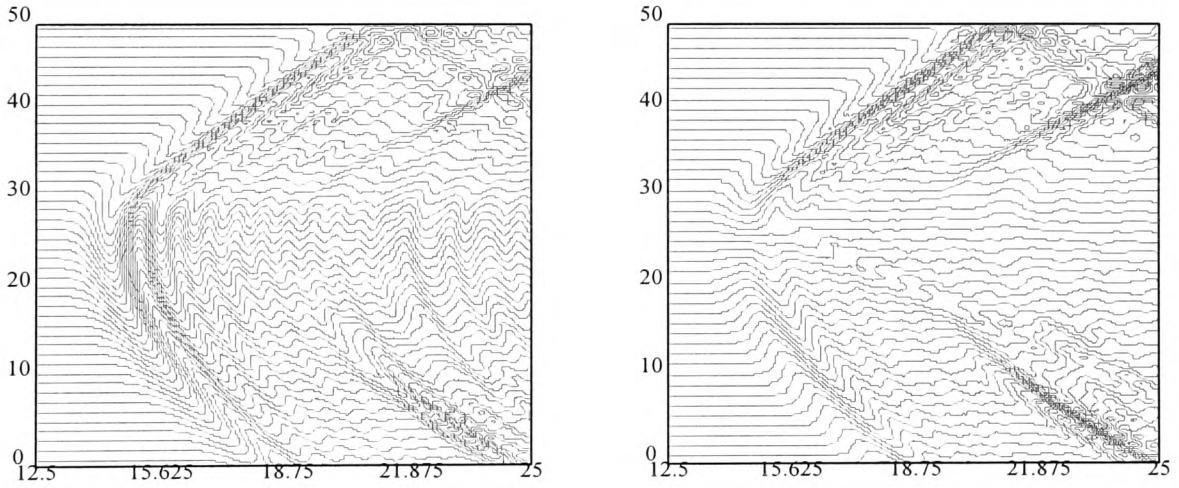

Figure (8.12) Synthetic horizontal and vertical seismograms generate the 2-D elastic VSM program with the Reynolds 's ABCs for multimedia.

We can see wave differences in the two media after 30 metres; the upper medium waves are slower than that for the lower medium. It can be seen clearly in Figures (8.11) and (8.12). Also all models free surface reflection waves visible.

8.6 3-D Results in Cartesian Coordinates

In this section we are concerned with both one and two borehole modelling. Numerical results are obtained by the staggered grid method and VSM for uncased boreholes.

8.6.1 One Borehole Results

In this section we employ one borehole modelling in 3-D Cartesian coordinates. The media properties are given in Table (8.1) from Yoon and McMechan [87].

Table 8.1. Physical Parameters of a Two Layer Elastic Model.

Layers	λ(Pa)	μ(Pa)	ρ(kg/m^3)	v_p(m/s)	v_s(m/s)
Sea-water	2.32E9	0.0	1030	1500	0.0
Shale	4.99E9	4.80E9	2450	2440	1400
Limestone	13.38E9	7.18E9	2400	3400	1730

The single medium inside the borehole contains sea-water and outside the borehole is shale as shown in Figure (8.13). The multimedia geometry is shown in Figure (8.14) with the upper layer being shale and the bottom layer limestone. The one medium model was solved by the staggered grid and VSM methods and Figure (8.15) shows the results obtained by the staggered grid method with the Reynolds's ABCs. Figure (8.16) shows the results the VSM with the horizontal and vertical seismograms for the Reynolds's ABCs. Both these figures exhibit similarity outside of the borehole, and inside of the borehole there is but a small difference. In Figures (8.15) and (8.16), the direct wave arrives after 18 ms, the free surface reflected wave arrives after 20 ms and the borehole reflected wave can be seen after 22 ms. Within the borehole all the waves arrive after the outside waves as expected.

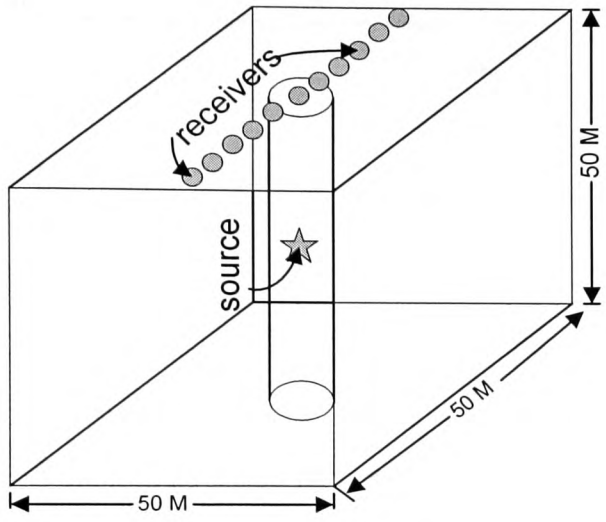

Figure (8.13) Physical model showing borehole geometry used to generate seismograms in the 3-D elastic staggered grid and VSM programs for one medium.

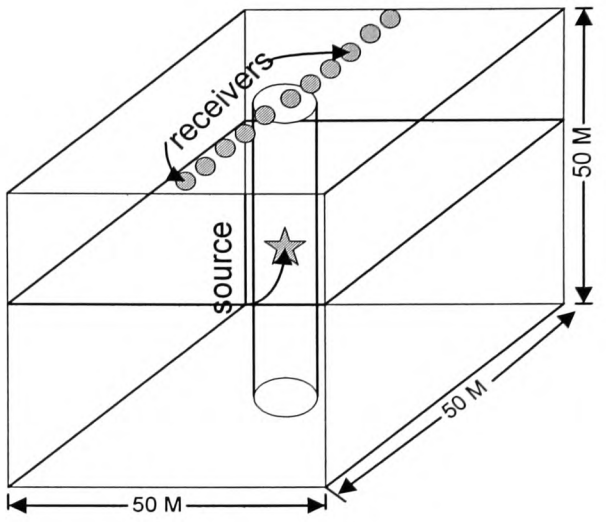

Figure (8.14) Physical model showing borehole geometry used to generate seismograms in the 3-D elastic staggered grid and VSM programs for multimedia.

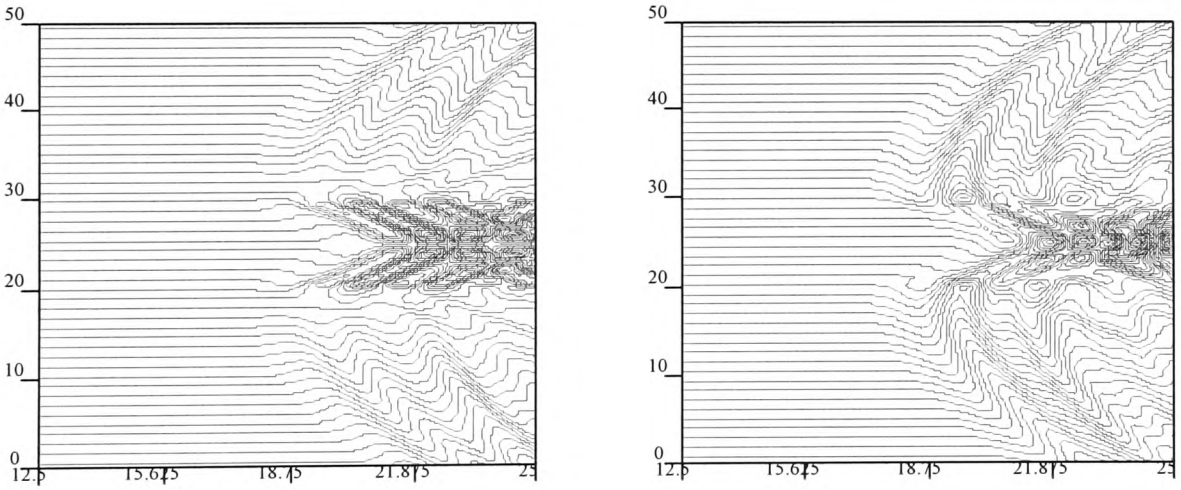

Figure (8.15) Synthetic horizontal and vertical seismograms generate the 3-D elastic staggered grid method program with the Reynolds's ABCs for one medium.

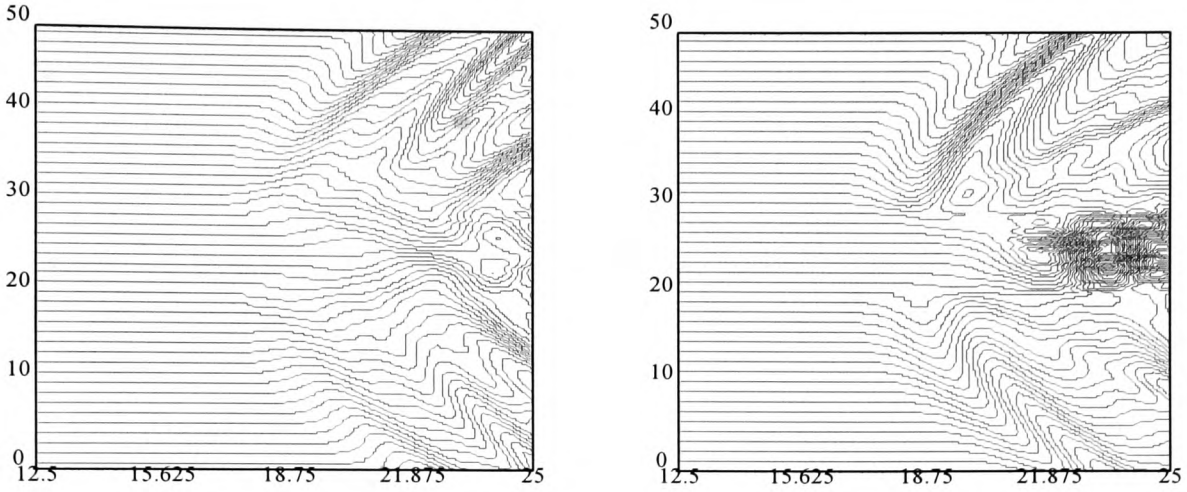

Figure (8.16) Synthetic horizontal and vertical seismograms generate the 3-D elastic VSM program with the Reynolds's ABCs for multimedia.

Figure (8.17) shows the horizontal and vertical displacements with Reynolds ABCs for the staggered grid method. The VSM results are shown in Figure (8.18) for the horizontal and vertical displacements. In Figures (8.17) and (8.18), the direct wave is seen to arrive after 18 ms, the free surface reflected wave arrive after 20 ms, and borehole interface reflected wave arrive after 22 ms. Within the borehole waves arrive after the exterior borehole waves. These two seismograms exhibit strong similarity with the one medium seismograms.

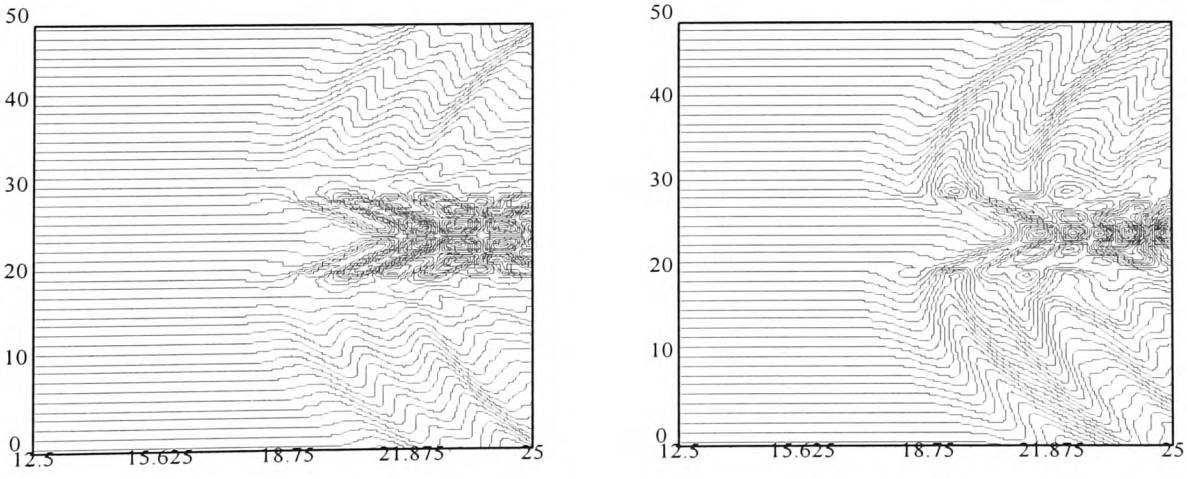

Figure (8.17) Synthetic horizontal and vertical seismograms generate the 3-D elastic staggered grid method program with the Reynolds's ABCs for multimedia.

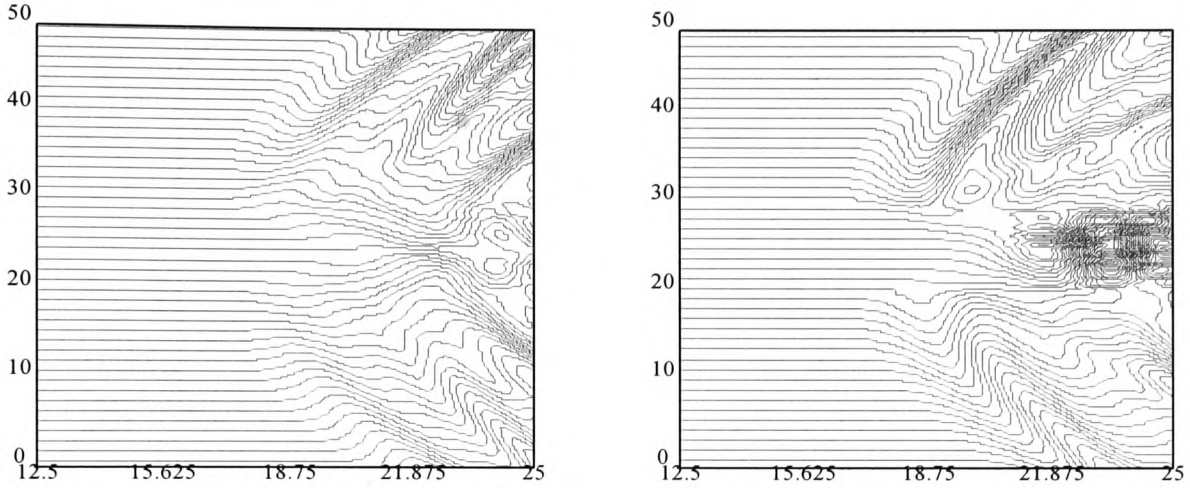

Figure (8.18) Synthetic horizontal and vertical seismograms generate the 3-D elastic VSM program with the Reynolds's ABCs for multimedia.

8.6.2 VSP with Two Boreholes

In this section we employ two borehole modelling in 3-D Cartesian coordinates. The media properties are given in Table (8.1) in the previous section. The one medium model results are shown in Figure (8.19) and the multimedia ones are shown in Figure (8.20). The two boreholes are located 25 m apart, and both are uncased with a 5 m radius and filled with sea-water. Outside of the borehole is shale for one medium with the upper layer being shale, and the bottom layer limestone for the multimedia model.

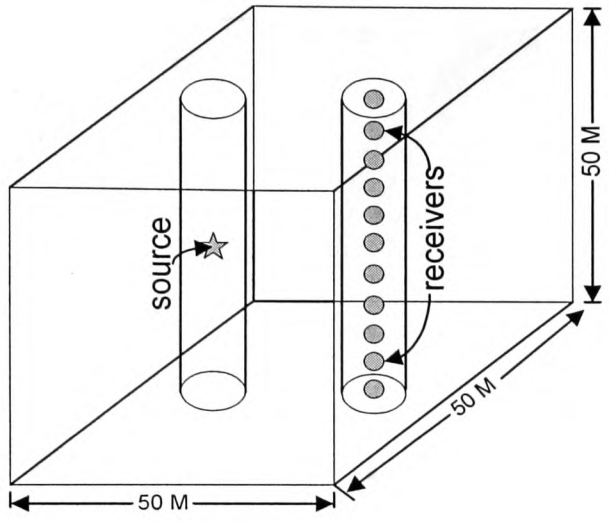

Figure (8.19) Physical model showing two borehole geometry used to generate seismograms in the 3-D elastic staggered grid VSM programs for one medium.

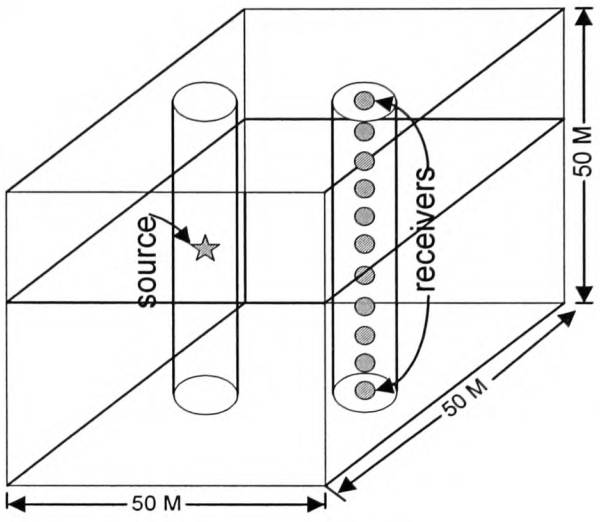

Figure (8.20) Physical model showing two borehole geometry used to generate seismograms in the 3-D elastic staggered grid VSM programs for multimedia.

Figure (8.21) shows the horizontal and vertical displacements with the Reynolds's ABCs for the staggered grid method and Figure (8.22) shows the results for the VSM with the Reynolds ABCs. For both seismograms, time runs along the horizontal axis and distance along the receivers vertical axis. These two seismograms are obtained for one medium. In Figures (8.21) and (8.22), the direct wave can be seen after 18 ms with the multiple reflected waves after 19, 20, 22 ms, respectively.

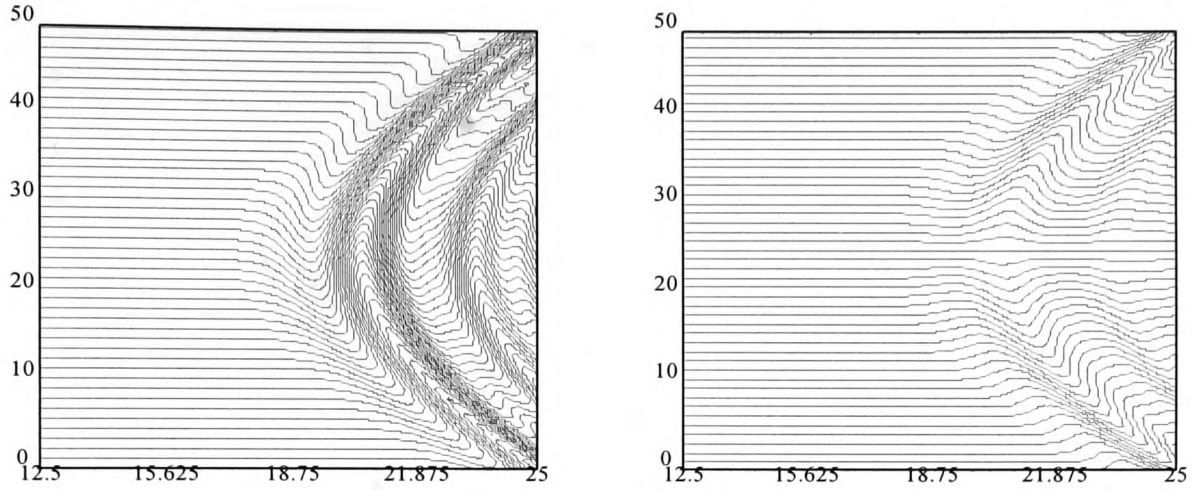

Figure (8.21) Synthetic horizontal and vertical seismograms generate the 3-D elastic staggered grid method program with the Reynolds's ABCs for one medium.

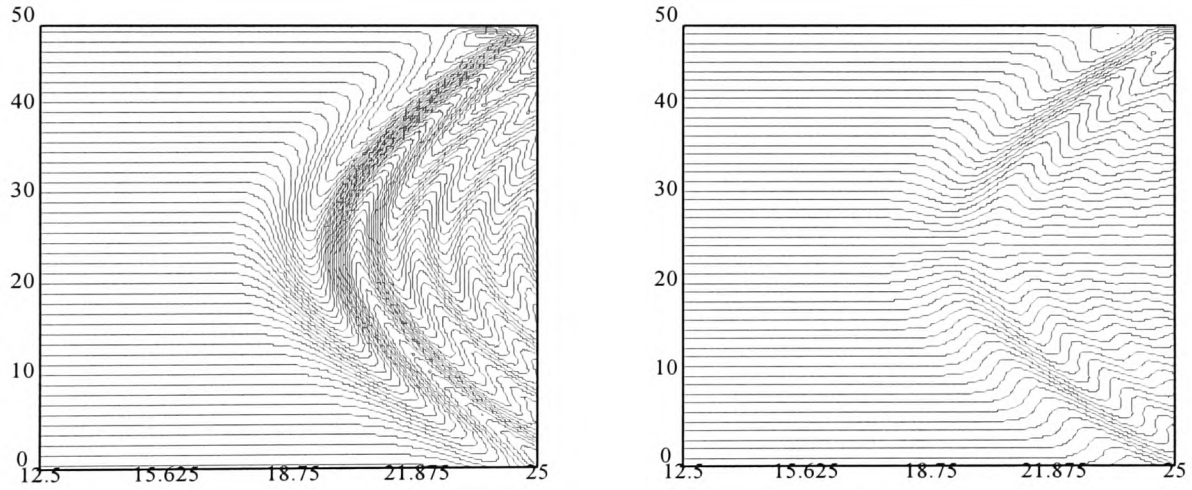

Figure (8.22) Synthetic horizontal and vertical seismograms generate the 3-D elastic VSM program with the Reynolds's ABCs for one medium.

The multimedia results are obtained by using the staggered grid method with the Reynolds ABCs which is shown in Figure (8.23). Figure (8.24) shows the horizontal and vertical displacements with the Reynolds's ABCs for the VSM. In these two seismograms, the direct wave arrives after approximately 18 ms, and the multiply reflected waves can be seen after 21, 22, 23 and 24 ms.

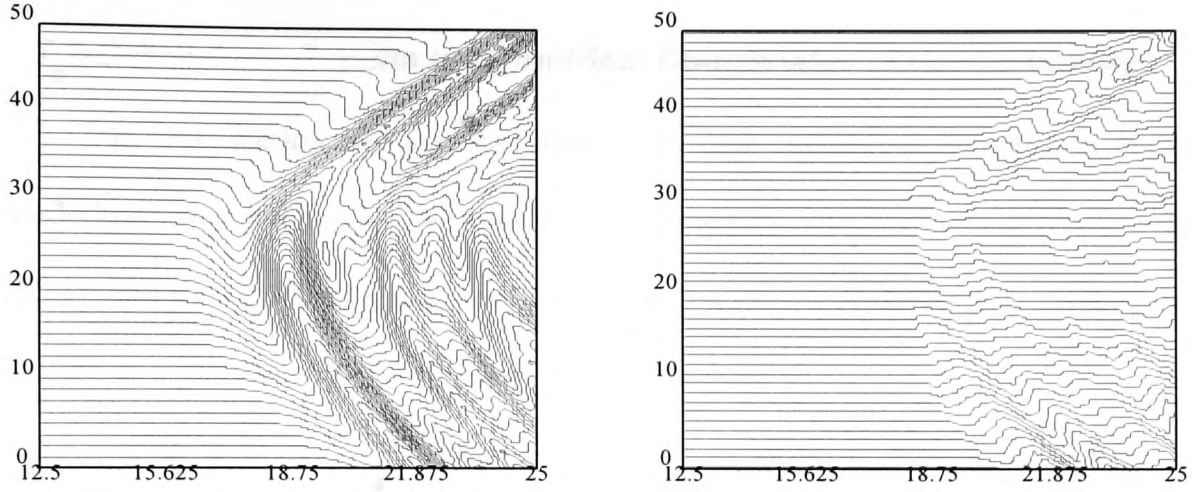

Figure (8.23) Synthetic horizontal and vertical seismograms generate the 3-D elastic staggered grid method program with the Reynolds's ABCs for multimedia.

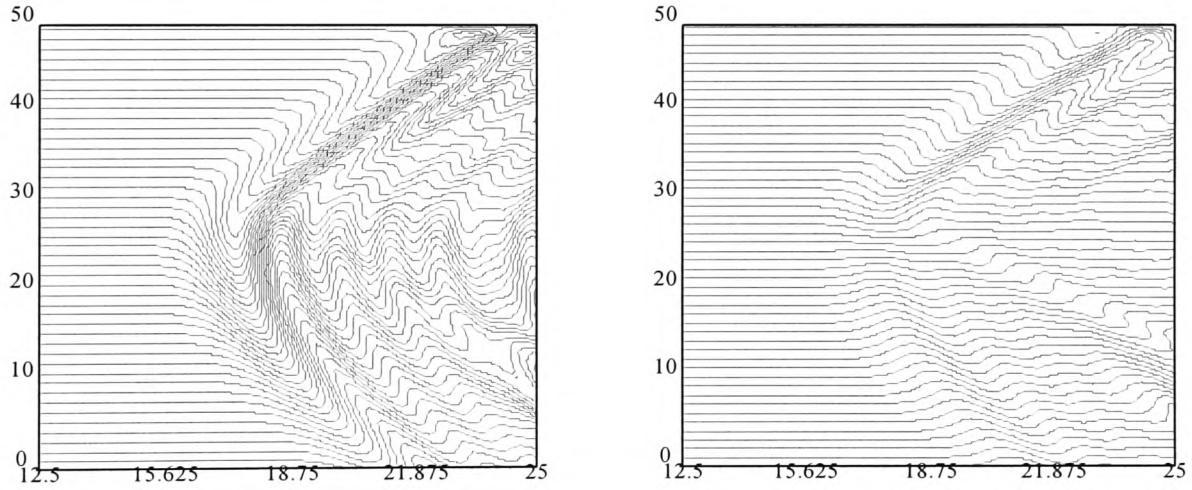

Figure (8.24) Synthetic horizontal and vertical seismograms generate the 3-D elastic VSM program with the Reynolds's ABCs for multimedia.

8.7 2-D Borehole Results in Cylindrical Coordinates (Axial Symmetry)

In this section we are concerned with 2-D cylindrical coordinates borehole modelling. The one medium and multimedia geometry of models are given in Figures (8.25), and (8.26) where a source is located on the radial symmetry axis with receivers located in a horizontal row 2 m below the free surface.

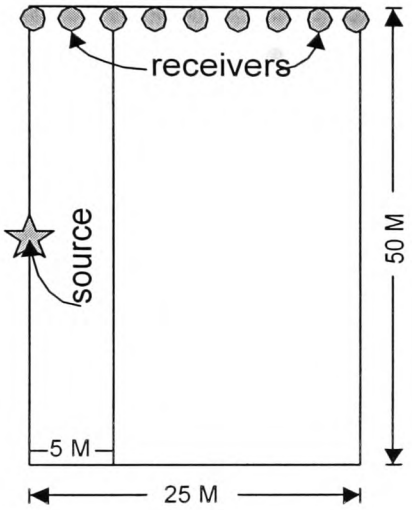

Figure (8.25) Physical model showing borehole geometry used to generate seismograms in 2-D cylindrical elastic staggered grid and VSM programs for one medium.

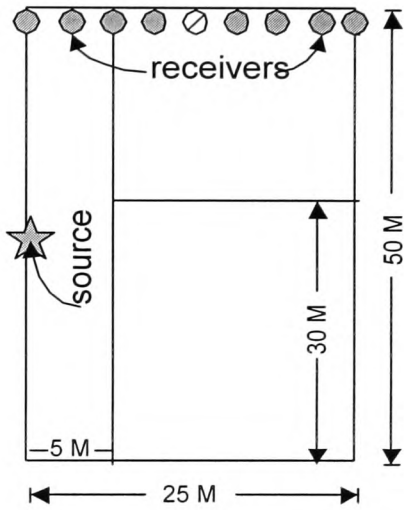

Figure (8.26) Physical model showing borehole geometry used to generate seismograms in 2-D cylindrical elastic staggered grid and VSM programs for multimedia.

All models used are 25 m wide by 50 m long (50 grid points at 0.5 m per grid point) and time series are generated out to 50 ms (500 time steps at 0.1 ms per time step). Accuracy of the synthetic seismograms is affected somewhat by grid dispersion. For P-wave propagation the derived expression for the maximum grid size (h) allowable in order to have acceptable grid dispersion is (Alford et al.[2], Stephen et al. [72]) $h = v_s / 10 f_{max}$, where v_s is the minimum body-wave velocity in the grid and f_{max} the maximum frequency of the source, generally defined as the upper half-power frequency. The 10 in

The 10 in the denominator represents the number of the grid points per wavelength of the shortest wavelength body wave.

The synthetic seismograms are obtained by the staggered grid method with the Reynolds's ABCs which is shown in Figure (8.27). Figure (8.28) shows the results for the VSM seismograms by using the Reynolds's ABCs. In Figures (8.27) and (8.28), the direct wave arrives after 18 ms, the free surface reflected wave can be seen after 24 ms, and within the borehole waves arrive after the exterior borehole waves. As is expected, the two results exhibit close similarity.

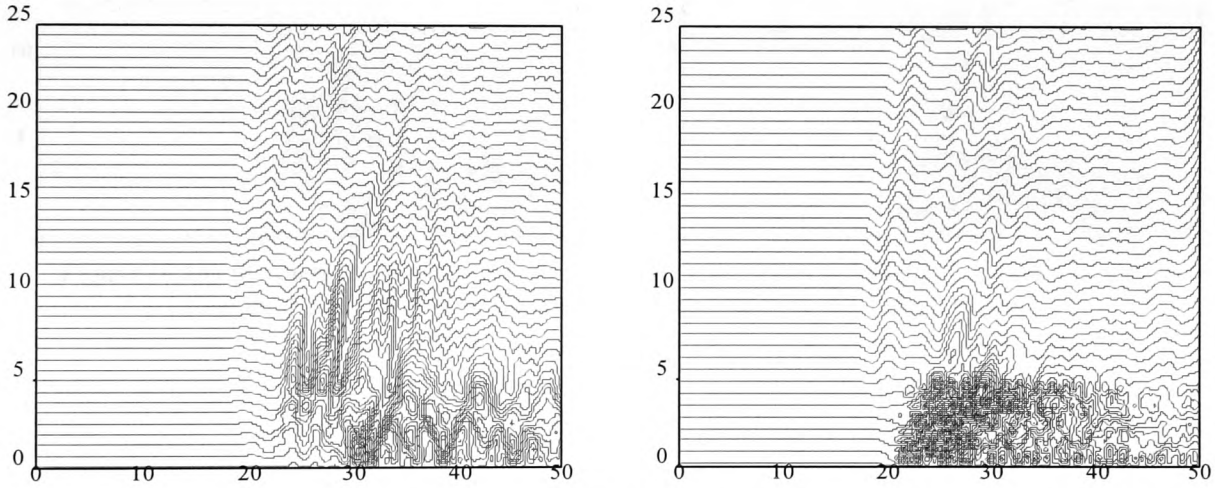

Figure (8.27) Synthetic horizontal and vertical seismograms generate the 2-D cylindrical elastic staggered grid method program with the Reynolds's ABCs for one medium.

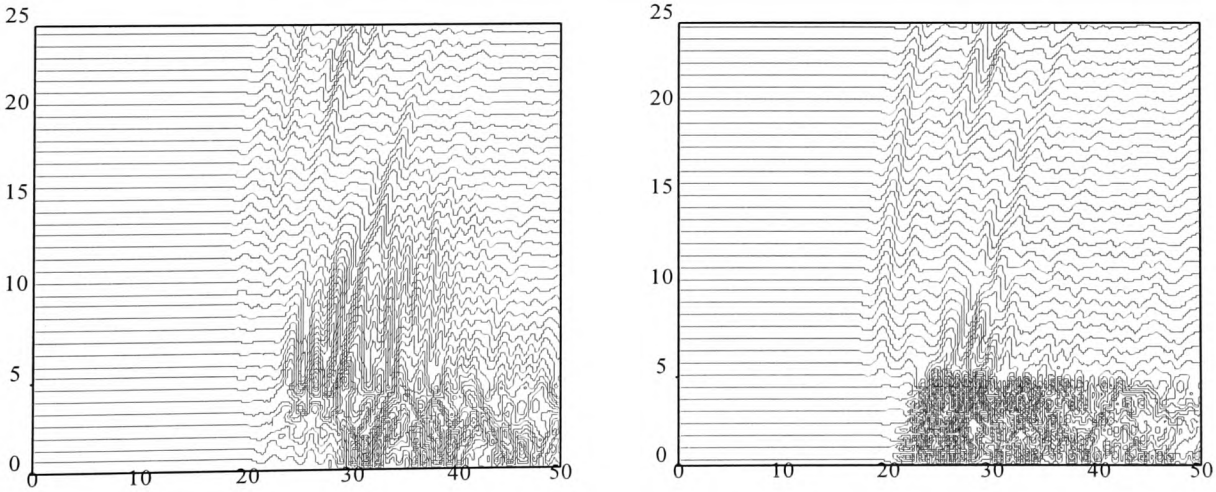

Figure (8.28) Synthetic horizontal and vertical seismograms generate the 2-D cylindrical elastic VSM program with the Reynolds's ABCs for one medium.

The multimedia results are obtained by using the staggered grid method and VSM which are shown in Figures (8.29) and (8.30), respectively. In both Figures (8.29) and (8.30), the direct wave can be seen at 18 ms, the free surface reflected wave can be seen after 24 ms. Again the borehole waves arrive after the exterior borehole waves. The one medium results and multimedia results again show good similarity.

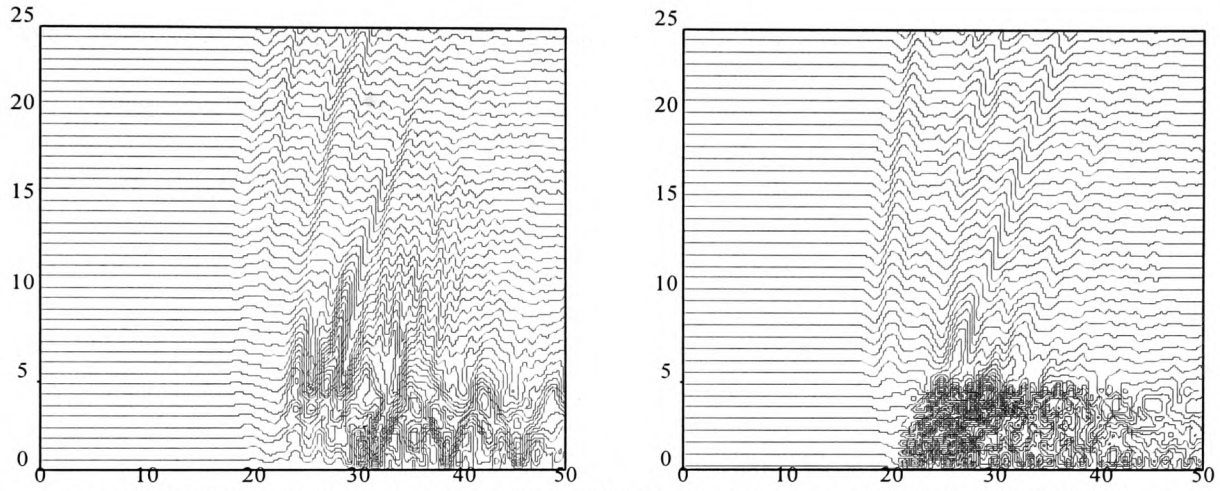

Figure (8.29) Synthetic horizontal and vertical seismograms generate the 2-D cylindrical elastic staggered grid method program with the Reynolds's ABCs for multimedia.

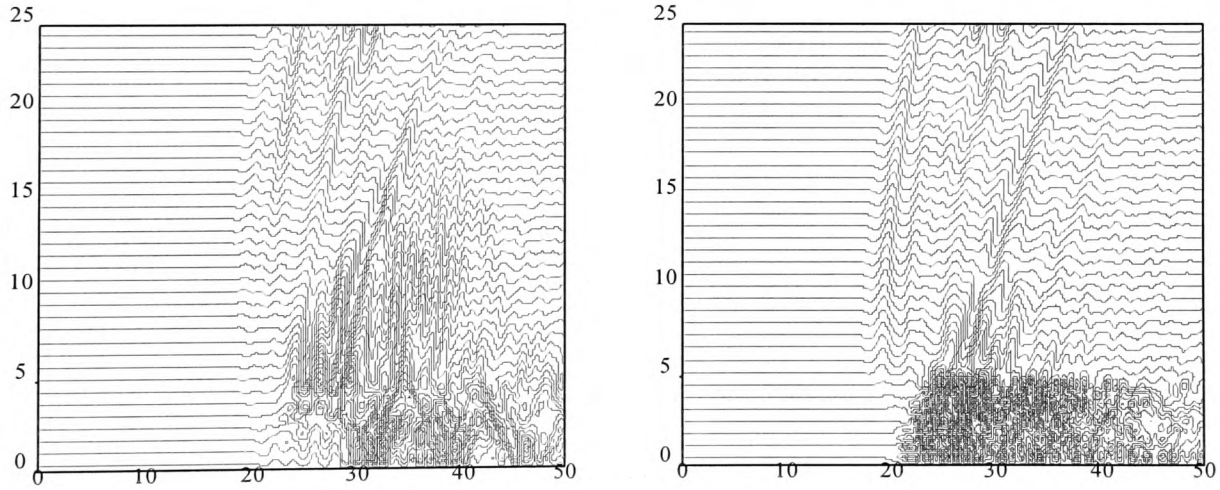

Figure (8.30) Synthetic horizontal and vertical seismograms generate the 2-D cylindrical elastic VSM program with the Reynolds's ABCs for multimedia.

We will employ two boreholes in 3-D cylindrical coordinates in the next section.

8.8 3-D Results in Cylindrical Coordinates

In this section we are concerned with the two borehole modelling with one media and multimedia. A source is located in sea-water on the axis of the borehole and the receivers are located vertically in sea-water on the axis of other borehole. Multimedia geometry contains outside the borehole, upper layer is shale and bottom layer is limestone. The boreholes inside contains sea-water. The grid size and time increment are 0.5 m and 0.1 ms respectively and the physical geometry of modelling are given in Figures (8.31) and (8.32), respectively.

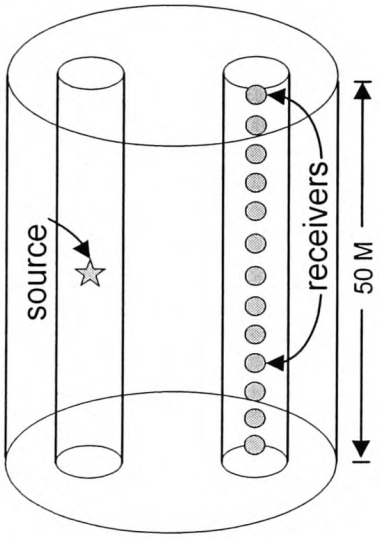

Figure (8.31) Physical model showing two borehole geometry used to generate seismograms in 3-D cylindrical elastic staggered grid and VSM programs for one medium.

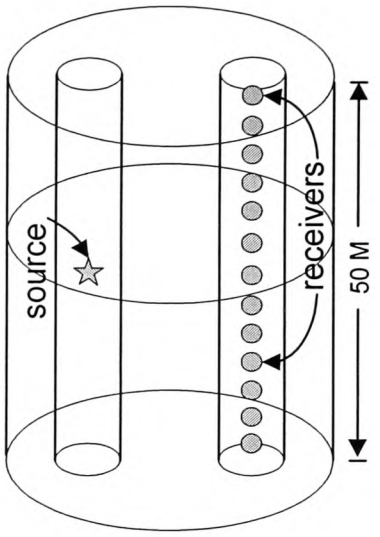

Figure (8.32) Physical model showing two borehole geometry used to generate seismograms in 3-D cylindrical elastic staggered grid and VSM programs for multimedia.

Figure (8.33) shows the horizontal and vertical one medium results for the staggered grid method with the Reynolds's ABCs and the VSM results in Figure (8.34). The direct wave arrives after approximately 18 ms, and the multiple reflected waves can be seen arriving after the direct wave. The free surface reflected wave can be seen approximately 35 ms.

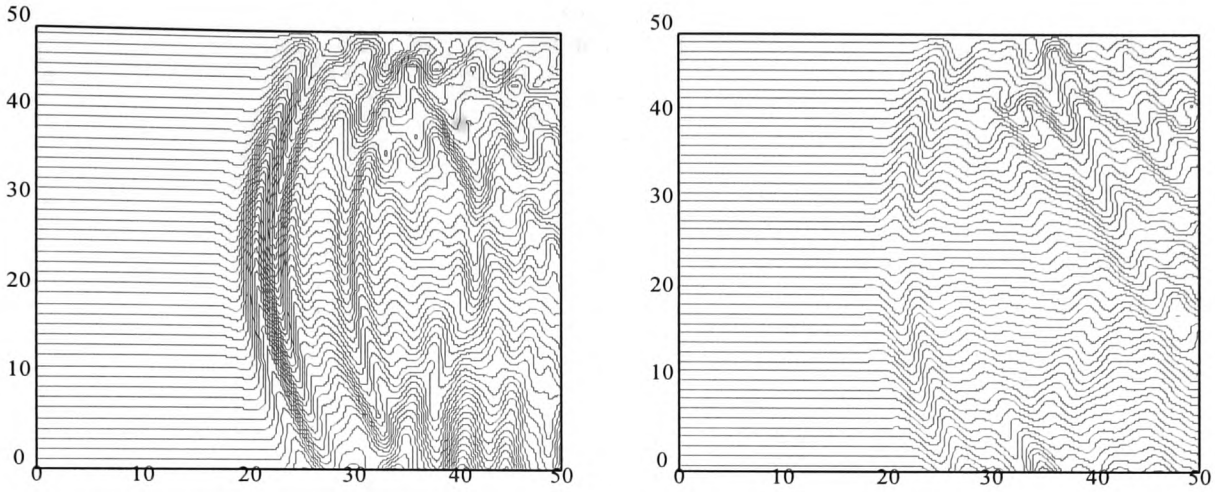

Figure (8.33) Synthetic horizontal and vertical seismograms generate the 3-D cylindrical elastic staggered grid method program with the Reynolds's ABCs for one medium.

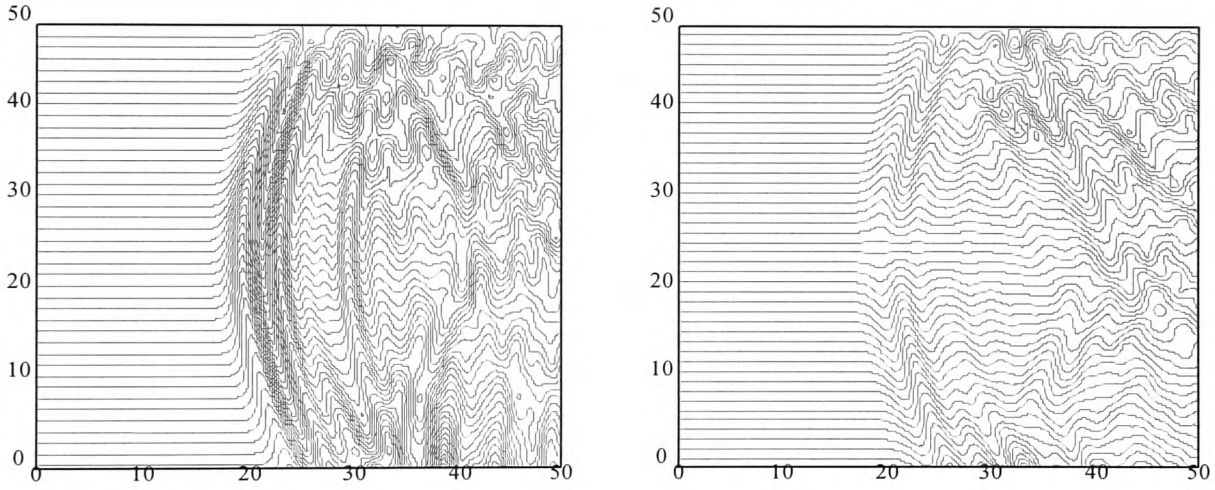

Figure (8.34) Synthetic horizontal and vertical seismograms generate the 3-D cylindrical elastic VSM program with the Reynolds's ABCs for one medium.

The numerical results have been obtained by using the staggered grid and VSM methods for the multimedia. Figure (8.35) shows the horizontal and vertical displacements for the staggered grid method. Figure (8.36) shows the horizontal and vertical displacements for the VSM. In both Figures (8.35) and (8.36), the direct wave arrive at the same time as the one medium results. The upper side of the direct wave arrives after the bottom side because the upper side velocity is lower than that of the bottom side.

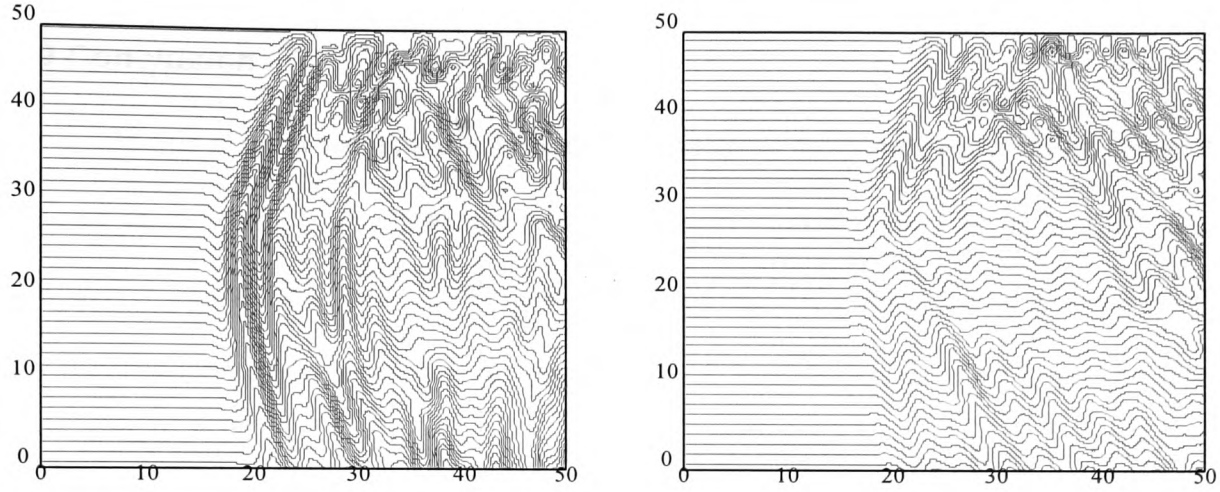

Figure (8.35) Synthetic horizontal and vertical seismograms generate the 3-D cylindrical elastic staggered grid method program with the Reynolds's ABCs for multimedia.

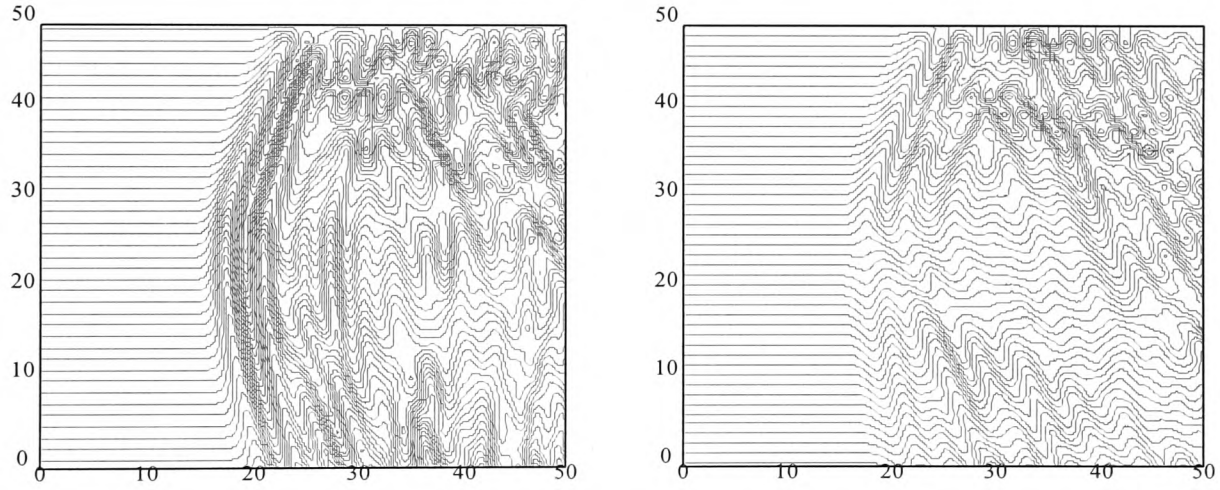

Figure (8.36) Synthetic horizontal and vertical seismograms generate the 3-D cylindrical elastic VSM program with the Reynolds's ABCs for multimedia.

8.9 Conclusion

In this chapter we examined borehole modelling for one medium and multimedia models in 2-D and 3-D Cartesian and cylindrical coordinates. Our new approaches (staggered grid & box, and VSM) gave very good results showing clearly the effect of the borehole. Our new approach (staggered grid & box) is found to be generally better than the VSM, especially inside the borehole. The waves are particularly difficult to synthesise in borehole environments because the VSM was not stable for large contrasts in Poisson's ratio, such as at fluid-solid interfaces (Stephen [71]). Borehole interface waves, however, can be seen clearly. The results in this chapter are believed to be novel. Two main approaches have been used by others to model borehole geometries; one using the inside of the borehole and the other the borehole exterior. We managed to model successfully the combined situation.

CHAPTER 9

SPECIAL CONSIDERATIONS

9.1. Introduction

In this chapter, we consider the problem of obtaining synthetic seismograms using the acoustic and elastic wave equations in regions containing regular and irregular interfaces. In reality, rock structures are not plane laminated layers. We now consider more realistic rock models which will prove a severe test of our numerical approaches. In particular we shall examine more closely the interfaces between media. We consider the heterogeneous schemes, in which the same formulae are used for all grid points except at the boundaries of a media. These formulae represent a discrete form of the equations of motion for heterogeneous media. The discontinuities are taken into account by spatial variation of the material parameters (Lame parameters and density). In most schemes, special formulas are employed at the free surface (Sochacki et al [**68**], Levander [**44**] and Zahradnik et al. [**90**]). A few schemes use the same formulae literally everywhere, including the free surface.

In most heterogeneous schemes, the material parameters are represented by their actual local values or by arithmetic averages from two grid points (Kelly et al. [**37**], Stephen, [**71**], Virieux, [**82**], Levander [**44**], Sochacki et al. [**67**], and Zahradnik et al. [**90**]). The accuracy problems are documented for heterogeneous schemes of this type.

Serious accuracy problems at solid-solid and liquid-solid interface were found by Stephen, [71,73].

The acoustic and elastic internal interfaces discontinuities are formulated by Sochacki et al. [68]. We use the staggered grid method for an elastic case and the standard FDM method for an acoustic case. The numerical results will be compared with those of other researchers.

9.2 The 2-D Acoustic Case

For the 2-D problem, we assume the well-defined interfaces can be described locally by a function f(x,z) = 0 as shown in Figure (9.1).

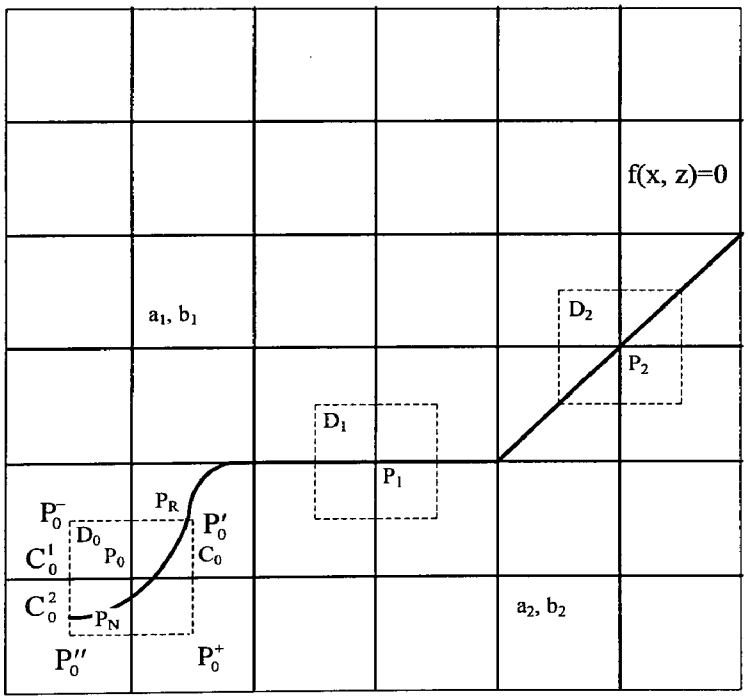

Figure (9.1) A cross-section of the model where two materials are in contact along a curved boundary. The density, wave velocities, and Lame parameters change only at the boundary.

The 2-D acoustic wave equation is given by

$$a\frac{\partial^2 u}{\partial t^2} = b\left(\frac{\partial^2 u}{\partial x^2} + \frac{\partial^2 u}{\partial z^2}\right) \tag{9.1}$$

where $a = 1/\rho v_p^2$ and $b = 1/\rho$ for the acoustic equation with interfaces. We consider Figure (9.1) and determine approximations at the points P_0, P_1, and P_2 for equation (9.1) (Sochacki et al. [**68**]) with interface conditions. Integrating over the domain D_0 gives

$$\int_{D_0} a u_{tt} dA = \int_{D_0} \nabla\cdot(b\nabla u) dA . \tag{9.2}$$

Performing the integration on the right-hand side first gives

$$\int_{D_0} \nabla\cdot(b\nabla u) dA = \oint_{C_0} b\nabla \mathbf{u}\cdot\mathbf{n} dA$$

Also

$$\int_{D_0} \nabla\cdot(b\nabla u) dA = \oint_{C_0^1} (b\nabla \mathbf{u})\cdot\mathbf{n_0^-} ds + \oint_{f(x,z)=0} b\nabla \mathbf{u}\cdot\frac{\nabla f}{\|\nabla f\|} ds + \oint_{C_0^2} b\nabla \mathbf{u}\cdot\mathbf{n_0^+} ds$$
$$+ \oint_{f(x,z)=0} b\nabla \mathbf{u}\cdot\left(-\frac{\nabla f}{\|\nabla f\|}\right) ds$$

which simplifies to give

$$\int_{D_0} \nabla\cdot(b\nabla u) dA = \oint_{C_0^1} b\nabla \mathbf{u}\cdot\mathbf{n_0^-} ds + \oint_{C_0^2} b\nabla \mathbf{u}\cdot\mathbf{n_0^+} ds$$

since $b\nabla \mathbf{u}\cdot\mathbf{n}$ is continuous along the interface. Splitting the integral on the right-hand side gives

$$\oint_{C_0^1} b\nabla u\cdot n_0^- ds + \oint_{C_0^2} b\nabla u\cdot n_0^+ ds = \int_{P_N}^{P_0^-} b_1\nabla u\cdot(-1,0) ds + \int_{P_0^-}^{P_R} b_1\nabla u\cdot(0,-1) ds$$

$$+ \int_{P_R}^{P_0'} b_2\nabla u\cdot(0,-1) ds + \int_{P_0'}^{P_0^+} b_2\nabla u\cdot(1,0) ds + \int_{P_0^+}^{P_0''} b_2\nabla u\cdot(0,1) ds + \int_{P_0''}^{P_N} b_2\nabla u\cdot(-1,0) ds$$

which simplifies to give

$$\int_{D_0} \nabla\cdot(b\nabla u)dA = \int_{Z_N}^{Z_0^-} -b_1 u_x(-dz)\Big|_{x=x_0^-} + \int_{X_0^-}^{x_R} -b_1 u_z dx\Big|_{z=z_0^-} + \int_{x_R}^{x_0^+} -b_2 u_z dx\Big|_{z=z_0^-}$$

$$+ \int_{Z_0^-}^{Z_0^+} b_2 u_x dz\Big|_{x=x_0^+} + \int_{x_0^+}^{x_0^-} b_2 u_z(-dx)\Big|_{z=z_0^+} + \int_{Z_0^+}^{Z_N} -b_2 u_x(-dz)\Big|_{x=x_0^-}$$

Performing the integration on the right-hand side gives

$$\int_{D_0} \nabla\cdot(b\nabla u)dA = -b_1 u_x\left(x_0^-, z_1\right)\left(z_N - z_0^-\right) - b_1 u_z\left(x_1, z_0^-\right)\times\left(x_N - x_0^-\right)$$

$$- b_2 u_z\left(x_2, z_0^-\right)\left(x_0^+ - x_R\right) + b_2 u_x\left(x_0^+, z_2\right)\left(z_0^+ - z_0^-\right)$$

$$+ b_2 u_z\left(x_3, z_0^+\right)\left(x_0^+ - x_0^-\right) - b_2 u_x\left(x_0^-, z_3\right)\left(z_0^+ - z_N\right),$$

where we have used the mean value theorem for integrals and $y_0^{\pm} = y_0 \pm \Delta x/2$, (y = x or z); $P_L = (x_L, z_L)$, L = R, N, $P_0^{\pm} = \left(x_0^{\pm}, z_0^{\pm}\right), P_0' = \left(x_0^+, z_0^-\right)$ and $P_0'' = \left(x_0^-, z_0^+\right)$. Dropping the small grid length terms (see Figure (9.1)), using centred differences, and replacing z_N with z_0^+, x_R with x_0^+, z_1, z_2, z_3 with z_0, and x_1 and x_3 with x_0 gives for the right-hand side of equation (9.2)

$$\int_{D_0} \nabla\cdot b(\nabla u)dA \approx -b_1\left(\frac{u_{i,j} - u_{i-1,j}}{\Delta x}\right)\Delta z + b_2\left(\frac{u_{i+1,j} - u_{i,j}}{\Delta x}\right)\Delta z$$
$$- b_1\left(\frac{u_{i,j} - u_{i,j-1}}{\Delta z}\right)\Delta x + b_2\left(\frac{u_{i,j+1} - u_{i,j}}{\Delta z}\right)\Delta x \qquad (9.3)$$

Splitting the integral on the left-hand side of equation (9.2) gives

$$\int_{D_0} a u_{tt} dA = \int_{D_0^2} a_2 u_{tt} dA + \int_{D_0^1} a_1 u_{tt} dA \qquad (9.4)$$

which simplifies to

$$\int_{D_0} a u_{tt} dA = a_2 u_{tt}(x_2, z_2, t)\Delta D_0^2 + a_1 u_{tt}(x_1, z_1, t)\Delta D_0^1$$

$$\int_{D_0} a u_{tt} dA = a_2\left[u_{tt}(x_0,z_0,t) + O(\Delta x \Delta z)\right]\Delta D_0^2 + a_1\left[u_{tt}(x_0,z_0,t) + O(\Delta x \Delta z)\right]\Delta D_0^1$$

then

$$\int_{D_0} a u_{tt} dA = (\alpha a_2 + \beta a_1) u_{tt}(x_0,z_0,t) + O(\Delta x \Delta z)$$

which simplifies to give

$$\int_{D_0} a u_{tt} dA = A u_{tt}(x_0,z_0,t)\Delta x \Delta z,$$

where we have used the mean value theorem for integrals and $\alpha = \Delta D_0^2$, $\beta = \Delta D_0^1$ and equal the area of D_0^2 and D_0^1. Equations (9.3) and (9.4) give

$$\begin{aligned} A u_{tt} = {} & \frac{1}{\Delta x^2}\left[b_2 u_{i+1,j} - (b_1 + b_2)u_{i,j} + b_1 u_{i-1,j}\right] \\ & + \frac{1}{\Delta z^2}\left[b_2 u_{i,j+1} - (b_1 + b_2)u_{i,j} + b_1 u_{i,j-1}\right] \end{aligned} \tag{9.5}$$

For the horizontal interface at P_1, the finite-difference equation that results on performing the above on equation (9.5) with D_0 replaced by D_1 gives

$$\begin{aligned} \left(\frac{a_1 + a_2}{2}\right) u_{tt}(x_1,z_1,t) = {} & \frac{1}{\Delta x^2}\left[\left(\frac{b_1 + b_2}{2}\right)\left(u_{i+1,j} + u_{i-1,j}\right) - (b_1 - b_2)u_{i,j}\right] \\ & + \frac{1}{\Delta z^2}\left[b_2 u_{i,j+1} - (b_1 + b_2)u_{i,j} + b_1 u_{i,j-1}\right], \end{aligned} \tag{9.6}$$

For the diagonal interface at P_2, the finite-difference equation is the same as equation (9.3), with $A = (a_1 + a_2)/2$. For the vertical interface, the finite-difference equation is similar to horizontal interface equation (9.5)

$$\begin{aligned} \left(\frac{a_1 + a_2}{2}\right) u_{tt}(x_1,z_1,t) = {} & \frac{1}{\Delta z^2}\left[\left(\frac{b_1 + b_2}{2}\right)\left(u_{i,j+1} + u_{i,j-1}\right) - (b_1 - b_2)u_{i,j}\right] \\ & + \frac{1}{\Delta x^2}\left[b_2 u_{i+1,j} - (b_1 + b_2)u_{i,j} + b_1 u_{i-1,j}\right], \end{aligned} \tag{9.7}$$

9.3 The 2-D Elastic case

The physical requirement at an interface for elastic P-SV wave propagation is that $(P_{xx}, P_{xz})\cdot\mathbf{n}$ and $(P_{zx}, P_{zz})\cdot\mathbf{n}$ must be continuous (Sochacki et al. [**68**]). For horizontal and vertical interfaces, these conditions can be handled with finite-difference schemes similar to those presented by Vidale and Clayton [**78**] and Sochacki et al. [**67**] for free surfaces. For slanted and curved interfaces, these schemes much more difficult to employ. This kind of interfaces were presented by Sochacki et al. [**68**]. We briefly show that these interfaces for equation (6.1). The equation (6.1) is written in divergence form as

$$\begin{aligned} \rho u_{tt} &= \nabla\cdot(P_{xx}, P_{xz}) \\ \rho w_{tt} &= \nabla\cdot(P_{zx}, P_{zz}) \end{aligned} \tag{9.8}$$

and again integrate using the divergence theorem. The mixed derivatives complicates the integration and more care has to be used in integrating the P_{xz} and P_{zx} terms. Here, we consider the u component of equation (9.8) as the point in Figure (9.1). This is done to minimise the notation, but it is straightforward to extend the ideas to points P_0 and P_2. We denote $P_1 = (i\Delta x, j\Delta z) = (x_0, z_0)$ and the boundary of D_1 including the interface by C_1. Integrating the u component of equation (9.8) over D_1 and following the same procedure used in the acoustic case, we obtain

$$\int_{D_1} \rho u_{tt}\, dA = \int_{D_1} \nabla\cdot(P_{xx}, P_{xz})\, dA$$

Performing the integration on the right-hand side first gives

$$\int_{D_1} \nabla\cdot(P_{xx}, P_{xz})\, dA = \oint_{C_1} (P_{xx}, P_{xz})\cdot\mathbf{n}\, ds = \oint_{C_1} \mathbf{P}\cdot\mathbf{n}\, ds$$

Using u'' to denote u_{tt}. We approximate the left-hand side by

$$\int_{D_i} \rho u_{tt} dA \approx u''_{i,j} \int_{D_i} \rho dA \approx u''_{i,j} \bar{\rho} \Delta x \Delta z = \frac{\rho_1 + \rho_2}{2} u''_{i,j} \Delta x \Delta z \tag{9.9}$$

and perform the integration on the right-hand side, remembering the continuity of **P** along the horizontal interface, to get

$$\begin{aligned} \oint_{C_i} \mathbf{P} \cdot \mathbf{n} ds = & \int_{(x_0^+, z_0)}^{(x_0^+, z_0^+)} \mathbf{P} \cdot (1,0) ds + \int_{(x_0^-, z_0^+)}^{(x_0^+, z_0^+)} \mathbf{P} \cdot (0,1) ds + \int_{(x_0^-, z_0^-)}^{(x_0^-, z_0)} \mathbf{P} \cdot (-1,0) ds \\ & + \int_{(x_0^-, z_0^-)}^{(x_0^-, z_0)} \mathbf{P} \cdot (-1,0) ds + \int_{(x_0^-, z_0^-)}^{(x_0^+, z_0^-)} \mathbf{P} \cdot (0,-1) + \int_{(x_0^+, z_0^-)}^{(x_0^+, z_0)} \mathbf{P} \cdot (1,0) \end{aligned}$$

which on simplification gives

$$\begin{aligned} \oint_{C_i} \mathbf{P} \cdot \mathbf{n} ds = & \int_{z_0}^{z_0^+} P^2_{xx} dz \big|_{x=x_0^+} + \int_{x_0^+}^{x_0^-} -P^2_{xz} dx \big|_{z=z_0^+} + \int_{z_0^+}^{z_0} P^2_{xx} dz \big|_{x=x_0^-} \\ & + \int_{z_0}^{z_0^-} -P^1_{xx} dz \big|_{x=x_0^-} + \int_{x_0^-}^{x_0^+} -P^1_{xz} dx \big|_{z=z_0^-} + \int_{z_0^-}^{z_0} P^1_{xx} dz \big|_{x=x_0^+} \end{aligned}$$

Performing the integration on the right-hand side gives

$$\begin{aligned} u''_{i,j} \approx & P^2_{xx}\left(x_0^+, z_0\right)\frac{\Delta z}{2} + P^2_{xz}\left(x_0, z_0^+\right)\Delta x - P^2_{xx}\left(x_0^-, z_0\right)\frac{\Delta z}{2} \\ & - P^1_{xx}\left(x_0^-, z_0\right)\frac{\Delta z}{2} - P^1_{xz}\left(x_0, z_0^-\right)\Delta x + P^1_{xx}\left(x_0^+, z_0\right)\frac{\Delta z}{2} \end{aligned}$$

which on simplification gives

$$\begin{aligned} u''_{i,j} \approx & (\lambda + 2\mu)_2 \frac{u_{i+1,j} - u_{i,j}}{\Delta x}\frac{\Delta z}{2} + \lambda_2 \frac{w_{i+1/2,j+1} - w_{i+1/2,j}}{\Delta z}\frac{\Delta z}{2} \\ & + \mu_2\left(\frac{u_{i,j+1} - u_{i,j}}{\Delta z} + \frac{w_{i+1,j+1/2} - w_{i-1,j+1/2}}{2\Delta x}\right)\Delta x \\ & - (\lambda + 2\mu)_2 \frac{u_{i,j} - u_{i-1,j}}{\Delta x}\frac{\Delta z}{2} - \lambda_2 \frac{w_{i-1/2,j+1} - w_{i-1/2,j}}{\Delta z}\frac{\Delta z}{2} \\ & - (\lambda + 2\mu)_1 \frac{u_{i,j} - u_{i-1,j}}{\Delta x}\frac{\Delta z}{2} - \lambda_1 \frac{w_{i-1/2,j} - w_{i-1/2,j-1}}{\Delta z}\frac{\Delta z}{2} \\ & - \mu_1\left(\frac{u_{i,j} - u_{i,j-1}}{\Delta z} + \frac{w_{i+1,j-1/2} - w_{i-1,j-1/2}}{2\Delta x}\right)\Delta x \\ & + (\lambda + 2\mu)_1 \frac{u_{i+1,j} - u_{i,j}}{\Delta x}\frac{\Delta z}{2} + \lambda_1 \frac{w_{i+1/2,j} - w_{i+1/2,j-1}}{\Delta z}\frac{\Delta z}{2} \end{aligned} \tag{9.10}$$

where one-sided differences are used at the interface. We now equate equation (9.9) and equation (9.10) to give

$$
\begin{aligned}
u''_{i,j} = \frac{1}{\overline{\rho}}\Bigg[& \frac{(\lambda+2\mu)_2 + (\lambda+2\mu)_1}{2}\frac{u_{i+1,j} - 2u_{i,j} + u_{i-1,j}}{\Delta x^2} + \mu_2 \frac{u_{i,j+1} - u_{i,j}}{\Delta z^2} \\
& - \mu_2 \frac{u_{i,j} - u_{i,j-1}}{\Delta z^2} + \lambda_2 \frac{w_{i+1/2,j+1} - w_{i+1/2,j}}{2\Delta x \Delta z} + \mu_2 \frac{w_{i+1,j+1/2} - w_{i-1,j+1/2}}{2\Delta x \Delta z} \\
& - \lambda_2 \frac{w_{i-1/2,j+1} - w_{i-1/2,j}}{2\Delta x \Delta z} - \lambda_1 \frac{w_{i-1/2,j} - w_{i-1/2,j-1}}{2\Delta x \Delta z} \\
& - \mu_1 \frac{w_{i+1,j-1/2} - w_{i-1,j-1/2}}{2\Delta x \Delta z} + \lambda_1 \frac{w_{i+1/2,j} - w_{i+1/2,j-1}}{2\Delta x \Delta z} \Bigg]
\end{aligned}
\tag{9.11}
$$

and similarly

$$
\begin{aligned}
w''_{i,j} = \frac{1}{\overline{\rho}}\Bigg[& \frac{(\lambda+2\mu)_2 + (\lambda+2\mu)_1}{2}\frac{w_{i,j+1} - 2w_{i,j} + w_{i,j-1}}{\Delta z^2} + \mu_2 \frac{w_{i+1,j} - w_{i,j}}{\Delta x^2} \\
& - \mu_2 \frac{w_{i,j} - w_{i-1,j}}{\Delta z^2} + \lambda_2 \frac{u_{i+1,j+1/2} - u_{i,j+1/2}}{2\Delta x \Delta z} + \mu_2 \frac{u_{i+1/2,j+1} - u_{i+1/2,j}}{2\Delta x \Delta z} \\
& + \lambda_2 \frac{u_{i,j+1/2} - u_{i-1,j+1/2}}{2\Delta x \Delta z} - \lambda_1 \frac{u_{i,j-1/2} - u_{i-1,j-1/2}}{2\Delta x \Delta z} \\
& - \mu_1 \frac{u_{i-1/2,j+1} - u_{i-1/2,j}}{2\Delta x \Delta z} - \lambda_1 \frac{u_{i+1,j-1/2} - u_{i,j-1/2}}{2\Delta x \Delta z} \Bigg]
\end{aligned}
\tag{9.12}
$$

The u and w terms involving subscripts i-1/2, i+1/2,j-1/2, and j+1/2 are again approximated to maintain second-order accuracy.

9.4 Results in Acoustic case

The model in Figure (9.2) depicts the corner problem of Sochacki et al. [**68**]. The model adds a smooth circular region in the right bottom corner with the same parameters. The model in Figure (9.5) represents a squared salt dome and is similar to the model presented in Sochacki et al. [**68**] and Virieux [**81**]. In both models, the source in time is the derivative of the Gaussian with the form

$$f(t) = A(t-t_s)\exp[-\alpha(t-t_s)] \quad (9.13)$$

and the Reynolds ABCs used are those presented in the previous Chapter 3. The source configurations were chosen for each seismograms so that any dispersion would be minimised, and an approximate 20 Hz source would result.

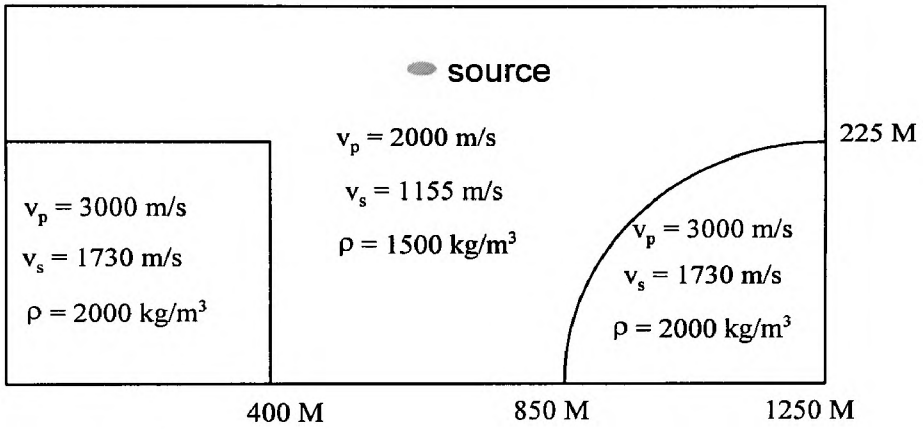

Figure (9.2) The geometry of the corner edge model.

The upper layer has a very low P-wave velocity of 2000 m/s and S-wave velocity of 1155 m/s compared to the velocity of the lower corners which is 3000 m/s and 1730 m/s. The upper layer has a density of 1500 kg/m^3 and the lower corners have a density of 2000 kg/m^3. The grid size is 4.17 m and the time step is 0.0009 s. The source is located at (625,500) and has parameters A = 250, t_s = 0.06525 s, and α = 11222. Figures (9.3), and (9.4) the show the reflected, transmitted, and diffracted waves from the two corners. The numerical solution obtained using the interface conditions in Figure (9.3). Figure (9.4) shows the results without interface conditions. The comparison with Figure (9.3) and (9.4) show good similarities with enhancements of reflected waves in Figure (9.3).

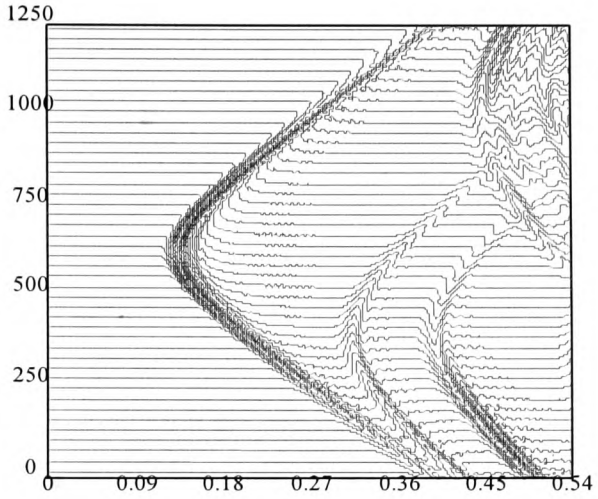

Figure (9.3) Synthetic seismogram generated from the FDM solutions of 2-D acoustic wave equation with the Reynolds ABCs for the corner-edge model the interface conditions.

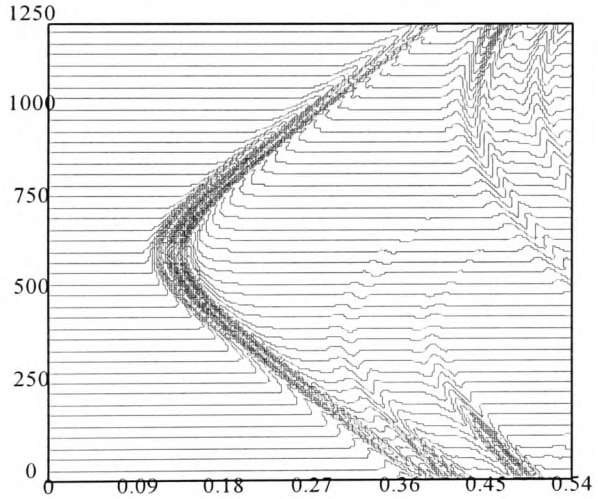

Figure (9.4) Synthetic seismogram generated from the FDM solutions of 2-D acoustic wave equation with the Reynolds ABCs for the corner-edge model without interface conditions.

The salt dome model contains of two layers with the dome rising from the lower medium intruding into the upper layer as shown in Figure (9.5). The velocities are 2500 m/s for the upper layer and 4500 m/s for the bottom layer. The grid size is 10 m and the time step is 0.0015 s. The source is located at (420, 210) and has parameters $A = 250$, $t_s = 0.126$ s, and $\alpha = 3118$ for optimal results presentation.

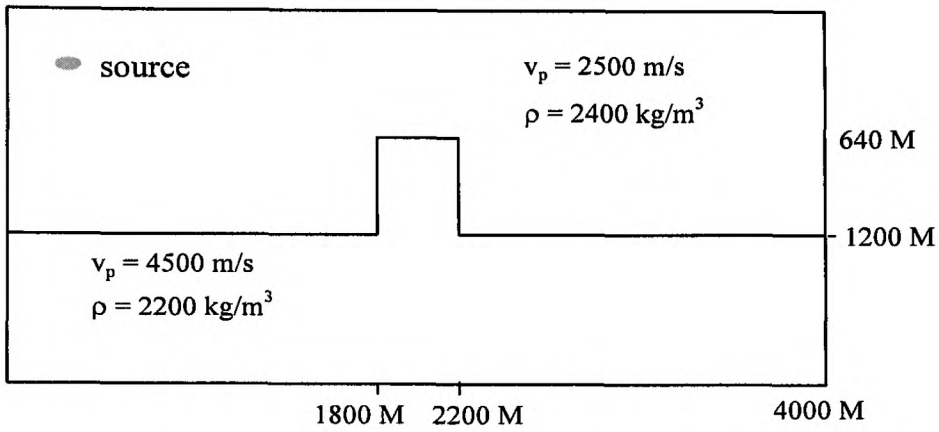

Figure (9.5) The geometry of the salt dome model.

Figure (9.6) shows the results obtained by using the interface conditions. Figure (9.7) shows the results for without interface conditions. The interface waves can be seen very clearly in Figure(9.6). Figure (9.7) shows the interface waves weaker than in Figure (9.6). The difference in waves travelling from the low velocity region into the dome and from the dome to the low velocity region are easily seen and is physically reasonable.

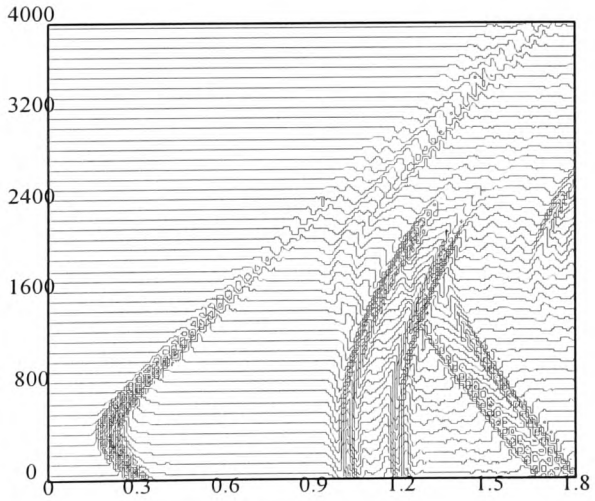

Figure (9.6) Synthetic seismogram generated from the FDM solutions of 2-D acoustic wave equation with the Reynolds ABCs for the corner-edge model with the interface conditions.

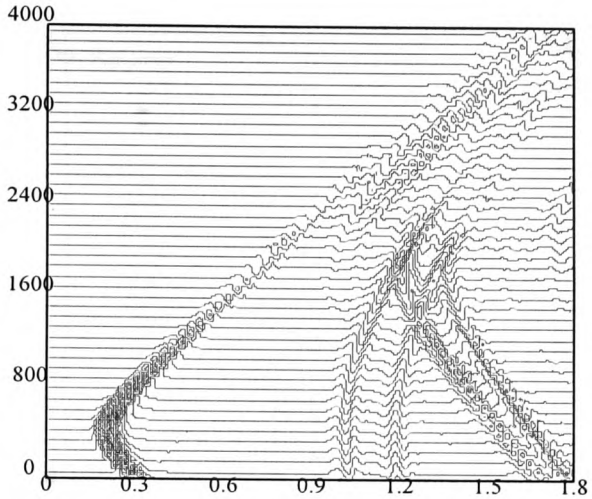

Figure (9.7) Synthetic seismogram generated from the FDM solutions of 2-D acoustic wave equation with the Reynolds ABCs for the corner-edge model without interface conditions.

9.5. Results in Elastic case

In this section we consider the interface conditions for an elastic medium. Three models are presented: the weathered-layer model for Rayleigh wave excitation by a point source at depth, and the corner-edge model for diffraction. The last model is for a complicated media.

9.5.1. Weathered-layer model

The geometry of the medium is shown in Figure (9.8). The upper layer has a very low P-wave velocity of 2000 m/s compared to the velocity of the half-space which is 6000 m/s and density is taken as a constant of 2500 kg/m^3. The compressional line source f(t), with a spectral content defined by $\alpha = 40$, see equation (9.13), is located near the surface in order to obtain efficient Rayleigh wave excitation.

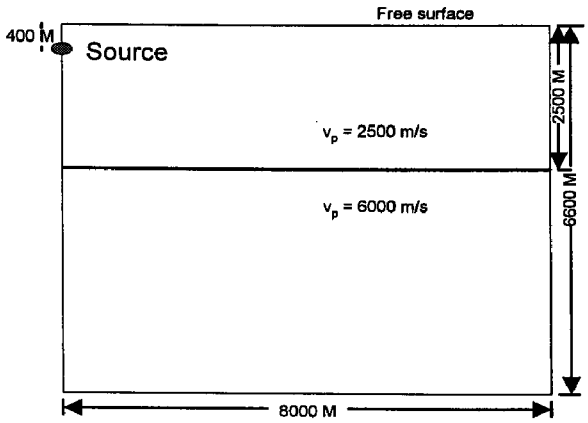

Figure (9.8) Geometry of the weathered-layer model.

In Figure (9.9a),and (9.9b), seismograms lasting 5 s present the features already studied in Kelly et al. [**37**], and Virieux [**82**]. A quantitative comparison is difficult because of the unknown spectral source content of Kelly et al. [**37**] and because of the graphical representation of seismograms. The direct P-wave and the Rayleigh wave dominate the seismograms. The PP- and PS- wave reflections clearly show a phase shift after the critical angle. The reflection at the free surface, which seems to come from a ghost source above the free surface, is called GP for the P-wave reflection and GS for the S-wave reflection. These phases are usually called pP and sP but we use the nomenclature of Virieux [**82**]. The GP phase is again reflected upward by the interface as a P-wave. This so called GPP phase stands between the PP and PS reflection. The head wave can be guessed, mainly when it arrives before the direct P-wave. With another choice of saturation for the picture, it would have been clearly seen. Then, the S reflection of GP phase, called GPS, and the P reflection of GS phase, called GSP, arrive in front of the phase obviously called GSS. The PPPP phase, which is the P incident phase twice reflected at the interface and once at the free surface, can hardly be seen at the bottom of

the seismogram. The Virieux results are shown in Figure (9.10). Small energetic phases are better seen on phase nomenclature.

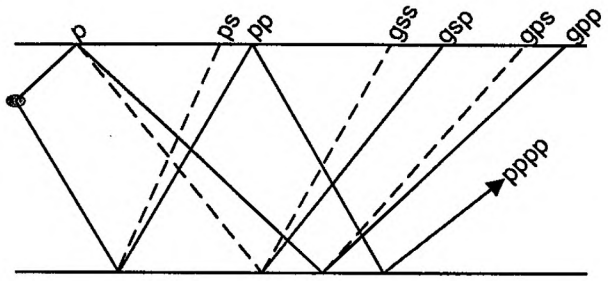

phase nomenclature

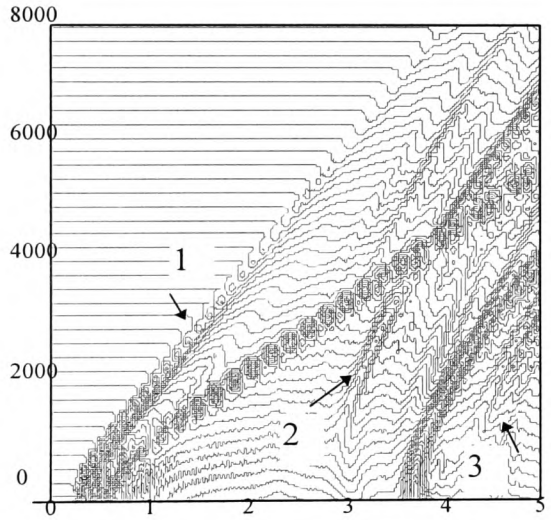

Figure (9.9a) The horizontal seismograms at the free surface for weathered-layer model. Theoretical arrival times are indicated for (1) P-wave, (2) PS reflection wave, (3) GSS wave.

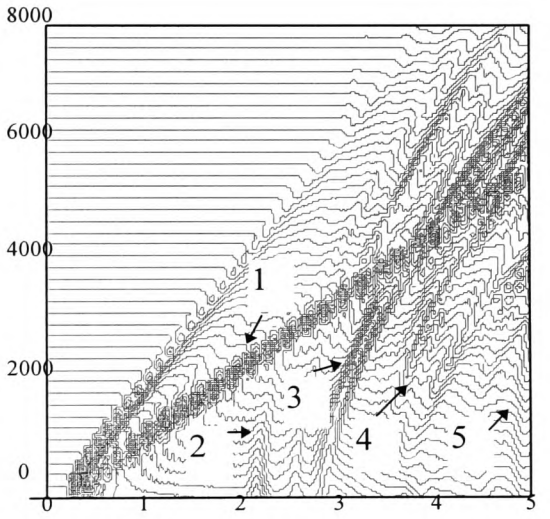

Figure (9.9b) The vertical seismograms at the free surface for weathered-layer model. Theoretical arrival times are indicated for (1) Rayleigh-wave, (2) PP-wave, (3) GPP wave, (4) GPS+GSP wave, and (5) PPPP wave.

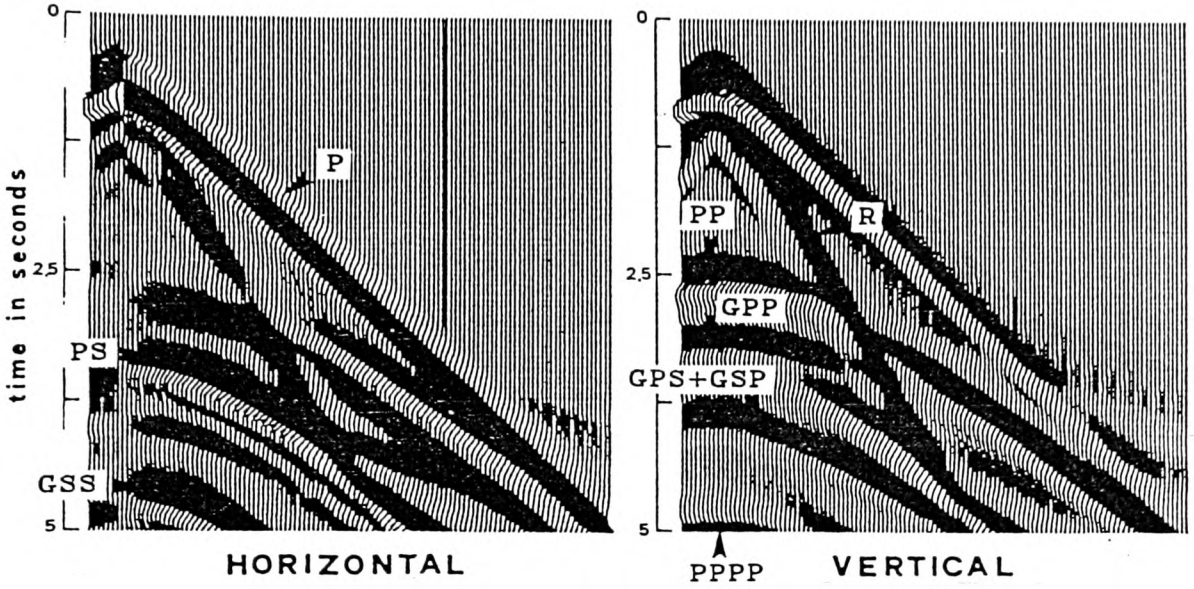

Figure (9.10) The horizontal and vertical seismograms show for Virieux results.

9.5.2 Corner edge model

The geometry of the medium is shown in Figure (9.11). The velocity of the upper medium is 6000 m/s while the lower medium has a velocity of 9000 m/s. The density of the lower medium is 2500 kg/m^3. The source f(t) has a spectral content defined by $\alpha = 40$, (see equation (9.13).

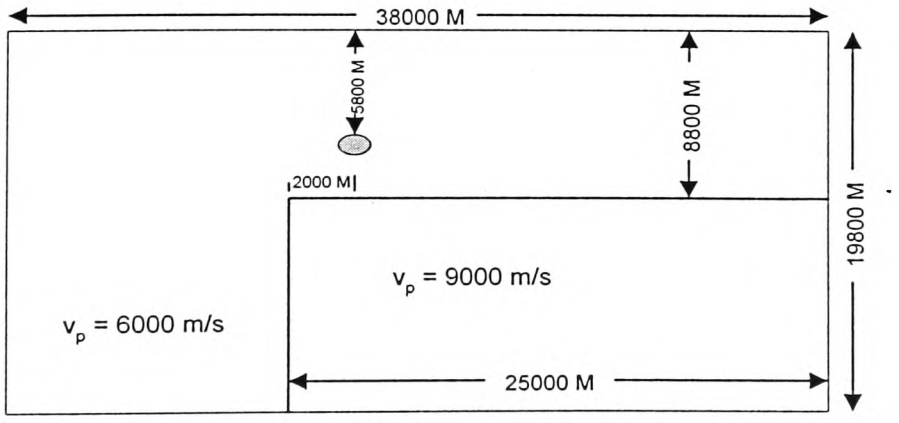

Figure (9.11) The geometry of the corner-edge model.

Figures (9.12a) and (9.12b) presents seismograms continuing 6 s on the free surface for grid increments h = 50 m. We use the same nomenclature of phases used in the previous section. After the direct P-wave, the PP reflection is associated with the PP diffraction. PS reflection is clearly seen on the horizontal component, but interfered later with the ghost GPP reflection and the ghost GPP diffraction, which are strong above the corner and source area. Another group of energetic waves, GPS and GSP waves, which are the S-wave reflection of the GP phase at the interface or the P-wave reflection of the GS phase, are not hidden by the residual reflection coming from the bottom where numerical radiation conditions were applied. Figure (9.13) shows the horizontal and vertical seismograms from the Virieux results.

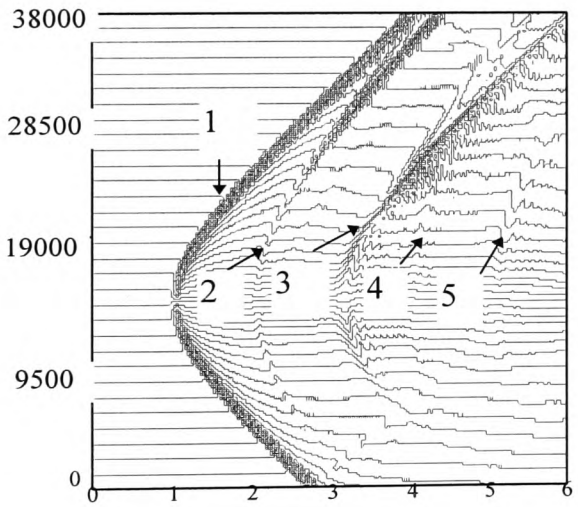

Figure (9.12a) The horizontal seismograms at the free surface for corner-edge model. Arrival times are indicated for (1) P-wave, (2) PP reflection wave, (3) PS reflection wave, (4) GPP ghost reflection wave, and (5) GPS + GSP wave..

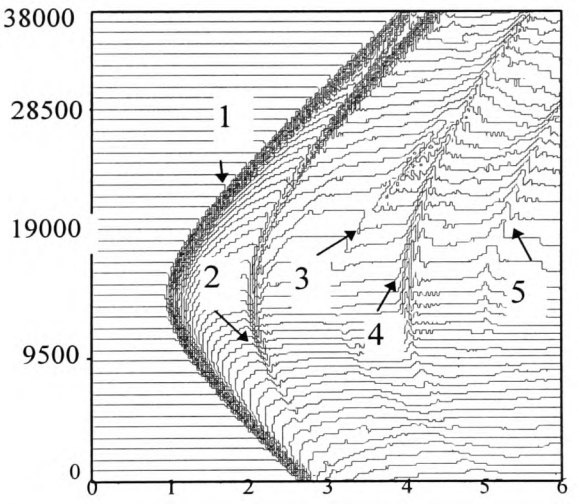

Figure (9.12b) The vertical seismograms at the free surface for corner-edge model. Arrival times are indicated for (1) P-wave, (2) PP reflection wave, (3) PS reflection wave, (4) GPP ghost reflection wave, and (5) GPS + GSP wave..

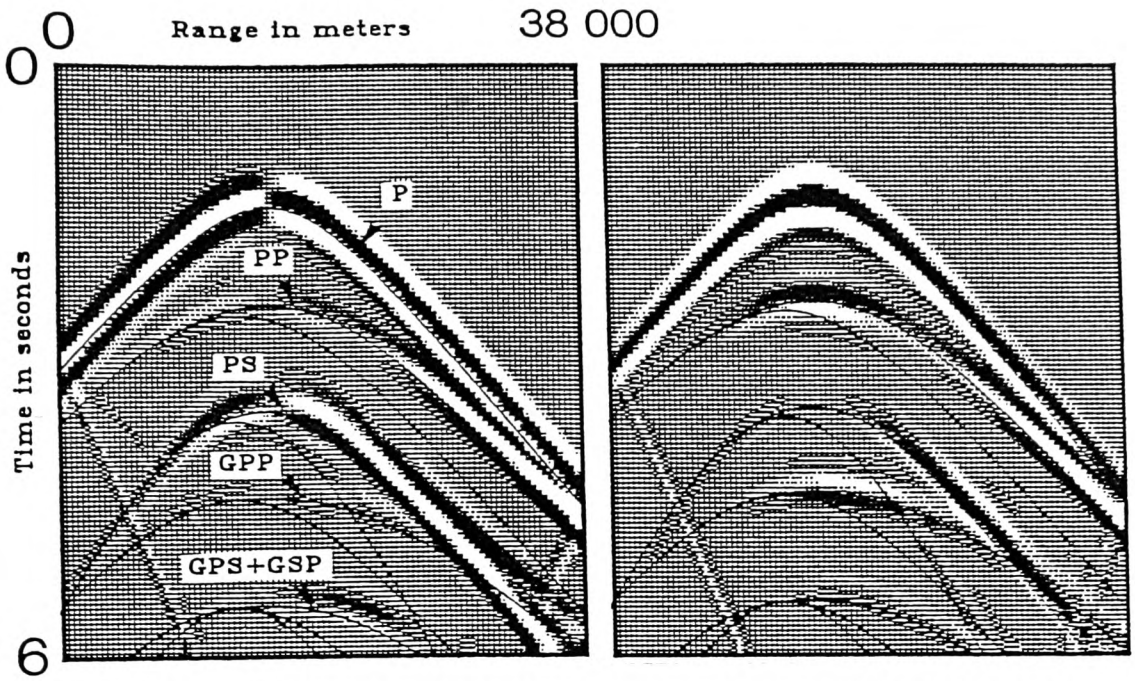

Figure (9.13) The horizontal and vertical seismograms show for Virieux results.

The model in Figure (9.2) is now employed for the elastic case. The synthetic seismograms are obtained by using the staggered grid method with interface conditions with results shown in Figure (9.14a) and (9.14b). Figures (9.15a) and (9.15b) show the results witout interface conditions.

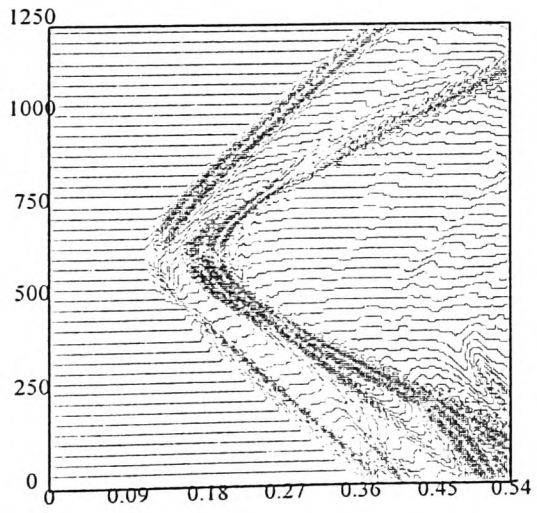

Figure (9.14a) The horizontal seismogram generated from the 2-D elastic wave equation with the interface conditions for the corner-edge model.

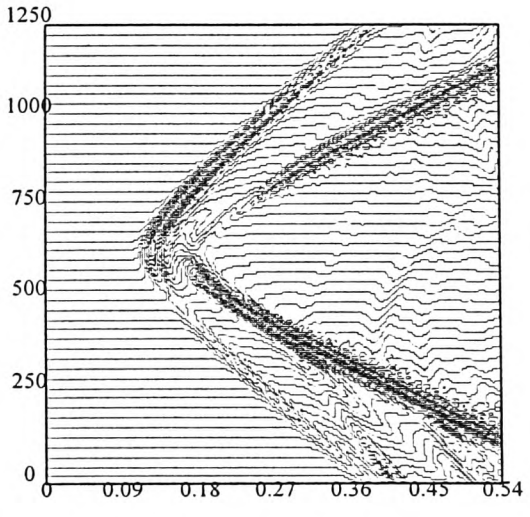

Figure (9.14b) The vertical seismogram generated from the 2-D elastic wave equation with the interface conditions for the corner-edge model.

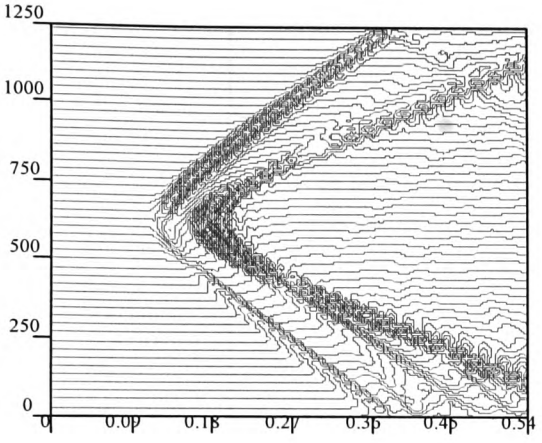

Figure (9.15a) The horizontal seismogram generated from the 2-D elastic wave equation without the interface conditions for the corner-edge model.

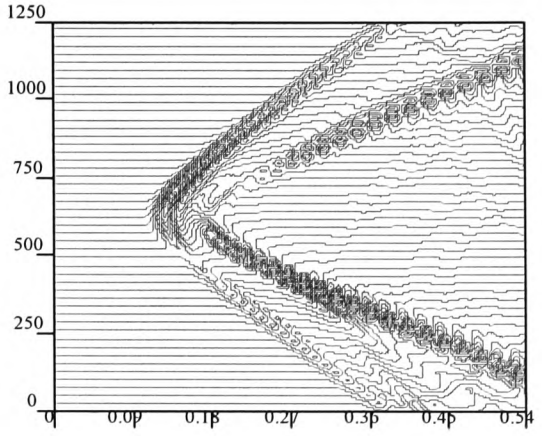

Figure (9.15b) The vertical seismogram generated from the 2-D elastic wave equation without the interface conditions for the corner-edge model.

The last model for Figure (9.16) shows a more realistic geologic formation; it is composed of four layered regions with a salt dome at the bottom and has a horizontal extent of 800 m and a vertical extent of 600 m. The compressional wave velocities from top to bottom are 2000 m/s, 3500 m/s, 4000 m/s, and 5500 m/s. The shear wave velocities are 1155 m/s, 2100 m/s, 2730 m/s, and 3100 m/s. The grid size is 4 m and the time step is 0.0006 s. The source is located on the surface at 400 m and has parameters $A = 0.25$, $t_s = 0.114$, and $\alpha = 3270$. Figures (9.17a) and (9.17b) show the results using interface condition for horizontal and vertical seismograms for this complicated region. Last Figures (9.18a) and (9.18b) show the results without interface condition for for horizontal and vertical seismograms.

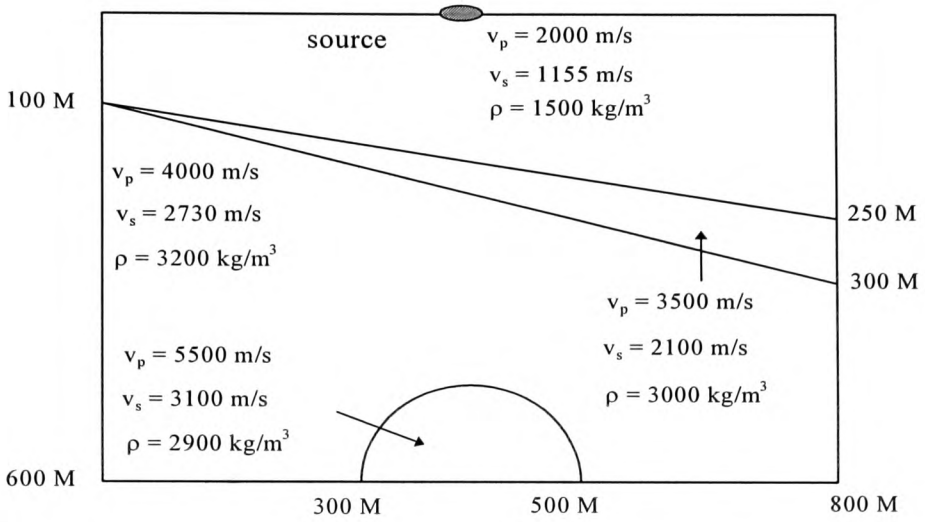

Figure (9.16) The geometry of comlicated region containing a wedge and dome model.

We compared 'without' interface condition results with interface condition results and exhibit good similarity.

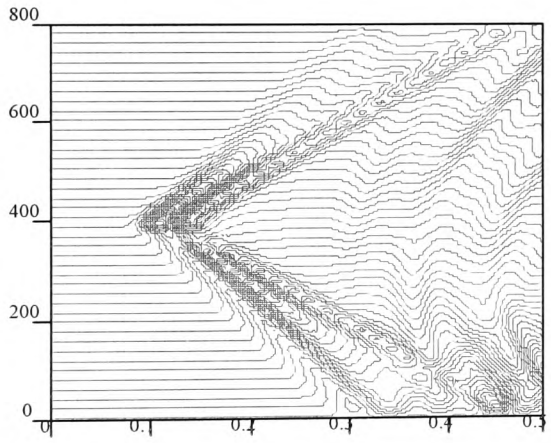

Figure (9.17a) The horizontal seismogram generated from the 2-D elastic wave equation with the interface conditions for complex region.

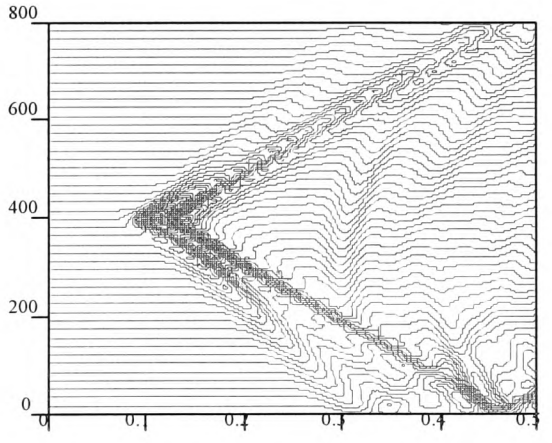

Figure (9.17b) The vertical seismogram generated from the 2-D elastic wave equation with the interface conditions for complex region.

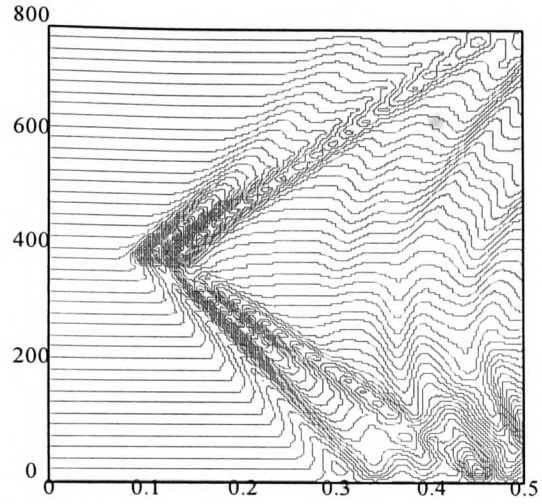

Figure (9.18a) The horizontal seismogram generated from the 2-D elastic wave equation without the interface conditions for complex region.

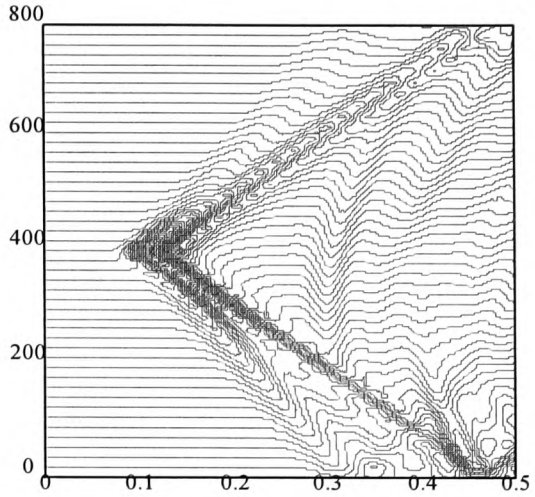

Figure (9.18b) The vertical seismogram generated from the 2-D elastic wave equation without the interface conditions for complex region.

9.6 Conclusion

In this chapter we examined the 2-D acoustic and elastic wave propagation with the interface conditions. Our approach (staggered grid & box) employs Sochacki interface conditions and found results to be good on comparison with Virieux and Sochacki. Reynolds ABCs are again used to good effect, and the use of Sochacki interface conditions yield results that are marginally better than those from the standard approach.

CHAPTER 10

CONCLUSIONS

10.1 Summary

The main aims of the thesis were (**1**) to determine the most satisfactory numerical approach to model numerical seismic wave propagation and also (**2**) to ascertain if rock interfaces could be inferred from signals received at geophones.

To this end the research work of this thesis is based on the computational simulation of seismic wave propagation generated by;

i) Equations of motion in 2-D Cartesian coordinates for acoustic and elastic cases.

ii) Equations of motion in 3-D Cartesian coordinates for acoustic and elastic cases.

iii) Equations of motion in 3-D cylindrical coordinates for acoustic and elastic cases.

In chapter 2 the equations of motion were presented in general coordinates. The seismic wave propagation problem is formulated more specifically for Cartesian, cylindrical and bipolar coordinates. Use of the bipolar coordinate system was found to be unsuited for the current approach. In chapter 3 the general FDM was presented. The numerical results from the FDM sometimes do not give the correct results. We examined the requirements of consistency, convergence and stability necessary to

provide the required results along with the difficulties associated with numerical dispersion and dissipation. After that we employed two different absorbing boundary conditions which are namely Reynolds and Clayton & Engquist ABCs.

In chapter 4 we found that many researchers had studied the standard FDM almost exclusively in seismic wave modelling with comparatively little use of other finite difference methods. The traditional approaches used tend to use differing methods. i.e. Alterman & Karal [**3**] used the "Box" method, Ottaviani [**55**] employed the "(ur+us)" method and Reynolds[**64**], and Stephen [**72**] just used traditional FDM. The staggered grid method was first employed by Virieux [**82**]. Building on this we developed the VSM approach. Later we studied the source and receivers. A compressional point source was used for 3-D cylindrical coordinates by Stephen [**72**] and Impulsive line source used for 2-D Cartesian coordinates by Ottoviani [**55**], and these formed the basis for our work.

In chapter 5 we solved the 2-D acoustic wave propagation problem numerically with Dirichlet and absorbing boundary conditions (ABCs) in one medium, two media and multimedia. The convergence criteria for the methods used were closely examined. One medium results converge approximately with 6 m grid space. As we expected the two media, and multimedia results converge as the one medium results because of the bigger wave velocity employed. We employed two different absorbing boundary conditions and the Clayton-Engquist ABCs were found not to be as good as those of Reynolds ABCs in our applications. The more Reynolds ABCs in cylindrical coordinates were most effective in numerical solutions. It is useful to compare our numerical solution with that of other researchers. We solved the 2-D acoustic wave

problem with the our new variable scale method (VSM) and obtained new results which are in strong agreement with the standard FDM results. It was pleasing to note that interface reflections were clearly visible from the seismograms, through rather weaker in cylindrical coordinates.

In chapter 6 we studied the elastic case for 2-D Cartesian, and cylindrical coordinates, and solved 2-D elastic case for three different methods namely the staggered grid, (UR+US) and box methods. We employed two different methods together, namely the "staggered grid" and the "Box" methods. So far as we are aware nobody has studied these two models together for this problem. The staggered grid method gives stable and acceptable results for material discontinuities. Firstly, we analysed the convergence criteria and we found to be convergence one medium and two media results at a 6 m grid space. As we expected the multimedia results converged approximately at 3 m. Generally we found the Reynolds's ABCs to be better than the those of Clayton & Engquist. Later we compared three methods to determine which one was the better method. The staggered grid and box method is generally better than the (UR+US) and standard FDM & box methods. On comparison of the (UR+US) results with those of Ottaviani's [55] and the Box method's results with the Alterman's results, good quantitative and qualitative agreement was found. Close agreement with the Reynolds's results was again found. Finally, in this chapter we studied a 2-D cylindrical elastic medium. We compared two methods and found results to be in good agreement with both staggered grid and box methods results. Again strong interface reflected waves were apparent though weaker for cylindrical coordinates.

In chapter 7 we investigated a 3-D acoustic and elastic wave equation with the boundary conditions for Cartesian coordinates. We investigated the use of the box & staggered grid, and standard FDM & box methods for one medium, two media and multimedia. Firstly, we analysed to convergence, criteria for all models and one medium results converged at a 25 m grid space, and as we expected two media and multimedia results converged as the one medium results. Secondly, we examined the 3-D acoustic wave problem for two methods, and we found good agreement between both. On comparison of our results with those of Chang and McMechan's [**14**] good agreement was again found. We also compared our 3-D elastic wave problem results for two methods again with those of other researchers and again favourable comparisons were found. Interface reflected waves again clearly apparent.

In chapter 8 we investigated 2-D and 3-D Cartesian and cylindrical coordinates for borehole modelling. Two methods for elastic waves in 2-D and 3-D homogeneous media were numerically investigated and compared in terms of their behaviour in the borehole and outside the borehole. We found the staggered grid & box method gave better results than the VSM approach. The waves are particularly difficult to synthesise in borehole environments because the VSM was not stable for large contrasts in Poisson's ratio, such as at fluid-solid interfaces (Stephen [**71**]). Both methods produced most acceptable results and these are novel results. Yet again interface reflections were strongly represented in seismograms.

In chapter 9 we investigated the 2-D acoustic and elastic wave propagation with the Sochacki interface conditions. We employed the staggered grid methods with

Sochacki interface conditions. We found results to be good agreement those of others. Use of the Sochacki approach leads to marginally clearer interface reflections waves.

10.2 Main Conclusions

1) Our new approach, which is the staggered grid method with box method enhances flexibility and accuracy of the numerical solution. This approach is the best of the techniques examined here for the analysis of the elastic wave propagation problems.

2) The ABCs which are needed to make it easier to analyse the far field wave propagation problem on the computer have been closely examined. The Reynolds's and Clayton-Engquist ABCs were conceived, implemented, and presented for both acoustic and elastic cases. The numerical solutions show that the both ABCs presented are acceptable for the acoustic case with those of Reynolds marginally better. However, The Clayton-Engquist ABCs are only stable when v_s/v_p is greater than 0.46. But the Reynolds ABCs used are stable in all cases and are ideal in an our appproach (staggered grid and box methods) because they uses only values on lines normal to the absorbing surface.

3) The VSM was implemented and presented for Cartesian and cylindrical coordinates. The α and β constant values were seen to have a significant role in the system and wave domain. The $A(\xi)$ value requires careful consideration in the VSM because of concerns related to numerical stability and accuracy of the numerical solution. The approach can prove most useful in single borehole modelling if used with care.

4) Strong interface reflections were visible in Cartesian seismograms through somewhat weaker in the case of cylindrical coordinates.

5) Modelling of boreholes was presented in 2-D and 3-D elastic wave propagation problems. Two main approaches have been used by others to model borehole geometries; one using just the inside of the borehole and the other just the borehole exterior. One goal of this work was to begin to fill in this gap by including simple borehole configurations within elastic media our new approach (staggered grid & box and VSM) modelling, which we have completed successfully.

6) The Sochacki interface conditions were presented in 2-D acoustic and elastic wave propagation problems that were tested on various geometries, and could be compared with other approaches without these special interface conditions. These conditions proved stable for both 2-D acoustic and elastic wave propagation and enhanced interface reflections.

It is expected that the our new approaches and associated computer programs will prove useful in computational seismology.

10.3 Recommendations for Future Work

On the basis of the research carried out we therefore have some ideas for future work to be developed based on that presented.

1) The research on single borehole modelling may be developed to obtain different variable scale functions for numerical solutions in 2-D and 3-D equations.

2) The acoustic and elastic wave propagation problem may be solved with either bipolar coordinates or with the use of two variable scale functions that fit naturally onto the two borehole geometry. This would require adaption of ABCs.

3) Because the Sochacki interface conditions can be an improvement on standard approaches in 2-D, the extension of this method to 3-D would seem justified.

4) The work carried out for the 2-D and 3-D elastic wave propagation may be extended to include thermal cases. For instance the temperature of the earth's crust increases by approximately 11^0C for each km of depth. With explicit temperature dependence in the model through λ and μ, say, such thermal effects can be examined.

REFERENCES

1. **Aki K., and Richards P.,** (1980), "Quantitative Seismology, Theory and Methods", W. H. Freeman& Co.

2. **Alford R. M., Kelly K. R., and Boore D. M.,** (1974), "Accuracy of Finite-Difference Modeling of the Acoustic Wave Equation", Geophysics, Vol. 39, P. 834-842.

3. **Alterman Z. and Karal F.** (1968) . "Propagation of Elastic Waves in Layered Media by Finite-Differences Methods" , Bull. Seism. Soc. Am. ,Vol. 58 , P. 367-398.

4. **Alterman Z. and Lowenthal D.,** (1970), "Seismic Waves in a Quarter and Three-quarter Plane", Geophysics, P. 101-126.

5. **Alterman Z. and Rotenberg, A.,** (1969), "Seismic Waves in Quarter Plane", Bull. Seism. Soc. Am., Vol. 59, P. 347-368.

6. **Archuleta, R. J., and Frazier, G. A.,** (1978), "3D Numerical Simulations of Dynamic Faulting in a Half-Space", Bull. Seism. Soc. Am., Vol. 68, P. 541-572.

7. **Astin J.** , (1974) , "Three-Dimensional Orthogonal Coordinates" , Int. J. Math. Educ. Sci. Technol. , Vol. 5 , P. 271-278.

8. **Batchelor G. K.** , "An Introduction to the Fluid Dynamics" , Cambridge University Press, 1967.

9. **Bayliss, A., Jordan, K.E., LeMesuier, B.J., and Turkel, E.,** (1986), "A Fourth-Order Accurate Finite-Difference Scheme for the Computation of Elastic Waves", Bull. Seism. Soc. Am., Vol. 76, P. 1115-1132.

10. Biot, M. A., (1952), "Propagation of Elastic Waves in a Cylindrical Bore Containing a Fluid", J. Appl. Phys. Vol. 23, P. 997-1005.

11. Birkeland P. W. and Larson E. E. , "Putnam's Geology" , Oxford University Press , 1978.

12. Boore, D.M., (1972), "Finite-Difference Methods for Seismic Wave Propagation in Heterogeneous Materials", in Methods in Computational Physics, Vol. 11, B.a. Bolt (editor), Academic Press, New York.

13. Bullen K. E. , "An Introduction to the Theory of Seismology" , Cambridge University Press , 1963.

14. Chang W., and McMechan G. A., (1989), "Absorbing Boundary Conditions for 3-D Acoustic and Elastic Finite-Difference Calculations", Bull. Seism. Soc. Am., Vol. 79, No. 1 P. 211-218.

15. Chen, K., (1984), "Numerical Modeling of Elastic Wave Propagation in Anisotropic Inhomogeneous media: a Finite-Element Approach", (Ext. Abst): Soc. Expl. Geophys. 54 th Intern. Meeting, P. 631-632.

16. Chen, H.W., and McMechan, G.A., (1993), "3-D Physical Modeling and Pseudo-spectral Simulation of Seismic Common Source Data Volumes", Geophysics, Vol. 58, P. 121-133.

17. Cheng, C. H., and Toksoz, M. N., (1981), "Elastic Wave Propagation in a Fluid-Filled Borehole and Synthetic Acoustic Logs", Geophysics, Vol. 46, P. 1042-1053.

18. Clayton R. and Engquist B. , (1977), "Absorbing Boundary Conditions For Acoustic And Elastic Wave Equations", Bull. Seism. Soc. Am. , Vol. 67(6), P.1529-1540.

19. Dai, N., Vafidis, A., and Kansewich, E. R., (1995), "Wave Propagation in Heterogeneous, Porous Media: a Velocity-Stress, Finite-Difference Method", Geophysics, Vol. 60, P. 327-340.

20. Dang, Z., and McMechan, G.A., (1995), "3D Viscoelastic Anisoptropic Modeling of Data from a Multicomponent, Multiazimuth Seismic Experiment in Northeast Texas", Geophysics, Vol. 60, P. 1128-1138.

21. Daudt, C. R., Braile, L. W., Nowack, R. L., and Chiang, C. S., (1989), "A Comparison of Finite-Difference and Fourier Method Calculations of Synthetic Seismograms", Bull. Seism. Soc. Am. Vol. 79, P. 1210-1230.

22. Dietrich, M., and Bouchon, M., (1985), "Synthetic Vertical Seismic Profiles in Elastic Media", Geophysics, Vol. 50, P. 224-234.

23. Emerman S. H. and Stephen R. A., (1983), "Comment on Absorbing Boundary Conditions for Acoustic and Elastic Wave Equations", Bull. Seism. Soc. Am. Vol. 72, P. 661-665.

24. Feshbach, H., and Morse, P. M., (1953), "Methods of Theoretical Physics", McGraw-Hill Book Company, New York

25. Fornberg B., (1990), "High-Order Finite Differences and The Pseudospectral Method on Staggered Grids", Siam J. Numer. Anal., Vol. 27 No. 4 P. 904-918.

26. Fuyuki M., and Matsumato Y., (1980), "Finite Difference Analysis of Rayleigh Wave Scattering at a Trench", Bull. Seism. Soc. Am. Vol.70, P. 2051-2069.

27. Gazdag, J., (1981), "Modeling of the Acoustic Wave Equation with Transform Methods", Geophyscis, Vol. 46, No. 6, P. 854-859.

28. Grant F. S., and West G. F., (1965), "Interpretation Theory in Applied Geophysics", McGraw-Hill Book Company, New York.

29. Graves R. W., and Clayton, R.W., (1992), "Modeling Path Effects in Three-dimensional Basin Structures", Bull. Seism. Soc. Am. Vol. 82, P. 81-103.

30. Graves R. W., (1996), "Simulating Seismic Wave Propagation in 3-D Elastic Media Using Staggered-Grids Finite Differences", Bull. Seism. Soc. Am. Vol. 86, No. 4, P. 1091-1106.

31. Hardage, B. A., (1981), "An Examination of Tube Wave Noise in Vertical Seismic Profiling Data", Geophysics, Vol. 46, P. 892-903.

32. Hardage, B. A., (1983), "Vertical Seismic Profiling", Part A: Principles: Geophysical Press.

33. Higdon R. L., (1991), "Absorbing Boundary Conditions for Elastic Waves", Geophysics, Vol. 56, P. 231-241.

34. Igel, H., Riollet, B., and Mora, P., (1992), "Accuracy of Staggered 3-D Finite-Difference Grids for Anisotropic Wave Propagation", 62 nd Ann. Int. Meeting, Soc. Expl. Geophys. Expended Abstracts, P. 1244-1246.

35. Igel, H., Mora, P., and Riollet, B., (1995), "Anisotropic Wave Propagation Through Finite-Difference Grids", Geophysics, Vol. 60, No. 4, P. 1203-1216.

36. Ilan, A., Ungar, A.U., and Alterman, Z., (1975), "An Improved Representation of Boundary Contions in Finite-Difference Schemes for Seismological Problems, Geophys. J. R. Astr. Soc., Vol. 49, P. 727-745.

37. Kelly K. R., Ward R. W., Treitel S., and Alford R. M., (1976), "Synthetic Seismograms: A Finite-Difference Approach", Geophysics, P. 2-27.

38. Kosloff, R., and Kosloff, D., (1986), "Absorbing boundaries for Wave Propagation Problems", J. Comp. Phys., Vol. 63, P. 363-376.

39. Kurkjian, A.L., Coates, R.T., White, J.E., and Schmidt, H., (1994), "Finite-Difference and Frequency-Wavenumber Modeling of Seismic Monopole Sources and Receivers in Fluid-Filled Boreholes", Geophysics, Vol. 59, No. 7, P. 1053-1064.

40. Lai W. M. , Rubin D. and Krempl E. "Introduction to Continuum Mechanics" , Pergamon Press , 1978.

41. Lapidus L., and Pinder G. F., (1982), "Numerical Solution of Partial Differential Equations in Science and Engineering", Wiley-Interscience.

42. Lavergne M., (1989), "Seismic Methods", Graham & Trotman Lmt.

43. Lee, M. W., and Balch, A. H., (1982), "Theoretical Seismic Wave Radiation from a Fluid-Filled Borehole", Geophysics, Vol. 47, P. 1308-1314.

44. Levander A. R. , (1988), "Fourth- Order Finite-Difference P-SV Seismograms", Geophysics, Vol.53 (11), P. 1425-1436

45. Lindman E. L., (1975), "Free Space Boundaries for The Scalar Wave Equation", J. Comp. Phys., Vol. 18, P. 66-78.

46. Long L. T. and Liow J. S., (1990), "A Transparent Boundary for Finite-Difference Wave Simulation", Geophysics, Vol. 55, No. 2, P. 201-208.

47. Luo Y. and Schuster G. , (1990) , "Parsimonious Staggered Grid Finite-Differencing of The Wave Equation" , Geophysical Research Letters , Vol. 17 , P. 155-158.

48. McMechan, G. A., (1985), "Synthetic Finite-Offset Vertical Seismic Profiles for Laterally Varying Media", Geophysics, Vol. 50, P. 627-636.

49. Mitchell A. R. , "Computational Methods in Partial Differential Equations" , Aberdeen University Press , 1969.

50. Miyatake, T., (1992), "Numerical Simulation of Three- Dimensional Faulting Processes with Heterogeneous Rate- and state -dependent Friction", Tectonophysics, Vol. 211, P. 223-232.

51. Mora, P., (1989), "Modeling Anisotropic Seismic Waves in 3-D", 59 th Ann. Int. Meeting, Soc. Expl. Geophys., Exp. Abstracts. P. 1039-1043.

52. Morton K. W., and Mayers D. F., (1994), "Numerical Solution of Partial Differential Equations", Cambridge University Press.

53. Nicoletis, L. M. A., Bamberger, A., Quiblier, J. A., Joly, P., and Kern, M., (1990), "Hole geometry and Anisotropic Effects on Tube-Wave Propagation: A Quasi-Static Study", Geophysics, Vol. 55, P. 167-175.

54. Ording, J. R., and Redding, V. L., (1953), "Sound Waves Observed in Mud-Filled Well after Surface Dynamite Charges", J. Acoust. Soc. Am., Vol. 25, P. 719-726.

55. Ottaviani M. , (1971) , "Elastic Wave Propagation in Two Evenly-Welded Quarter-Spaces". Bull. Seism. Soc. Am. , Vol. 61 , P. 1119-1152.

56. Peterson, E. W., (1974), "Acoustic Wave Propagation along a Fluid-Filled Cylinder", J. Appl. Phys., Vol. 45, P. 3340-3350.

57. Pitarka A., Suetsugu D., and Takenaka H., (1996), "Elastic Finite-Difference Modelling of Strong Motion in Ashigara Valley for the 1990 Odawara, Japan, Earthquake", Bull. Seism. Soc. Am. Vol. 86, No. 4, P. 981-990.

58. Quin, H., and Das, S.X., (1989), "A Hybrid Boundary integral Equation Method for the Computation of Source Time Functions for 3-D Rupture Propagation", Geophysics, Vol. 96, P. 163-177.

59. Randall C. J., (1988), "Absorbing Boundary Condition for the Elastic Wave Equation", Geophysics, Vol. 53, No. 5, P. 611-624.

60. Randall C. J., (1989), "Absorbing Boundary Condition for the Elastic Wave Equation: Velocity-Stress Formulation", Geophysics, Vol. 54, No. 9, P. 1141-1152.

61. Randall C. J., Scheider, D.J., and Wu, P.T., (1991), "Multiple Borehole Acoustic Waveforms Synthetic Logs with Beds and Borehole Washouts", Geophysics, Vol. 56, P. 1757-1769.

62. Renaut R. A. and Petersen J., (1989), "Stability of wide-angle Absorbing Boundary Conditions for The Wave Equation", Geophysics, Vol. 54, No. 9, P. 1153-1163.

63. Reshef, M., Kosloff, D., Edwards, M., and Hsiung, C., (1988), "Three-Dimensional Elastic Modeling by the Fourier Method", Geophysics, Vol. 53, No. 9, P. 1175-1193.

64. Reynolds A. C. , (1978) , "Boundary Conditions for the Numerical Solution of Wave Propagation Problems" , Geophysics, Vol. 43 , P. 1099-1110.

65. Smith, G. D. , "Numerical Solutions of Partial Differential Equations" , Oxford University Press , 1985.

66. Smith, W.D., (1974), "A Nonreflecting Plane boundary for Wave Propagation Problems", J. Comp. Phys., Vol. 15, P. 492-503.

67. Sochacki J., Kubichek R., George J., Fletcher W. R., and Smithson S., (1987), "Absorbing Boundary Condition and Surface waves", Geophysics, Vol. 52, P. 60-71.

68. Sochacki J., George J., Ewing R. E, and Smithson S., (1991), "Interface Conditions for Acoustic and Elastic Wave Propagation", Geophysics, Vol. 56, P. 168-181.

69. Spiegel, M. R., (1974) "Vector Analysis and an Introduction to Tensor Analysis", McGraw-Hill Book Company.

70. Stacey, R., (1988), "Improved Transparent Boundary Formulations for the Elastic Wave Equation", Bull. Seism. Soc. Am., Vol. 78, P. 2089-2097.

71. Stephen R. A.,(1983), "A Comparison of Finite-difference and Reflectivity seismograms for Marine Models", Geophysics, Vol. 72, P. 39-57.

72. Stephen R. A. , Cardo-Casas F. and Cheng C. H. , (1985) , "Finite-Difference Synthetic Acoustic Logs", Geophysics , Vol. 50 , P. 1588-1609.

73. Stephen R. A.,(1988), "A Review of Finite-Difference Methods for Seismo-Acoustics Problems at the Seafloor: Rev. Geophys. Sp. Phys., Vol. 26, P. 445-458.

74. Sun R., McMechan G., (1987), " Line Sources for Seismic Modelling by Finite Differences in Inhomogeneous Media", Geoexploration, Vol. 24 P. 1183-196.

75. Sun , R., and McMechan G. A., (1988), "Finite-Difference Modelling of Borehole Resonances", Energy Sources, Vol. 10, P. 55-75.

76. Temme, P., and Muller, G., (1982), "Numerical Simulation of Vertical Seismic Profiling", Geophysics, Vol. 50, P. 177-188.

77. Thomas J. W., (1995), "Numerical Partial Differential Equations", Springer-Verlag.

78. Vidale J. E., and Clayton R. W., (1986), "A Stable Free-Surface Boundary Condition for Two-Dimensional Elastic Finite-Difference Wave Simulation", Geophysics, Vol. 51, P. 2247-2249.

79. Vidale J. E., (1990), "Finite-Difference Calculating of Traveltimes in Three Dimension", Geophysics, Vol. 55, No. 5, P. 521-526.

80. Villarreal, A., and Scales, J.A., (1997), "Distributed 3-D Finite-Difference Modeling of Wave Propagation in Acoustic Media", Computers in Physics, Vol. 11, No. 4, P. 388-399.

81. Virieux J. (1984) , "SH Wave Propagation in Heterogeneous Media: Velocity - Stress Finite-Difference Method" , Geophysics , Vol. 49 , P. 1933-1937.

82. Virieux J. (1986) , "P-SV Wave Propagation in Heterogeneous Media: Velocity - Stress Finite-Difference Method" , Geophysics , Vol. 51 , P. 889-901.

83. White J. E. ,(1962), "Elastic Waves along a Cylindrical Bore", Geophysics, Vol. 27, P. 327-333.

84. White J. E., and Sengbush, R. L., ,(1963), "Shear Waves from Explosive Sources", Geophysics, Vol. 6 1001-1019.

85. White J. E. ,(1983), "Underground Sound (Application of Seismic Waves)" , Elsevier ,.

86. Wild A. J., (1995), "Finite-Difference Considerations Directed Towards A Hybrid Method For Three- Dimensional Seismic Waveform Modelling", Ph.D. Thesis, University Of Cambridge.

87. Yoon K-H. and McMechan G. A. , (1992), "3-D Finite-Difference Modelling Of Elastic Waves In Borehole Environments", Geophysics, Vol. 57(6), P.793-804.

88. Yoon K-H. and McMechan G. A. , (1995), "Simulation of Long-Period 3-D Elastic Responses for Whole Earth Models", Geophys. J. Int., Vol. 120, P. 721-730.

89. Yoon K-H. and McMechan G. A. , (1996), "3-D Eight-Order Elastic Finite-Difference Modeling of Refraction and Strong-Motion Data from the Coyote Lake Region, California", Bull. Seism. Soc. Am., Vol. 86, No. 3, P. 616-626.

90. Zahradnik J., Moczo P., and Hron F., (1993), "Testing Four Elastic Finite-Difference Schemes for Behavior at Discontinuities", Bul. Seism. Soc. Am., Vol. 83, No. 1, P. 107-129.